Pre-yield shearing regime of a magnetorheological fluid (MRF)

Waad Nassar

A Thesis
submitted to the École Polytechnique Palaiseau-France
In fulfillment of the requirements for the degree of

Doctor of Mechanical Engineering

presented by

Waad NASSAR

Pre-yield shearing regime of a magnetorheological fluid (MRF)

prepared at

Solid Mechanics Laboratory- École Polytechnique (CNRS UMR 7649)
and at Laboratoire d'Interfaces Sensorielles- CEA

Thesis Committee

Yannick Peysson	Researcher at *IFP Energies nouvelles*, Professor at *École Polytechnique*	Referee
Alain Ponton	CNRS research Director at *Paris Diderot University*	Referee
Élise Lorenceau	CNRS Researcher at *École des Ponts-ParisTech*,Professor at *École Polytechnique*	Examiner
José Lozada	Engineer and Researcher at *CEA*	Co-Supervisor
Xavier Boutillon	CNRS Research director at *École Polytechnique*,Professor at *École Polytechnique*	Supervisor

Dedicated to

My family
for their unlimited love, blessings and encouragements

Acknowledgments

I am experiencing sincere feelings of achievement and satisfaction after accomplishing this PHD project. Looking into the past I realize how difficult it was for me to succeed on my own. I wish to express my deep gratitude to all those who have supported me throughout this thesis and who without their help and support, this research project would not have been possible.

It gives me immerse pleasure to express my deep sense of gratefulness and appreciation to my supervisor, Professor Boutillon Xavier, Solid mechanics laboratory, École Polytechnique. I owe him my most sincere gratitude for giving me the opportunity to work with him, for his invaluable guidance, his support and constant encouragement even in my most difficult moments.

I wish to extend my warmest thanks to all those who have helped me with my work in the Solid Mechanics Laboratory especially Guimbretière Jean-Erik, Eytard Jean-Christophe, De Greef Vincent and Tanguy Alexandre.

I would also like to convey thanks to the Commissariat à l'énergie atomique et aux énergies alternatives, CEA, for providing the financial means and facilities. I want to also thank my co-supervisor Lozada José.

I am indebted to many of my colleagues who supported me during these three years specially Grasso Eva, Tabibian Shadan, Auffray Nicolas, Sleiman Hussein and Besse Camille as well as all the PhD students in the LMS. I thank you all from my heart four your help and encouragement. Not to forget my best friends who have always been there for me: Haddad Carmen, El Masri Aya and Assi Ghaydaa. Really by having you, I feel myself very fortunate.

Lastly, I wish to express my love and gratitude to my beloved family; thank you for you understanding, support and endless love throughout my life.

Contents

1 MRF literature review **11**

1 Literature review . . . 12
1.1 MRF description . . . 12
1.2 MRF time response . . . 14
2 MRF applications . . . 14
2.1 MRF common operational modes . . . 14
2.2 MRF in civil engineering . . . 15
2.3 MRF in automotive . . . 16
2.4 MRF in human prosthesis . . . 17
2.5 MRF in military and defense . . . 17
2.6 MRF in human interfaces . . . 17
3 Rheology . . . 19
3.1 Definition of rheology . . . 19
3.2 Methods of modelisation in rheology . . . 19
4 Literature review of MRF rheology . . . 19
4.1 Preyield behavior . . . 20
4.1.1 Microscopic approach . . . 20
4.1.2 Macroscopic approach . . . 22
4.2 Measurements and model adjustments for the yield threshold . . . 25
4.3 Post-yield behavior . . . 33
5 Conclusion . . . 37

2 Experimental techniques **39**

1 Device description . . . 40
2 Mechanical elements . . . 41
2.1 Stepper motor . . . 41
2.1.1 Description . . . 41
2.1.2 Command . . . 42
2.2 Plate support . . . 43
2.3 Transmission system . . . 44
2.3.1 Transmission cables . . . 44
2.3.2 Transmission path . . . 44
3 Magnetic and electrical circuits . . . 45
3.1 Electrical circuit . . . 45
3.1.1 Magnetic circuit . . . 46
3.1.1.a Basic magnetic equations . . . 47
4 Sensors . . . 48
4.1 Displacement measurement . . . 48
4.2 Force measurement . . . 49
4.3 Magnetic field measurements . . . 51
5 Microscopy . . . 51
5.1 High resolution numerical microscope observations . . . 51
5.1.1 Scanning electron microscope (SEM) . . . 52

5.2 Stereo microscope observations . . . 53
5.3 Particle image velocimetry PIV . . . 54
5.3.1 Definition . . . 54
5.3.2 Application to MRF observation . . . 55
6 Tests . . . 56
6.1 Motion . . . 56
6.1.1 High frequency isolation . . . 57
6.1.2 Plate holder velocity response . . . 61
6.1.3 Forces: F_y and F_z . . . 62
6.2 Shearing force F_x . . . 63
6.2.1 Noise level . . . 63
6.2.2 Drag Force $F_{bias\,1}$ . . . 63
6.2.3 Shearing force due to the unmagnetized region of the plate $F_{bias\,2}$. . . 64
6.3 Magnetic field . . . 64
6.4 Degaussing process . . . 65
7 Conclusion . . . 67

3 Microscopic observations 69
1 Micro-structure . . . 70
1.1 SEM description . . . 70
1.2 Scanning electron microscopy of MRF . . . 71
1.2.1 Geometric analysis of particles . . . 71
1.2.2 Chemical analysis of particles . . . 72
2 Particles and aggregates . . . 74
3 Internal MRF structure dependency with B . . . 77
3.1 Increasing B on initially isotropic MRF suspension . . . 77
3.2 Increasing B in an initially formed chain outside the fluid . . . 79
3.3 Influence of B on initially formed chains inside the fluid . . . 81
3.4 Decreasing B on an isotropic suspension and chains outside the fluid. . . . 83
4 Internal MRF structure during shearing . . . 85
4.1 Volume shearing . . . 87
4.2 Fluid plate interfacial shearing . . . 92
5 Conclusion . . . 97

4 Regime of initial shearing 99
1 Reversibility . . . 101
2 Internal fluid structure dependency . . . 103
3 Shear modulus K_1 . . . 107
3.1 Magnetic field dependency B . . . 108
3.2 Shearing rate dependency $\dot{\gamma}$ . . . 108
3.3 Particle volume fraction dependency . . . 109
3.4 Shearing plate thickness dependency e . . . 110
3.5 Influence of the nature and surface state of the shearing plate on K_1 . . . 110
4 Limit of the initial shearing regime τ_{12} . . . 112
4.1 Magnetic field dependency B . . . 112
4.2 Shearing rate dependency $\dot{\gamma}$ . . . 114
4.3 Particle volume fraction dependency ϕ . . . 115
4.4 Influence of the nature and surface state of the shearing plate on τ_{12} . . . 116
4.5 τ_{12} shearing plate thickness dependency e . . . 117
5 Conclusion . . . 117

5 Intermediate shearing regime **119**
1 Microscopic observations . . . 122
2 Shear modulus K_2 . . . 123
2.1 Internal fluid structure dependency . . . 123
2.2 Magnetic field dependency B . . . 124
2.3 Shearing rate dependency $\dot{\gamma}$ . . . 125
2.4 Particle volume fraction dependency ϕ . . . 126
2.5 Shearing plate thickness dependency e . . . 127
2.6 Influence of the nature and surface state of the shearing plate on K_2 . . . 128
3 Interpretation . . . 130

6 Sliding regime **133**
1 Maximum measured force F_{23} . . . 134
1.1 Internal fluid structure dependency . . . 134
1.2 Magnetic field dependency B . . . 136
1.3 Shearing rate dependency $\dot{\gamma}$ . . . 138
1.4 Particle volume fraction dependency ϕ . . . 138
1.5 Shearing plate thickness dependency e . . . 139
1.6 Influence of the nature and surface state of the shearing plate on F_{23} . . . 140
2 Discussion . . . 142
2.1 MRF yield stress literature review . . . 142
3 Comparison between Lord datas and my experiments . . . 142
4 Interpretation and modelisation . . . 144
5 Conclusion . . . 147

Introduction

Both laboratories LMS at École Polytechnique and LISA at CEA-LIST are engaged in the development of haptic MRF interface. The first goal is to reproduce the tactile feedback of a traditional piano key.

MRF are a dispersion of magnetic micro-particles in a non-magnetic carrier fluid. Their rheological properties depend on the ambient magnetic field. They are used in several controllable industrial applications such as mechanical dampers, actuators and clutches [25, 27, 34, 45, 42].

The Bingham model is the basic model describing the behavior of this type of fluids. With this model, the variation of the shear stress $\Delta\tau$ is supposed to vary linearly with the shearing rate variation $\Delta\dot{\gamma}$. The point where the shear rate is zero, $\dot{\gamma}$=0, is called yield point or threshold stress τ_y (Eq: 1). The yield stress τ_y depends strongly on the magnetic field H.

$$\begin{cases} \tau = \tau_y(H) + \eta\dot{\gamma} & \tau \geq \tau_y \\ \dot{\gamma} = 0 & \tau < \tau_y \end{cases} \tag{1}$$

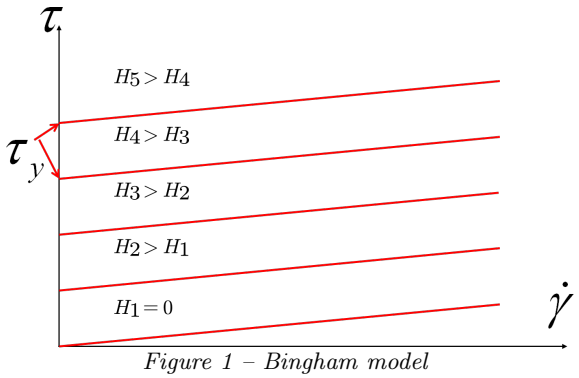

Figure 1 – Bingham model

With its tunable flow behavior, the MRF has been proved to be useful in the design of several controllable fluid-based devices (Sec. 2 in Chap. 1). The Bingham model has been used for the control and characterization of most of these devices. However this model makes no prediction with regard to the MRF behavior in the pre-yield regime and does not predict any dependency between the shear stress τ and the shear rate $\dot{\gamma}$ for shear stresses values $\tau < \tau_y$, therefore drawing a line in the above curves (fig. 1) between 0 and τ_y will be a misunderstanding.

The behavior of the MRF below yield stress has received less attention.

No microscopic observations of the phenomenon taking place in the internal MRF structure at work have been treated until nowadays. Theoretical predictions of the mechanisms are suggested by microscopic rheological models [23, 4, 48] without taking into consideration real rheological mechanisms into account in the modeling. Macroscopic quantitative studies of the MRF resistance force to shearing have been done by several researchers [18, 5, 1], their corresponding models are based on mathematical polynomial fits of experimental MRF resistance force with shearing stress in the post-yield zone. In these approaches, no physical explanation is presented.

The understanding of the MRF mechanisms under yield stress is needed when a MRF is used in human-machine interfaces. The existing MRF models being based on theoretical assumptions (at the microscopic level) and neglecting the physical phenomena ruling the MRF behavior (at the

macroscopic level) are unsatisfying for our haptic application. In order to take maximum advantages of the fluid, an understanding of the pre-yield regime, at the macroscopic and microscopic level, is necessary.

My PHD report will be organized as follows:

In the first chapter, I present a literature review on MRF applications and properties.

Chapter two is dedicated to the description of the experimental device used to study the pre-yield regime. Macroscopic and microscopic measurement means and efficiency tests done to the experimental device are presented in chapter three.

Experimental results and comparison with literature will be discussed in chapters four, five and six.

Chapter 1

MRF literature review

Contents

1	**Literature review**	**12**
2	**MRF applications**	**14**
3	**Rheology**	**19**
4	**Literature review of MRF rheology**	**19**
5	**Conclusion**	**37**

This chapter presents a literature review of both rheological and magnetic properties of the MRF. It includes a description of the different MRF applications and behavioral models.

1 Literature review

1.1 MRF description

Magnetorheological fluids are a dispersion of magnetisable micron-sized particle in a non-magnetic carrier fluid. Their diameter a may reach 10μm and their volume concentration in the carrier fluid may range between $20\% < \phi < 40\%$ [8, 6, 14, 22, 55].

MRF are part of controllable fluids of which characteristics change from fluid-like to solid-like behavior upon the application of a magnetic field B [19, 15, 11]. The essential physical mechanism for this behavior change, as presented in the literature, is thought to be that the application of the magnetic field H induces a magnetic polarization in each particle. The dipole-dipole attraction between the dispersed magnetic particles leads to the formation of chains in the direction of the magnetic field. Once aligned in this manner, the motion of the iron particles is restricted and the MRF liquid hardens into a near-solid state. When the magnetic field is removed, the particles return to their free-flowing liquid state [19, 12]. For an applied magnetic field H of 150-250 kA.m^{-1}, a MRF can exhibit a maximum yield stress of 50-100 kPa [3, 9, 5].

Figure 1.1 shows the activation steps of the MRF as presented in the literature.

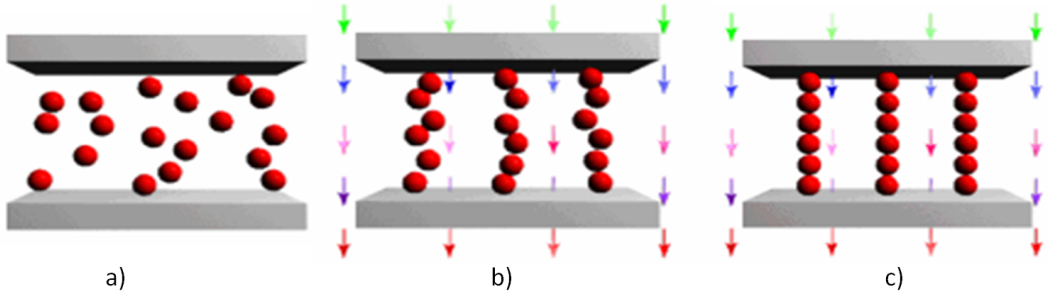

Figure 1.1 – Activation steps of MR fluid, arrows present the magnetic field B direction (after Fernando Goncalves [20]).

A technical drawback of the MRF is their tendency to sedimentation; additives are used to prevent settling and agglomeration without affecting their magnetic properties. It was found that adding nano-wires to a MRF suspension reduces significantly the rate of particle-settling without affecting its yield stress value (figure 1.2)[44]. The coating of cast iron particles with guar gum helps the particles to form a three-dimensional network structure and hence prevents their sedimentation and hardening (figure 1.3)[14]. According to Zisper, the addition of a thin non magnetic film to the MRF particles has the same effect [55]. Additional sub-micron particles or sized fillers such as carbon monotubes, fumed silica (FS) to the MRF suspension as proposed by Bong Jun and co-workers, was found to increase the particle dispersion stability in mineral oil (MO) (figure 1.4)[3, 49].

a)

Table 4. Sedimentation percentages of the samples

Sample ID	Composition	Sedimentation percentage (%)
3	50 wt% spheres	72.9
4	44 wt% spheres 6 wt% wires	23.4
5	60 wt% spheres	66.7
6	52 wt% spheres 8 wt% wires	14.0
7	80 wt% spheres	14.8
8	78 wt% spheres 2 wt% wires	8.8
9	76 wt% spheres 4 wt% wires	5.7

b)

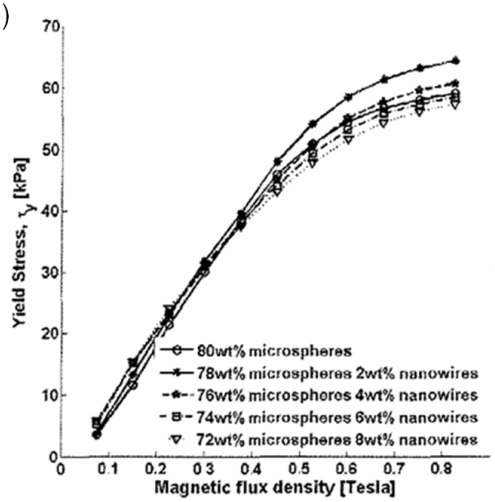

Figure 1.2 – Effect of nanowires on MRF yield stress (after Ngatu et al., [44]).

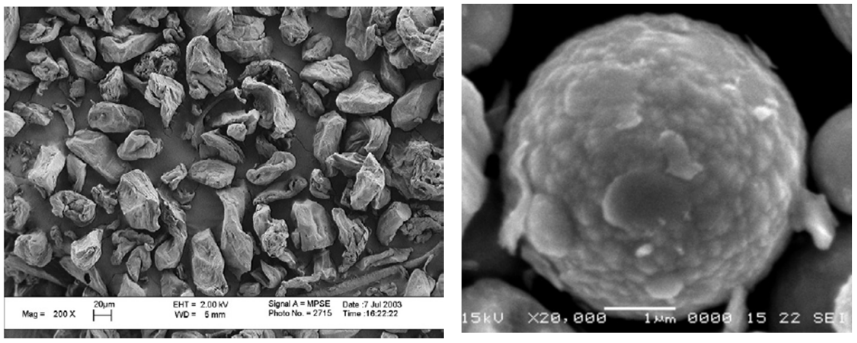

Figure 1.3 – SEM photograph of a)guar gum powder; b)cast iron particle coated with guar gum (after Fang et al.,[14]).

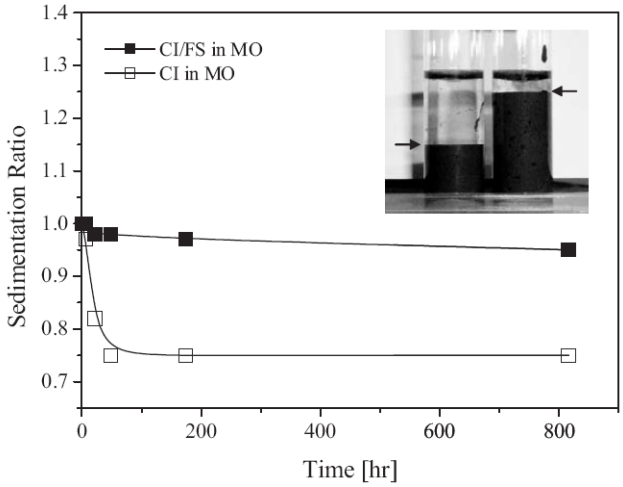

Figure 1.4 – Comparison between sedimentation ratio of carbonyl iron (CI) and carbonyl iron fumed silica mixture (CIFS) in mineral oil solution (MO) (after Sung et al.,[49]).

1.2 MRF time response

MRF time response, T, is defined as the transition time required by the fluid to reach 95% of its final performance. It is one of the important criteria to study MRF devices performance.

In the literature, the response time of MRF covers a broad range from 0.1 ms up to 100 ms. This broad span in the reported response duration is due to the determination of the device time characteristic (electric and magnetic circuit) rather than the fluid itself.

The response time for a whole MRF clutch device was estimated by Kavlicoglu *et al*, it was found to be varying between 20ms$< T <$ 65ms. The input current and shearing velocity were also found to have a big effect on it [36].

By imposing a step current to a plate-plate magnetho-rheometer (MCR501) Laun and co-workers estimated a switching time equal to T=2.8 ms (start-up) and T=1.8 ms (shutdown) [37]. Goncalves *et al.* have shown that the change in the particle configuration upon the application of a magnetic field B occurs in less than 1 millisecond. This short response time allows their use in many mechanical devices.

2 MRF applications

MRF are used in a wide range of applications: civil engineering, automotive, human prosthesis, military and defense, optics and human interfaces.

In this section I present a brief literature review of the various MRF applications and a presentation of our haptic interface.

2.1 MRF common operational modes

Depending on the type of stresses that the MRF is subjected to, we can distinguish three different operational modes[9]:

1. flow mode (known also as valve mode): the fluid is flowing between two stationary poles (figure 1.5a);

2. direct shear mode: the fluid is sheared between two plates, one moving relative to the other (figure 1.5b);

3. squeeze flow mode: the fluid is sheared between two plates moving in the direction perpendicular to their planes (figure 1.5c).

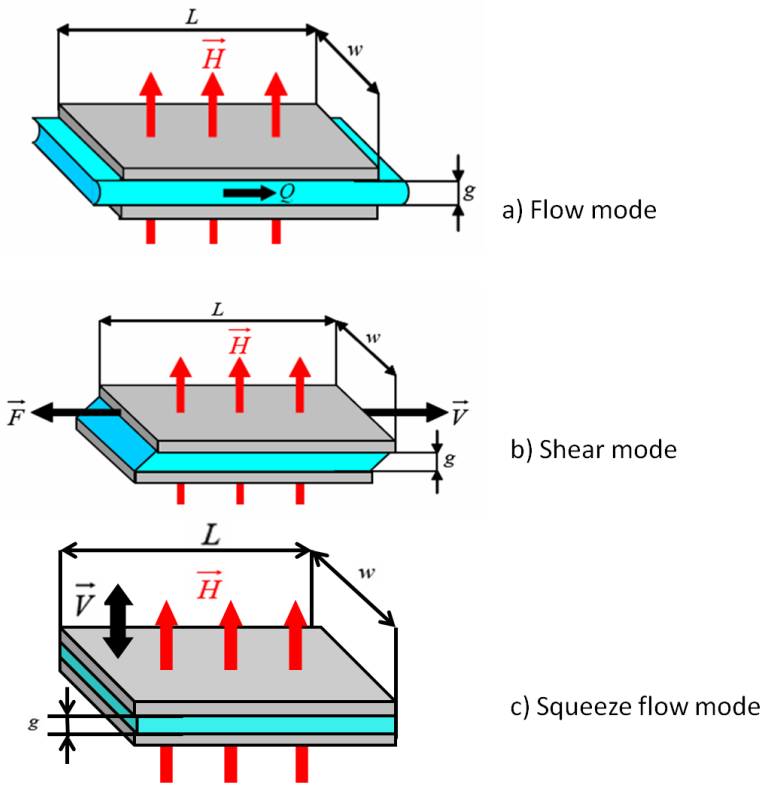

Figure 1.5 – Basic operational modes of MRF.

In all operational modes, the magnetic field is perpendicular to the planes of the plates.

2.2 MRF in civil engineering

In the field of civil engineering, MR dampers act essentially as shock absorbers, their resistance force is used to control excessive structural response and to absorb the detrimental shocks resulting form strong earthquakes and high winds [34].

Figure 1.6 shows the MR damper inaugurated in 2002, in the Dongting bridge in China. Valve shearing operational mode is used in this case.

Figure 1.6 – MRF in Dongting bridge in China (after J.M., Ko, Y. Q., and Ni, [13]).

2.3 MRF in automotive

MRF has been widely used in several fields in the automotive industry. Its low operating power requirements, high dynamic range, large force capacity and little time response make them adequate to these applications [53, 7]. It has been used by Audi in their magnetic system ride (figure 1.7) where conventional oil dampers are replaced by MRF shock absorbers. The flow mode operation is used in this application. The appropriate damping force delivered is controlled by varying the electromagnetic field within the fluid. MRF has also been used by Porsche in 2010 (Porsche GT3 and GT2) and by Honda on their 2011 models.

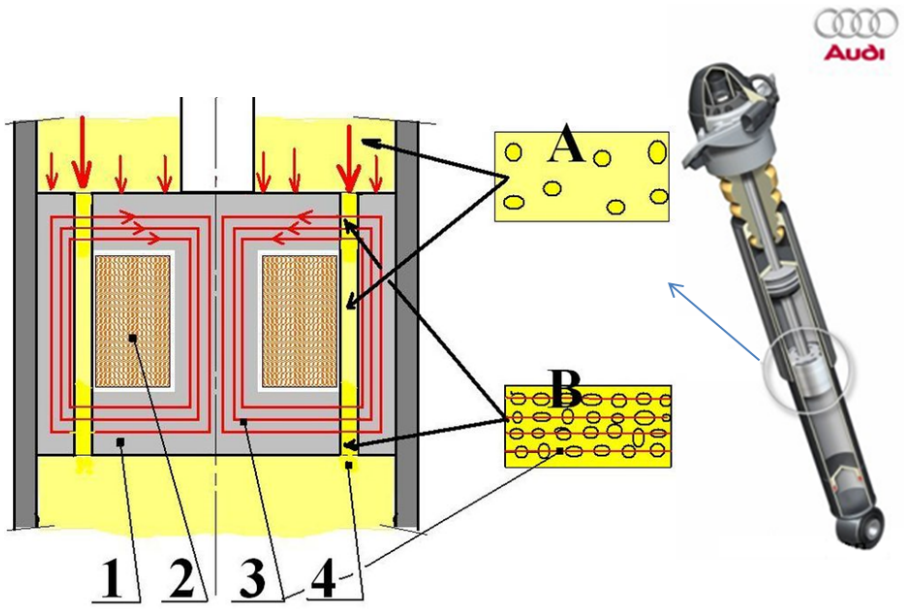

Figure 1.7 – Audi magnetic ride; 1:valve 2:coil 3:magnetic field 4:MRF (after www.audi.com).

MRF is also used in car seats as shock absorber in the event of a crash (figure 1.8).

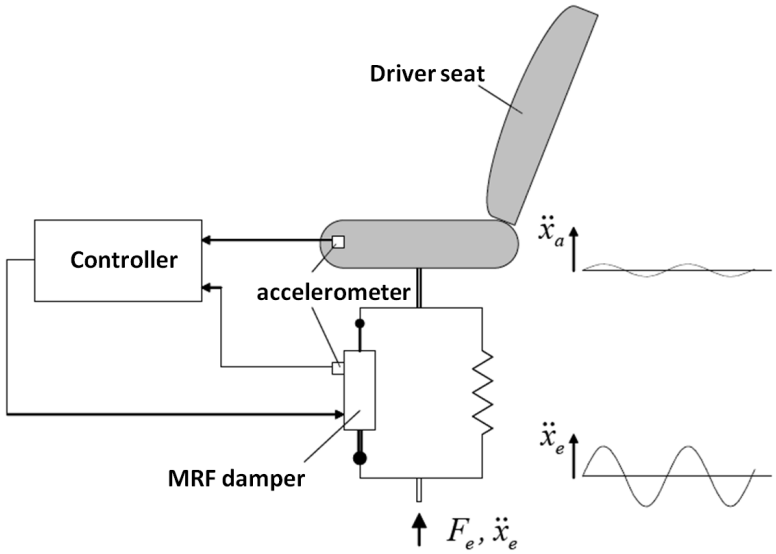

Figure 1.8 – "Motion Master Ride Management" commercialized by Lord Corporation (after Janocha et al., [30]).

2.4 MRF in human prosthesis

Biedermann Motech 8 markets since 2000 "Smart Magnetix", a magnetorheological damper used in human prosthetic legs [31]. It decreases the shock delivered to the patients leg, when jumping for example (figure 1.9). The damping system is self-contained; its controlling loop (measuring and command system) is integrated within the prosthesis.

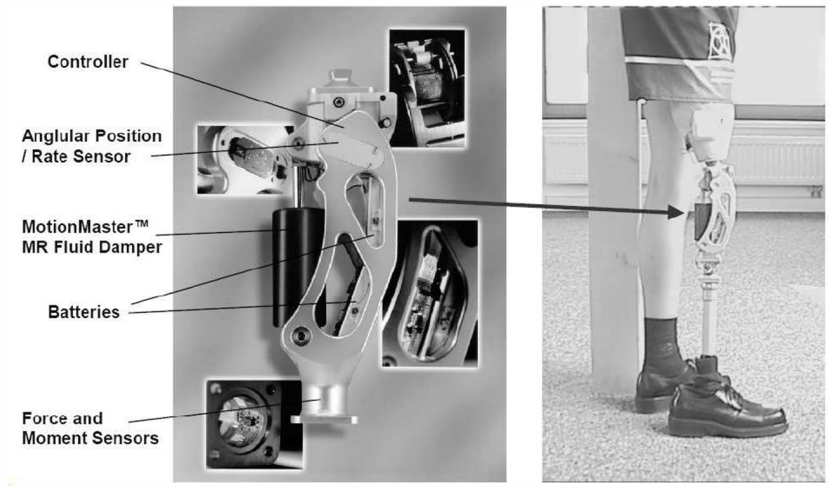

Figure 1.9 – Commercial "Smart Magnetix" prosthesis provided by a MotionMaster MR fluid clamper (after J. David Carlson [7]).

2.5 MRF in military and defense

MRF is also used in the military. Its application as dynamic shock absorber and damper decreases the shock delivered to a passenger's spinal column and consequently attenuates the rate of permanent injuries during crash [52]. The research office of the U.S. army is currently funding researches into using MR fluid to enhance body armor.

2.6 MRF in human interfaces

W.H.Li *et al* presented a two degrees of freedom MR actuator joystick for virtual reality applications (figure 1.10).

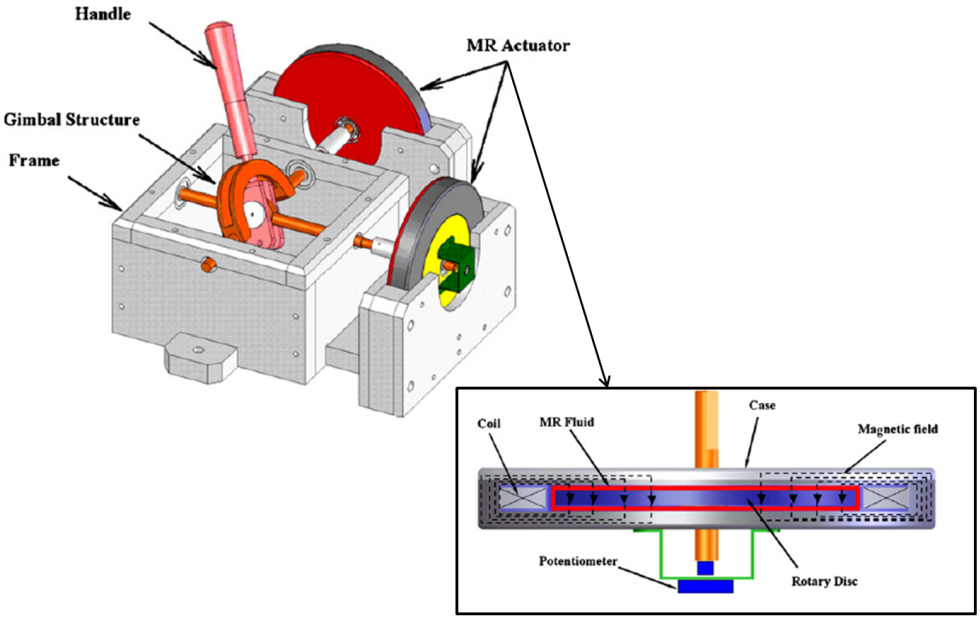

Figure 1.10 – MRF joystick (after W.H.Li et al., [40]).

The MR actuator operates in the direct-shear mode. MRF is sheared between the disc surface and the plate. Its viscosity changes in the presence of a magnetic field, therefore the resistance torque will change consequently [40]. The Bingham plastic model is used to control the MRF response.

During his PhD thesis, Lozada presented a MRF device to brake the movement of the piano key [32](Lozada design figure 1.11). In his piano key prototype, the MRF is sheared in the direct shear operational mode. Crankshaft system is used to transform the key rotation to a plate translation. The fluid is placed in a cavity between two magnetic poles. Depending on the force exerted by the pianist, a control loop evaluates the needed current. To solve guiding problems Lozada suggested the use of an amagnetic shearing plate.

To improve this invention many points were reviewed. First the transformation of the rotation to translation necessitated the use of the crankshaft and a problem of butting appeared. Second the system used to guide the plate in the cavity generates passive forces. According to Lozada conception, the linear shearing mode used in the device seems to be effective while Bingham plastic model will not be sufficient to its control.

The modified piano key conception is presented in figure 1.11. The linear shearing mode is conserved. The linear shearing plate is replaced by a curved one fixed to the piano therefore the transmission system is eliminated. The fluid cavity has the form of the plate. According to this conception, both types of shearing plate magnetic and amagnetic can be used.

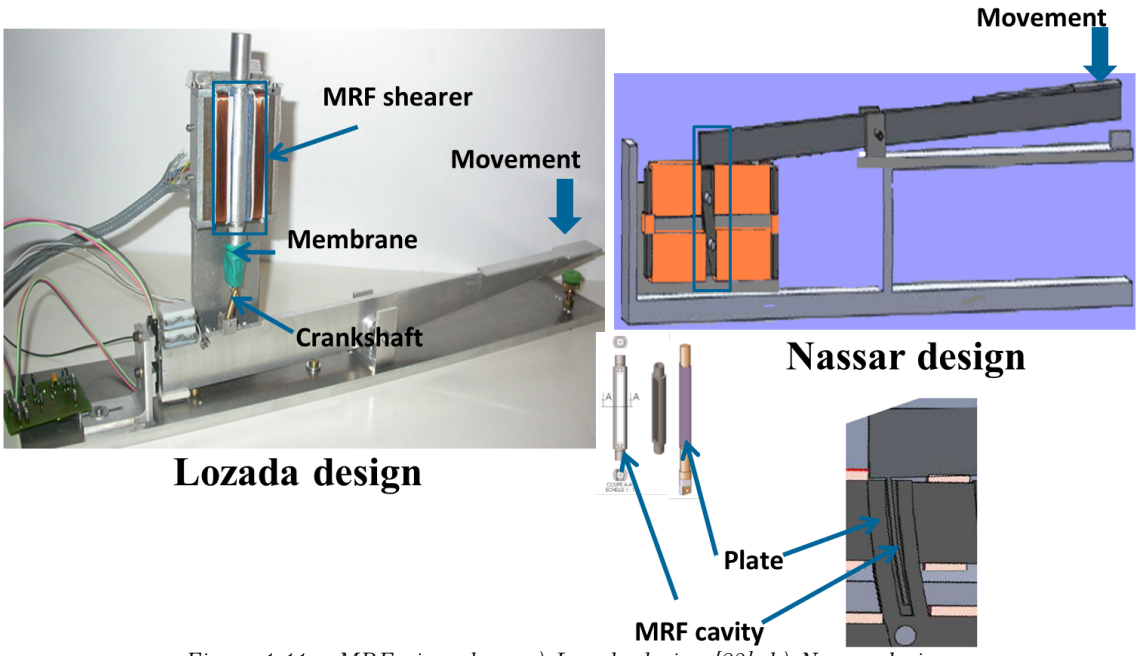

Figure 1.11 – MRF piano key: a) Lozada design [32]; b) Nassar design.

3 Rheology

3.1 Definition of rheology

Rheology is the study of complex substances whose mechanical behavior cannot be described with the classical disciplines. It is concerned with establishing theoretical relationships of a mechanical behavior depending on its internal micro-structure.

3.2 Methods of modelisation in rheology

Two main approaches are used while modeling a physical phenomenon:

1. the microscopic approach: it is a theoretical analysis based on assumptions valid only under specific geometric configurations, it can give the right order of magnitude in some cases and fail in others. It consists in studying the phenomenon at the scale of its smallest constituents. The microscopic approach has the advantage to present a qualitative understanding of the studied phenomenon [23, 4, 48].

2. macroscopic approach: it consists in fitting experimental results to a mathematical expression. It does not take into consideration the internal structure of the phenomenon and therefore does not present physical explanations of the observed phenomenon. However, once the working conditions are fixed, a quantitatively prediction of the system response can be achieved [16, 39, 25, 29].

4 Literature review of MRF rheology

The Bingham model is widely adopted for describing the MRF behavior (Eq: 1)(figure 1); it describes the fluid flow in the large shear-rate regimes $\tau(\dot{\gamma})$ and assumes that for small shear-rates, the fluid remains rigid. Fluids obeying this model exhibit a linear relation between the shear-stress/shear-rate variation after an initial shear stress threshold $\tau_{\mathrm{y}}(H)$ has been reached.

At the microscopic level, the magnetic effects dominates the Brownian forces. The literature presents the ratio between the competing dipole-dipole energy and the thermal disordering energy by λ (Eq: 1.1)[4].

$$\lambda = \frac{4\,\pi\,\mu_0\,\mu_f\,H_0^2\,a^3}{8\,K_B\,T} \tag{1.1}$$

$\frac{K_B\,T}{a}$ represents the scale of the thermodynamic forces acting on the MRF; K_B is the Boltzmann's constant $K_B = 1.381\,10^{-23} J.K^{-1}$, T is the temperature and a is the magnetic particle's diameter. The computing of the ratio λ for a magnetic field H_0=10 kA/m (which corresponds to $B = 0.035T$ for MRF-122), μ_0= $4\pi\,10^{-7}$ USI and with a particle diameter a=1μm is $\lambda = 1.3 \times 10^5$.

4.1 Preyield behavior

The pre-yield regime occurs for shear stress below the yield value. It has been described at takes place at static shearing rates [55]. The variation of the shear stress, in this zone, is supposed to increase linearly with the strain [23, 46, 4, 48, 23].

The shearing stress in this regime is considered as the contribution of the inter-particle attraction forces in the shearing direction; if F_r is the radial attraction force between two magnetic particles, N the total number of particles and θ the shearing angle, the resultant resistance force F is:

$$F = \Sigma N F_r \sin(\theta) \tag{1.2}$$

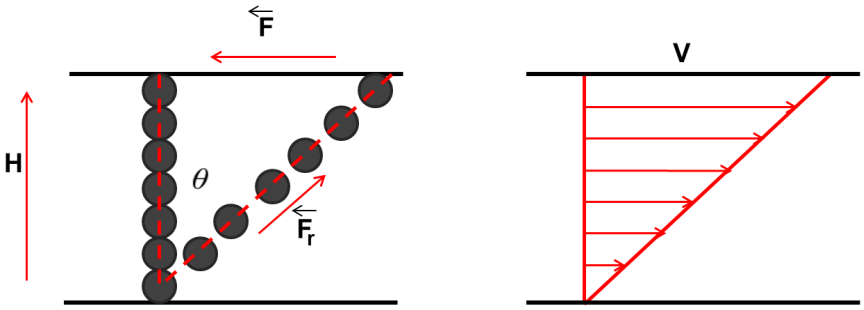

Figure 1.12 – Schematic representation of the affine deformation of a chain of spheres.

4.1.1 Microscopic approach

A microscopic approach has been adopted for describing the MRF in the pre-yield regime. This approach is used by Bossis, Peng, Si and other researchers [4, 46, 48]. The main parameters in these studies are the number of particles and sheared chains, their orientation and the inter-particle distance.

The comparison between the analytical solutions of Bossis (shearing-stress equation (Eq: 1.3)).

$$\tau(\gamma) = N\frac{F_r}{L^2}\sin(\theta)\cos^2(\theta) = \frac{3}{2}\phi\frac{F_r}{\pi a^2}\frac{\gamma}{1+\gamma^2} \tag{1.3}$$

a is the magnetic particle diameter, ϕ is the volume concentration, H the magnetic field, γ the strain and F_r the radial force between two neighboring magnetic particles.(Eq: 1.4).

$$F_r = \frac{\mu_0}{2}\int_a^0 (H_s - H)^2 2\pi\rho d\rho \tag{1.4}$$

Experimental results shows that the behavior of MRF in the pre-yield regime is well predicted by the theoretical model Eq 1.3 but with a yield stress value greater than the experimental (figure 1.13). According to Bossis, the pre-yield regime is supposed to occur at a shearing $\gamma \ll 1$. The shear stress τ was found to be varying with H as: $\tau \cong H^{1.23}$

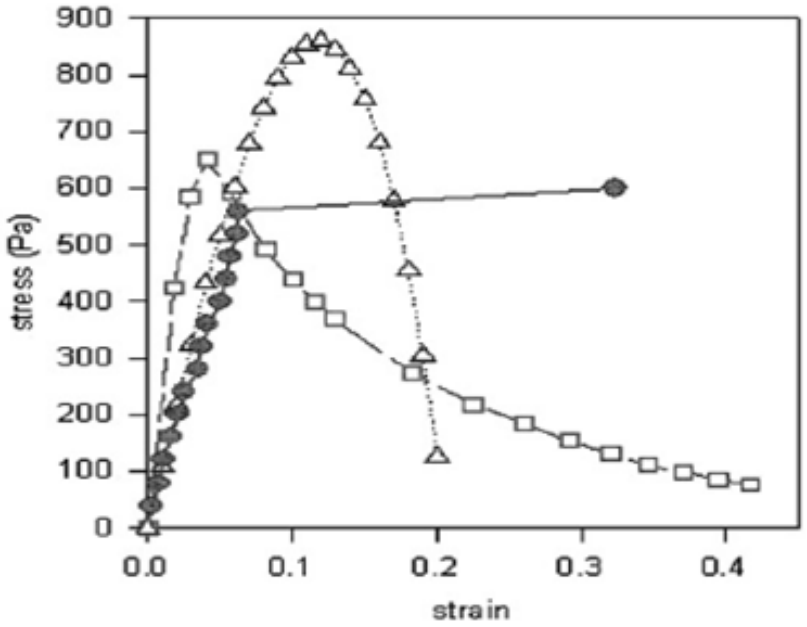

Figure 1.13 – Stress-strain dependency: (Δ)Eq 1.4; (•) experimental results; (□) finite element calculation (after Bossis [4]).

The numerical assumptions taken by Bossis in this study are summarized in table 1.1.

N	a_p	ϕ	H
7	10mm	15%	14.3kA/m

Table 1.1 – Bossis numerical assumptions.

Peng *et al.* adopted a linear model to describe stress variation with strain in the pre-yield regime (figure 1.14) [46]. In their model expression presented in Eq: 1.5 the storage module G is the same as the one given by Bossis.

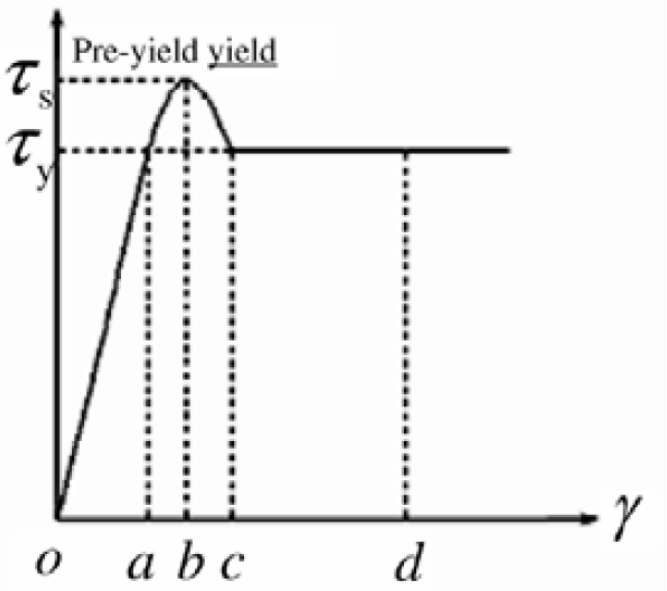

Figure 1.14 – Variation of τ with γ in the pre-yield zone (after Peng et al.,[46]).

$$\tau = G\gamma + \frac{24k\phi\mu\ d_1 F_r}{\pi(\frac{a}{2})^2 v}\dot{\gamma} \Rightarrow G = \begin{cases} 3\mu_0\phi M_s H & 0 < \gamma < b \\ -3\mu_0\phi M_s H & b < \gamma < c \\ 0 & \gamma > c \end{cases} \tag{1.5}$$

μ is a friction coefficient, k is a coefficient of correction, d_1 is the sheared distance, v the velocity of the shearing plate and M_s is the saturation magnetisation of MRF.

The expression of the dipole-dipole attraction in the Bossis equation is calculated as the integral of the magnetic field on the plane separating the two spheres. In Si *et al.* micro-mechanical model [48] the magnetostatic force between nearby particles is expressed as (Wan and Xinglong, 1994):

$$f_p = K\frac{m^2}{R^2} \tag{1.6}$$

where $K = \dfrac{1}{4\pi\mu_0}$and R is the distance between two neighboring particles. The resulting shearing resistance force proposed is:

$$\tau = \int N f_p \sin(\gamma) P(\gamma) d\gamma \tag{1.7}$$

m being the particles magnetic moment m=$\dfrac{2}{3}\pi(a/2)^2\chi H_0$ and χ its magnetic susceptibility).

P(γ)is a normal distribution of the particles chains and f_p is the interaction force between two magnetic particles,

These microscopic models (Eq: 1.3, Eq: 1.5 and Eq: 1.7), treat the MRF problem as single magnetic linear chains which do not interact between each other. Only dipole-dipole attractions between adjacent particles located in the same MRF chain are at the origin of the resultant resistance force. The inconvenient of this approach is that the interaction between adjacent single-chains is ignored also magnetic effect of non adjacent magnetic particles in the same MRF chain are neglected. These assumptions of internal isolated chains fluid structure are far from the observed real aggregates within the fluid.

4.1.2 Macroscopic approach

A: Linear models with localized constants

Phenomenological models are a class of models that includes elastic springs, viscous dashpots, and friction elements.

Gandhi, Weiss and Gavin present the hypothesis of a solid behavior of the MRF in the pre-yield regime [21] and choose to represent the fluid response, most simply by the Kelvin-Voigt model (figure 1.15) . Their hypothesis is based on experimental data and physical phenomena involved in the preyield regime.

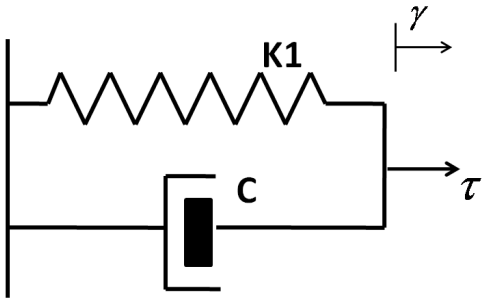

Figure 1.15 – Kelvin-voigt model.

In a Kelvin-Voigt material, shear stress τ, strain γ and their rates of change with respect to time t are governed by equation 1.8:

$$\tau(t) = K_1\gamma(t) + C\frac{d\gamma(t)}{dt} \tag{1.8}$$

where K_1 is the modulus of elasticity and C the viscosity.

Gamota and Filisko presented a viscoelastic behavior of the MRF below the threshold value τ_y (figure 1.16).

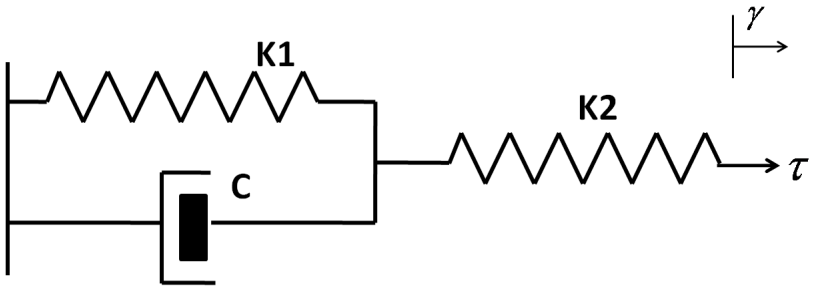

Figure 1.16 – Gamota and Filisko model.

K_1 et K_2 are the springs stiffnesses and describe the elastic characteristic of the MRF, while C is the coefficient of viscosity and denotes the fluidal property.

The shearing tests done by W. H. Li under constant strain γ show that for $\gamma < 0.1\%$ the stress relaxation modulus G(t,γ) (Eq: 1.9 and 1.10) is independent of the applied strain and therefore concluded that for strain smaller than $\gamma < 0.1\%$, the MRF has a solid like behavior (figure 1.17). The proposed phenomnological model is the same as the one proposed by Gamota and Filisko. The volumic concentration of the MRF used in these experiments is $\phi = 32\%$ [39].

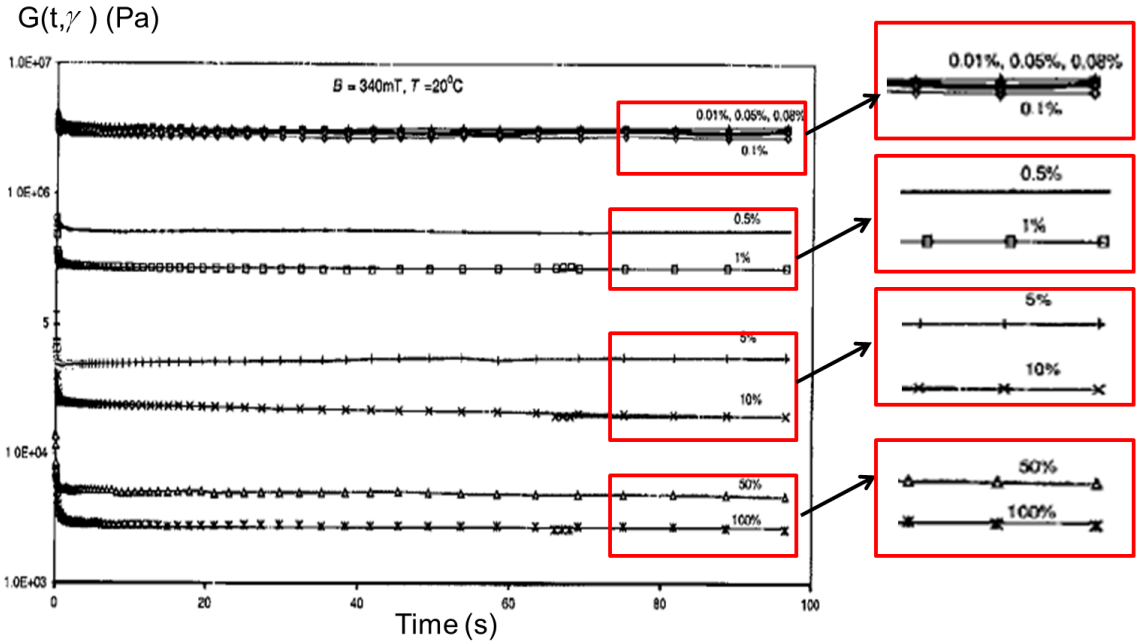

Figure 1.17 – Stress relaxation G(t,γ) under various step stain (after W.H.Li et al., [39]).

$$G(t,\gamma) = \tau(t,\gamma)/\gamma_0 \tag{1.9}$$

$$G(t) = K_2\frac{K_2^2}{K_1} + K_2(1 - \exp(-t)/p_1) \tag{1.10}$$

and $p_1 = \dfrac{C_1}{K_1 + K_2}$

These macroscopic models, similarly to the microscopic models, propose a linear behavior of the MRF response $\tau(\gamma)$ in the preyield regime.

B: Non linear models

Measurements of shearing stress at low shear rate were presented by Claracq (figure 4.1.2)[16]. He found that when $\dot{\gamma} \to 0, \tau = \eta_0 \dot{\gamma}$ and the system has a newtonian flow, whereas at high shear rates ($\dot{\gamma} \to \infty$) the system behaves like a Bingham fluid with a deduced apparent yield stress $\tau_s = \dfrac{\eta_0 - \eta_\infty}{\lambda}$ and a plastic viscosity η_∞ (figure 4.1.2). To synchronize this fluid response, he proposes a cross-model (Eq: 1.11) where the MRF is supposed to behave as pseudoplastic material.

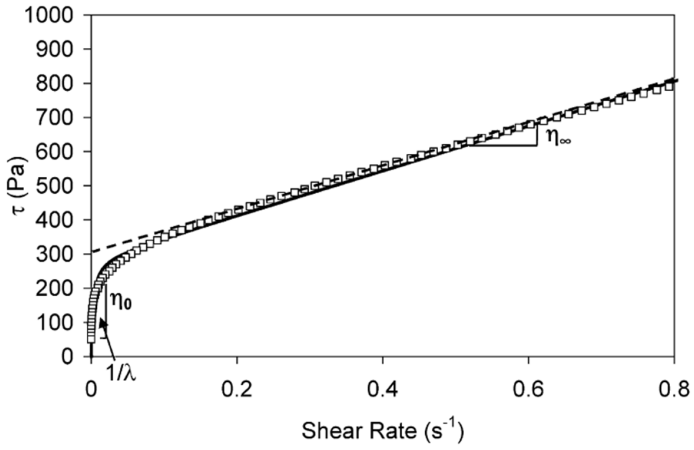

Figure 1.18 – Shear rate fluid behavior (15V5e5, H=28kA/m): Bingham-model (dashed line) and Cross-model (line) (after Claracq et al., [16]).

$$\tau = \eta_\infty + \frac{\eta_0 - \eta_\infty}{1 + \lambda \dot{\gamma}} \dot{\gamma} \tag{1.11}$$

According to Claracq, due to the small ranges of shear rates reached in his experiments, no yield stress was observed and therefore yield models like Bingham (Eq: 1), Casson (Eq: 1.12), Hershell-Buckley (Eq: 1.13), were not able to describe his measurements.

$$\tau^{1/2} = \tau_y^{1/2} + (\eta_\infty \dot{\gamma})^{1/2} \tag{1.12}$$

$$\tau = \begin{cases} \tau_y + \mu_{eq} \dot{\gamma} & \tau > \tau_y \\ 0 & \tau \leq \tau_y \end{cases} \tag{1.13}$$

$\mu_{eq} = K \dot{\gamma}^{n-1}$. The exponent n is called the flow behavior index and K is called the consistency.

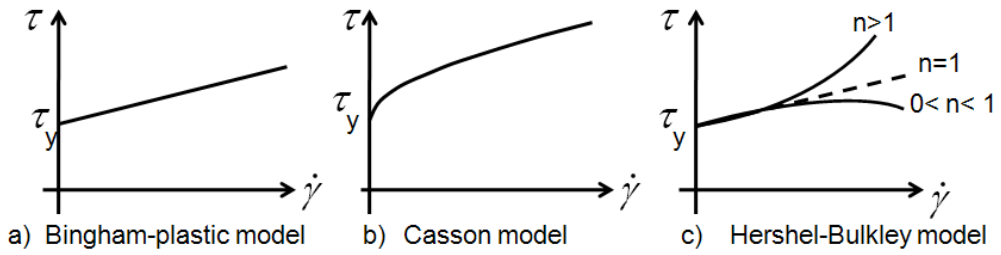

Figure 1.19 – Diagrams of: a)Bingham-plastic; b)Casson; and c)Hershel-Bulkley constitutive models.

4.2 Measurements and model adjustments for the yield threshold

The prediction of the strength of a MRF suspension as a function of the applied field relies on the prediction of its yield stress. Many studies were conducted to investigate the MRF yield stress and several models have been proposed to its description.

Ginder and co-workers presented analytical models describing the flux-density-yield-stress relationship. At low magnetic field intensities (where B is supposed to be linear to H), the proposed relationship between magnetic field and yield stress is:

$$\tau_{\mathrm{ys}} \alpha \phi \mu_0 H^2 \tag{1.14}$$

For flux densities beyond the linear region (but lower than those needed to cause complete saturation) the proposed yield-stress and magnetic field relationship is:

$$\tau_{\mathrm{ys}} = (6^{1/2}) \phi \mu_0 (M_{\mathrm{s}})^{1/2} H^{3/2} \tag{1.15}$$

This model of τ_{y} is also adopted by Bossis[4].

For magnetic field levels that cause complete saturation, the relation $\tau_{\mathrm{y}}(H)$ becomes:

$$\tau_{\mathrm{sat\,ys}} = \frac{4}{5^{5/2}} \xi \phi \mu_0 (M_{\mathrm{s}})^2 \tag{1.16}$$

where ξ is a constant equal to ξ=1.202.

Han and Hong used the least-square curve fitting method to experimental measurements to get an approximated polynomial expression of τ_{y}. Figure 1.20a) is from Han while figure 1.20b) is from Hong [25, 29]. MRF-132 is the fluid used in these tests.

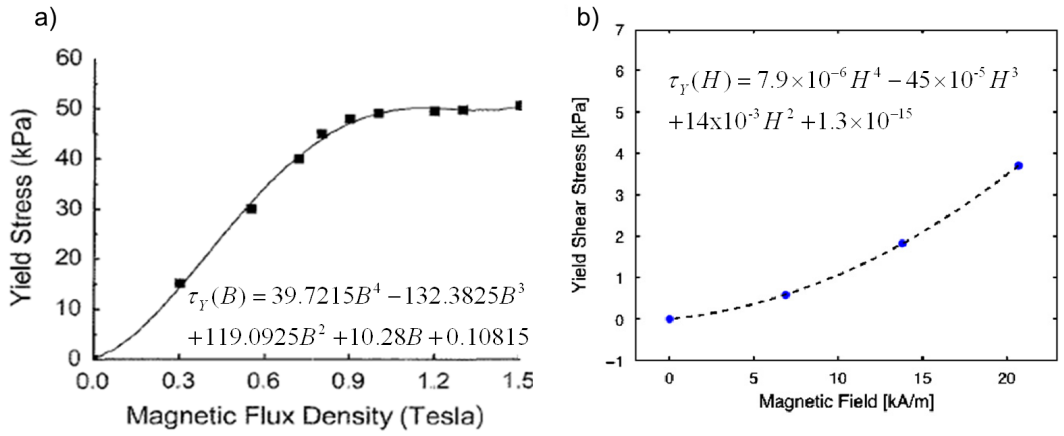

Figure 1.20 – Yield stress polynomial fitting a)after Hanet al., [25] b)after Hong et al., [29].

The maximum level of yield stress τ_{y} reached in Hong experiments for a magnetic field H=20kA/m (which corresponds to a magnetic field B equal to B=0.126T) is $\tau_{\mathrm{y\,Hong}}$=3.45kPa. For the same magnetic field B (B=0.126T), this value of the measured yield stress $\tau_{\mathrm{y\,Hong}}$ is 11% higher than the value of the yield stress calculted by the model proposed by Han ($\tau_{\mathrm{y\,Han}}$=3.04kPa).

The polynomial fits of yield stress τ_{y} for magnetic field values ranging between 0.2T< B< 0.8T and shear rate $25s^{-1} < \dot{\gamma} < 200s^{-1}$ done by Genc and co-workers are presented in figure 1.21. Two different particle volume fractions ϕ and diameters a were tested; ϕ=33% and ϕ=44%, the particles diametre of the sample grade A being larger than those of sample grade B[22].

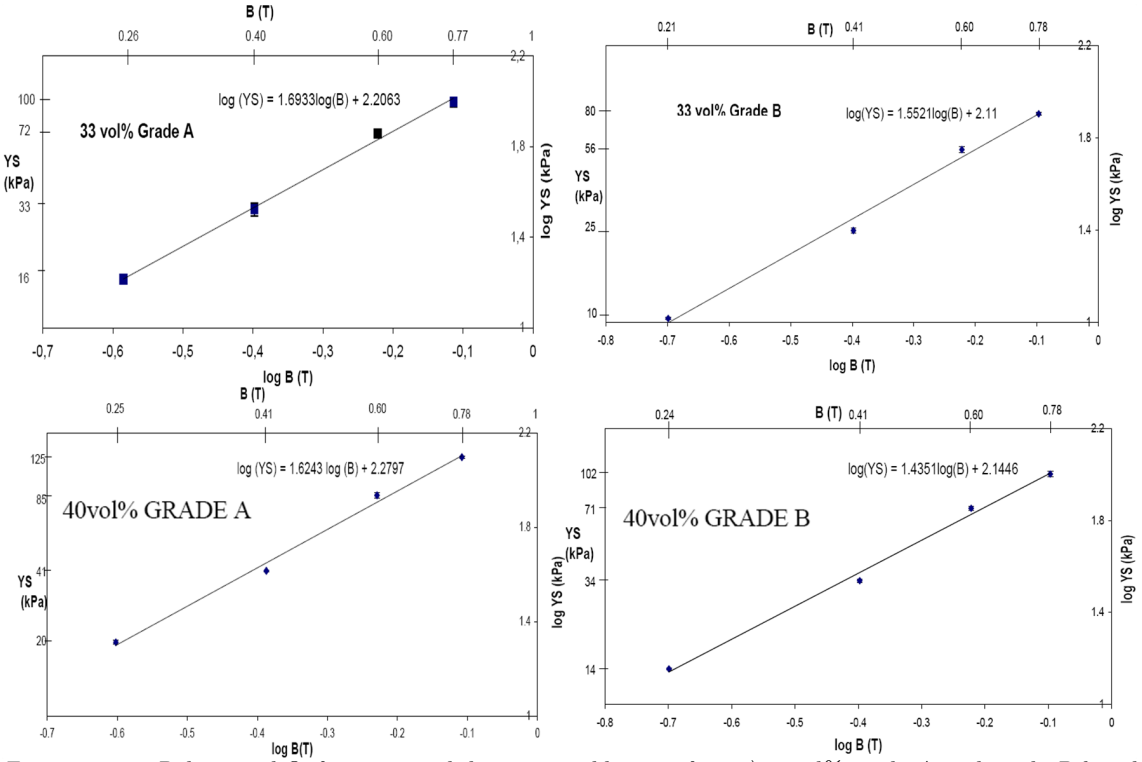

Figure 1.21 – Polynomial fit for measured dynamic yield stress for: a)33 vol% grade A and grade B based MRF; b)40 vol% grade A and grade B based MRF (after Genc et al., [22]).

Figure 1.22 presents He *et al.* experimental device used to study the yield stress over a wide range of magnetic field intensity [26].

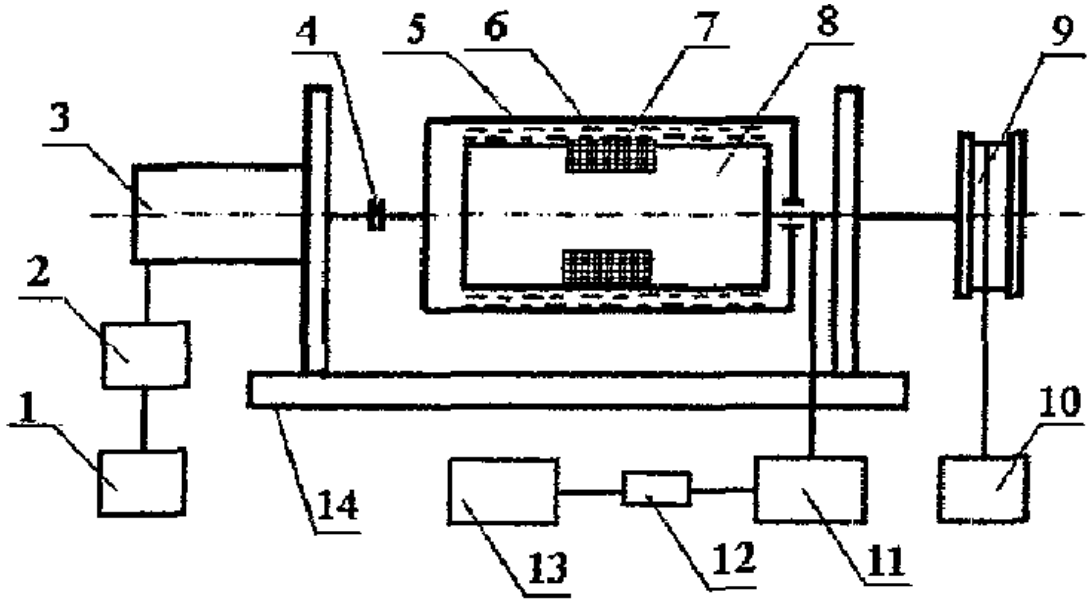

Figure 1.22 – He test system: 1: signal source A; 2: motor controller; 3: motor; 4: coupling; 5: outer cylinder; 6: MRF; 7: circuit; 8: inner cylinder; 9: wheel; 10: weight; 11: magnetic field measure; 12: on/off circuit ; 13: signal source B; 14: base (after He et al.,[26])

The MRF sample is sheared in the annular gap between the inner (8) and the outer cylinder (5). The yield stress values are deduced by evaluating the values of the torque and the rotational speeds of the inner cylinder once the MRF is submitted to magnetic field.

Equation 1.17 presents the model used by Huang *et al.* to evaluate the MRF yield stress.

$$\tau y(H) = \frac{r\phi\mu_0(\mu_r - 1)^2 C^2 H^2 \sin\theta}{12R} \tag{1.17}$$

where C is a function of the magnetic field $C = C(H)$, its value ranges between 3.4 (for H greater than 700kA/m) to a maximum value of 4 (for H less than 20kA/m). θ is the polar angle between the line of centers and the axis of magnetic field direction, r is the particles radius and R is the distance separating to neighbor particles.

The effect of MRF particles diameter and concentration on the yield stress is also studied by Genc [22]. He found that the increase in MRF particle diameter and volume fraction leads to a increase in measured yield stress. (figure 1.23)(in figure 1.23 the particle diameter of Grade B are smaller than those of grade A).

According to Bombard, " mixing carbonyl iron powders with different particle sizes can improve the performance of MR suspension, decreasing the 'off plastic viscosity, and increasing the MR effect"[2].

a)

B(T)	Grade A Measured dynamic yield stress (kPa)	Grade B Measured dynamic yield stress (kPa)
0 2	16 ± 3	10 ± 1
0.4	33 ± 3	26 ± 2
0 6	72 ± 5	56 ± 5
0 8	100 ± 3	80 ± 8

b)

B(T)	Grade A Measured dynamic yield stress (kPa)	Grade B Measured dynamic yield stress (kPa)
0 2	22 ± 1	14 ± 0 6
0.4	45 ± 3	35 ± 1
0 6	84 3 ± 2	71 ± 2
0 8	124 ± 3	102 ± 2

Figure 1.23 – Measured yield stess for: a)33 vol% grade A and grade B based MRF; b)40 vol% grade A and grade B based MRF (after Genc et al., [22]).

Surface effect on the yield stress of MRF under deformation have been investigated by Lemaire, Joung, Tang and Gordaninejad and Peng [33, 46, 24]. Their studies demonstrated that the yield stress is highly dependent on the surface topography. According to Joung, change in wall structure causes substantially different morphology in the sheared MRF [33]. Figure 1.24 shows that the increase in the friction coefficient f of the shearing wall surface (f=0.4 and f=0.1) induces an increase in the measured yield-stress.

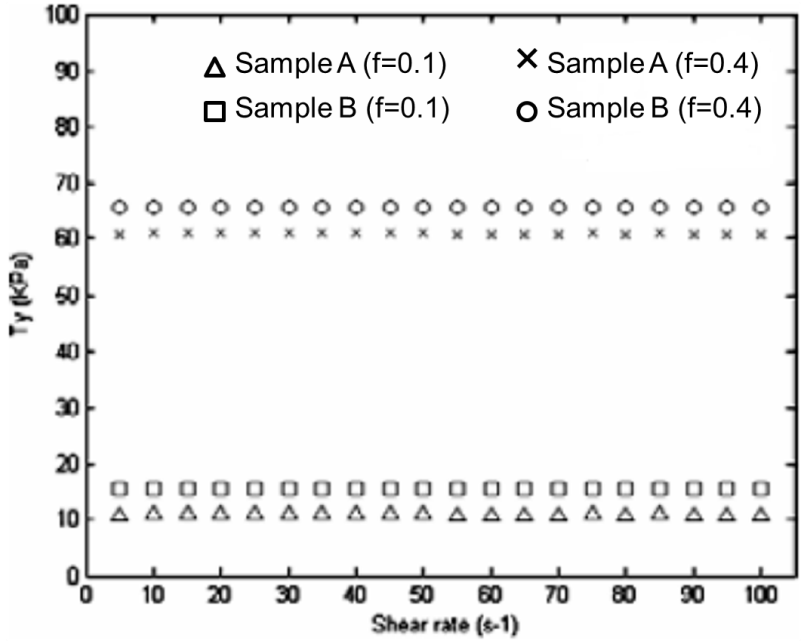

Figure 1.24 – Measured yield stress in different friction wall coefficient for MRF a)suspension A(ϕ=35vol%); b)suspension B(ϕ=40vol%) (after Peng et al., [46]).

Gordaninejad studied the MRF flow in nine different grooved channel configurations. The experimental setup used by Gordaninejad while experimenting is presented in figure 1.25. The measured pressure drops δP across the different grooved channels are presented in figure 1.26. It was found that the increase in the depth of grooves leads to an increase in the measured yield stress.

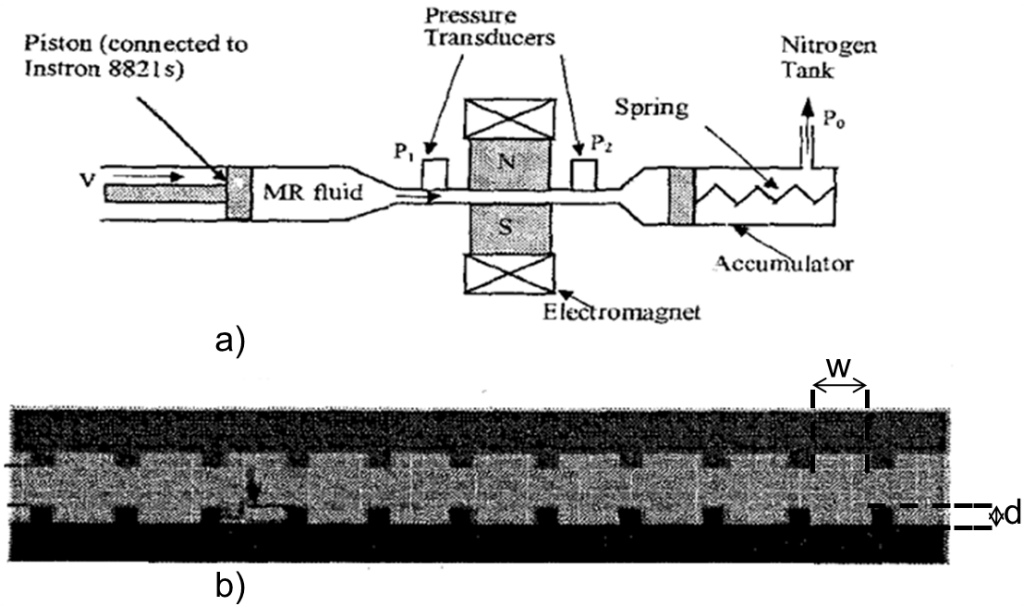

Figure 1.25 – Experimental setup to study wall effect on MRF response (after Gordanine et al., [24]) a)schematic experimental setup ; b)cross-section of a grooved channel.

a)

	w (mm)	d (mm)
G1	0.76	0.38
G2	0.76	0.64
G3	0.76	0.76
G4	1.02	0.38
G5	1.02	0.64
G6	1.02	0.76
G7	1.27	0.38
G8	1.27	0.64
G9	1.27	0.76
G0	smooth surface	

Dimensions of Different Groove Configurations Tested in the Flow Type Rheometer.

b)

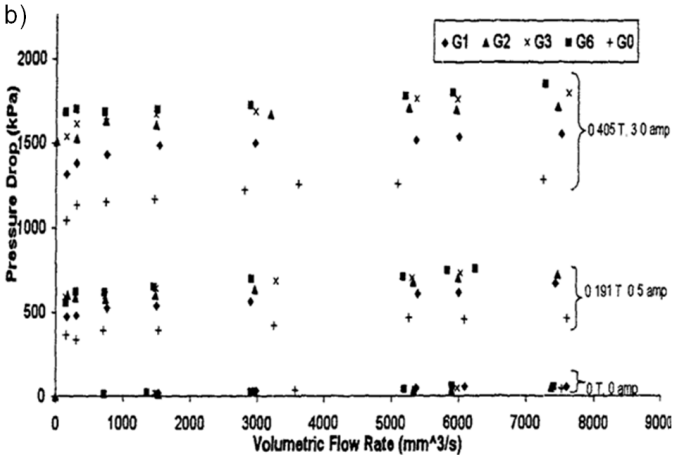

Figure 1.26 – Effect of groove configuration on the measured pressure drop force (after Gordaninejad et al.,[24]).

The dependency of surface topography on yield stress was also investigated by Zhang [54] (figure 1.27). He concluded the existence of the wall effect on the yield stress.

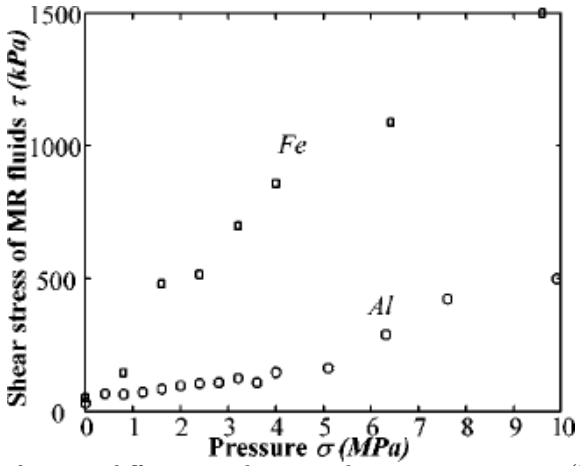

Figure 1.27 – Comparison between different work pieces shear stress response (B=275 mT). (after Zhang et al.,[54]) Fe: iron test slice; Al: Aluminum test slice.

Also he studied the squeeze-strengthen effect on the MRF yield stress (figure 1.28) and concluded that when a MRF is compressed the measured yield stress can reach 25 times of yield stress without compression [54].

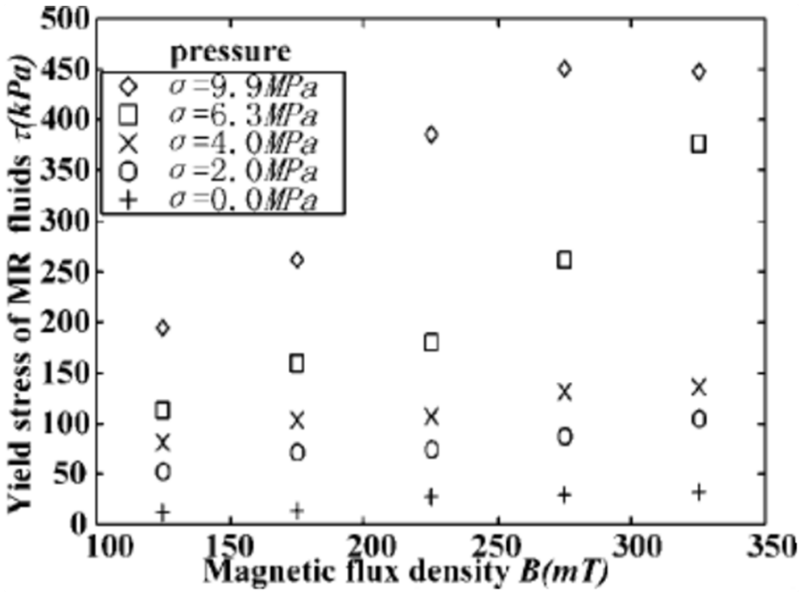

Figure 1.28 – Experimental results of MRF yield stress measured by Zhang[54] and subjected to initial compression.

From above we can conclude that the fluid yield response is affected by the particles diameter, particle volume fraction and shearing wall surface.

The Lord corporation one of the leading companies in developing MRF fluids. Figure 1.29 presents the estimated values of the MRF yield stress τ_y for MRF-122, MRF-132, MRF-140. Table 1.2 summarizes the typical properties of the Lord corporation MRF's.

Particle volume fraction ϕ	22%	32%	40%
Viscosity (Pa.s)	0.042 ± 0.020	0.092 ± 0.015	0.280 ± 0.070
Density (g/cm^3)	2.28-2.48	2.98-3.18	3.54-3.74
Operating Temperature °C	-40 to +130	-40 to +130	-40 to +130
Appearance	Dark Gray Liquid	Dark Gray Liquid	Dark Gray Liquid

Table 1.2 – Typical MRFs properties after Lord Corporation data [10].

Figure 1.30 presents the relation between the magnetic field B and magnetic field H for the three MRF from Lord.

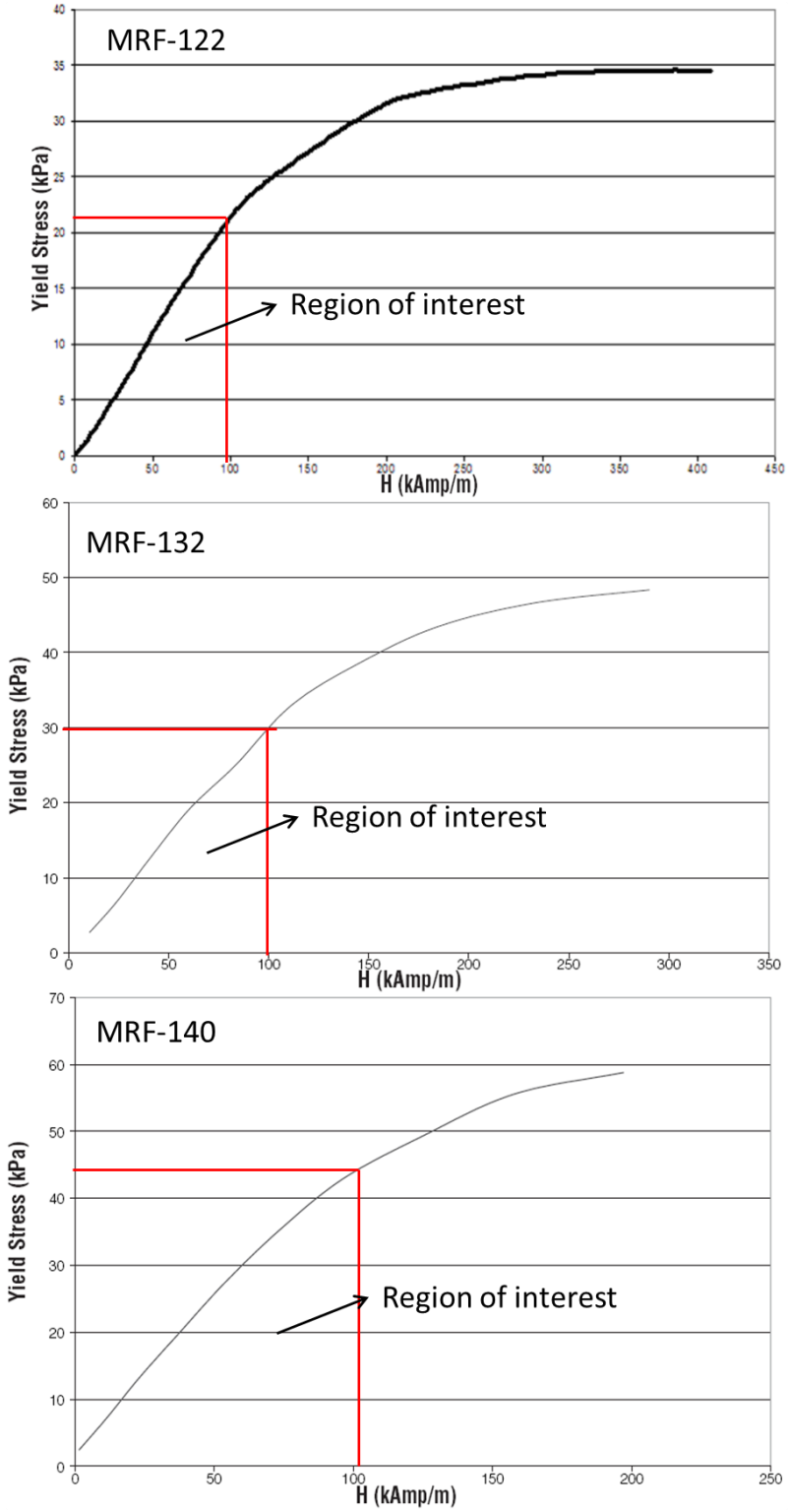

Figure 1.29 – Yield stress vs. magnetic field strength for Lord MRFs [10].

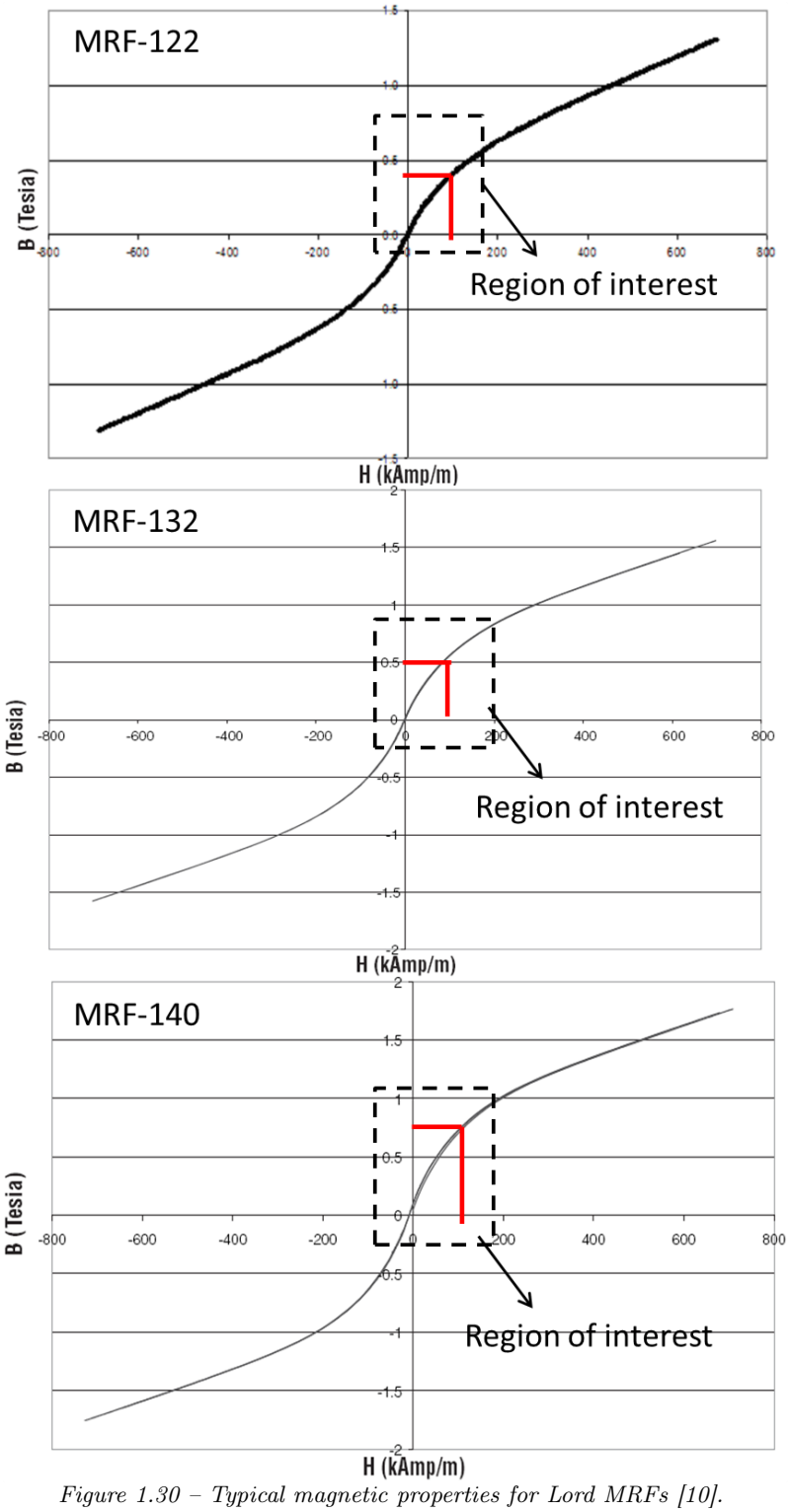

Figure 1.30 – Typical magnetic properties for Lord MRFs [10].

To be able to well control the MRFs the researchers and I, restricted our studies to the region below MRF saturation (where the magnetic field B varies linearly with magnetic field H). In these regions the variation of τ_y is linear with H.

4.3 Post-yield behavior

Yao, Dominguez and Butz used a mathematical model that exhibits hysteresis response, the Bouc-Wen model, in the controlling design of their MRF devices [53, 17, 18, 5, 1](figure 1.31).

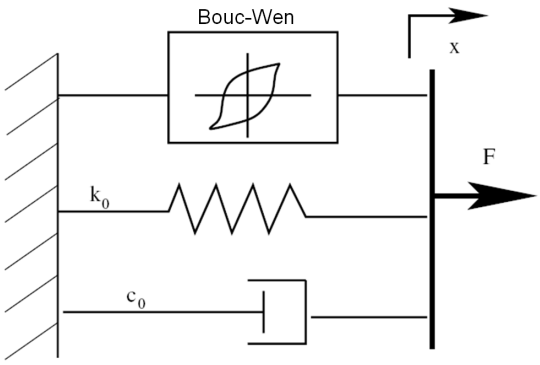

Figure 1.31 – Bouc-Wen model for MRF (after Yao et al.,[53]).

This model is given by Eq: 1.18 and 1.19:

$$F = c_0\dot{x} + K_0.x + \alpha.z \tag{1.18}$$

The first term $c_0\,\dot{x}$ describes the force associated with the viscous dissipation, K_0.x represents the linear force associated to the elastic spring and the last term α z is the evolutionary force due to the hysteresis portion of the total force F. $z(t)$ obeys to the nonlinear differential equation (Eq: 1.19) with zero initial condition $z(0)$=0 and hence has the dimension of a length.

$$\dot{z} = -\gamma\,|\dot{x}\,|z\,|z^{n-1}| - \beta\,\dot{x}\,|z|^n + A\,\dot{x} \tag{1.19}$$

γ, β and A are dimensionless quantities controlling the behavior of the hysteresis loop. These parameters are adjusted to experimental results and thus a mathematical model of behavior can be generated.

Figure 1.32 shows an example of comparison between Bouc-Wen model results and experimental results done by Yao [53].

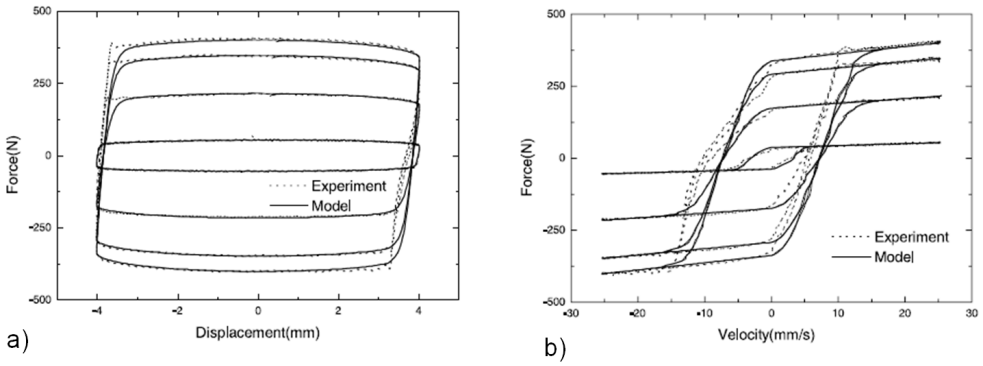

Figure 1.32 – Comparison between experimental measurements and Bouc-Wen model (after Yao et al., [53]).

The Bouc-Wen model does not describe well the hysteretic variation of force in the low velocity profile; to a better prediction of the MRF response in this region, Spencer proposed the modified Bouc-Wen model(figure 1.33)[1].

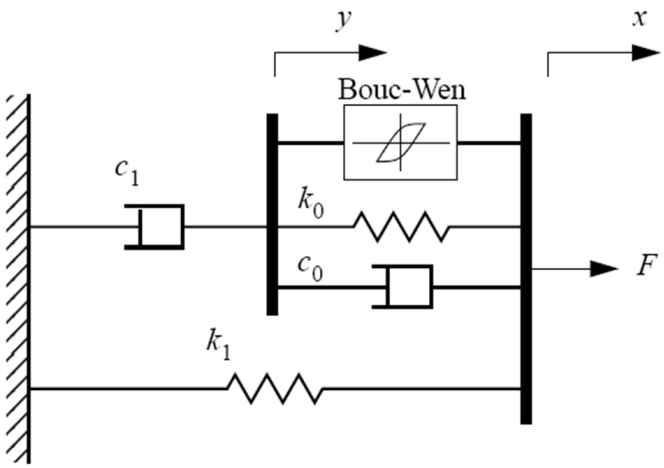

Figure 1.33 – Modified Bouc-Wen model for MRF after [1]

Comparisons between the predicted responses of the modified Bouc-Wen (Eq: 1.20, 1.21 and 1.21), and the experimental results are shown in figure 1.34.

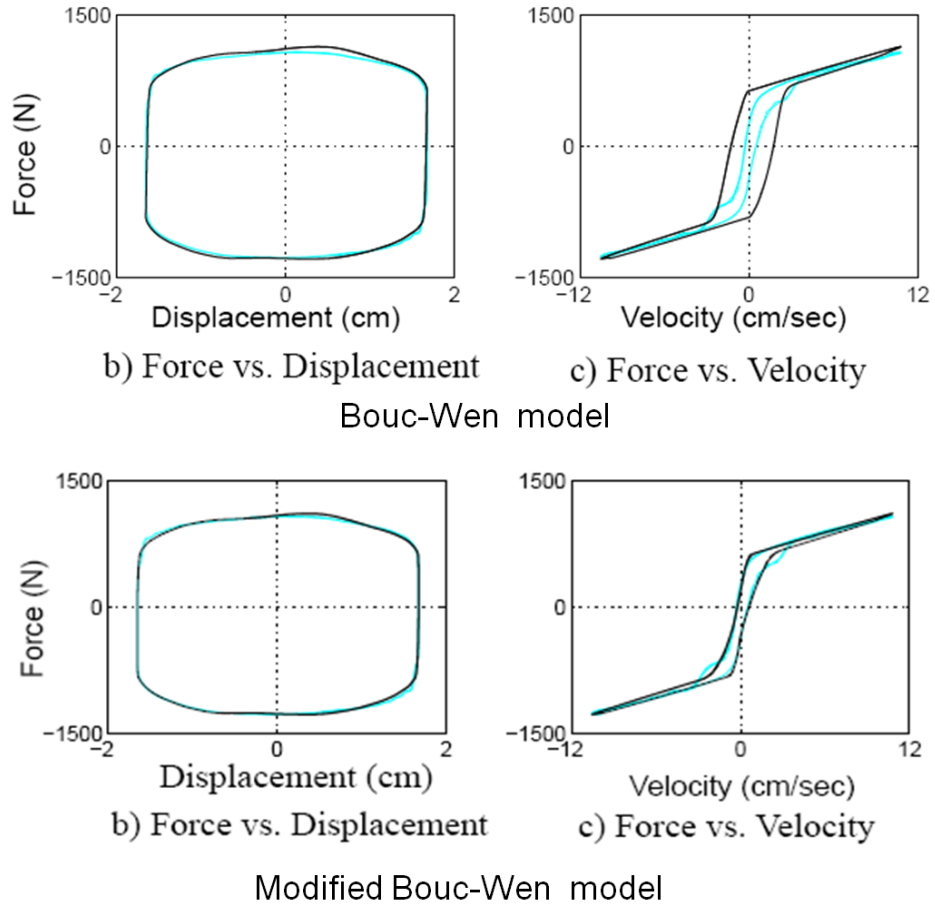

Figure 1.34 – Comparison between experimental measurements and Bouc-wen and modified Bouc-Wen simulations results (after Spencer et al., [1]).

$$F = \alpha.z + c_0(\dot{x} - \dot{y}) + K_0.(x - y) + K_1(x - x_0) \tag{1.20}$$

Considering only the upper part of the mechanical modified Bouc-Wen model, the forces on either side of the rigid bar are therefore equivalent:

$$c_1\dot{y} = \alpha\, z + K_0(x - y) + c_0(\dot{x} - \dot{y}) \tag{1.21}$$

and $\dot{z}$ is defined by:

$$\dot{z} = -\gamma|\dot{x} - \dot{y}|z.z^{n-1} - \beta(\dot{x} - \dot{y})|z^n| + A(\dot{x} - \dot{y}) \tag{1.22}$$

γ, β and A describes the smoothness of the transition from the pre-yield to the post-yield region, hence their adjustments will allow a control of the yield stress value.

See suggests a fit to the Hershel-Bulkley model (figure 1.35[47]). The proposed equation of the polynomial fitting is presented in Eq: 1.23.

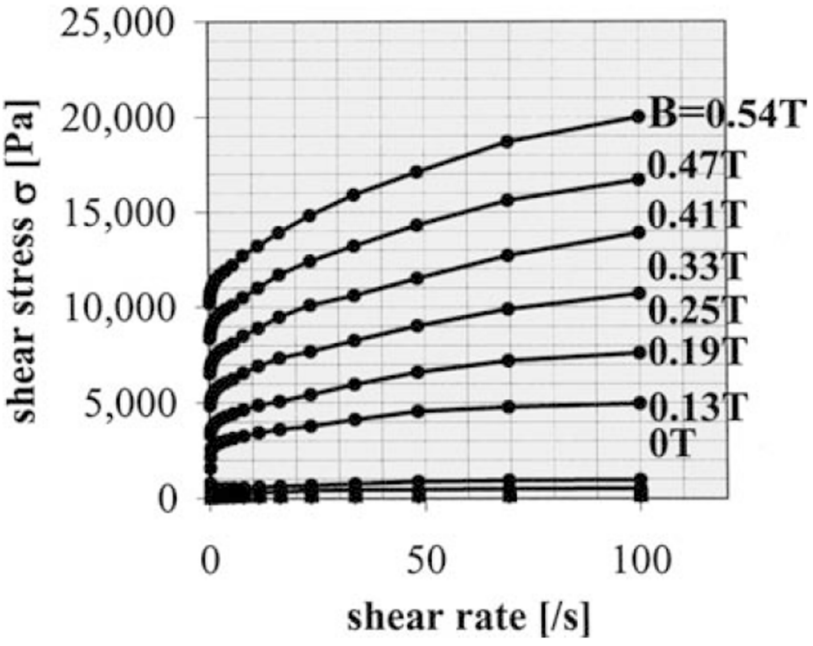

Figure 1.35 – Hershel-Bulkley shear stress response (after See et al.,[47]).

$$\tau = \tau_y + k\dot{\gamma}^n \quad with \quad \tau_y = 26.3\, B^{1.4} \tag{1.23}$$

With n=0.53 and k=710 (units Pa.s^n).

Hong proposed a Herschel-Bulkley model with a preyield viscosity to describe MRF behavior (figure 1.36)[28]. The post-yield regime is presented by a viscosity power law and the pre-yield regime is a linear function of the shear rate (Eq: 1.24).

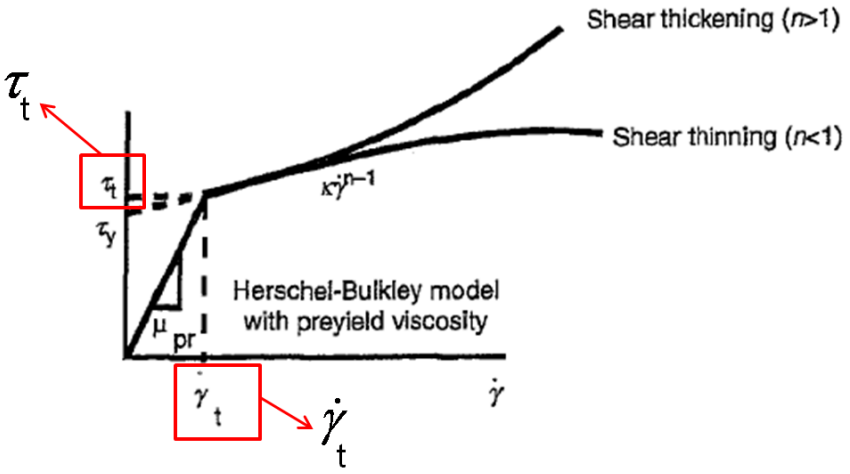

Figure 1.36 – Herschel-Bulkley with pre-yield regime (after Hong et al.,[28]).

$$\tau = \begin{cases} [\tau_{\mathrm{d}} + k|\dot{\gamma}|^{n}]sgn(\dot{\gamma}) & |\tau| > \tau_{\mathrm{t}} \quad or \quad |\dot{\gamma}| > \dot{\gamma}_{\mathrm{t}} \\ \mu_{\mathrm{pr}}\dot{\gamma} & |\tau| \leq \tau_{\mathrm{t}} \quad or \quad |\dot{\gamma}| \leq \dot{\gamma}_{\mathrm{t}} \end{cases} \tag{1.24}$$

Zisper and Li suggested a Bingham model to describe the MRF-132 behavior [55, 41]. Figure 1.37 presents his experimental tests.

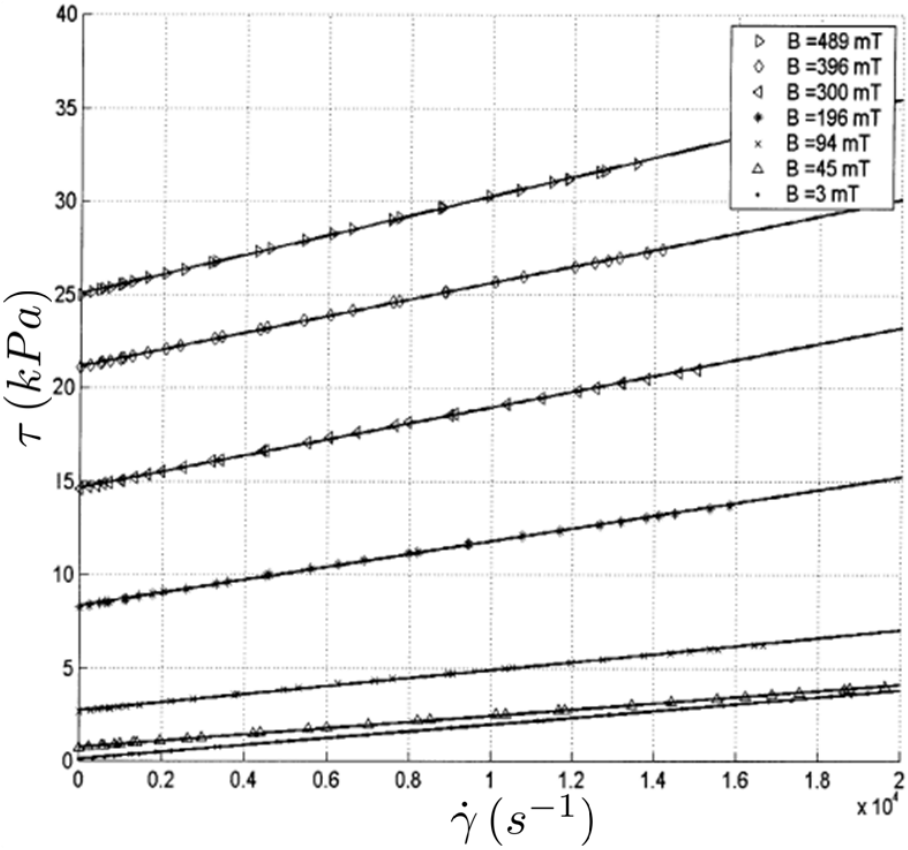

Figure 1.37 – Approximated Bingham functions of MRF-132 [55]

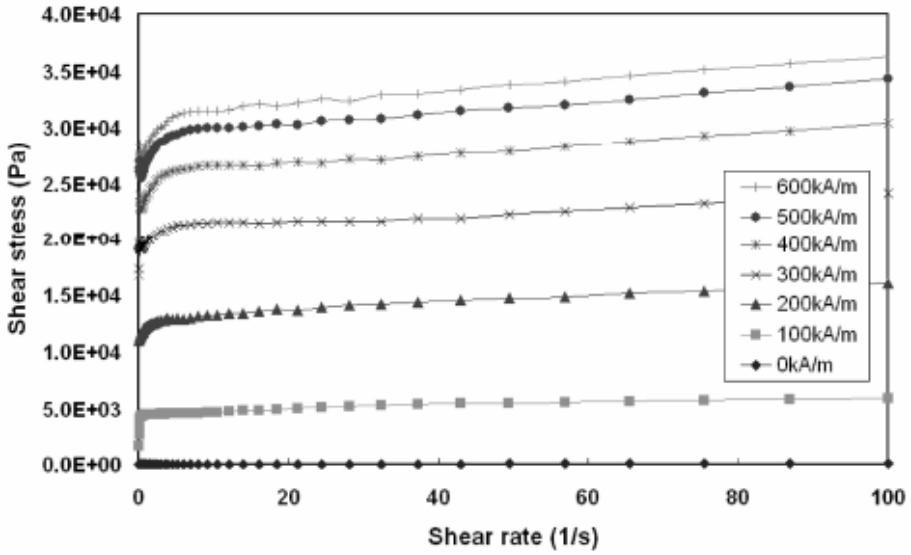

Figure 1.38 – Dependency of shear stress on shear rate for the MRf-132 exposed to various magnetic fields [41].

5 Conclusion

MRF are part of controllable materials that are widely used in applied research. Until nowadays MRF are used to exhibit large damping forces and are modeled by the Bingham model.

Literature studies affirm that Bingham model describes well the MRF response at large shear rate: post-yield regime. However the Bingham model makes no prediction with regard to the pre-yield regime.

The microscopic theoretical approach has been used for studying the MRF behavior in the pre-yield regime. So far the limitations of these models prevent them from being predictive in a wide rang of situations. The models are qualitative.

All microscopic approach attributes a solid-like behavior to the MRF in the pre-yield regime $\tau_{\text{pre-yield}} = G\,\gamma$. However the prediction of G coefficient varies between the different studies, it depends on the way the magnetic interaction force, in the fluid, is computed.

The fluid behavior in the post yield regime is considered as a liquid-like behavior $\tau(\dot{\gamma})$. An experimental approach is usually used to study the fluid in this regime and a mathematical fitting is therefore suggested for the MRF modeling behavior. The variation of the experimental conditions in these approaches (shearing plate nature, MRF concentration and fluid internal structure) are not taken into consideration while modeling the MRF behavior, therefore no predective conclusions can be drawn.

Based on these considerations, and comparing with the needed qualitative and quantitative prediction for the use of the MRF in a human-machine interface both quantitative and qualitative understanding of the pre-yield regime remains necessary.

Chapter 2

Experimental techniques

Contents

1	**Device description**	**40**
2	**Mechanical elements**	**41**
3	**Magnetic and electrical circuits**	**45**
4	**Sensors**	**48**
5	**Microscopy**	**51**
6	**Tests**	**56**
7	**Conclusion**	**67**

In this chapter I present a detailed description of the measurement device designed to study the MRF behavior below the yield-threshold τ_y.

The first section provides a general description of the device. The next sections are devoted to the tests of the measuring system.

1 Device description

The purpose of the device is to shear a MRF with a thin plate. The shear strain is imposed by a stepper motor and the shearing force is measured by an external force sensor. The measurement means are presented in sections Sec. 2 3 and 4. The presentation of the different types of microscopic observations are described in Sec 5. Sec. 6 is dedicated to the experimental apparatus testing and characterization.

Figure 2.1 shows a front view of the measuring device system, the top view is presented in figure 2.2.

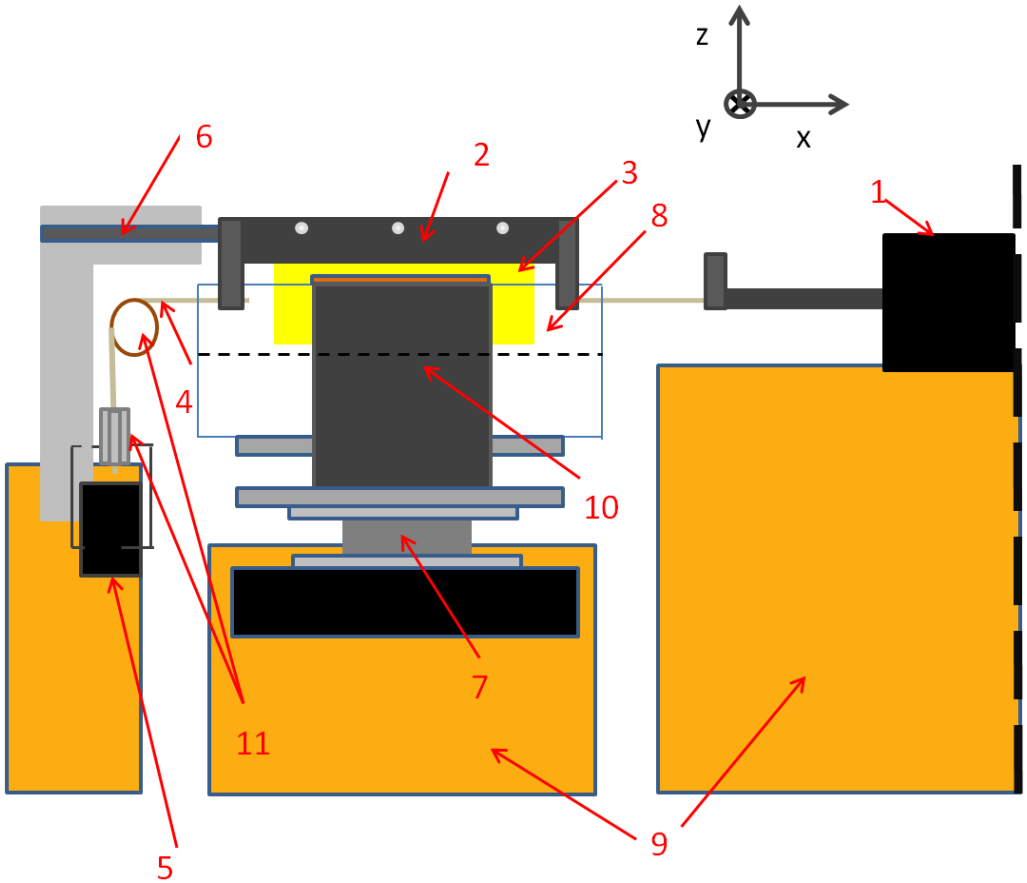

Figure 2.1 – Front view of the experimental apparatus. 1: stepper motor; 2: plate holder; 3: shearing plate; 4: cables; 5: equilibrium mass ; 6: displacement sensor; 7: force sensor; 8: MRF cavity; 9: sand tank; 10: magnetic circuit; 11: pulleys.

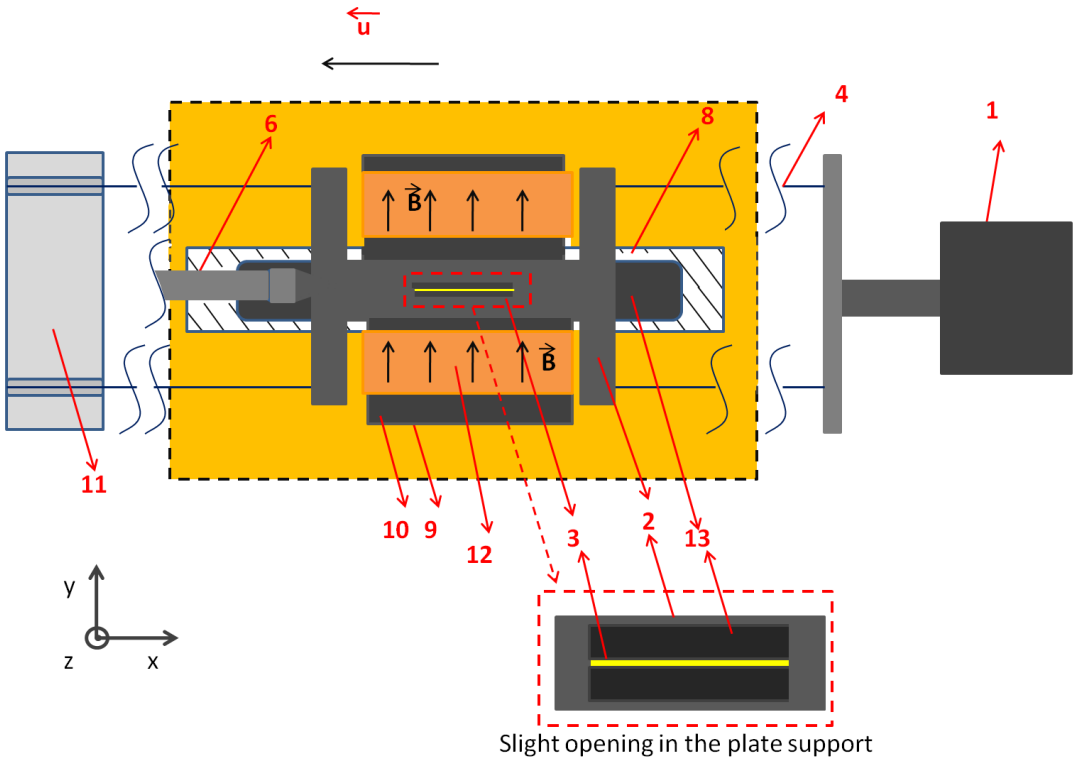

Figure 2.2 – Top view of the experimental apparatus. 1: stepper motor; 2: plate holder; 3: shearing plate; 4: cables; 6: motion sensor; 8: MRF cavity; 9: sand tank; 10: magnetic poles; 11: pulleys; 12: coils; 13: MRF.

In order to characterize the pre-yield regime of the MRF (13) in the shearing stress/strain plane(τ,γ), tests must be done at low shearing rates. High positioning accuracy and low vibration levels are required. To these ends, we use a stepper motor (1) to drive linearly a thin shearing plate (3) in a 1 mm-wide open cavity (8). The stepper motor (1) is driven at a controlled velocity $\vec{v}(t)=v(t)\,\vec{e_x}$ by Matlab functions. The cavity is connected to its support only by a force sensor (7). The displacement of the plate is measured by a motion sensor (6). Stainless steel cables (4) connect the plate holder (2) to the stepper motor and mass (5). The weight of the mass ensures a constant tension in the cables. All equipment parts are sunk into separate sand tanks(9) to filter the vibrations.

The magnetic field B in the fluid is generated by the current I in two coils (12) polarizing a magnetic circuit (two U-shaped magnetic poles (10)).

From the measurement of the force F, the displacement u and the current I we can calculate the shear stress τ, the shear strain γ and the magnetic field H. The magnetic field B is measured separately (Sec. 4.3).

2 Mechanical elements

2.1 Stepper motor

2.1.1 Description

Figure 2.3 shows the internal structure of our stepper motor.

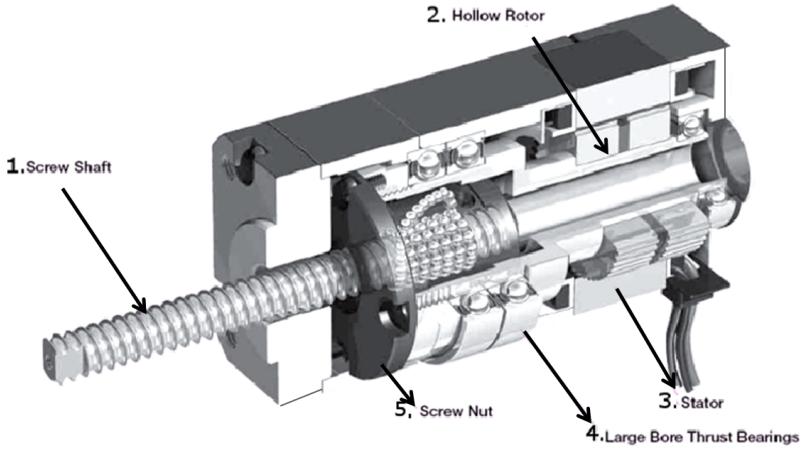

Figure 2.3 – Internal stepper motor structure (after www.orientalmotor.com).

The Oriental Motors DRL42PA2G-04G is the linear actuator used in our experiments. The screw shaft (1) moves the plate support forward and backward. Its stepping displacement is 1 μm. This resolution is sufficient for this study since the fluid particles are typically 1 μm in diameter. Table 2.1 presents the maximum operating speed, acceleration /deceleration and push/pull thrust of the actuator.

$a_{\max}$	Acceleration (m/s^2)	0.4
$v_{\max}$	Maximum velocity (mm/s)	30
$F_{\max}$	Thrust force (N)	100

Table 2.1 – Specifications of the stepper motor (after www.orientalmotor.com).

The motor maximum operating speed corresponds to a virtual shearing rate $\dot{\gamma_v} = \dfrac{v_{max}}{g_f} = \dfrac{30}{0.5} = 60\ \mathrm{s}^{-1}$; g_f being the MRF sheared gap. The thrust force $F_{\max}$ corresponds to a virtual shear stress $\tau_v = \dfrac{F}{S_\mathrm{m}} = \dfrac{100}{10^{-3}} = 100$ kPa; S_m being the magnetic sheared surface.

2.1.2 Command

When the tension at the input of the stepper motor is a 0-5V-0 square signal, the stepper motor does one displacement step (step displacement=1μm). The variation of the velocity is obtained by varying the frequency of the square signal. The command block diagram of the stepper motor is presented in figure 2.4.

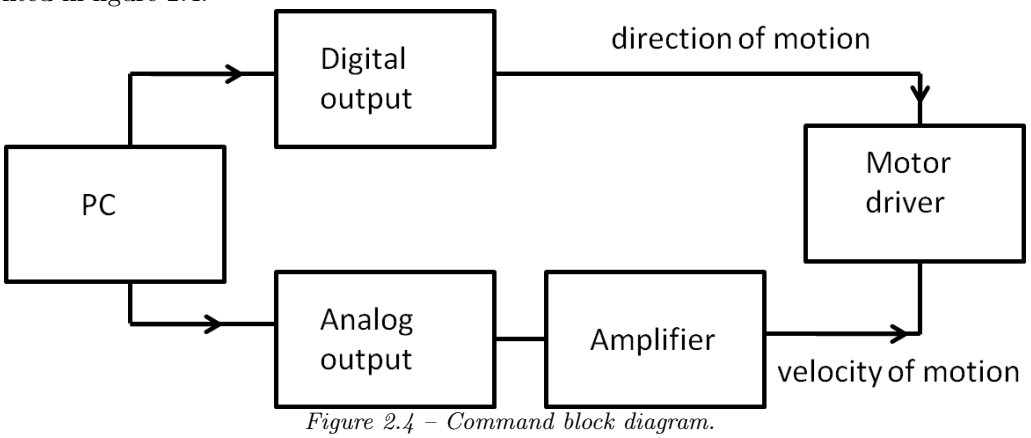

Figure 2.4 – Command block diagram.

A Matlab function with displacement extension u and constant velocity v as input parameters and a constant frequency square signal as output drives the stepper motor. To guarantee the value of 5 VDC with the current needed by the motor, the analog output is connected to a PM5171 Philips logarithmic converter. PM5171 amplifier can amplify constant voltage input. The Matlab function sends also a digital signal to the motor driver input/output to specify the

movement direction.

Figure 2.5 shows an example of the command signals. The input parameters displacement and velocity are $u = 800\mu$m and $v = 150\mu$m/s .

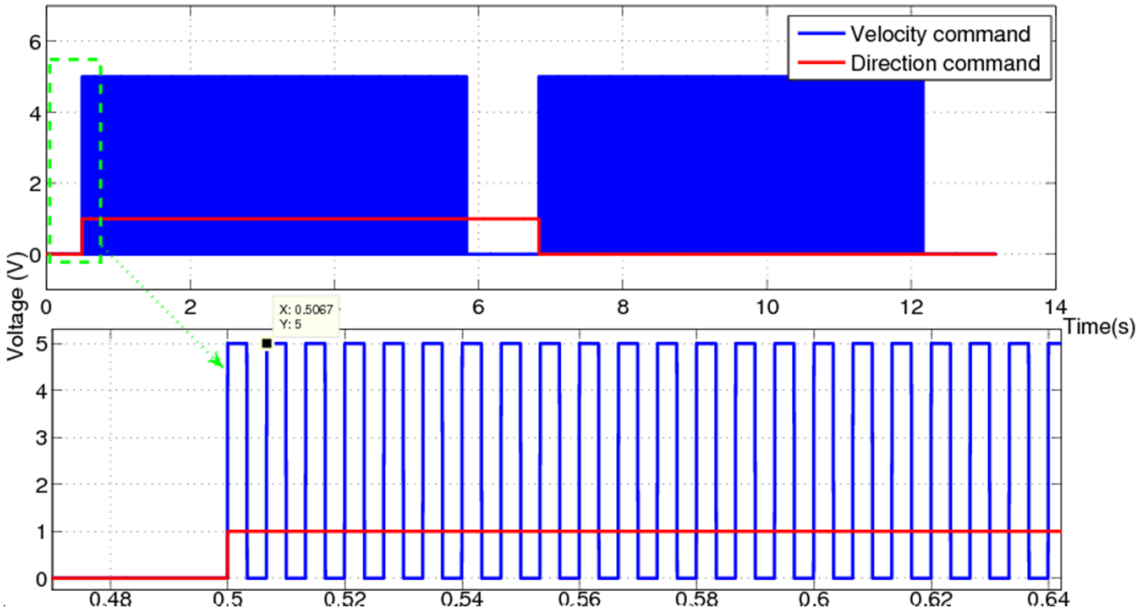

Figure 2.5 – Commnand signals of stepper motor.

2.2 Plate support

The shearing plate is tightened by screws between two aluminum supports as shown in the figure 2.6.

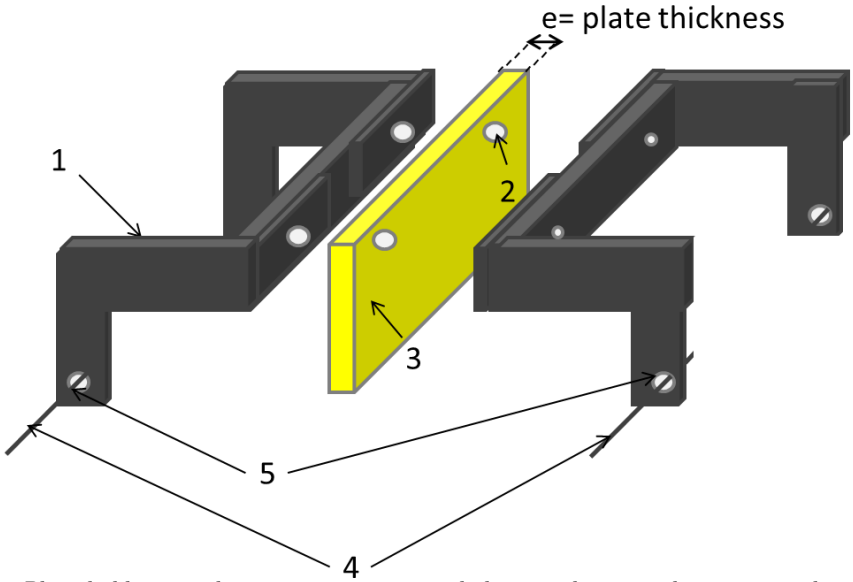

Figure 2.6 – Plate holder; 1: plate support; 2: screw holes; 3: shearing plate; 4: stainless steel cables; 5: stainless steel cable passage.

To eliminate vertical rotation of the plate, connection points of the transmission cables with the plate holder are fixed in the middle magnetic plan. This possible rotation results from the momentum of the magnetic resistance force and the pulling force (figure 2.7).

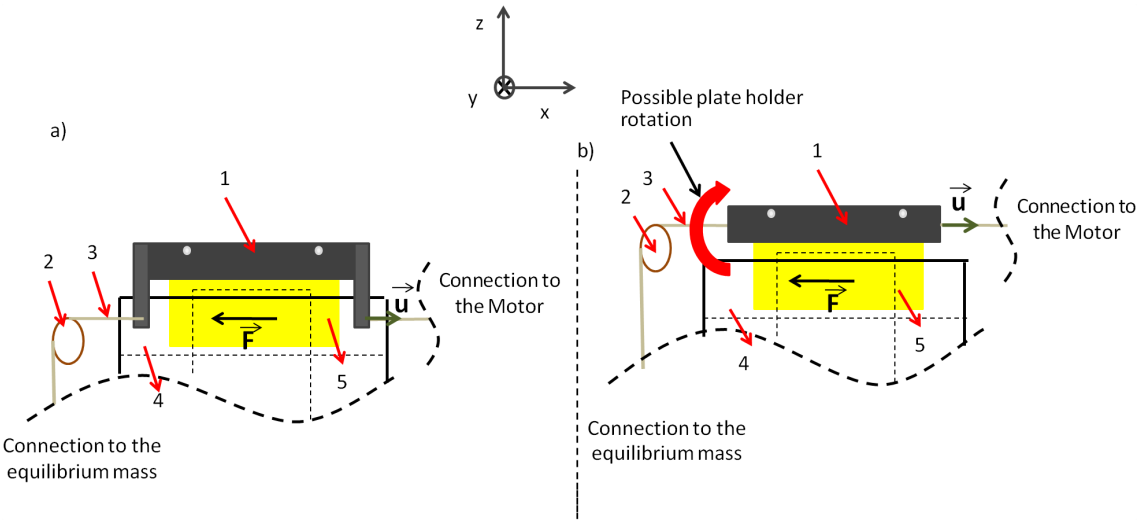

Figure 2.7 – Possible holder plate geometry: 1:plate holder; 2: pulley; 3: transmission cables; 4:MRF cavity; 5: shearing plate.

2.3 Transmission system

2.3.1 Transmission cables

Stainless steel cables (7X19) with a diameter ϕ=0.45mm are used for transmission. These wire ropes are twisted helically. They were chosen for their high tensile strength and light weight, 7 refers to the numbers of strands and 19 to the number of outer wires.

Figure 2.8 shows wire ropes structure and characteristics.

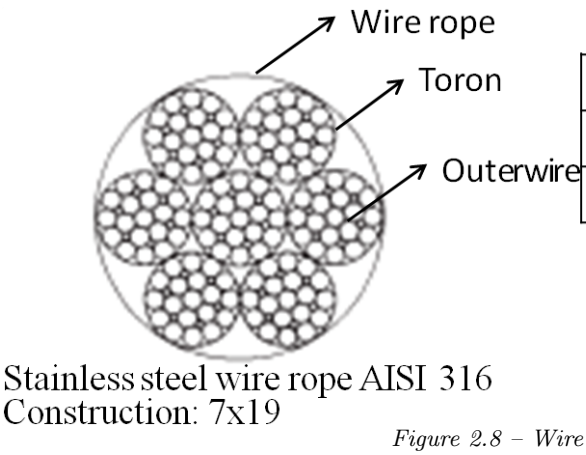

Nominal diameter (mm)	0.45
Minimum break load (N)	152
Weight (kg/1000 m)	0.81

Figure 2.8 – Wire rope structure.

Cylindrical brass stop sleeve are used for rope terminations.

2.3.2 Transmission path

Wire ropes run over pulleys (see figure 2.9). Pulleys structure is presented in figure 2.9. Its chemical composition, and highly crystalline molecular structure guarantee a high mechanical tensile strength and high impact resistance to the transmitted mass running over it.

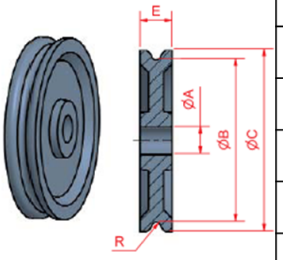

For cable ϕ up to mm	2-2.5
A (error= 0.01mm)	10
B (error= 0.30 mm)	56
C (error= 0.50 mm)	63.5
E (error= 0.15 mm)	6.4
R	1.27
Capaciy (N)	880
Weight (kg/100 pcs)	1.956

Figure 2.9 – Pulley structure.

3 Magnetic and electrical circuits

The total flow Ψ induced in the N turns of the coil, the electrical inductance L, the electric current I and the magnetic flux ϕ in the magnetic coil are related by:

$$\Psi = N\,\phi = L\,I \tag{2.1}$$

Therefore the knowledge of the coil inductance is necessary to characterize and to control the magnetic circuit .

3.1 Electrical circuit

Figure 2.10 presents the equivalent electrical network of the coils.

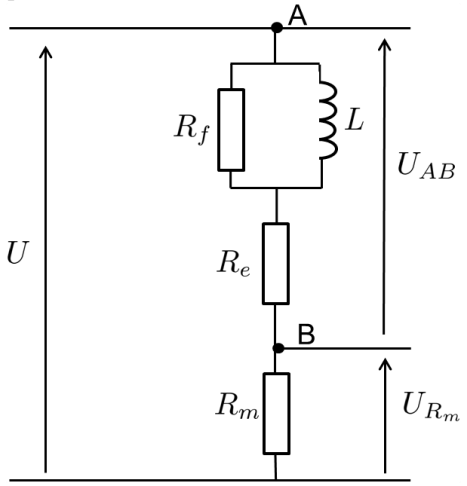

Figure 2.10 – Equivalent electric network of the coils.

R_{e} is the electric resistance of the coil and L its induction. The resistance R_{m}=1.5 Ω, placed in series with the coils (fig: 2.10), is used to measure the electric current I.

The energy losses due to eddy currents are noted by R_{f}. These power losses are inversely proportional to the square of the frequency f ($R_{\mathrm{f}} = \dfrac{\alpha}{f^2}$).

R_{e} is the ratio of voltage to current when the coils are subject to direct current signals. The constants R_{f} and L are obtained by impedance measurements at two frequencies values. These tests are done with an empty cavity.

When the magnetic circuit is subject to direct current, the voltage value across the branch AB, U_{AB}, is equal to the difference between the voltage U and the voltage across the resistance R_{m} (U_{Rm}); hence the expression of the resistance R_{e} will be:

$$R_{\mathrm{e}} = \frac{U_{\mathrm{AB}}}{I} = \frac{U}{I} - \frac{U_{\mathrm{Rm}}}{I} \tag{2.2}$$

For an input voltage value equal to U_{AB}=4 V the voltage value across R_{m} is U_{Rm}=0.47 V and therefore R_{e}= 12 Ω.

When an input sinusoidal voltage with a frequency f=100Hz and a peak value V=480 mV is applied to the magnetic circuit, the peak value of the measured electric current through R_{m} is I=11.6 mA, therefore the value of the equivalent impedance of the coils is Z_{AB}=41 Ω.

The measured electric current I with an input frequency signal f=1000 Hz and a peak value V=2.5V, is I=13.3mA. The equivalent impedance of the coils is Z_{AB}=187Ω .

Checked by an oscilloscope, both signals: input voltage and current within the magnetic circuit are perfect sine waves. The magnetic pole does not seem to be saturated.

Eq. 2.3 shows the relation between the equivalent circuit impedance L, the frequency f and the inductance Z_{AB}:

$$Z_{\mathrm{AB}} = \frac{R_{\mathrm{e}} R_{\mathrm{f}} + jLw(R_{\mathrm{e}} + R_{\mathrm{f}})}{R_{\mathrm{f}} + j\, L\, w} \tag{2.3}$$

where w=$2\,\pi\,f$. The values of L and α are obtained by solving numerically the system of non linear equations resulting from the calculation of the absolute value $|Z_{\mathrm{AB}}|$ for the two frequencies values f=100Hz and f=1000Hz.

The numerical values of the electric circuit components are presented in table 2.2.

L (mH)	inductance	62
R_{m} (Ω)	electrical resistance	1.5
R_{e} (Ω)	electrical resistance	12
α $(\Omega.s^{-2})$	coefficient losses	$1.75\,10^{8}$

Table 2.2 – Electric characteristics of the magnetic circuit.

The time constant in the circuit is $t_{\mathrm{circuit}} = \dfrac{L}{R_e + R_m} = \dfrac{62\,10^{-3}}{13.5} = 5$ ms. The value of the inductance L increases once the MRF is added to the cavity (Eq 2.9). The estimated value of L in this case will be L=78 mH which corresponds to a time constant t_{circuit}=5.8 ms.

Once the MRF is added to the MRF cavity the inductance of the circuit varies L=7.8mH and the time constant will be therefore equal to t=5.78ms.

While experimenting, after applying an electric voltage to the coils, and before the start of the shearing process, the system is leaved at rest for t=0.5s.

This time t, being larger than the time needed by the magnetic circuit to reach its final state (t=0.6s»5 t_{circuit}), this electrical time constant t_{circuit} will not be therefore harmful to our experiments.

3.1.1 Magnetic circuit

Figure 2.11 shows a three dimensional view of the magnetic circuit. It has a total mean length of L_{m}=260 mm and a cross-section area of $S_{\mathrm{m}} = 5{\times}10^{2}$ mm^2.

The total number of turns resulting from the two coils, placed in a series configuration on each side of the magnetic pole, is N_{total}=600.

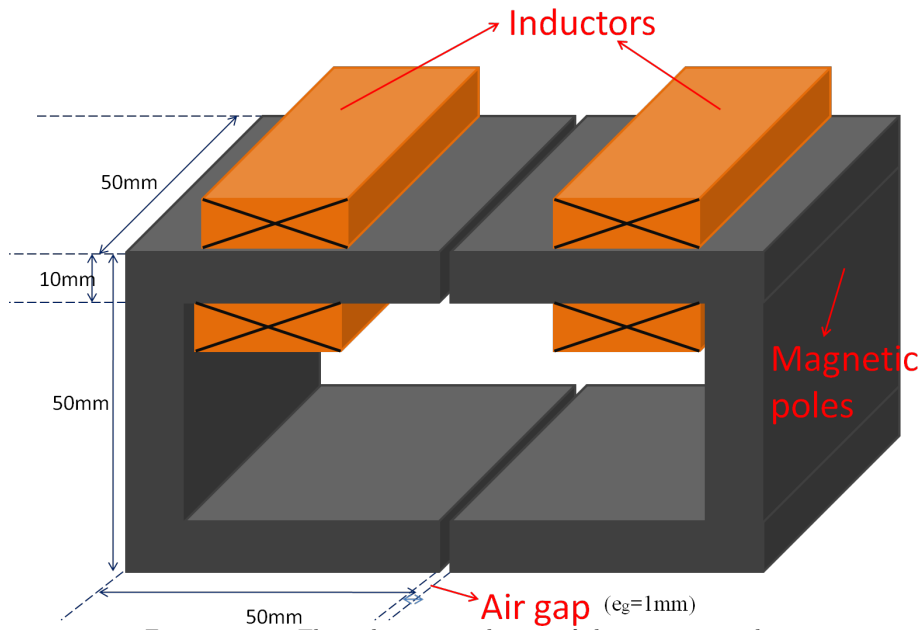

Figure 2.11 – Three dimensional view of the magnetic pole.

The magnetic circuit is characterized by its permeability μ. The magnetic permeability describes the ability of a material to support the formation of a magnetic field within itself.

The iron magnetic permeability denoted by μ_{iron} is acquired by solving the basic magnetic equations presented below (refer to paragraph 3.1.1.a).

The MRF is supposed to be placed in the upper gap between the two magnetic poles. The MRF has a nonlinear magnetic properties. We restrict our studies to the area presented in the figure 2.12 (0T $<B<$0.45T) where B and H are supposed to be varying linearly. The MRF-122 relative permeability is $\mu_{122\text{MRF}} \approx 2.8$.

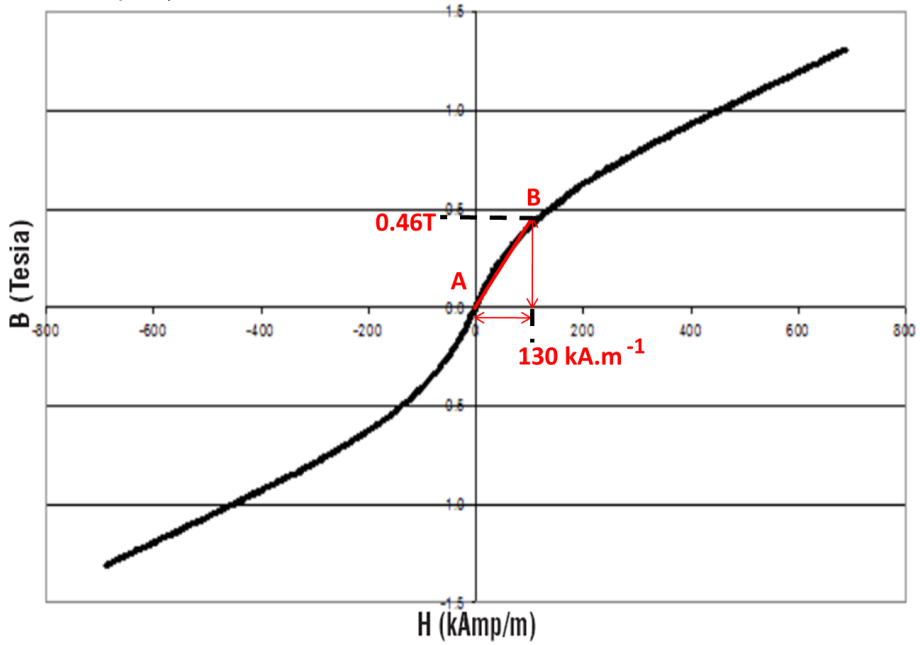

Figure 2.12 – Typical magnetic permeability of MRF-122EG, after Lord Corporation data [10].

3.1.1.a Basic magnetic equations

Ampère circuital law relates the magnetic flux ϕ to the reluctance $\mathcal{R}$, the electric current I and the number of turns N in the coil as following:

$$\mathcal{R}\phi = N\,I \Leftrightarrow \phi = \frac{N\,I}{\mathcal{R}} \tag{2.4}$$

The magnetic flux ϕ is defined by:

$$\phi = B.S \tag{2.5}$$

The magnetic reluctance $\mathcal{R}$ describes the magnetic resistance of the circuit to its penetration by the magnetic field. In a uniform magnetic circuit, $\mathcal{R}$ is calculated as:

$$\mathcal{R} = \sum_i \frac{l_\mathrm{i}}{\mu_0 \mu_\mathrm{i} S_\mathrm{i}} \tag{2.6}$$

where l_i is the length (in meters) of the circuit of material type i, μ_ri its relative magnetic permeability (dimensionless), S_i its cross-sectional area (in m^2) and μ_0 the free space magnetic permeability ($\mu_0 = 4\pi \times 10^{-7}$ H.m^{-1}).

μ_ri is the ratio of the magnetic permeability of the material i μ_i to the free space one μ_0 ($\mu_\mathrm{ri} = \frac{\mu_\mathrm{i}}{\mu_0}$).

Therefore, the total reluctance of our magnetic circuit is:

$$\mathcal{R}_\mathrm{total} = \mathcal{R}_\mathrm{air\ gap} + \mathcal{R}_\mathrm{shearing\ plate} + \mathcal{R}_\mathrm{fluid} + \mathcal{R}_\mathrm{magnetic\ iron\ pole} \tag{2.7}$$

In the experiments, H and B are time-invariant and are related by the following expression:

$$B_\mathrm{i} = \mu_\mathrm{ri}\mu_0 H \tag{2.8}$$

Combining equations 2.4 and 2.1 leads to

$$L = \frac{N^2}{\mathcal{R}} \tag{2.9}$$

From Eq. 2.7 we conclude that with an empty fluid cavity and without a shearing plate the equivalent reluctance of the circuit will be:

$$\mathcal{R} = \mathcal{R}_\mathrm{top\ gap} + \mathcal{R}_\mathrm{bottom\ gap} + \mathcal{R}_\mathrm{iron\ pole} = \frac{10^{-3}}{\mu_0\, S_\mathrm{m}} \left[2 + \frac{260}{\mu_\mathrm{iron}}\right] \tag{2.10}$$

Use of Eq. 2.10 in Eq. 2.9 leads to

$$\mu_\mathrm{r\ iron} = \frac{0.26L}{N^2\,\mu_0\,S_\mathrm{m} - 2\,10^{-3}\,L} \tag{2.11}$$

By solving numerically equation 2.11 we obtain the relative magnetic permeability $\mu_\mathrm{r\,iron}$ of the iron used in the magnetic circuit $\mu_\mathrm{r\ iron} = 158$.

Table 2.3 presents the values of the magnetic field H associated with an input current I=1A for the three tested fluid concentration.

ϕ	H (kA/m)
22%	71.3
32%	41.3
40%	35.3

Table 2.3 – Magnetic filed H values for an input current of I=1A.

4 Sensors

4.1 Displacement measurement

The plate support displacement is measured by a linear variable differential transformer (LVDT Solartran A/1-S). The LVDT structure and specifications are presented in figure 2.13.

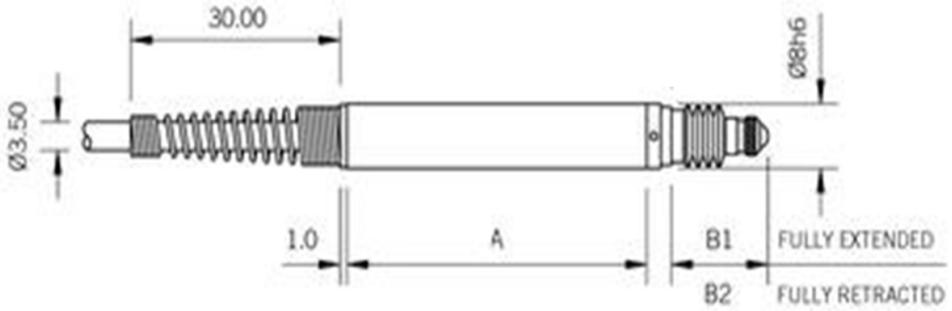

Description				Measurment range ([-1 1] mm)			
A (mm)	B (mm)	B1 (mm)	B2 (mm)	Post-travel (mm)	Repeatability (μm)	Accuracy (% of reading μm)	Pre-travel (mm)
43	3.5	13.9	11.4	0.35	0.15	0.5, 1 μm	0.15

Figure 2.13 – Characteristics of the displacement sensor (after www.solartronmetrology.com).

The high positioning accuracy, measurement range and external physical dimensions of the LVDT makes it suitable for our experiments.

Figure 2.14 shows an example of a measured motor displacement signal u with the LVDT sensor. The measured electronic noise calculated for the LVDT, evaluated as the root mean square of the acquired displacement signal when the system is left at rest (figure 2.14), is n=0.5μm.

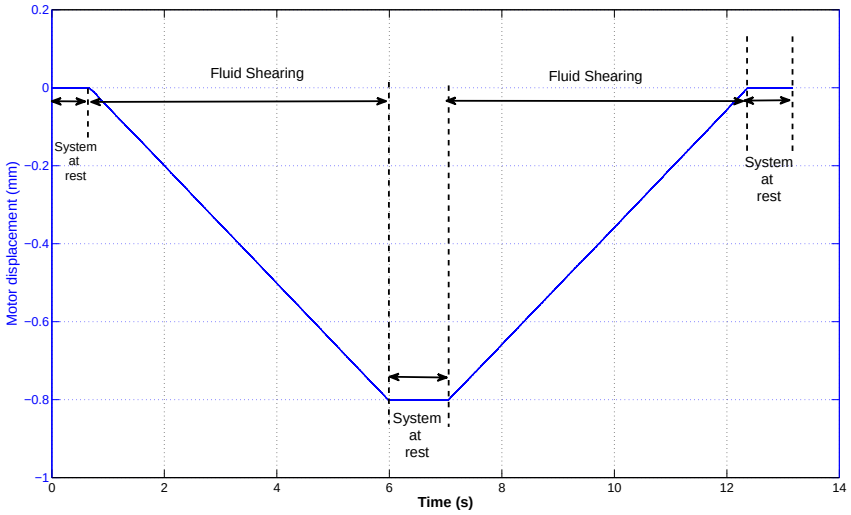

Figure 2.14 – Typical displacement imposed by the motor.

When a displacement measurement exceeding u=2mm is needed, the laser displacement sensors Keyence LB-12 is used. The laser sensor specifications are presented in table 2.4.

Measuring range	± 10 mm
Resolution	2 μm
Output	0.4 V/mm

Table 2.4 – Specifications of the laser displacement sensor (after www.keyence.com).

4.2 Force measurement

The bottom of the fluid cavity is only in contact with the top face of the force sensor. In this disposition, the fluid plate interaction and the weight of the fluid cavity are the only forces exerted to the force sensor.

Figure 2.15 highlights the fluid, plate and force sensor dispositions in the measuring device.

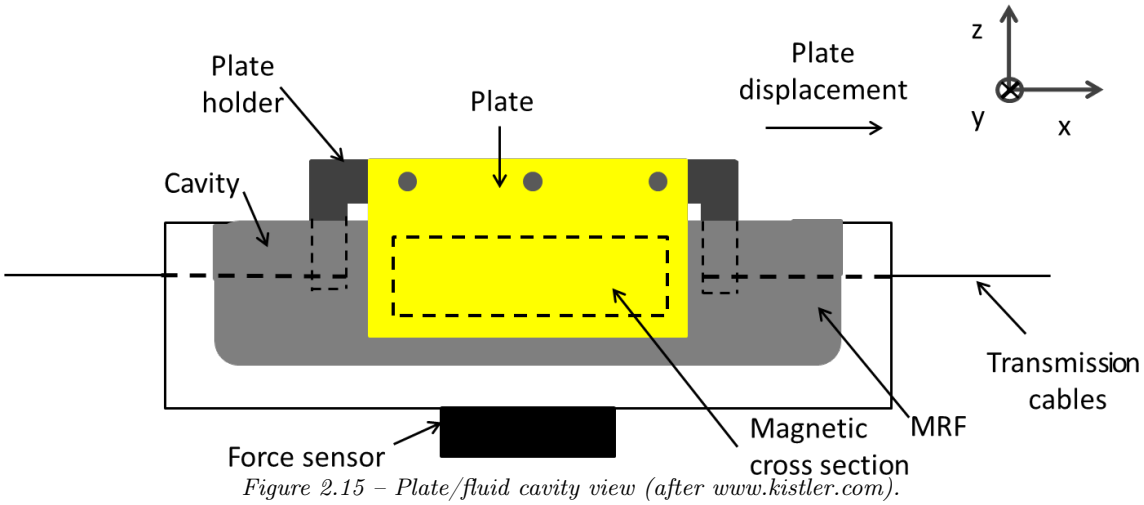

Figure 2.15 – Plate/fluid cavity view (after www.kistler.com).

Kistler 9251A is the piezoelectric force sensor used in force measurement (figure 2.16). Its carateristics are presented in table 2.5

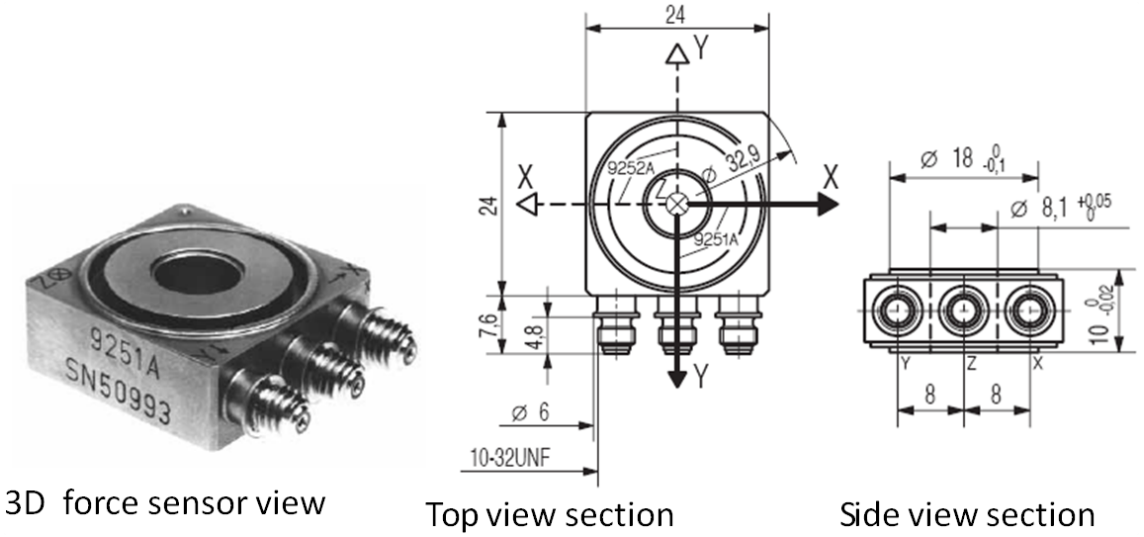

Figure 2.16 – Force sensor type: Kistler 9251A (after www.kistler.com).

Measuring range	F_xF_y Fz	± 2.5 kN ±5 kN
Sensitivity	F_xF_y Fz	≈ -8pC/N ≈ -4 pC/N
Cross talk	$F_z \rightarrow F_x, F_y$ $F_x \leftrightarrow F_y$ $F_x, F_y \rightarrow F_z$	$\leq \pm 1\%$ $\leq \pm 3\%$ $\leq \pm 3\%$

Table 2.5 – Specifications of the force sensor (after www.kistler.com).

The force sensor is chosen so that the maximum value of the theoretical measured force in the x-direction F_x will be within its measuring limits. The output signal of the piezoelectric force sensor is amplified by the charge amplifier KISTLER TYPE 5015.

The maximum value of magnetic field induction reached in my experiments is B=0.4T. Its corresponding magnetic field value H is H=112 kA/m and the theoretical maximum yield stress is equal to τ_y=24 kPa (figure 2.12). Since the sheared surface is equal to $S_{total} = 2 \times S_m = 1 \times 10^{-3} m^2$ therefore the maximum value of resistance force will be F_{xmax}=24N.

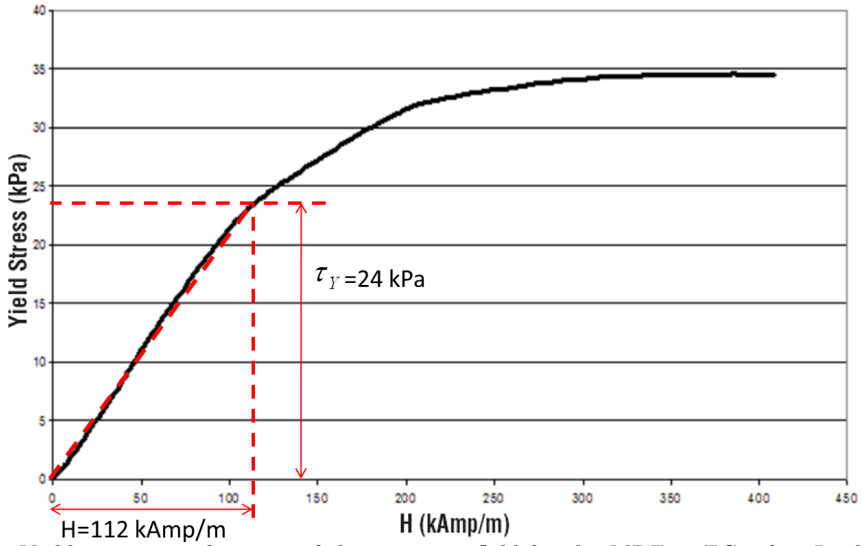

Figure 2.17 – Yield stress as a function of the magnetic field for the MRF122EG, after Lord Corporation data [10].

4.3 Magnetic field measurements

The magnetic field B is measured by a probe GM07-HIRST inserted in the air gap e_g between the magnetic poles (see figure 2.11).

Measuring range	Range 1	0.0 - ±3.000 T
	Range 2	0.0 - ±299.9 mT
	Range 3	0.0 - ±29.99 mT
	Range 4	0.0 - ±2.999 mT
Reproducibility		≤ ±0.5%
Dimensions	Length	175 mm
	Width	89 mm
	Height	40 mm

Table 2.6 – Specifications of the gaussmeter (after www.gaussmeter.co.uk).

5 Microscopy

5.1 High resolution numerical microscope observations

Basic magnetic effects were observed by the VHX-1000 digital microscope from Keyence. A real-time camera is included within the system. The maximum zoom ratio is 5000X and the image resolution is 2000 pixels x 2000 pixels. The particle scale (2μm) can be noticed with this type of microscope and observation in presence of magnetic field B are achievable.

Figure 2.18 shows an example of fluid suspension observed with the VHX-1000 digital microscope.

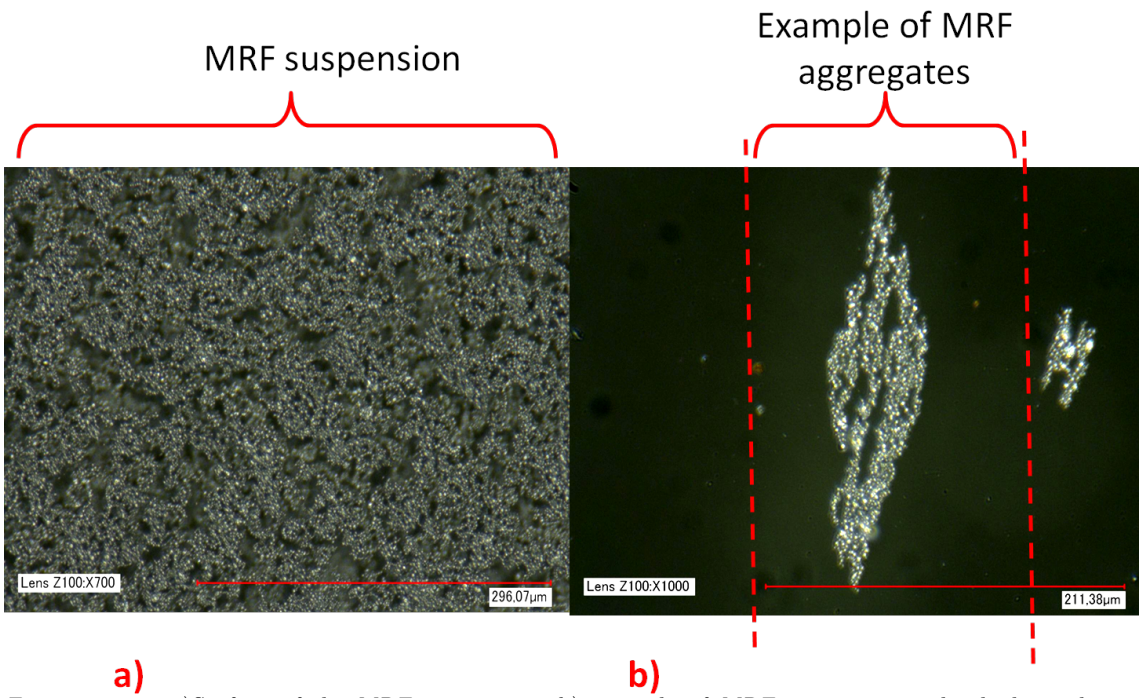

Figure 2.18 – a)Surface of the MRF suspension, b) example of MRF aggregates under high resolution optical microscope.

5.1.1 Scanning electron microscope (SEM)

To observe the fluid in the scale of its smallest constituents (particle scale), we proceed to a scanning electron microscopy.

Two principal operating modes can be used in SEM:

- the Z contrast: gives informations about chemical composition of the sample;
- the SE contrast: gives informations about the external topography of the sample.

For SEM observations a specimen is normally required to be completely dry since the SEM chamber is in high vacuum. The add of magnetic field to the specimens while observing is impossible. The MRF samples were prepared as following: I proceed to a settling of the MRF, the sample is then taken from the sediment, spread and dried on a metallic support. The MRF sample positioning in the SEM chamber is presented in figure 2.19. Figure 2.20 shows magnetic particles suspensions in the fluid in the two different observation modes.

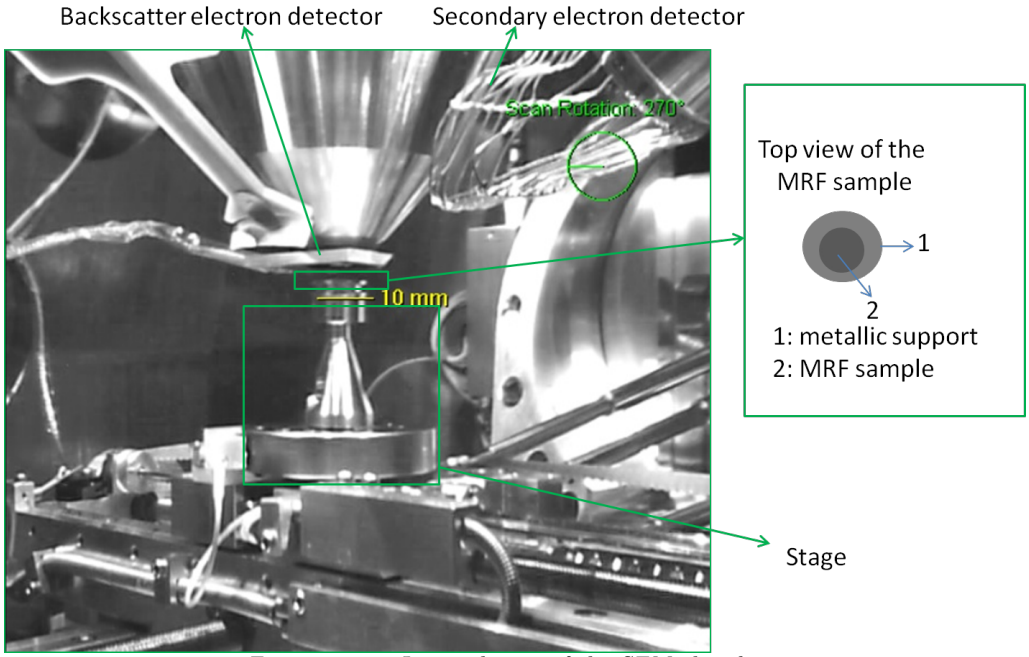

Figure 2.19 – Internal view of the SEM chamber.

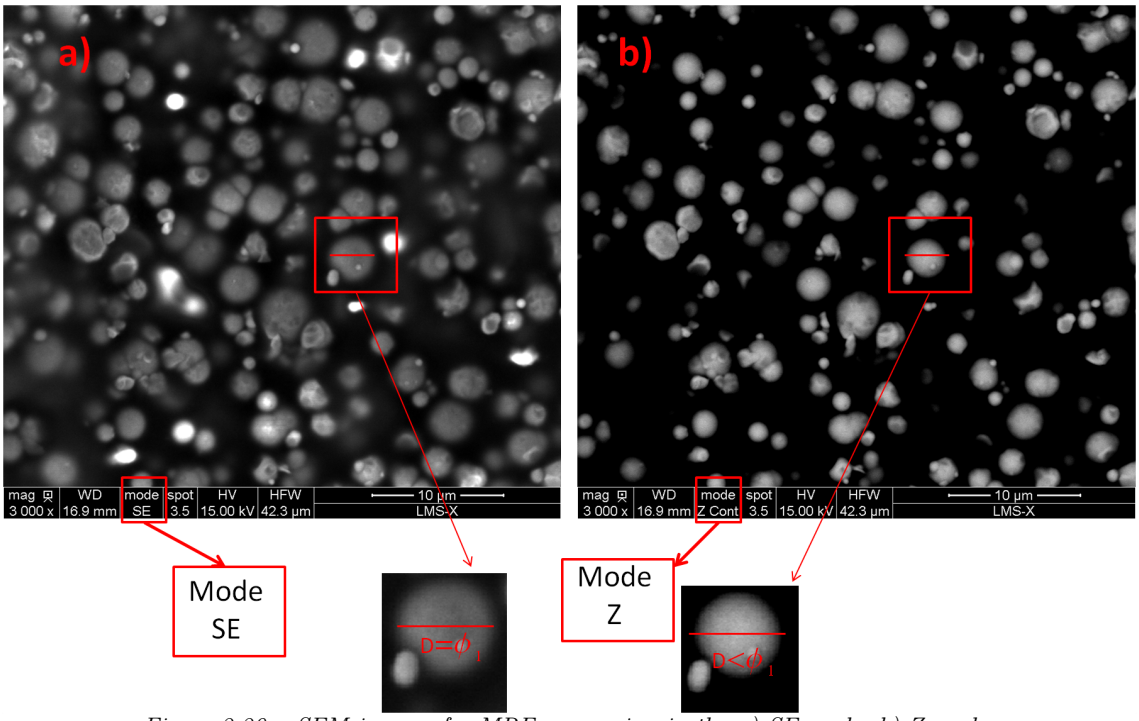

Figure 2.20 – SEM image of a MRF suspension in the a) SE mode, b) Z mode.

5.2 Stereo microscope observations

By microscopic observation, it was possible to see the fluid internal composition in the scale of its chain-like structure.

The MRF linear shearing phenomenon is acquired by a high resolution and low noise camera Pike F421 connected to the optical microscope SMZ1000 from Nikon. This type of microscope uses visible light and a system of lenses to magnify the samples, therefore the presence of magnetic field will not affect its functioning. The maximum zoom ratio of this stereo microscope is 8X.

The camera characteristics are summarized in table 2.7

Resolution	2048 pixels x 2048 pixels
Pixels size	7.4μm x 7.4μm
Max. Line/Frame Rate	15 fps

Table 2.7 – Pike F421 characteristics.

The system camera/microscope is placed above the slight opening in the plate holder as shown in figure 2.2. It is fixed on a heavy metallic support to prevent vibration transmission.

While experimenting two principle micro-structure states of MRF were observed:

- isotropic suspension: uniform repartition of particles in the MRF suspension; the fluid has identical properties and invariant structure in all directions (figure 2.21a));
- anisotropic chain structure suspension: internal chain-like structure of particles in the oil medium (figure 2.21b)).

An example of these micro-structure, taken by the pike, is presented in the figure 2.21

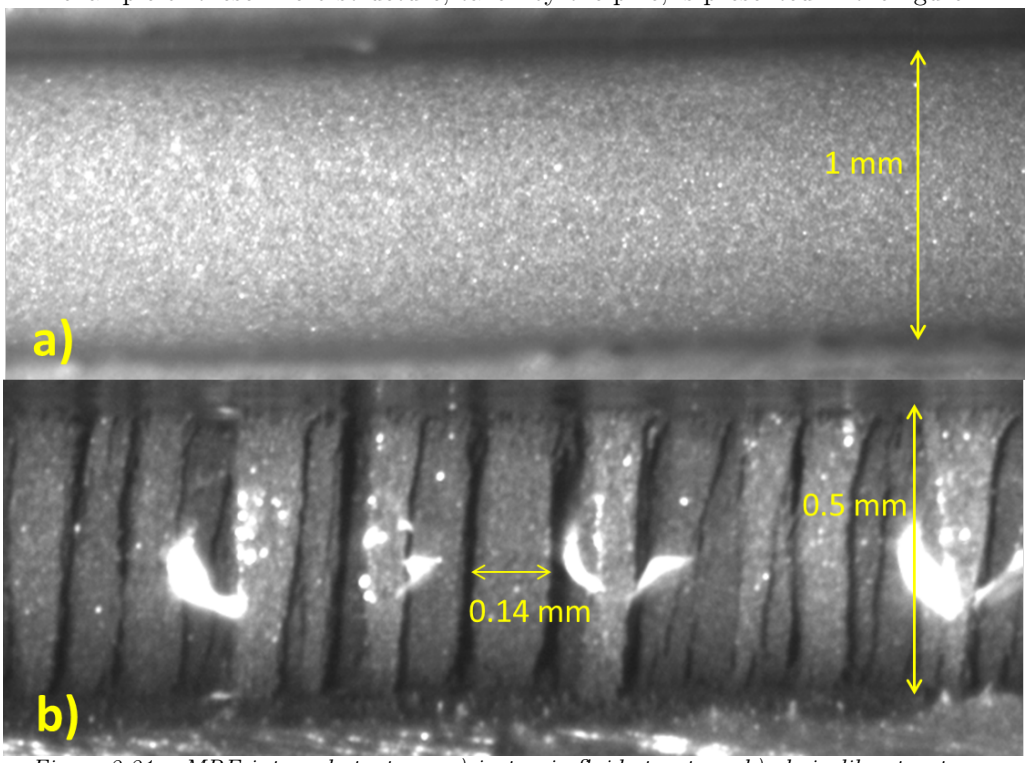

Figure 2.21 – MRF internal stucture: a) isotropic fluid structure; b) chain like structure.

5.3 Particle image velocimetry PIV

To observe the velocity field within the MRF observations, done as described in Sec 5.2, we proceed to an internal tracking velocimetry of the particles suspended in the fluid. The biorthogonal decomposition, BOD, is the method used to achieve a space-time decomposition of the MRF phenomena. It generates an orthogonal sets of temporal and spatial modes coupled to each other.

5.3.1 Definition

If U(x,t) is a signal function of a space variable $x \in \Re^3$, and time variable $t \in \Re$, it's corresponding BOD decomposition will be:

$$U(x,t) = \sum_{K=1}^{\infty} \alpha_k \Psi_k(t) \phi_k(x) \tag{2.12}$$

Ψ_k, ϕ_k, α_k are the elements of the spectral decomposition.

The BOD was introduced first by Aubry *et al.* [43]. Temporal functions Ψ_k are called "chronos", and spacial functions ϕ_k "topos". Their relative combination at a given k is called spatio-temporal mode of the fluctuating system. α_k are the eigenvalues, they represent the square root of the fluctuation energy contained in the corresponding modes.

The chronos Ψ_k and topos ϕ_k satisfy the following orthogonality relation:

$$\sum \Psi_k(i)\Psi_l(i) = \sum \phi_k(i)\phi_l(i) = \delta_{kl} \tag{2.13}$$

A detailed mathematical formulation on the biorthogonal decomposition can be found in Aubry et *al.* [43].

Figure 3.15 presents an example of a PIV generated during the MRF chain formation process, in the direction of the magnetic field B.

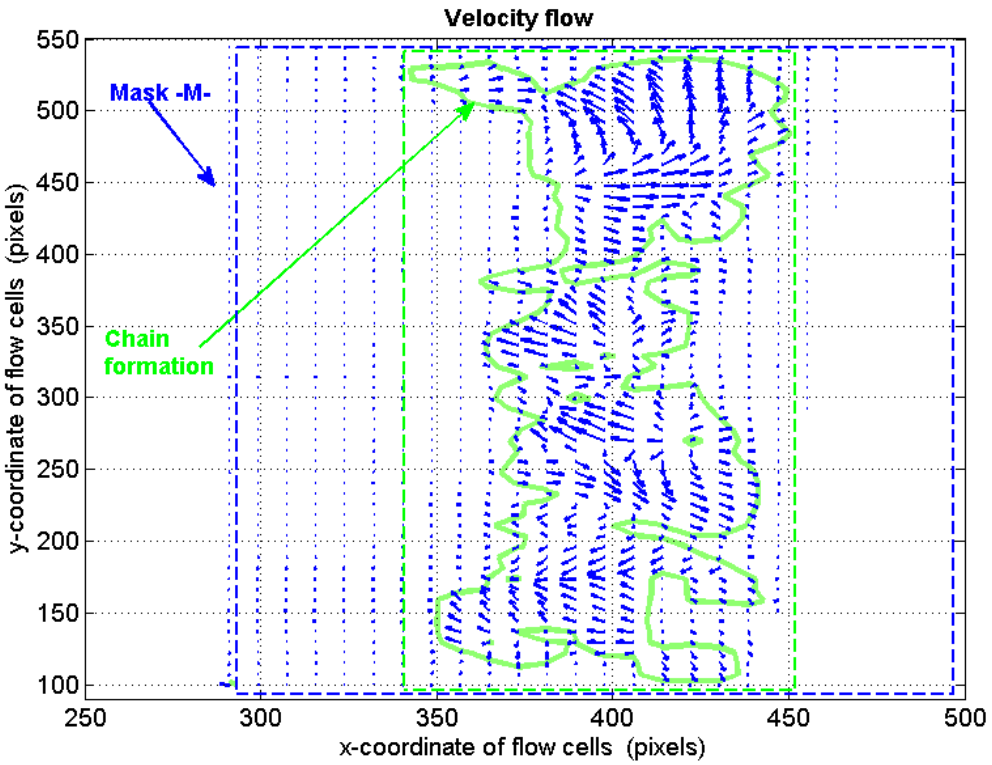

Figure 2.22 – Velocity field of MRF particles during the formation of the chain like structure.

The height of the formed MRF chain (limited by the mask M in figure 3.15)corresponds to the fluid gap thickness g_f.

5.3.2 Application to MRF observation

The image treatement is done by the CRtoolbox package of Matlab. This toolbox is implemented by Julien Dienner and is founded by the ANR research project Chene -Roseau in a collaboration between LadHyx, Piaf and Evasion teams.

The image processing steps are user interface and are done as following:

1. choice of region of interest or mask ;
2. decomposition of the mask into a regular grid of square patches;
3. computation of the optical flow using KLT features tracker (based on the independent pixels motion from each video image to the next);

4. BOD of the computed optical flow: the CR-BOD returns the chronos, topos, alpha as well as the coordinates of flow cells.

Figure 2.23 shows an example of mask computation. The red points in this figure present the mask grid used to track the fluid flow.

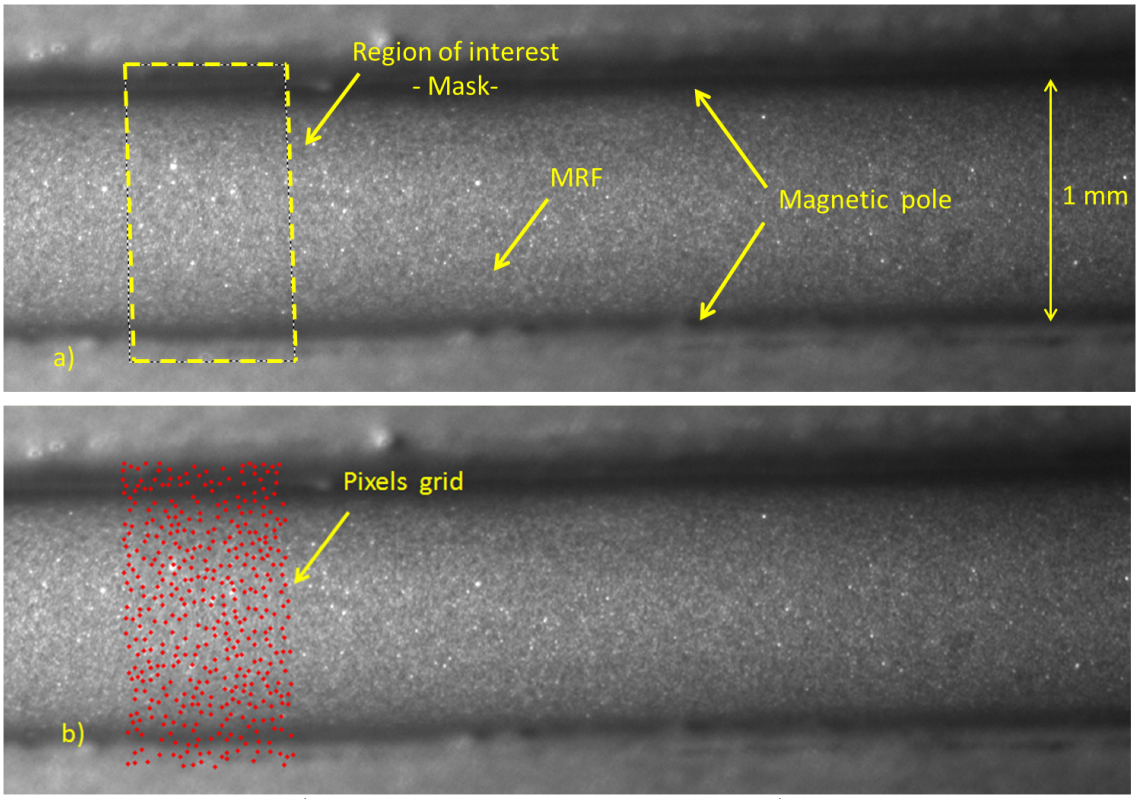

Figure 2.23 – a)Choice of region of interest for CR-BOD; b) grid of the mask M.

In the following BOD studies the u and v parts of the computed optical flow are plotted in their corresponding coordinates flow cells.

6 Tests

The goal of our studies is to model the MRF response in the direct shear mode; x being the translation movement direction of the shearing plate in the fluid cavity.

6.1 Motion

Six degrees of freedom describe the position and orientation of the plate support in three dimensions (see figure 2.24).

The vector $\vec{u}\begin{cases} u_x \\ u_y \\ u_z \end{cases}$ denotes plate support displacement and $\vec{\theta}\begin{cases} \theta_x \\ \theta_y \\ \theta_z \end{cases}$ indicates possible plate rotations around the x y and z axis.

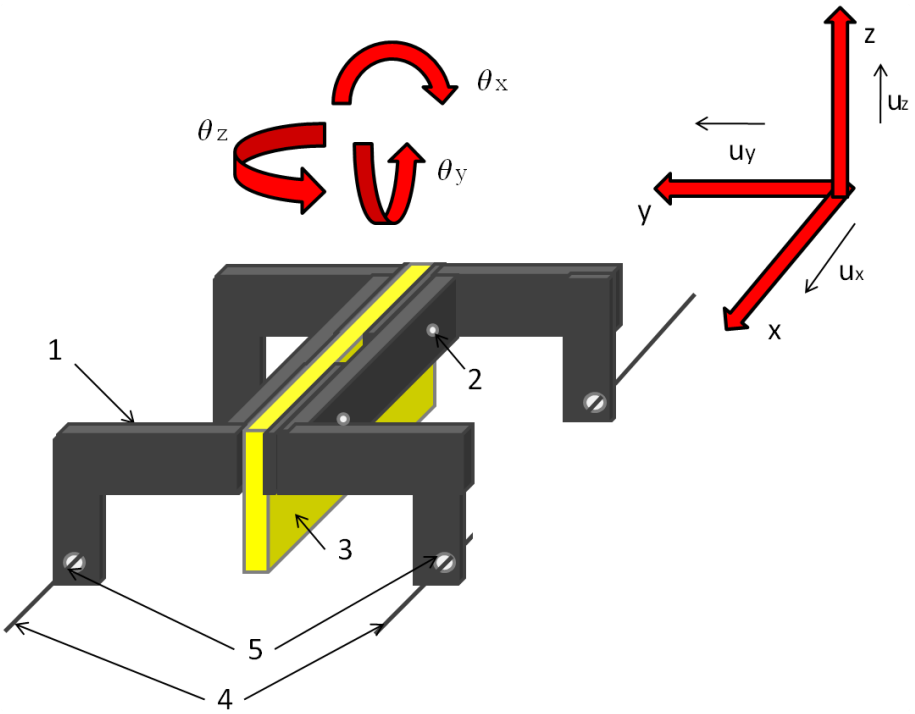

Figure 2.24 – Plate holder; 1: plate support; 2: screws; 3: plate; 4: stainless steel cables; 5: stainless steel cable passage.

6.1.1 High frequency isolation

The motor generates high-frequency vibrations in the x direction (figure 2.26). Thanks to the cable transmission system and isolating sand tank, these vibrations are not transmitted to the fluid cavity, the motion sensor support, and the plate holder (figure 2.25).

In the following tests, the motor is driven by a variable speed profile starting from V_s=10μm/s and ending at a velocity value V_e=10mm/s. The system is at rest during the first two seconds and the last four seconds. The sampling rate is f_s=25kHz and the acquisition duration is 10s. The vibration signal's are measured by accelerometers.

The accelerometers output are amplified and filtered electrically by a low pass filter with a cutoff frequency f=30kHz. The amplifier time constant is t=0.1s.

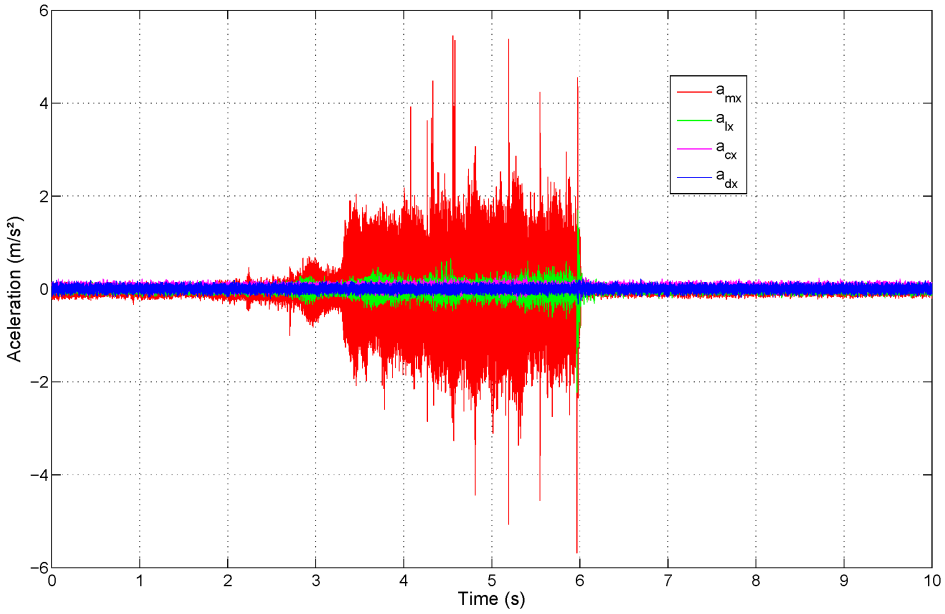

Figure 2.25 – Acceleration of the different parts system.

The vibrations of the motor a_{mx}, the plate support a_{lx}, the fluid cavity a_{cx} and the motion sensor a_{dx} in the x direction are presented in the Figure 2.25.

Figure 2.25 shows clearly that the vibrations measured on the fluid cavity and motion sensor seems to be invariant whether the motor is putted on motion or not. The cavity and the motion sensor are supposed to be stationary. The noise level of the accelerometer evaluated as the root mean square of the measured acceleration when the motor is switched off is: n_{acc}=RMS($a_{\mathrm{mes\,mot\ off}}$)= 0.04 m.s^{-2}.

Once the motor is switched on, the accelerometers depict an increase in the measured acceleration a_{mx} and a_{lx}. The Fourier transform of these signals are presented in figure 2.26. The FFT was done for the part of the signals elapsing between 2.5s <T < 5s; it includes N=62501 points.

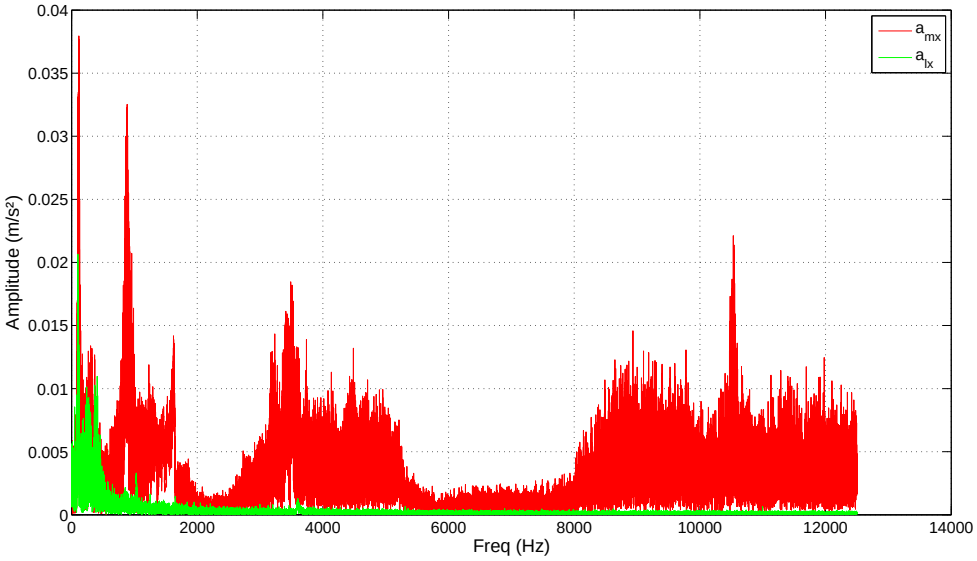

Figure 2.26 – Fourier transform of the motor and the plate support acceleration.

The values of the plate holder and motor vibration in term of displacement are presented in figure 2.27. These signals are generated by dividing the FFT by the square of ω (ω=2π f) for f higher than f > 10Hz. The maximum calculated level of the displacement is d_{mx}=0.8μm and d_{lx}=0.7μm.

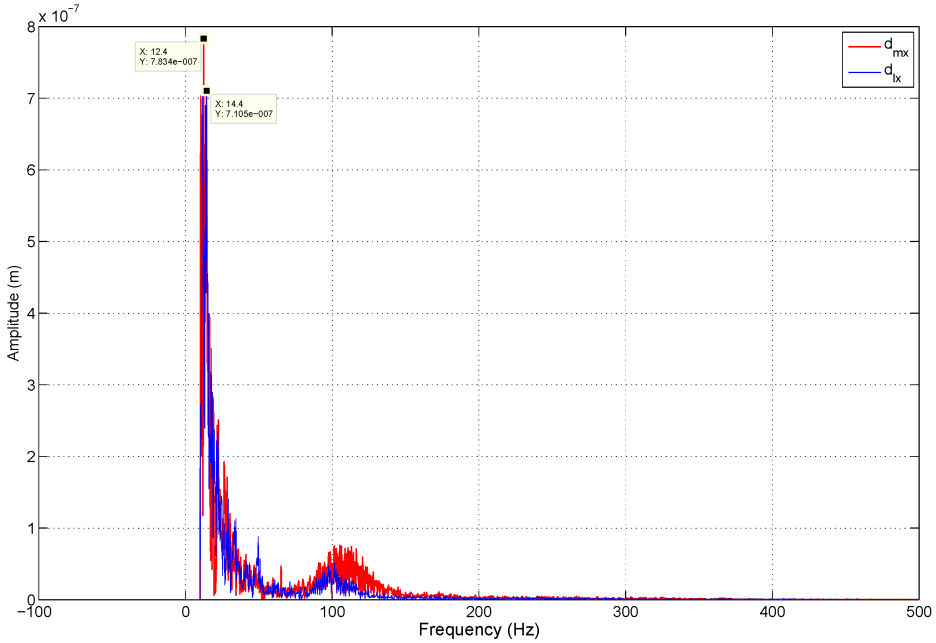

Figure 2.27 – Motor and plate holder displacement measurement.

The vibrations of the plate support in the y (a_{ly}) and z (a_{lz}) directions were also investigated. The resulting measurements (figure 2.28) show clearly that the levels of vibration measured in the opposite sides of the shearing plate holder for both directions y and z are equal.

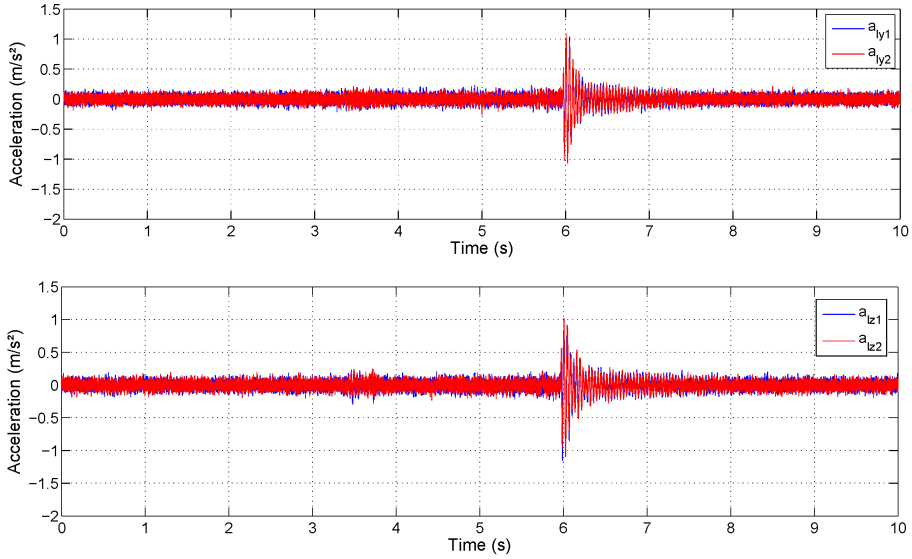

Figure 2.28 – Plate support acceleration in the y and z directions.

Figure 2.29 shows the FFT of the signals a_{ly1} and a_{lz1} for 2.5s <T< 6.5s and the maximum calculated levels of their corresponding displacements d_{ly} and d_{lz} (d_{ly}=d_{lz}=1.6 μm).

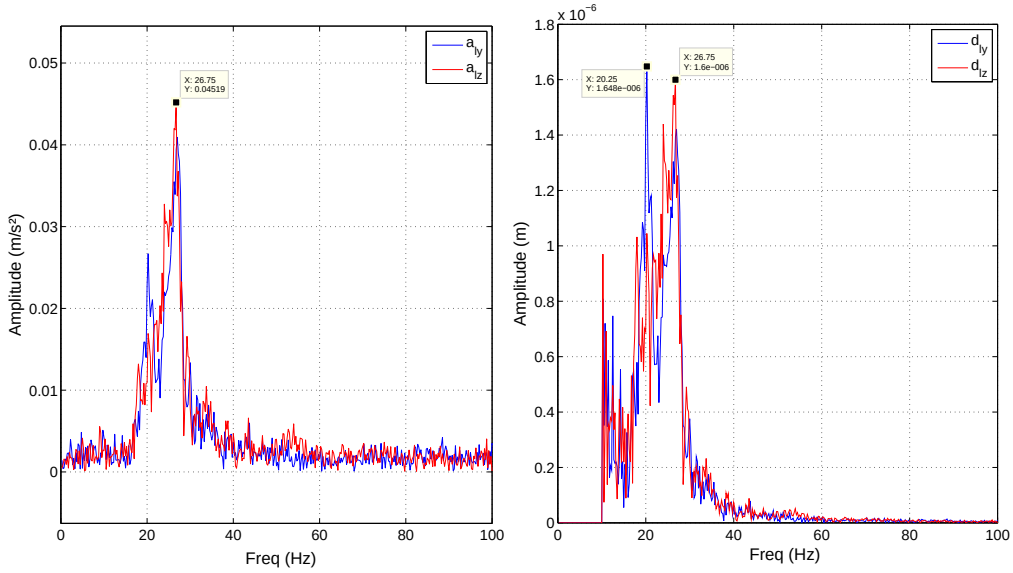

Figure 2.29 – Plate support vibrations in the y and z directions; left:acceleration right:displacement.

Neglecting the ending of the shearing motion 2.5s <T <5.8s the calculated level of the plate displacement in the z and y directions decreases to d_{ly}=d_{lz}=0.9μm (figure 2.30).

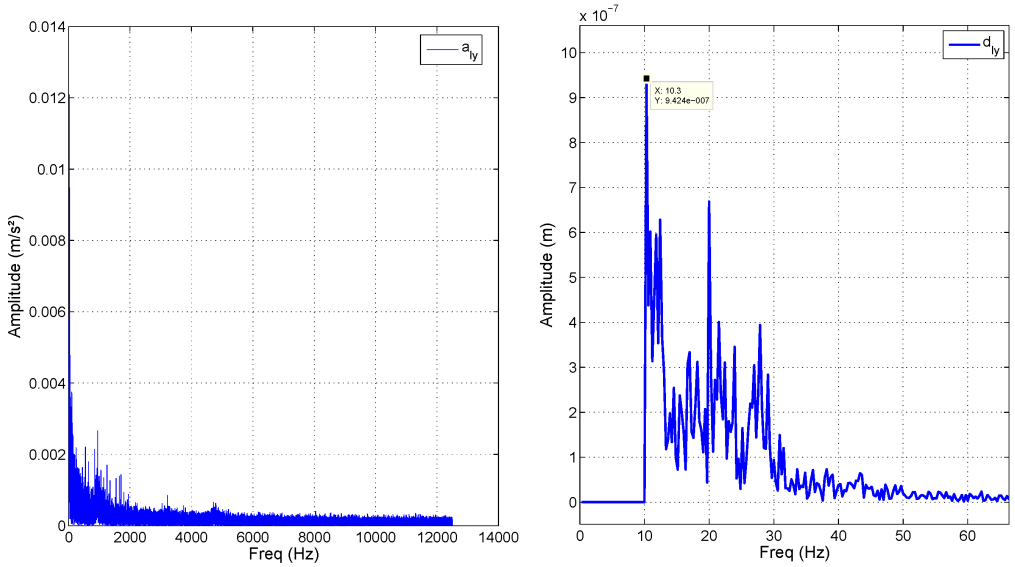

Figure 2.30 – Plate support vibrations in the y and z directions; left:acceleration right:displacement.

The positioning of the accelerometers in these tests is illustrated in figure 2.31.

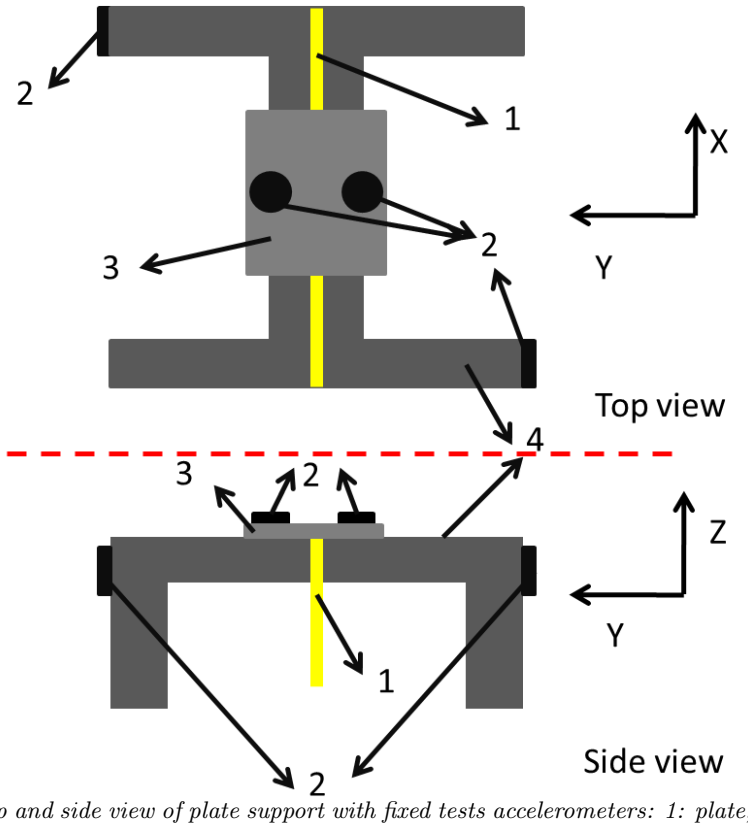

Figure 2.31 – Top and side view of plate support with fixed tests accelerometers: 1: plate; 2: accelerometers; 3: thick aluminum plate; 4: plate support.

6.1.2 Plate holder velocity response

Figure 2.32 shows the measured motor displacement u_{m} and the calculated velocity profile v_{m} to the forward and backward command signals of the figure 2.5. From this we can conclude that both command and measured displacement are equal u_{m}=u=800μm, calculated and imposed velocity matches as well v_{m}=v=150 μm/s.

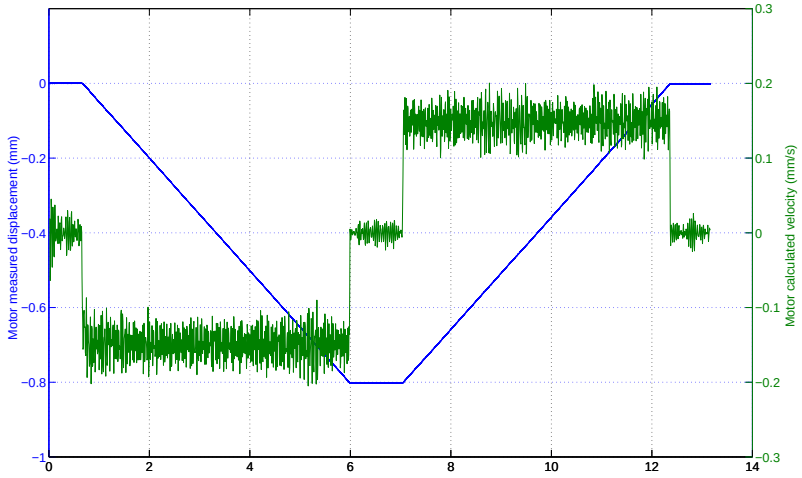

Figure 2.32 – Typical comparison between imposed motion and measured motion of the motor.

The velocity profile v_{m} is generated by finite difference of the filtered measured displacement u_{m} . The filter process consists on reducing the original sampling rate of the acquired displacement

u_m to a lower rate and therefore filters the input data with a low pass filter. In this example (figure 2.33) the sample rate of u_m is reduced by a factor of 100. The calculated velocity profiles before and after filtering, of the displacement signal presented in figure 2.32, are shown in figure 2.33.

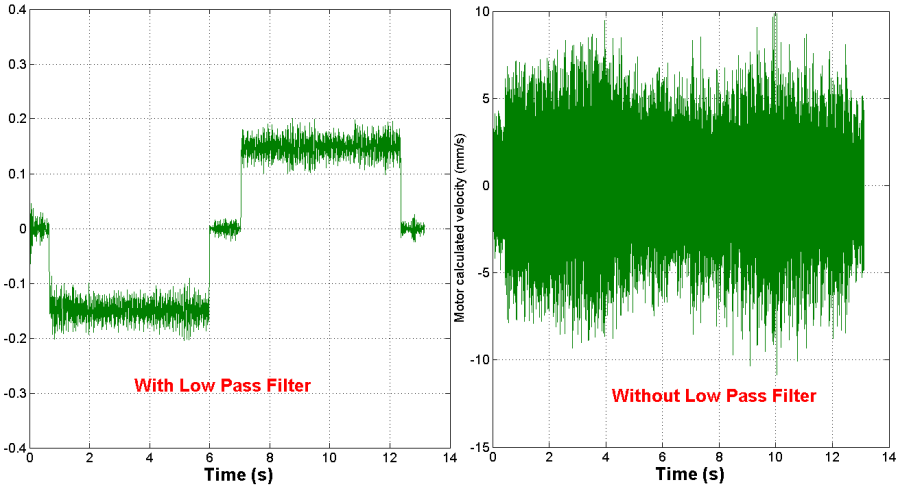

Figure 2.33 – Velocity profile with and without digital filtering.

6.1.3 Forces: F_y and F_z

Figure 2.34 presents the measured forces in the y and z directions (F_y and F_z) once the shearing plate is animated by a translation motion in the x direction.

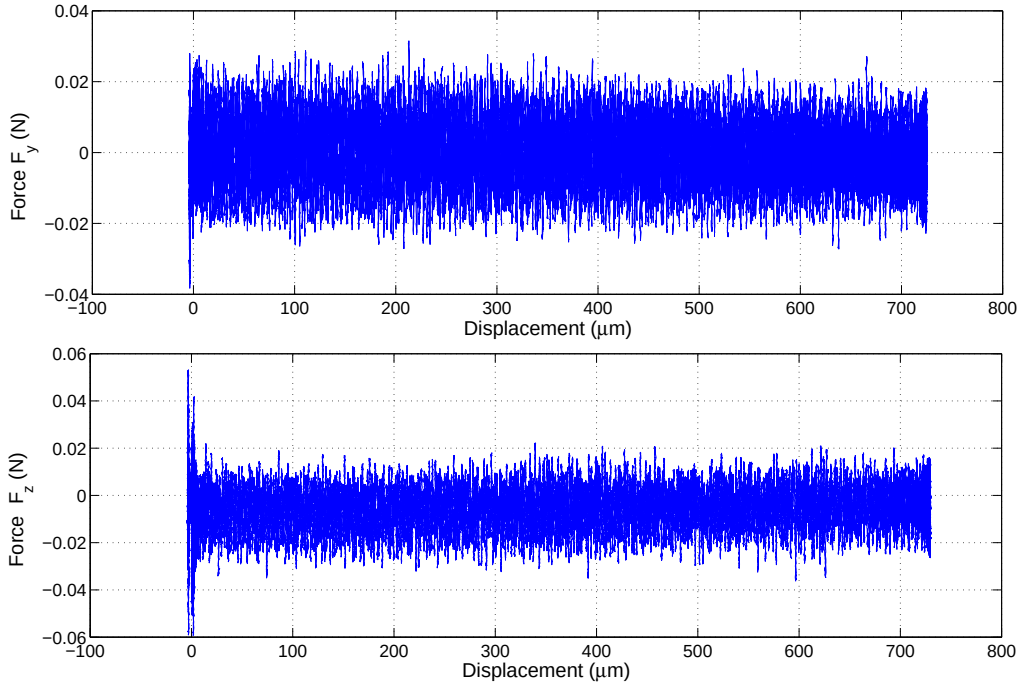

Figure 2.34 – Measured force components with shearing plate displacement.

No significant variations of the F_y and F_z forces are detected in figure 2.34. The measured impulsions at the beginning of the F_z signal corresponds to the start of the motor motion. The noise level of these measurements are evaluated by the calculation of their the root mean RMS= 0.01N.

6.2 Shearing force F_x

The reliability of the force measuring system depends on:

- the noise level;
- the bias due to:
  1. the drag force $F_{\text{bias}\,1}$ acting on the shearing plate in the direction of the relative fluid flow velocity;
  2. the fluid shearing force $F_{\text{bias}\,2}$ exerted by the whole plate in the unmagnetized region of the fluid.

6.2.1 Noise level

The noise level originating from the measuring system is found to be F_{noise}=0.01N corresponding to a shear stress τ=0.01kPa.

6.2.2 Drag Force $F_{\text{bias}\,1}$

The drag force is:

$$F_{\text{bias}\,1} = \frac{1}{2}\,\rho\,V^2\,C_{\text{D}}\,A \tag{2.14}$$

where ρ is the fluid density, V is the speed of the object relative to the fluid, C_{d} is the drag coefficient and A is the reference area defined as the shearing plate area in the direction of motion.

The maximum shearing velocity reached in our experiments is V_{max}=1000μm/s. The largest thickness of the shearing plates is e_{max}=0.45mm with a width l=150mm (figure 2.35) and therefore the maximum reference area will be A_{max}=6.7 10^{-5}m^2.

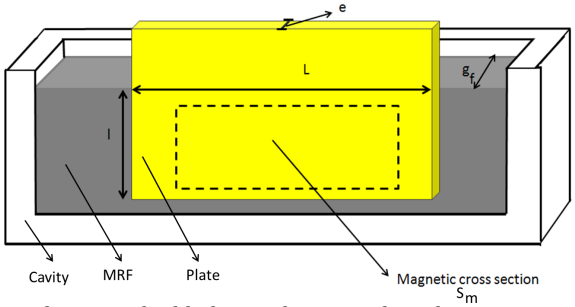

Figure 2.35 – Vertical section highlighting shearing plate disposition in the MRF cavity.

Table 2.8 summarizes the values of the $F_{\text{bias}\,1}$ for the three fluid concentration ϕ=22%, 32% and 40%, the order of magnitude of the drag coefficient being C_{d}=1.

ϕ	$F_{\text{bias}\,1}$ (N)
22%	$0.8\,10^{-7}$
32%	$1\,10^{-7}$
40%	$1.3\,10^{-7}$

Table 2.8 – Drag force of unmagnetized MRF at shearing velocity V=1000$\mu m/s^{-1}$.

The largest calculated value of $F_{\text{bias}\,1}$=1.3 10^{-7}N corresponds to a shear stress τ= 1.3 10^{-7}kPa.

The expression of $F_{\text{bias}\,2}$ is:

6.2.3 Shearing force due to the unmagnetized region of the plate $F_{\mathbf{bias\,2}}$.

The expression of the total MRF shear stress is:

$$\tau = \frac{F_{\mathrm{x}}}{S_{\mathrm{plate}}} \tag{2.15}$$

where F_{x} is the total shear force and S_{plate} the sheared surface immersed in the MRF S_{plate}=L× l=12×10^{2}mm^2.

The measured shear force F_{x} includes the shear force F_{m} resulting from the MRF shearing in the magnetized region and $F_{\mathrm{bias\,2}}$ originating from the fluid shearing in the unmagnetized region.

$$F_{\mathrm{bias\,2}} = 2 \times \eta\,(S_{\mathrm{plate}} - S_{\mathrm{m}})\frac{V}{g_{\mathrm{f}}} \tag{2.16}$$

where η is the fluid dynamic viscosity, g_{f} is the fluid sheared gap and $\mathrm{S_m}$ is the magnetic circuit cross section area $\mathrm{S_m}$=5× 10^{2}mm^2 (figure 2.35). The force is amplified by 2 since the MRF is sheared on both sides of the shearing plate.

Table 2.9 summarizes the values of the $F_{\mathrm{bias\,2}}$ for the three fluid concentration ϕ=22%, 32% and 40%.

ϕ	$F_{\mathrm{bias\,2}}$ (N)
22%	$1.16\,10^{-4}$
32%	$3\,10^{-4}$
40%	$9.8\,10^{-4}$

Table 2.9 – Shear force $F_{bias\,2}$ at shearing velocity V=1000m/s^{-1}.

The maximum value of $F_{\mathrm{bias\,2}}$ is $F_{\mathrm{bias\,2}}$=9.8^{-4} which corresponds to a shear stress on S_{m} $\tau_{\mathrm{bias\,2}}$= $9.8\,10^{-4}$kPa. For measured shear stress τ_{mes} less than the estimated value of shear stress τ_{est},

τ_{est}> 10×($\tau_{\mathrm{bias\,2}}$+ $\tau_{\mathrm{bias\,1}}$+ τ_{noise})= 10×0.0110 =0.1kPa, will be neglected.

6.3 Magnetic field

Since the magnetic circuit is closed, and its cross section S_{m} is constant, we suppose that the magnetic flux is concentrated in the magnetic pole and its value is equal in both fluid and air gap ϕ_{f}=ϕ_{a}. This hypothesis is examined in what follows.

Figure 2.36 shows the finite element solution for the magnetic flow in the circuit. Femm 4.2 is the finite element package used for solving this magnetic problem. This figure depicts clearly the concentration of magnetic field in the fluid gap and hence confirms that the magnetic surface is equal to the magnetic pole surface.

The total reluctance of the circuit is $\mathcal{R}_{\mathrm{total}}$=4.8 × 10^{6}H^{-1}. For an applied current value of I=1A the corresponding calculated value of the magnetic field is B=0.25T. The plate used in these conditions has a thickness of e=0.1mm. The fluid used is the MRF 122EG, its magnetic permeability of μ_{r}=2.8.

The femm 4.2 simulation gives for the previous experimental conditions a magnetic field in the fluid cavity equal to B_{fluid}=0.27T which is 8% higher than the calculated one $\frac{B_{\mathrm{fluid}}}{B} = \frac{0.27}{0.25} = 1.08$. This may be due to the fact that the magnetic circuit mean length was overestimated; the mean length of the different types of materials, constituting the magnetic circuit, was considered to be centered in their corresponding sections whereas the femm 4.2 simulation (figure 2.36) shows that the magnetic field lines are more concentrated toward the inner of the magnetic circuit section.

In the air gap $B_{\text{air gap}}$=0.244T which is 2.4% less than the calculted one $\frac{B_{\text{air gap}}}{B} = \frac{0.244}{0.25} = 0.98$. The ratio of B_{fluid} to $B_{\text{air gap}}$ is $\frac{B_{\text{fluid}}}{B_{\text{air gap}}} = 1.1$; therefore our hypothesis of equal magnetic flux in fluid and air gap is justified.

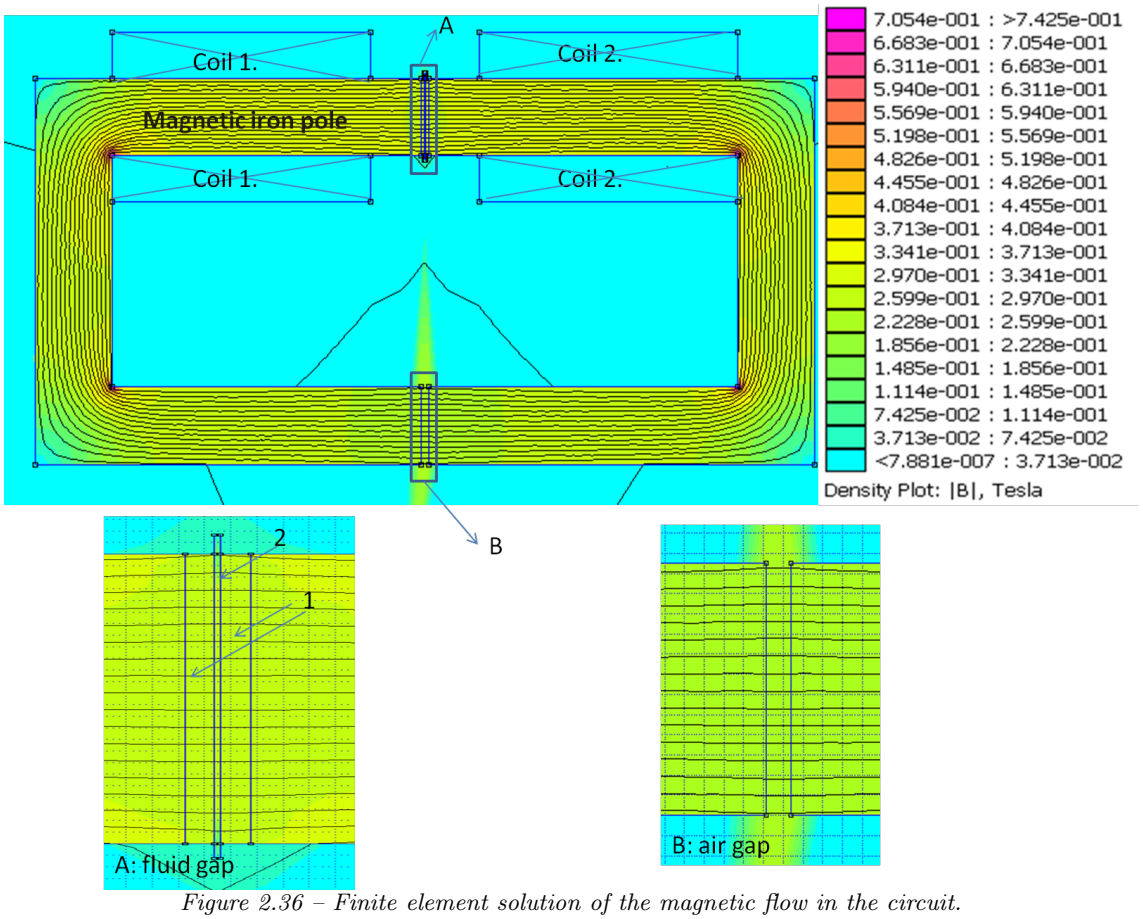

Figure 2.36 – Finite element solution of the magnetic flow in the circuit.

6.4 Degaussing process

For an applied electric current of I=0A, the field intensity H=0, however ferromagnetic materials have the property to remain magnetized even if the external field is removed B=B_{r}≠0. B_{r} is called remnant magnetic field. To ensure B=0T in the MRF a degaussing process must be applied.

Figure 2.37 shows a typical magnetic field hysteresis loops in a ferromagnetic material.

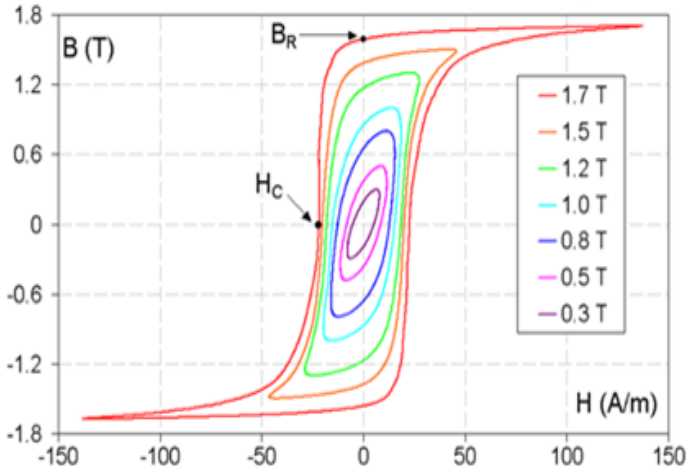

Figure 2.37 – Example of a family of B-H loops in a sinusoidally varying field in a ferromagnetic material.

While degaussing two methods can be used:

1. heating the magnetic material above its Curie temperature, obviously out of question here.

2. applying a sinusoidal field with a slowly decreasing amplitude, starting with coercif magnetic field H_c and ending with the value zero $H = 0$.

The maximum value of the magnetic field reached in our tests is $B_{\max} = 0.4T$. Three plate thickness e and particle volume fraction ϕ are tested. Table 2.10 shows that the maximum calculated value of current reached in our tests is $I_{\max}$=1.64A.

Fluid	μ_r	Plate thickness -e- (mm)	Electric current -I- (A)
MRF 122	2.75	0.08	1.62
		0.1	1.63
		0.13	1.64
MRF 132	5	0.08	1.54
		0.1	1.55
		0.13	1.56
MRF 140	5.9	0.08	1.53
		0.1	1.54
		0.13	1.55

Table 2.10 – Maximum electric current values when varying plate thickness and particle volume fraction of the MRF.

The block diagram of the degaussing process is presented in figure 2.38. A decreasing Matlab sinusoidal signal from 1V to 0V is sent to the audio amplifier (DENON PMA-280) and then transmitted to the magnetic circuit.

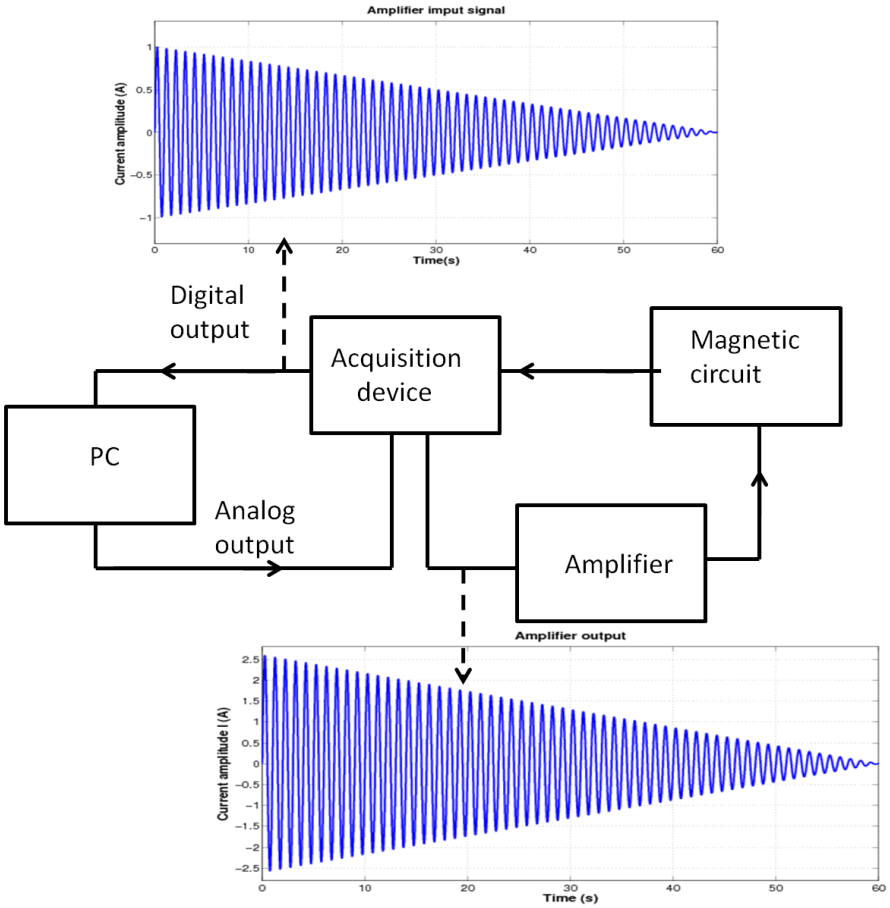

Figure 2.38 – Degaussing block diagramm.

The amplifier is adjusted so that its maximum amplitude current output is I_{m}=2.6A for an input voltage of 1V(see figure 2.38). In practice this process yields B<0.3mT, as measured according to Sec: 4.3.

Table 2.39 presents the calculated magnetic field H for a magnetic field B of B=0.3mT and the corresponding estimated yield stress τ_{y}.

ϕ	H(kA/m)	τ_{y} (kPa)
22%	0.87	0.0165
32%	0.48	0.018
40%	0.4	0.02

Figure 2.39 – Yield shear stress at magnetic field B=0.3mT.

These estimated values of the yield stresses are less than 10% of the minimum measured yield stress obtained while experimenting.

7 Conclusion

The experimental device presented in this chapter allows both microscopic and macroscopic studies of the MRF behavior below yield stress τ_{y}, thus qualitative and quantitative analysis can be achieved. Efficiency tests done to the several parts of the experimental apparatus reveals a noise level within the acceptable ranges. The limits of the system performance were also presented.

Chapter 3

Microscopic observations

Contents

1	**Micro-structure**	**70**
2	**Particles and aggregates**	**74**
3	**Internal MRF structure dependency with B**	**77**
4	**Internal MRF structure during shearing**	**85**
5	**Conclusion**	**97**

In this chapter I present a description of some microscopic mechanisms at work in the MRF.

I start by a general description of the MRF internal structure, at its particle scale level, obtained by scanning electron microscopy SEM (Sec 1). Then I will be highlighting, by high resolution microscopic observation, the basic effects of the magnetic field B on the MRF internal structure (Sec 2). The variation of the magnetic field B and its repercussions on the MRF internal structure are also discussed (Sec 3). The last section is dedicated to the description of the MRF internal structure during shearing (Sec 4).

To the best of my knowledges there is no published observations of the MRF internal structure when variating magnetic field B or during shearing, whereas few general observations of the magnetic particles with various composite materials (mixture of cast iron with polymers) were presented in the literature [3, 49, 22].

1 Micro-structure

To observe the fluid at the scale of its smallest constituent the particle scale, we proceed to a scanning electron microscopy. The specimen in the SEM can be magnified at very high levels (magnification ratio reached= 20 000X). SEM reveals informations about the external morphology and chemical composition of the materials making up the sample.

1.1 SEM description

The two principal operating modes used in SEM are: the Z and SE contrast. These two modes are presented in figure 3.1.

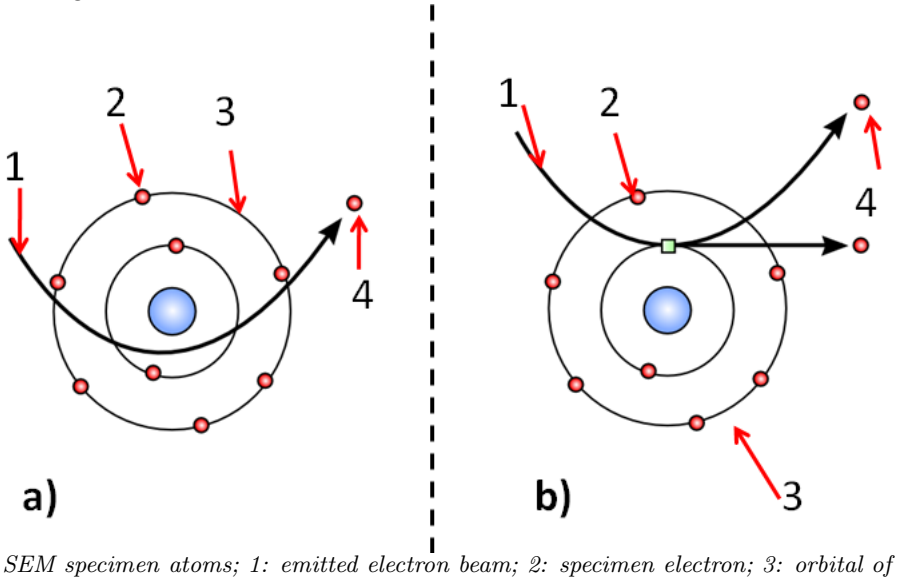

Figure 3.1 – SEM specimen atoms; 1: emitted electron beam; 2: specimen electron; 3: orbital of specimen atom; 4: reflected electrons. a) Z contrast- backscattered electron; b)SE contrast- secondary electron.

- In the Z-contrast, the backscattered electrons consist of high-energy electrons originating in the electron beam. They are reflected or back-scattered out of the specimen interaction volume by elastic scattering interactions with specimen atoms. The electrons in the Z-contrast mode are used to detect contrast between areas with different chemical compositions and therefore present a qualitative analysis of the sample;

- in the SE-contrast, the low energy electrons rejected from the k-orbital of the specimen atoms are collected. These electrons originate within a few nanometers from the sample surface and give information about the topography of the sample.

1.2 Scanning electron microscopy of MRF

1.2.1 Geometric analysis of particles

Figure 3.2 presents a suspension of MRF particles observed in the Z mode. It shows that the MRF is a poly-dispersion suspension of micro sized spherical particles, their diameter varies between 600nm$<a<5\mu$m.

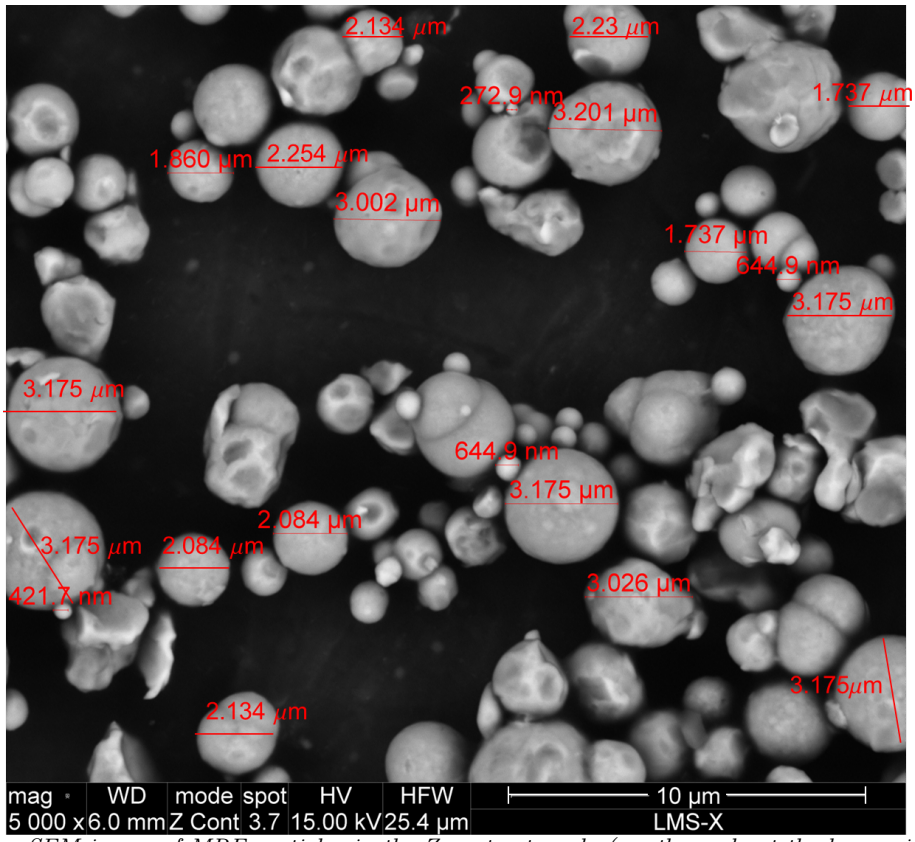

Figure 3.2 – SEM image of MRF particles in the Z contrast mode (see the scale at the lower right corner of the picture).

The nominal diameter of the magnetic particles, in the MRF, is a=2μm and is calculated as following:

$$a = \frac{\sum_1^n a_n}{N} \tag{3.1}$$

where N is the total number of particles studied and a_n the diameter of the nth particle.

The observation exhibits aggregates. The SE mode (figure 3.3) reveals an assemblage of particles with irregular external surfaces (figure 3.4). Since the MRF samples are partially dried rests of carrier oil fluid are depicted in some observations (figure3.3).

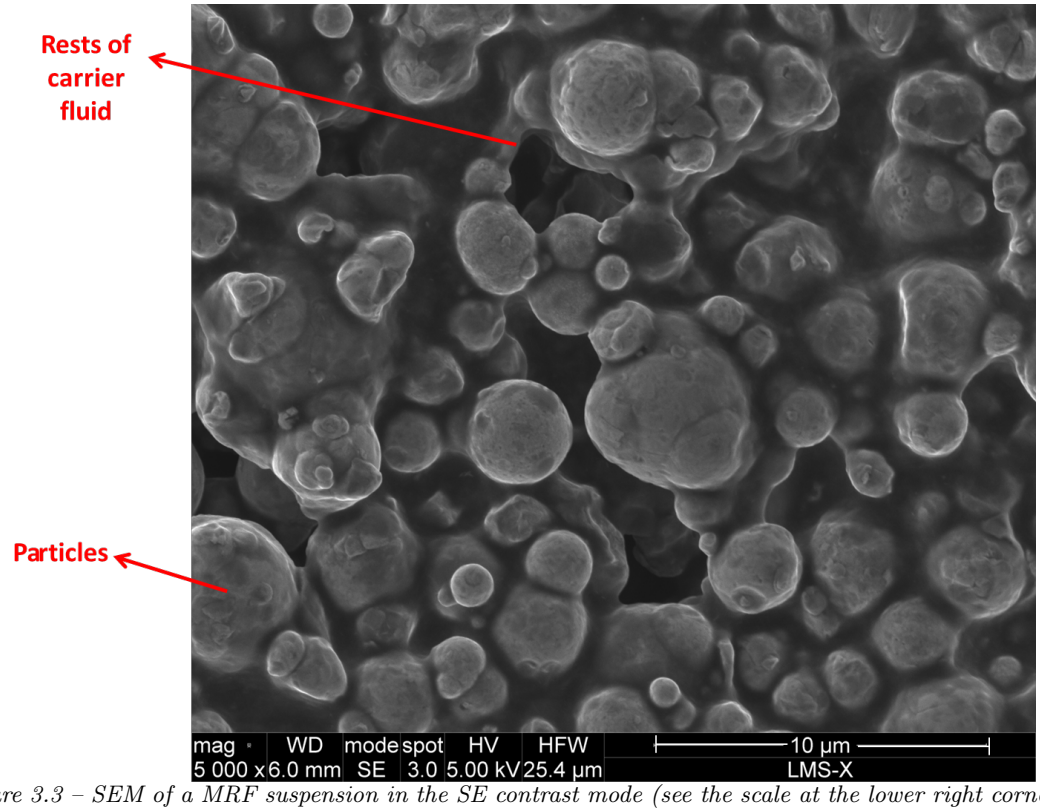

Figure 3.3 – SEM of a MRF suspension in the SE contrast mode (see the scale at the lower right corner of the picture).

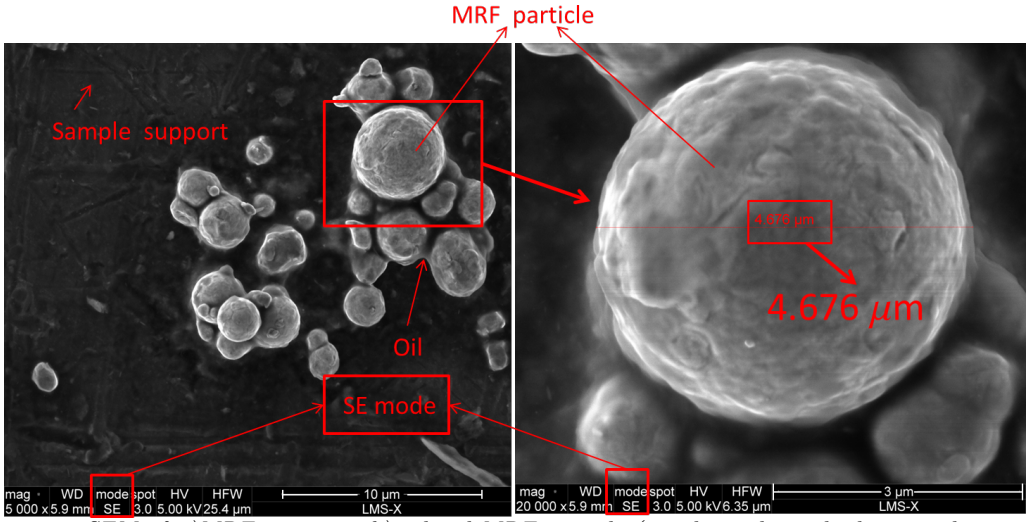

Figure 3.4 – SEM of a)MRF aggregate b)isolated MRF particle (see the scale at the lower right corner of the picture).

1.2.2 Chemical analysis of particles

For the same conditions of observation one can notice that all diameters in the figure 3.5b), where the Z mode is used in the scanning electron microscopy, are slightly less than the one observed in figure 3.5a) where the SE mode is the mode chosen for the microscopic observation.

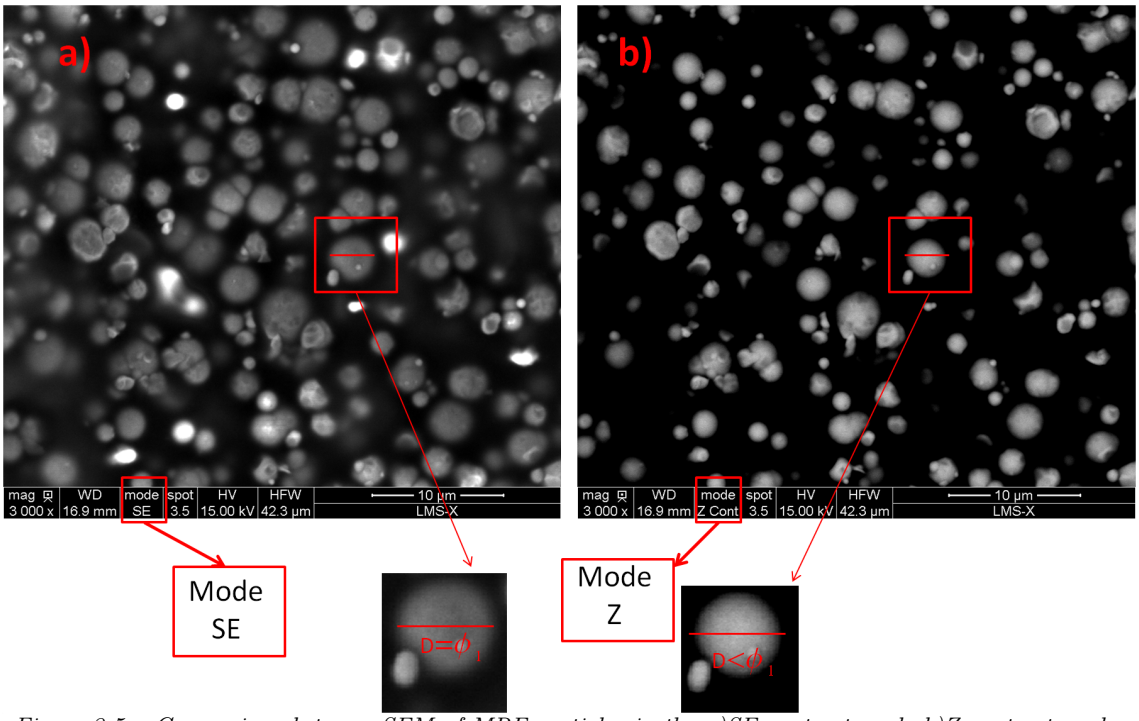

Figure 3.5 – Comparison between SEM of MRF particles in the a)SE contrast mode b)Z contrast mode.

The electrons in the Z mode are high energy electrons and therefore can reach deeper layer, electrons in the SE mode are low energy and are rejected from surface layers (figure 3.1). Consequently, we can conclude that this difference in diameter is due to a difference in the materials type constituting the internal and external layers of the MRF particles. We suppose that the MRF particles are coated by a layer of light elements undetectable in the Z mode, while the nucleus of the MRF particles, having a more heavy chemical composition, is detectable.

Fang studied the effect of the addition of the green additive guar gum on the properties of magnetorheological fluid [14]. He concluded that these type of polymers help the carbonyl iron particles to form a three-dimensional network structure and therefore prevent particle sedimentation and hardening. His scanning electron microscopy of the cast iron particles coated with guar gam is very similar to the zoomed view of our MRF-132DG magnetic particle (figure 3.6).

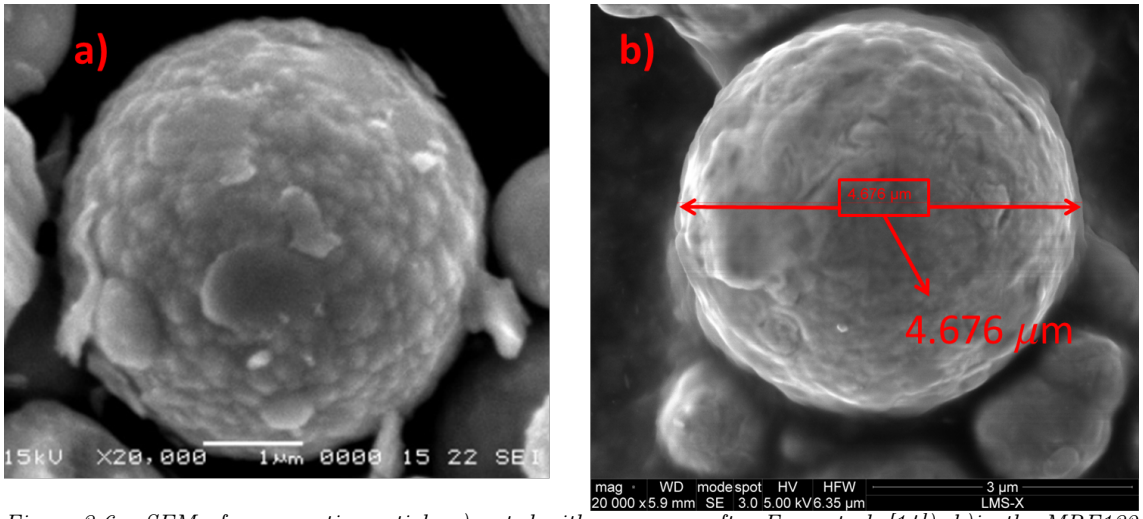

Figure 3.6 – SEM of a magnetic particle a)coated with guar gum after Fang et al.,[14]); b)in the MRF132

The chemical composition of guar gum (an association of hydrogen and oxygen atoms)

explains the absence of indication of these coatings in the Z mode and clarifies the presence of particles aggregates.

From these observations, we can conclude that the observed MRF from Lord Corporation is a poly-dispersion of micro sized particles coated with a thin nanometric film of polymer. The MRF internal structure resembles more to aggregates rather than to dispersed individual particles.

2 Particles and aggregates

With the high resolution digital microscope VHX-1000 (Keyence), basic magnetic effects in the MRF were observed at the particle scale. Figure 3.7 shows a 3D view of the MRF suspension subjected to magnetic field. The cohesion between the MRF aggregates is more complex than the one predicted by the microscopic approaches (Sec: 4.1.1 in Chap. 1), it is a three-dimensional cohesion.

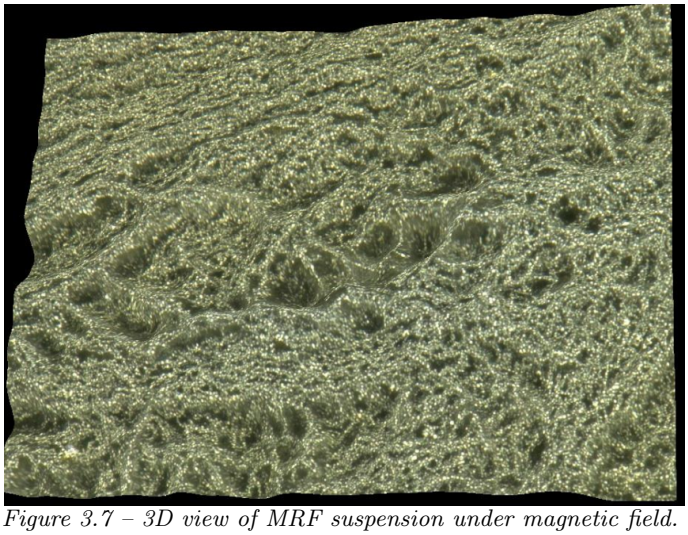

Figure 3.7 – 3D view of MRF suspension under magnetic field.

The application of the magnetic field in the following studies was done through an external permanent magnet (figure 3.8). The top magnetic bar surface is circular, its external diameter is d=0.7cm and can therefore cover the whole surface of interest presented in figures 3.10 and 3.11.

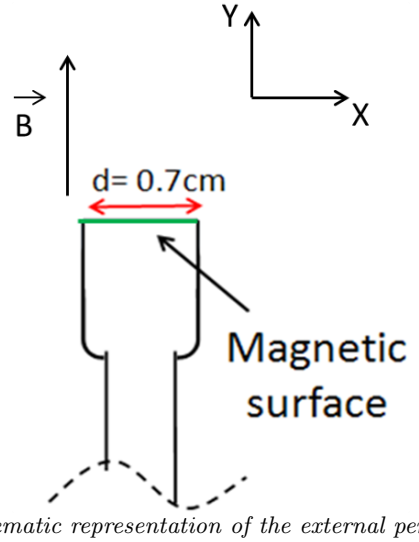

Figure 3.8 – Schematic representation of the external permanent magnet.

In the observations presented in figure 3.9 and 3.10, the MRF sample is inserted between two thin glass plates. The assembly is held at its two extremities by crocodile clips. Figure 3.9 presents the observation of the fluid flowing between the plates until equilibrium is reached.

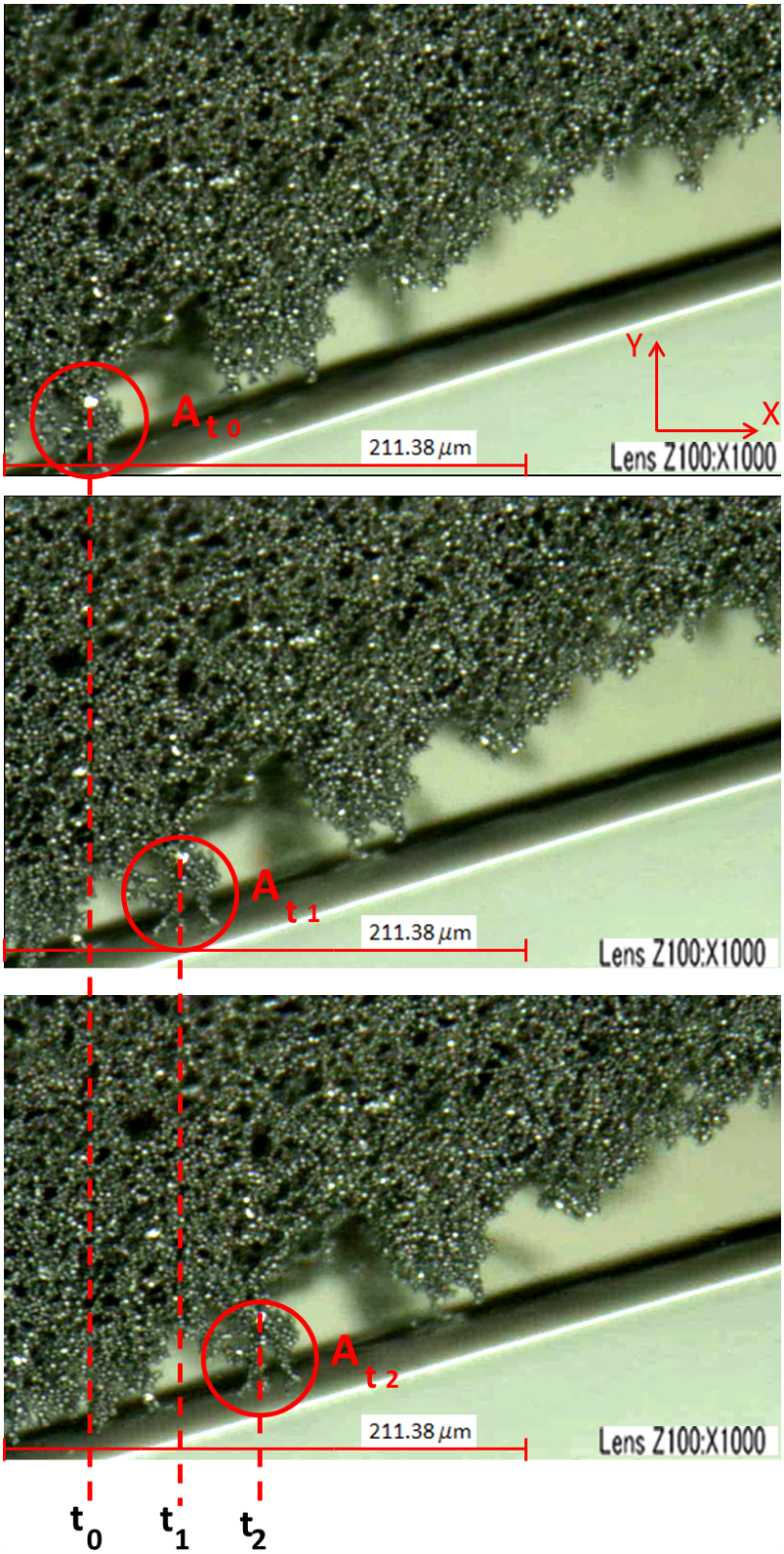

Figure 3.9 – MRF between two thick glass plates at three successive instants. Up: $t{=}t_0$. Center: $t = t_1$. Bottom: $t{=}t_2$.

Once a magnetic field B is applied by the external permanent magnet, the liquid hardens into a near-solid and its motion is therefore restricted. The tracking of zone A in figure 3.9 shows the MRF flow (magnetic particle and oil medium), while tracking of point B in figure 3.10, where

the MRF is subjected to magnetic field, depicts oil flow only; the zone A composed of aggregates of magnetic particles remains stationary[19][12] while the isolated particle B is carried by the flow.

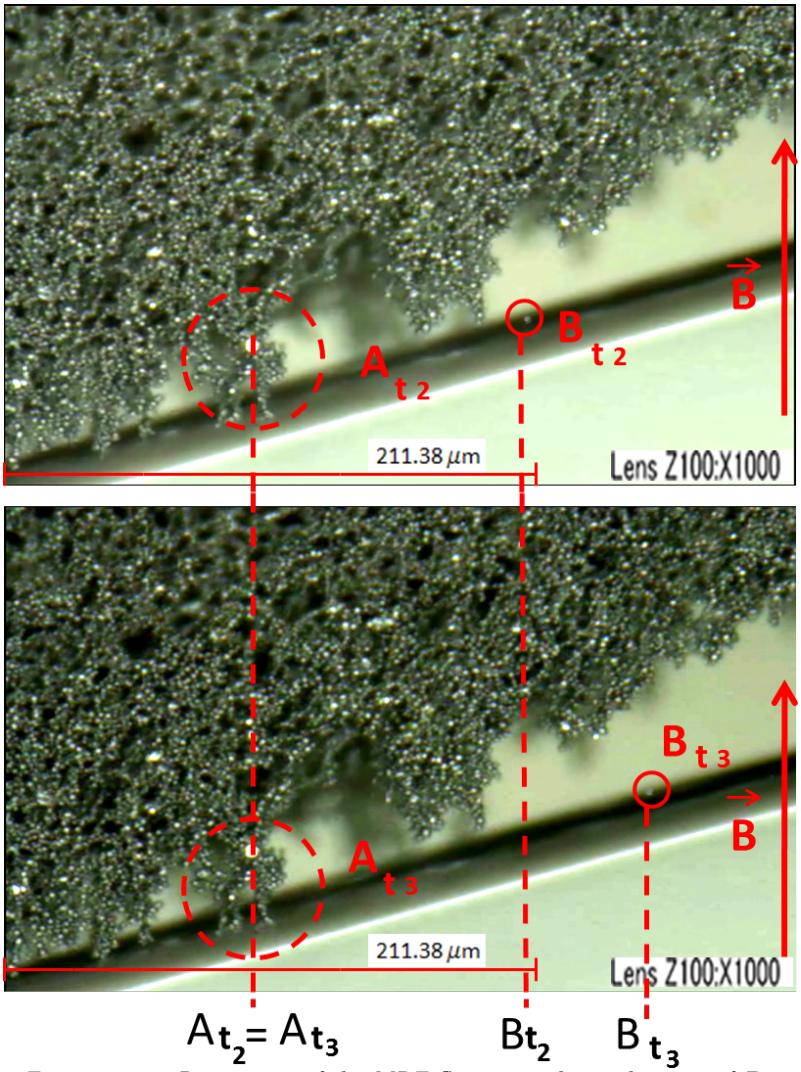

Figure 3.10 – Restriction of the MRF flow upon the application of B.

One should notice that applying the magnetic field B to the MRF suspension did not have any notable effect on the global structure configuration of the particles, contrary to what intuition would suggest (figure 3.10).

Figure 3.11 shows how isolated chain orientation varies with the orientation of the magnetic field. In these observations the MRF sample was prepared by centrifugation of a MRF drop on a glass plate.

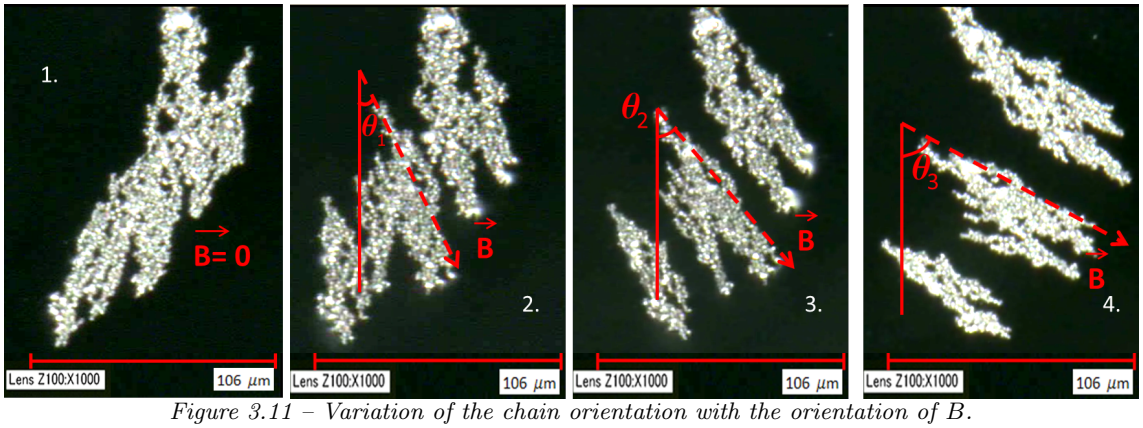

Figure 3.11 – Variation of the chain orientation with the orientation of B.

Isolated chains react to magnetic field and change its structure and orientation with B, as opposed to whole integrated aggregates structure's which does not seem to be conditioned by the magnetic field B.

3 Internal MRF structure dependency with B

3.1 Increasing B on initially isotropic MRF suspension

The internal structure of the fluid during the increase of the magnetic field is presented in the set of images in figure 3.12. The magnetic field B is increased manually from a value $B \approx$0T up to an estimated value equal to B_3=0.35T.

The MRF beards are due to the magnetization of isolated iron particles located on the magnetic pole surface. The tracked grid is limited by the mask M presented in the first image of figure 3.12. The u and v velocity components arising from the BOD decomposition of the increasing-decreasing magnetic field observations are null (figure 3.13). No movement is detected in the MRF isotropic suspension while increasing magnetic field.

The MRF particle cohesion is independent of the magnetic field B.

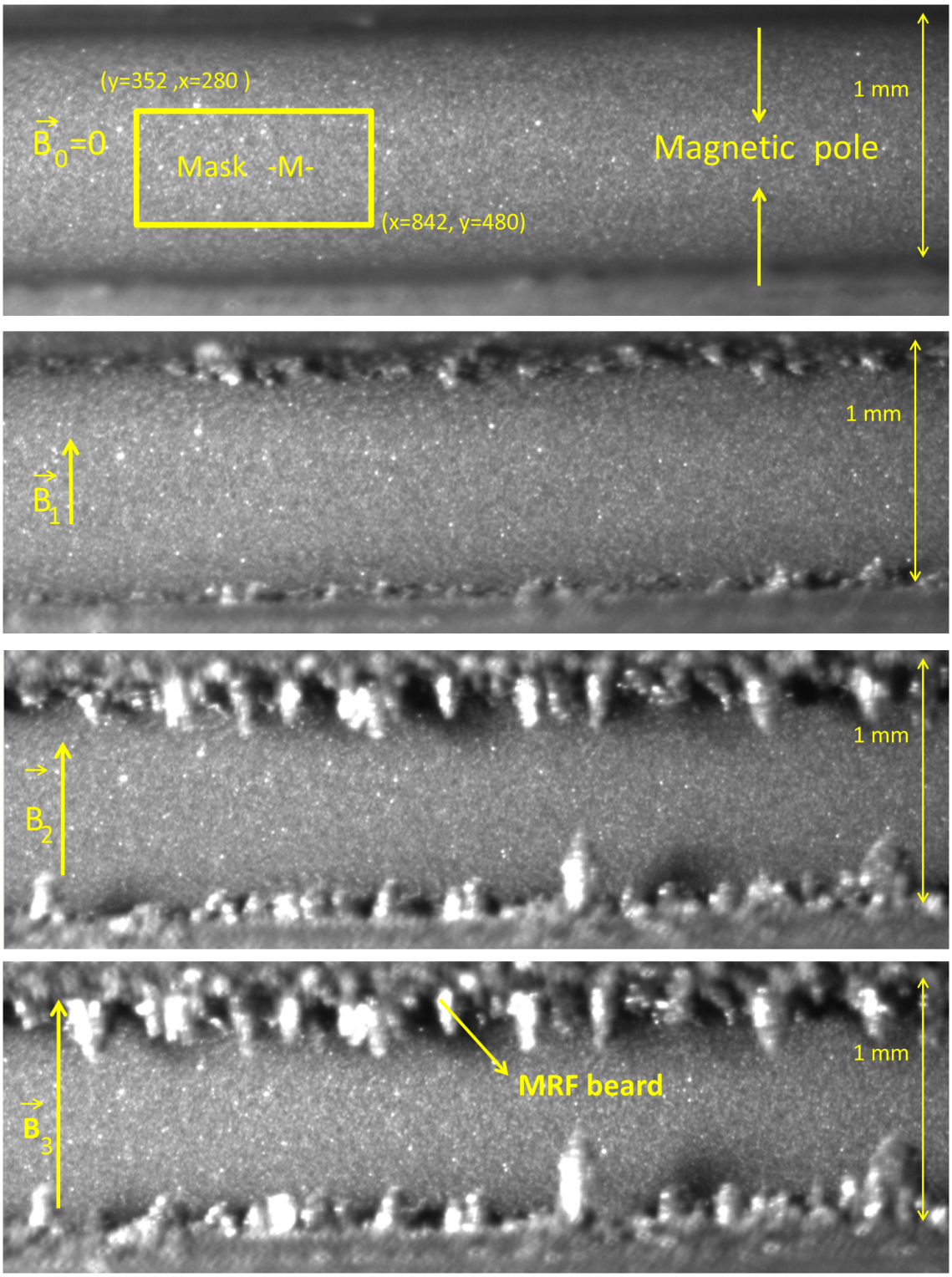

Figure 3.12 – MRF internal structure while increasing magnetic field. Top to bottom corresponds to the succession of $B_0 < B_1 < B_2 < B_3$.

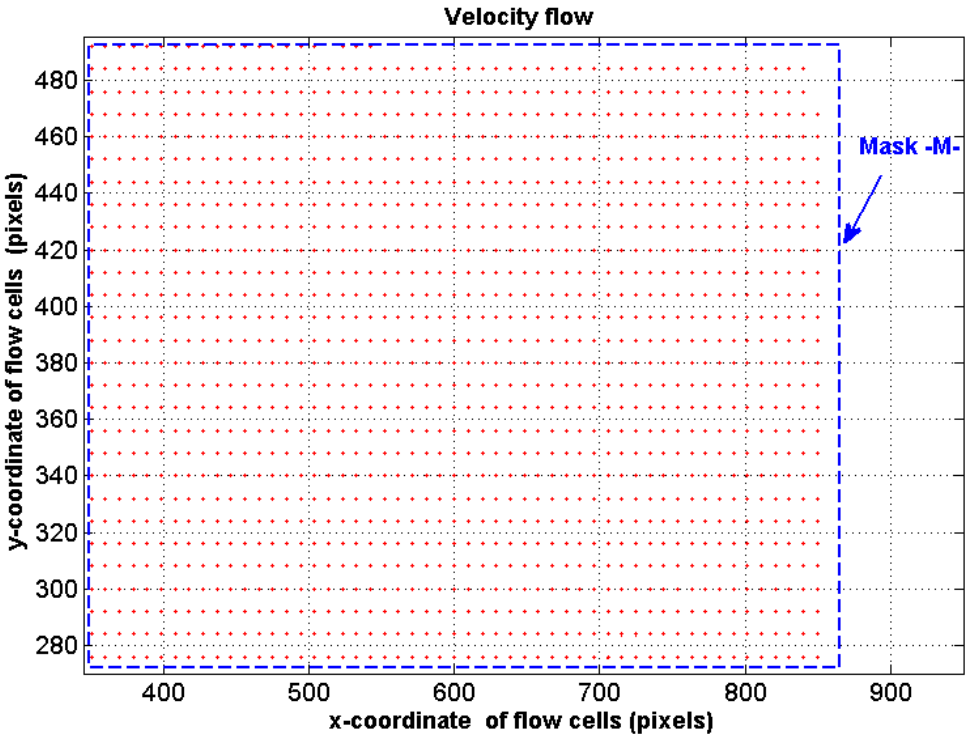

Figure 3.13 – Velocity field of the MRF particles during increasing magnetic field process.

3.2 Increasing B in an initially formed chain outside the fluid

As seen in figure 3.15, the increase of the magnetic field B induces the formation of MRF beards in the magnetic pole surface. The beards results from magnetic attraction between MRF particles outside the fluid. Figure 3.14 depicts the chain formation process, in the direction of the magnetic field. Unlike the BOD decomposition for the MRF isotropic suspension, we notice that the u and v velocities components for isolated magnetic particles while increasing magnetic field, are not null (figure 3.15).

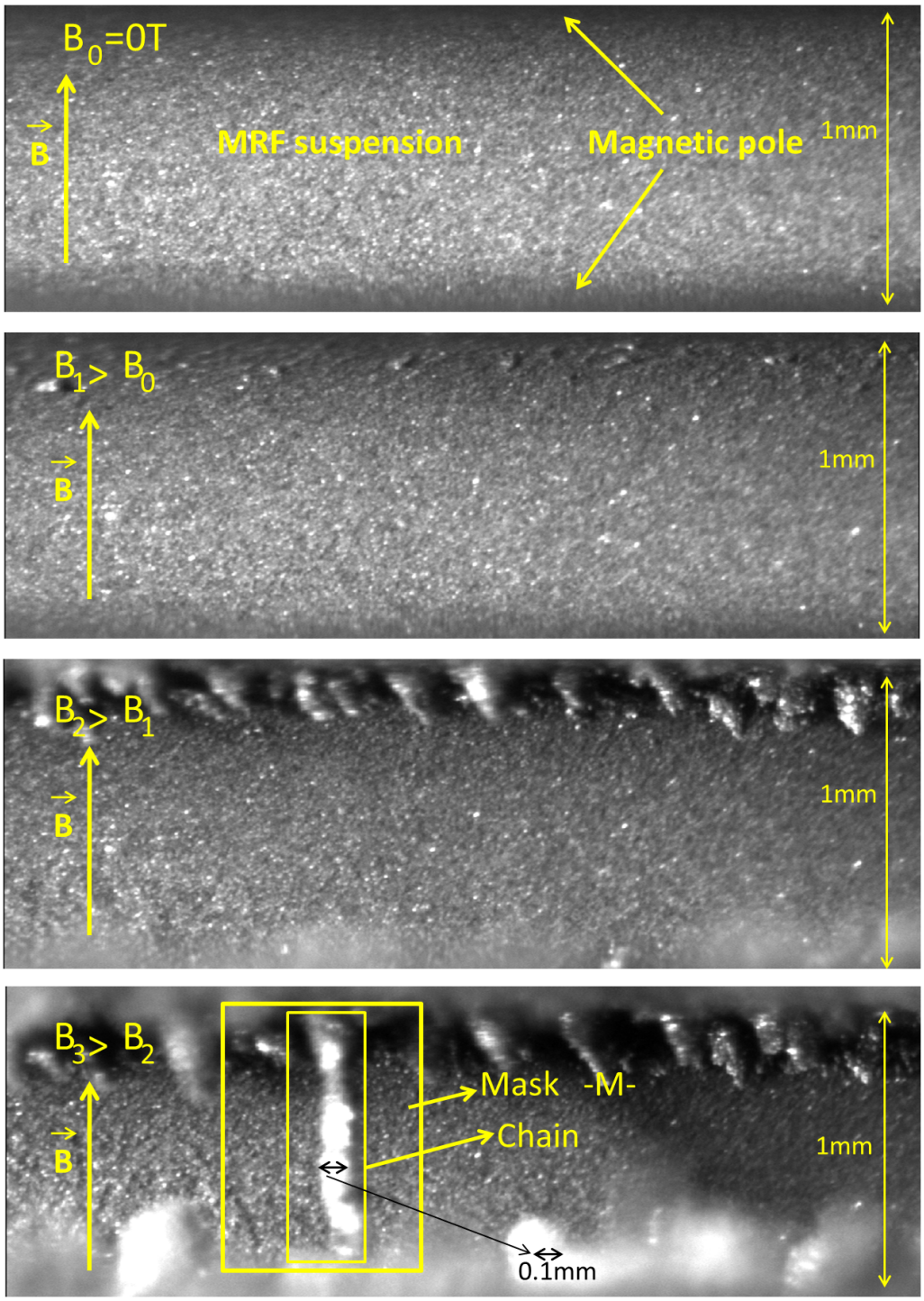

Figure 3.14 – MRF varying internal structure with increasing magnetic field. Top to bottom corresponds to the succession of $B_0 < B_1 < B_2 < B_3$.

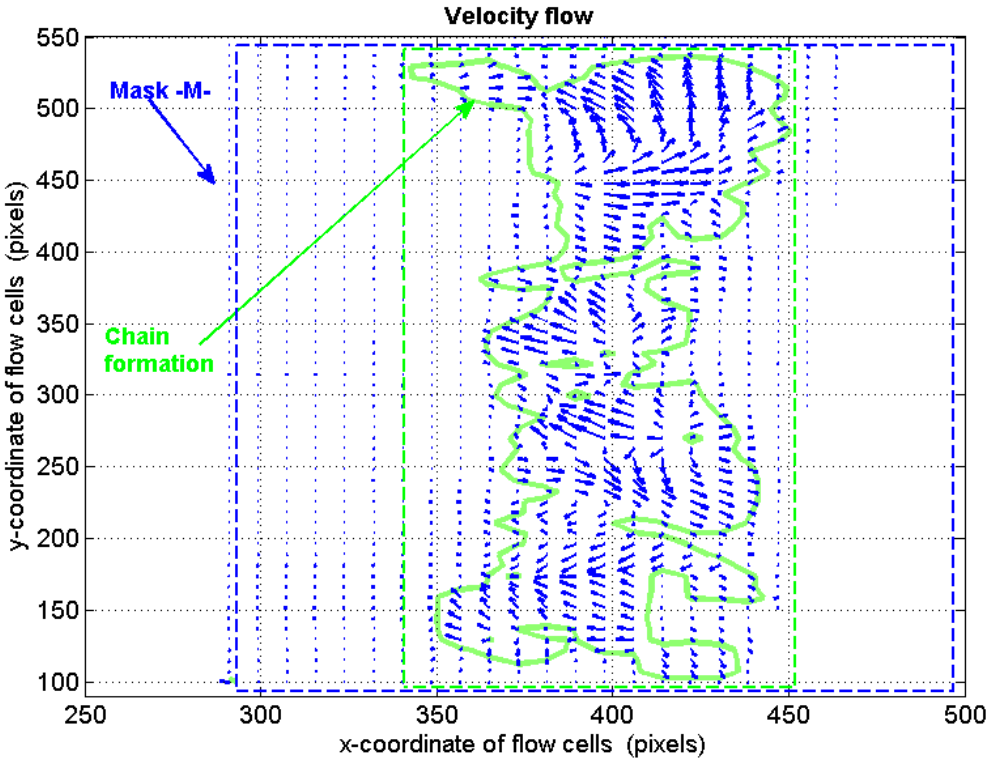

Figure 3.15 – Velocity field of MRF particles during the formation of the chain like structure.

3.3 Influence of B on initially formed chains inside the fluid

Figure 3.16a) presents the internal MRF structure during the degaussing process. The initial MRF structure is a chain-like structure and the value of the magnetic field is equal to $B{=}B_{\mathrm{r}}$(B_{r} is the remnant magnetic field). The second to the last image of figure 3.16 corresponds to the succession of a sinusoidal decreasing magnetic field starting with a magnetic field value $B_{\mathrm{d1}}{>}\ B_{\mathrm{r}}$ (figure 3.16b). The degaussing process lasted 60 seconds.

From these observations one should conclude that the global MRF structure has not been affected by the degaussing process, it is an additional evidence on the independence of the MRF particle cohesion from magnetic field B. An external agitation of the MRF suspension with the amagnetic shearing plate is necessary to destroy the chain-like structure(figure 3.17).

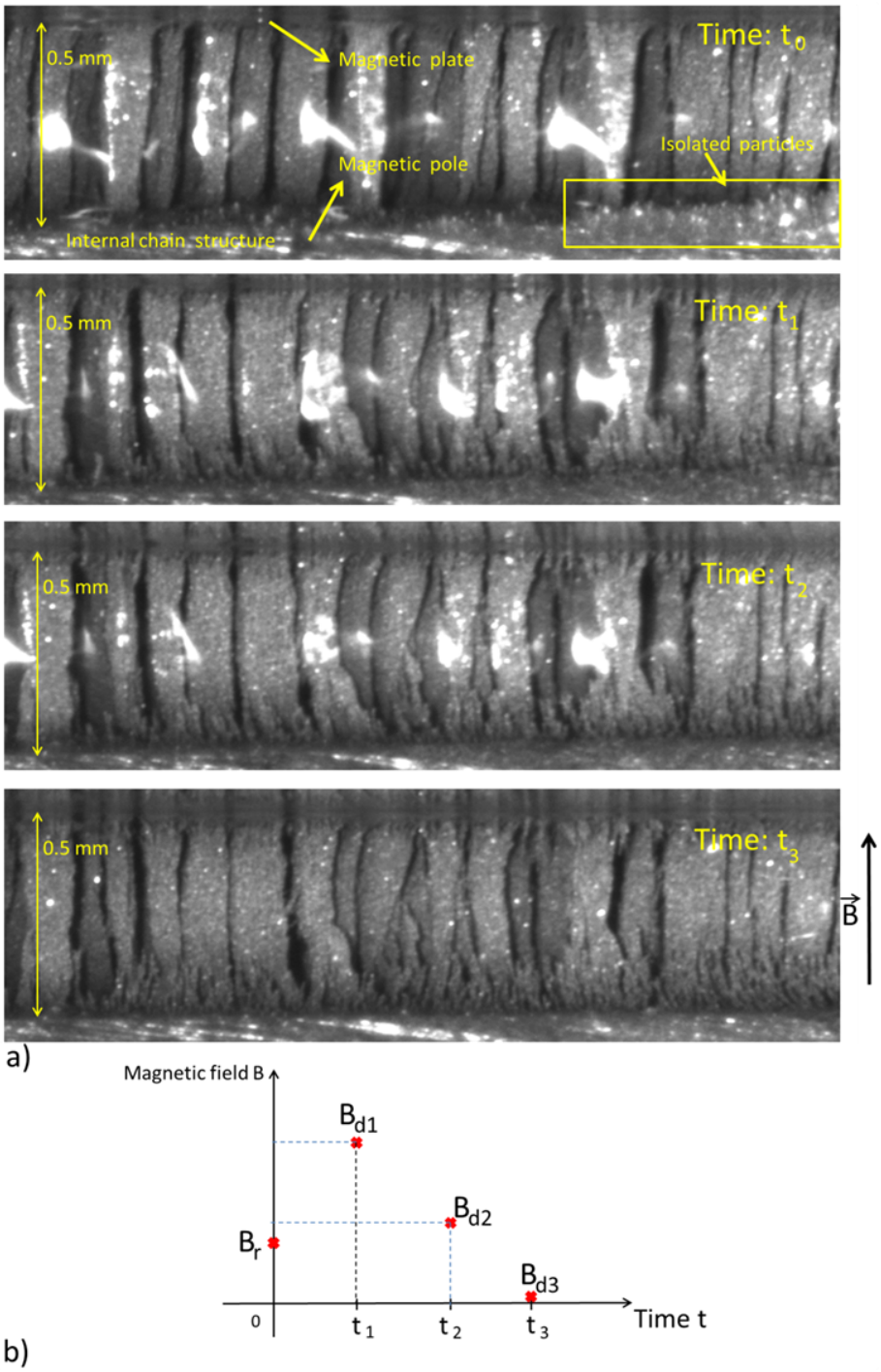

Figure 3.16 – Degaussing of a MRF chain like structure a)internal MRF structure, b) corresponding magnetic field values.

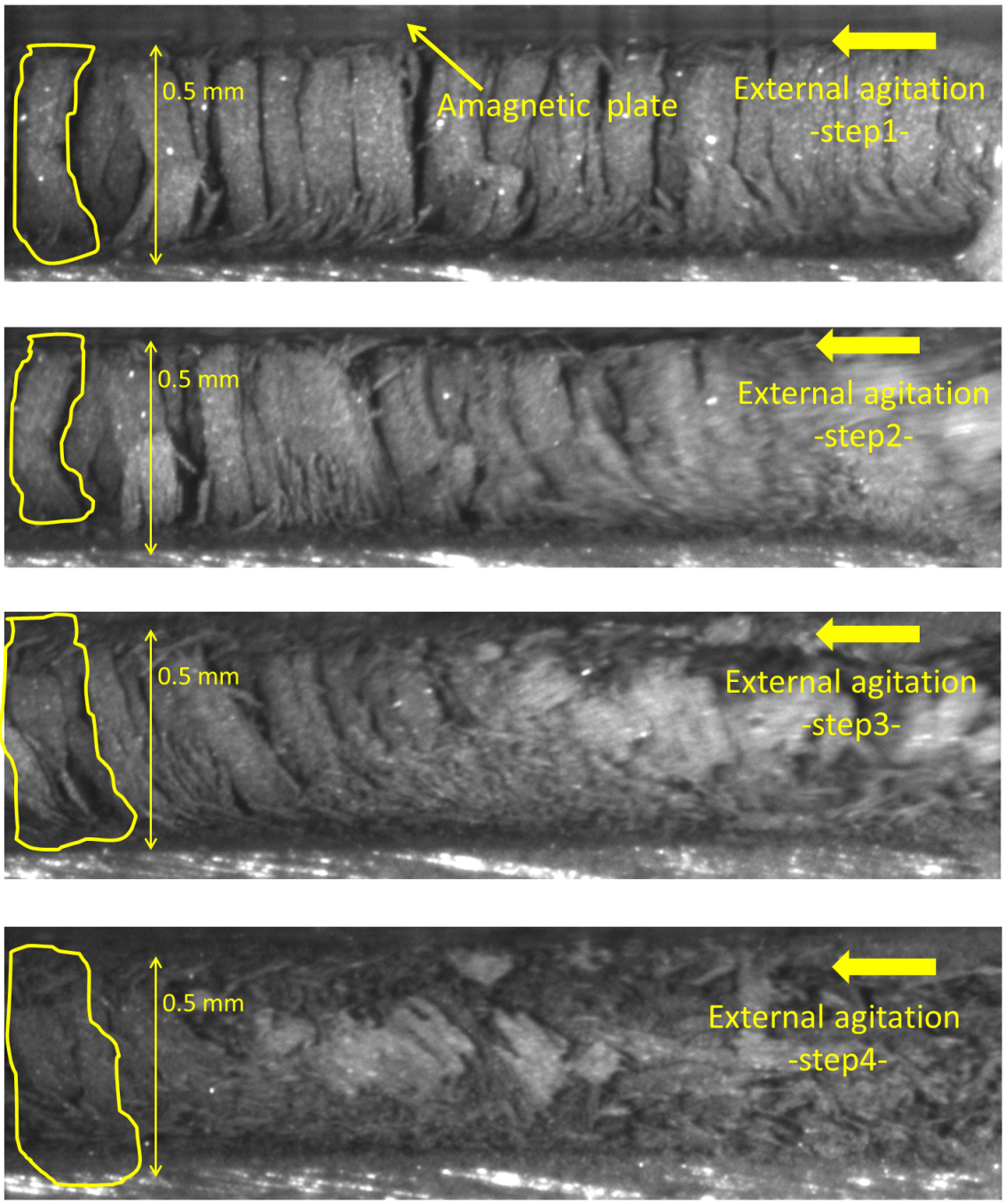

Figure 3.17 – Destruction of MRF internal chain structure.

3.4 Decreasing B on an isotropic suspension and chains outside the fluid.

Figure 3.18a) presents the MRF internal structure while decreasing the magnetic field B. The initial MRF structure is isotropic with MRF beards on the magnetic pole surface. Figure 3.18b) presents a schematic representation of the magnetic field in the different degaussing instants. The whole degaussing process lasted 60 seconds.

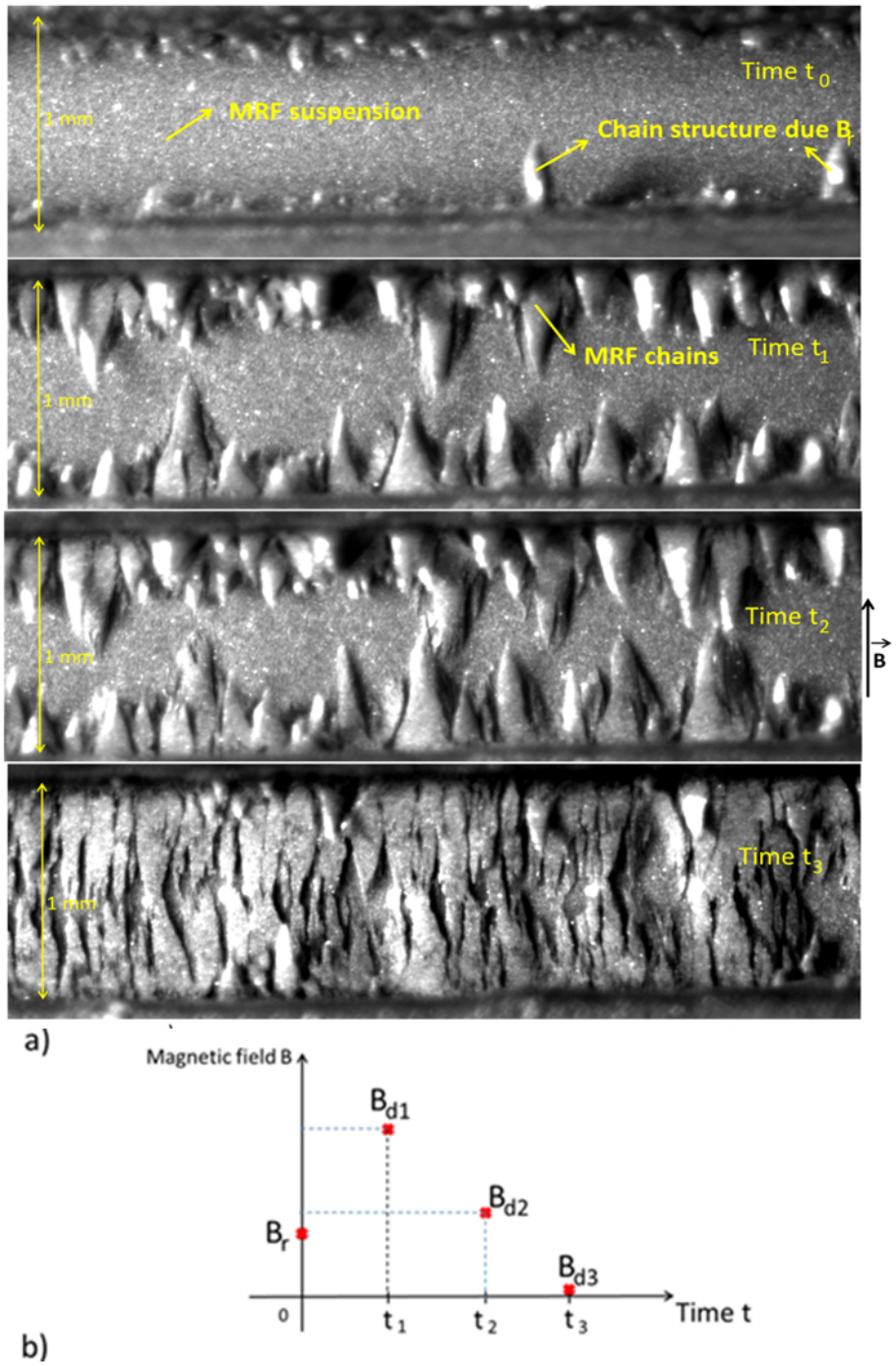

Figure 3.18 – a) Degaussing of a MRF isotropic structure a)internal MRF structure, b) corresponding magnetic field values.

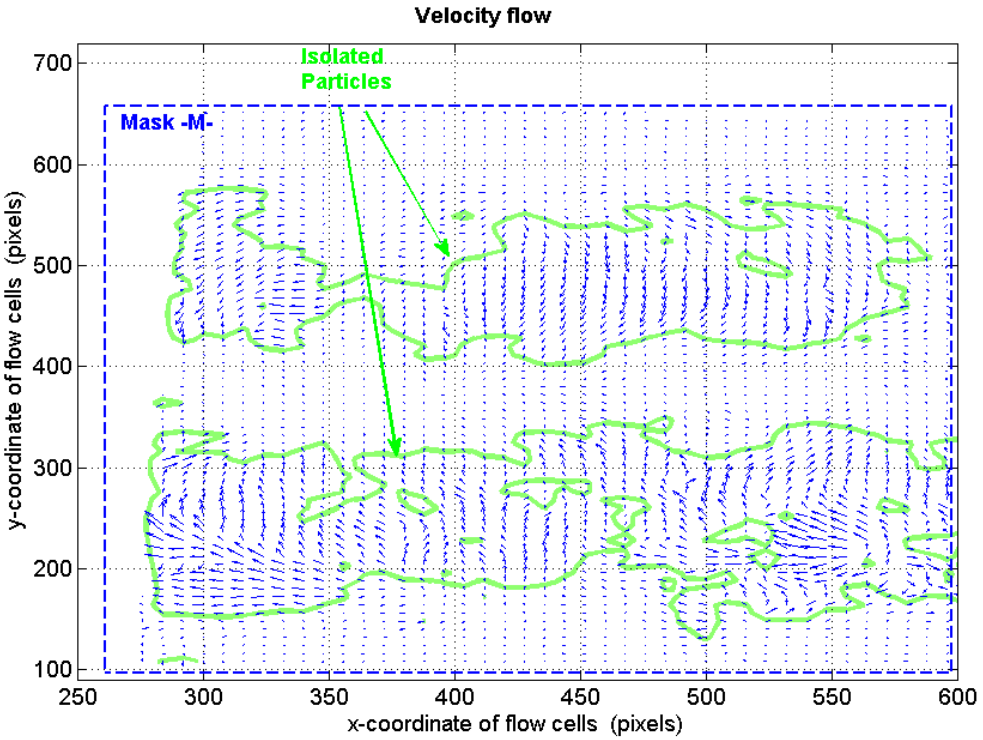

Figure 3.19 – Velocity field of MRF particles during part of the the degaussing process.

Once again, we conclude that in region of condensate magnetic particle, magnetic field has no apparent effect on the MRF global structure, whereas in region where magnetic particles are isolated, the particles align themselves in the direction of the magnetic field (chain region limited by the green borders in figure 3.19).

4 Internal MRF structure during shearing

An example of the MRF response to shearing is presented in figure 3.20 (a complete study is presented in Chap. 4, 5 and 6). The value of the magnetic field B is the same in both measurements presented in figure 3.20 (B=0.15T), whereas the nature of the shearing plate varies from magnetic plate in figure 3.20a) to amagnetic in figure 3.20b). The dynamic microscopic observations, done with the optical microscope SMZ100 and Pike F421 camera, reveal for both shearing plates (magnetic and amagnetic) two principle phases:

- MRF shearing;

- sliding of the shearing plate against the MRF.

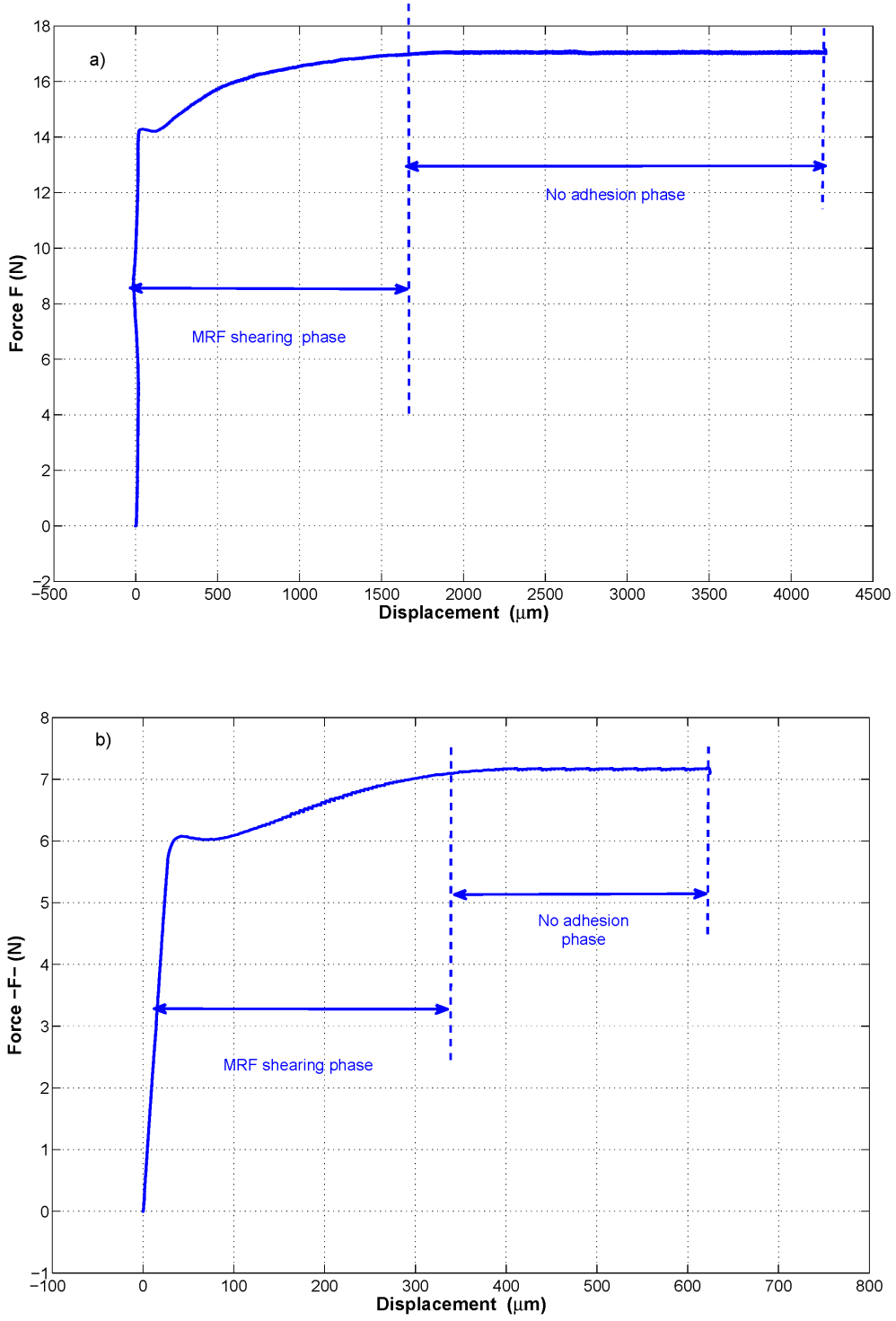

Figure 3.20 – Force variation with shearing plate displacement in case of shearing with a) a magnetic shearing plate; b) an amagnetic shearing plate.

From above measurements one should notice that the *No adhesion* regime, in case of shearing with a magnetic plate, occurs for shearing displacement larger than those depicted in case of shearing with an amagnetic plate.

The correspondence between macroscopic measurements (force as function of displacement) and microscopic observations (internal fluid structure) is detailed in § 4.1 and 4.2.

The effects of the shearing plate nature and the internal MRF structure on the shearing response $F(u)$ are also examined.

4.1 Volume shearing

The internal structure of the magnetized MRF at different instants of the shearing phase is displayed in figures 3.21 and 3.23. The shearing plate in these tests is amagnetic and the shearing velocity is V=10μm/s. The measured magnetic field B is B=0.07T in figure 3.21 and the imposed displacement is u=350μm while and B=0.1T in figure 3.23 and u=800μm.

In figure 3.21 the fluid has an internal chain structure in the direction of the magnetic field B. When subjected to shearing, the MRF chains are titled and then bent.

The BOD decomposition exhibits only the α_1 mode (figure 3.22top) therefore only the corresponding u and v parts of the optical flow for this mode (α_1) are computed (figure 3.22bottom). Figure 3.22bottom) displays the cartesian coordinates of the corresponding velocity field; it is clear that the shear rate (having u and v as components) is scattered in the whole shearing gap.

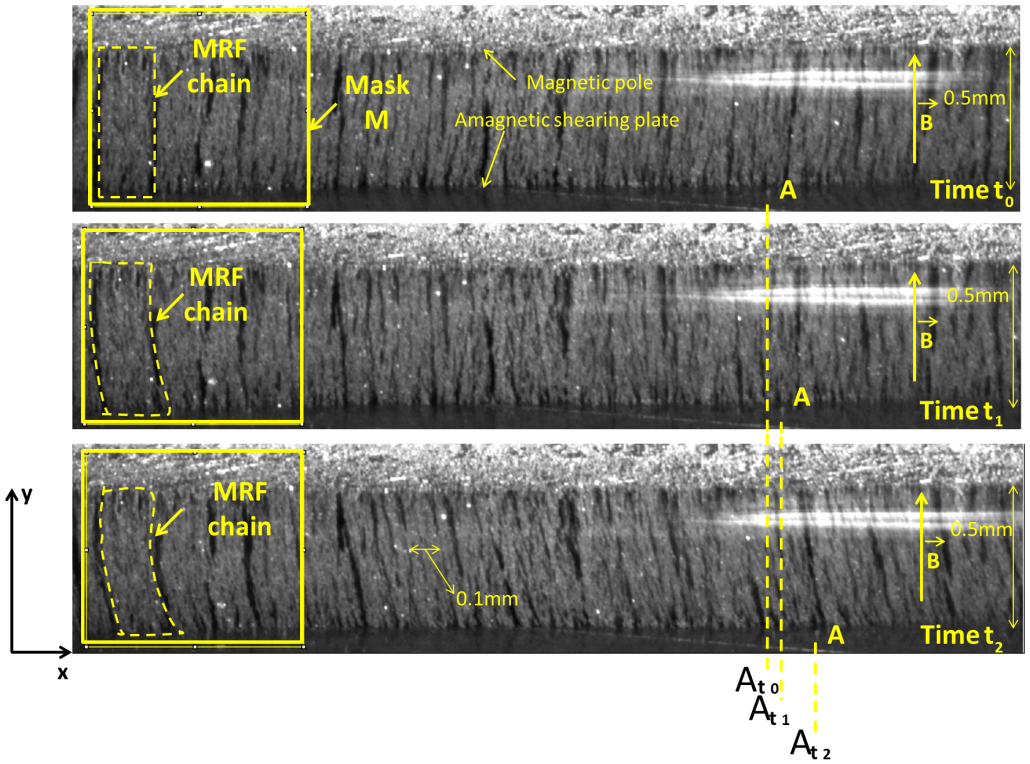

Figure 3.21 – Microscopic observations of the MRF structure when sheared with an amagnetic plate, in the first shearing phase. (Top to bottom corresponds to the succession of the shearing moments with a time interval equal to Δt=24s).

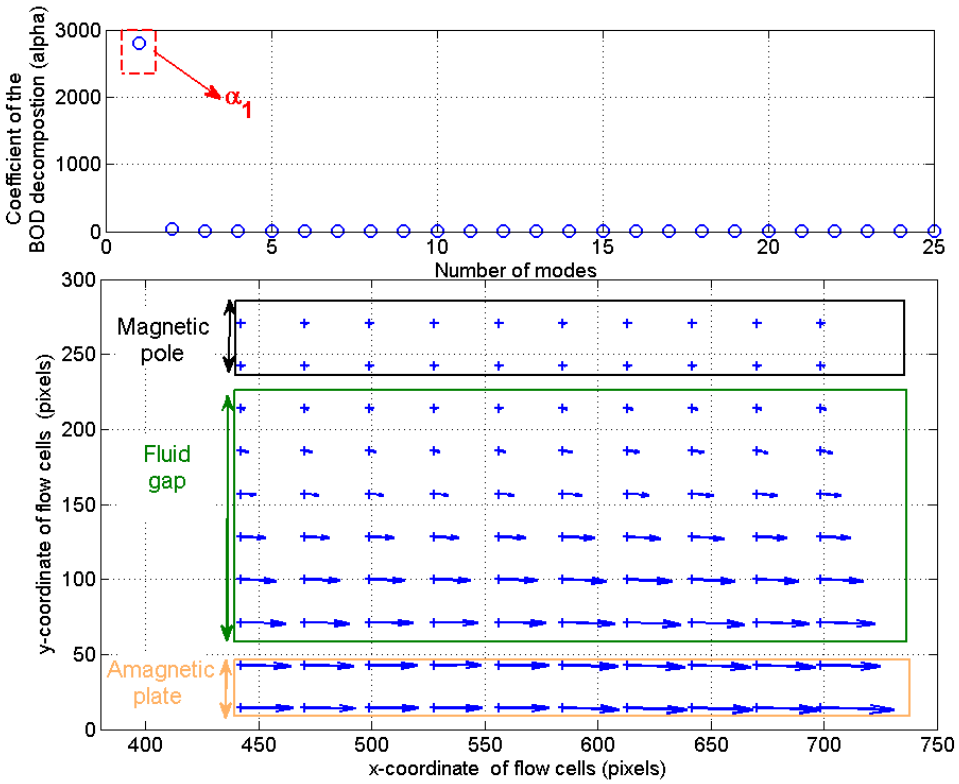

Figure 3.22 – BOD of the MRF shearing phase with an amagnetic plate. Top figure: eigen values α; bottom figure: cartesian coordinates of the velocity in the α_1 mode.

Figure 3.23 shows a different internal structure of the magnetized MRF in the shearing phase. In this study the internal MRF structure has an initial bent chain-like structure also the average thickness of the chains differs from figure 3.21. Although the internal MRF structure is different in the two figures (figure 3.21 and 3.23), the BOD decomposition of the fluid flow reveals the same nature of phenomenon in both cases (figures 3.22 and 3.24): shearing of the MRF gap.

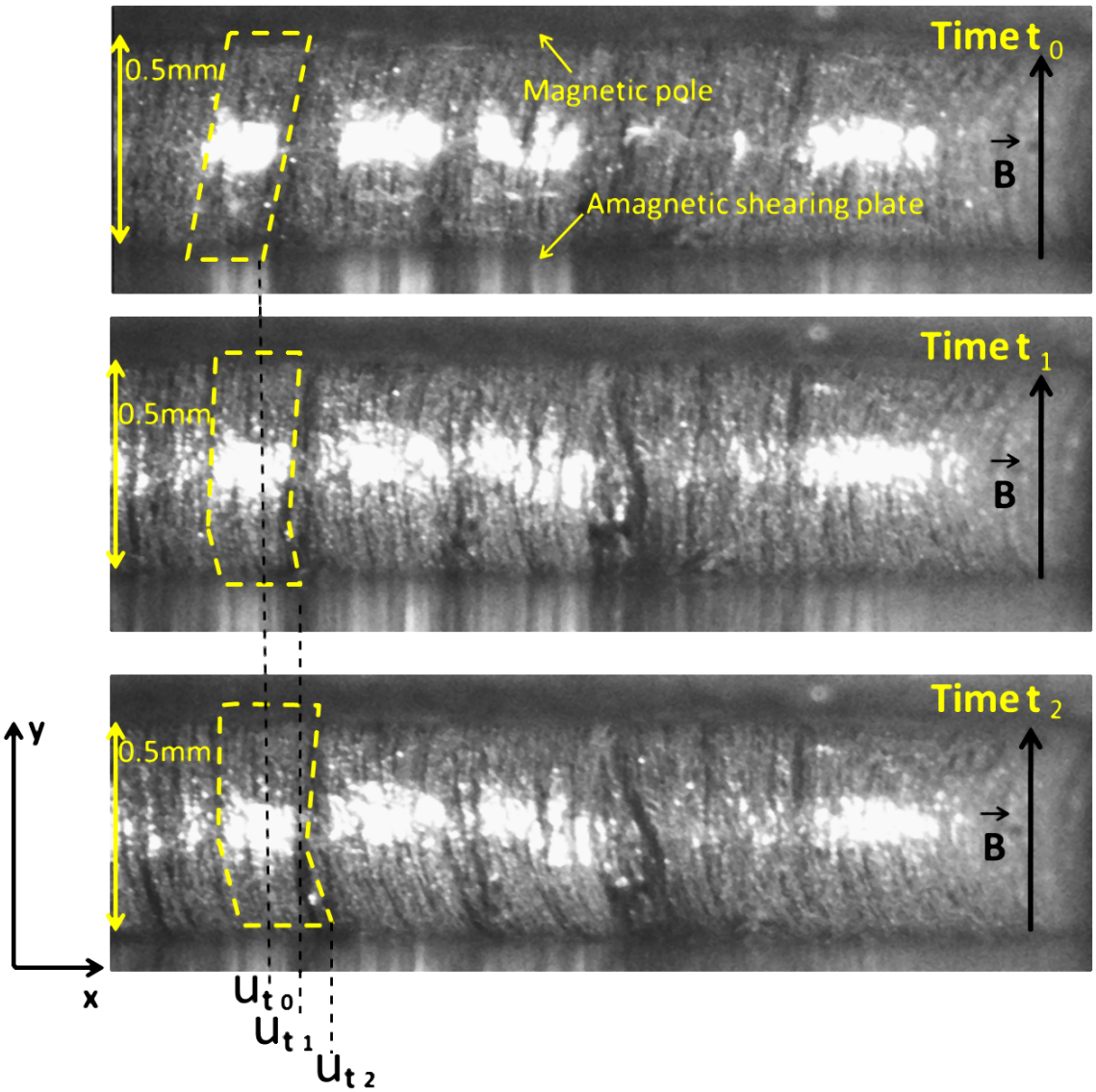

Figure 3.23 – Microscopic observations of the MRF structure when sheared with an amagnetic plate, in the first shearing phase. (Top to bottom corresponds to the succession of the shearing moments with a time interval equal to Δt=25s).

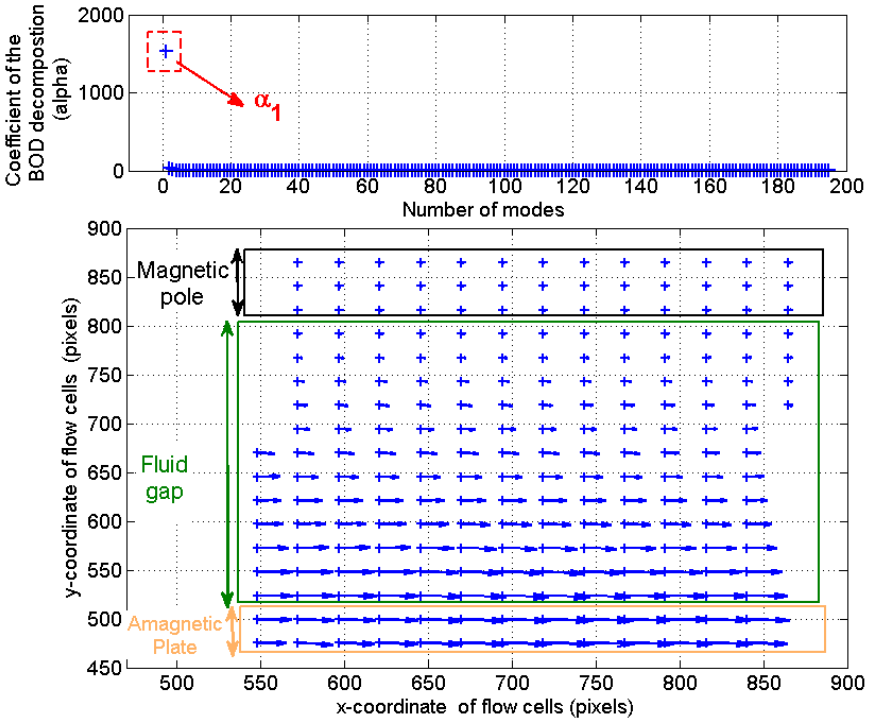

Figure 3.24 – BOD of the MRF shearing phase with an amagnetic plate. Top figure: eigen values α; bottom figure: cartesian coordinates of the velocity in the α_1 mode.

Figure 3.26 displays the MRF internal structure in the shearing phase when a magnetic plate is used for shearing. Although figure 3.26 shows a different MRF structure from above observations (figure 3.21 and 3.23) the BOD decomposition reveals the same nature of the MRF response to shearing (figure 3.26).

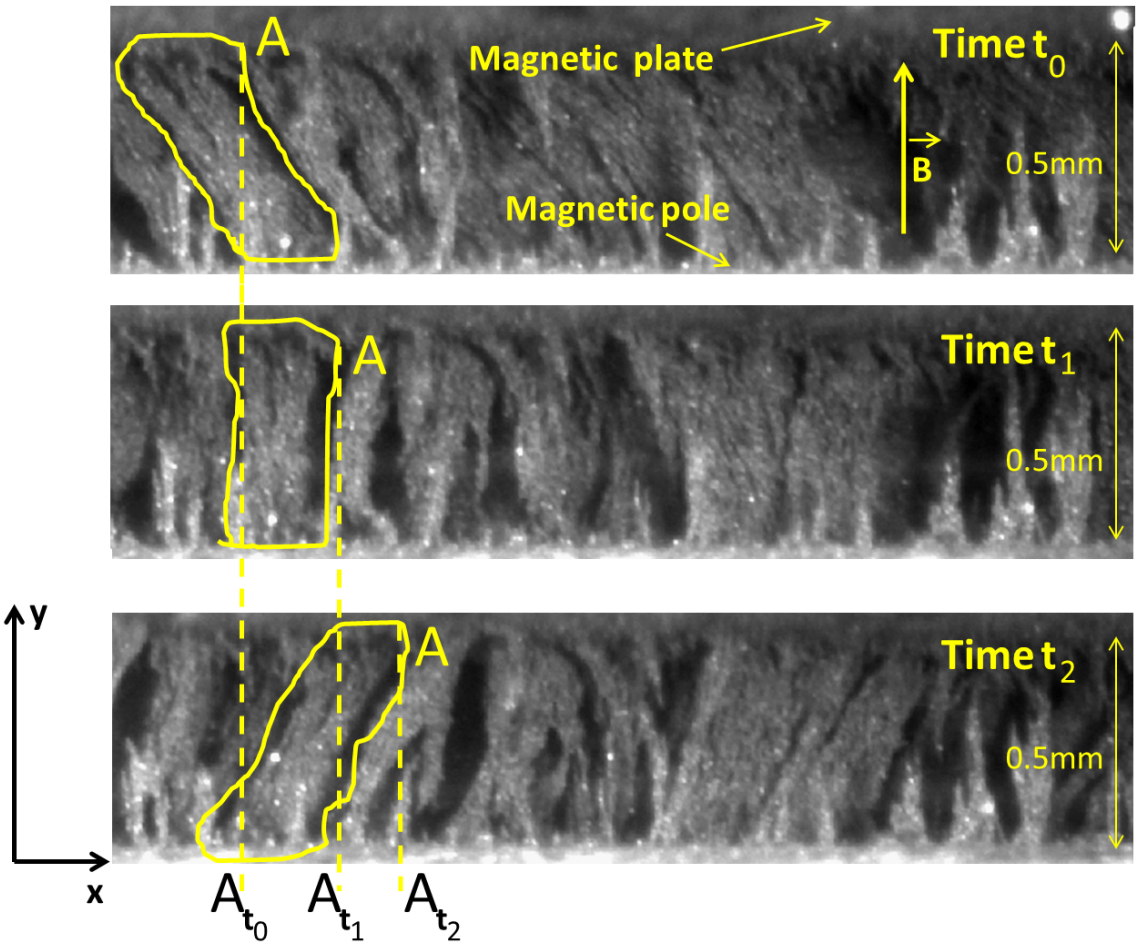

Figure 3.25 – Microscopic observations of the MRF structure when sheared with a magnetic plate, in the first shearing phase. (Top to bottom corresponds to the succession of the shearing moments).

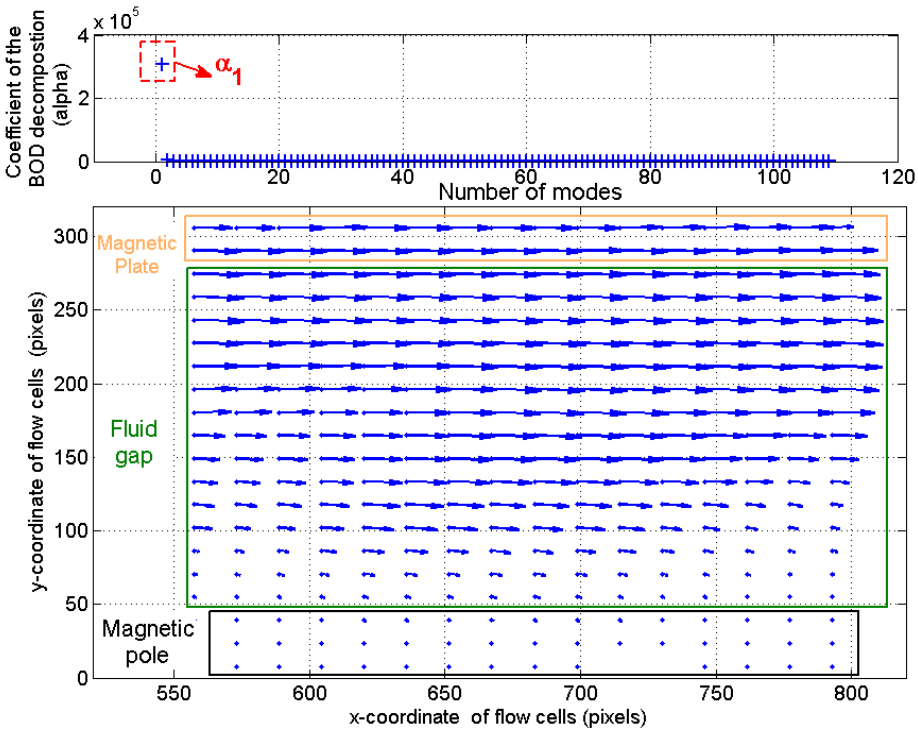

Figure 3.26 – BOD of the MRF shearing phase with a magnetic plate. Top figure: eigen values α; bottom figure: cartesian coordinates of the velocity in the α_1 mode.

4.2 Fluid plate interfacial shearing

Figure 3.27 and 3.29 presents the MRF internal structure at different instants in the *No adhesion* phase (figure 3.20). The set of pictures in image 3.27 corresponds to the continuation of the shearing phase presented in figure 3.21, while figure 3.29 shows the continuation of the shearing phase of figure 3.23. The tracking of point A in figure 3.27 and the light zone L in figure 3.29 proves that while the fluid is being stationary the shearing plate continues its horizontal translation. An additional evidence of the loss of adhesion between the shearing plate and the MRF fluid in the *No adhesion* phase is presented by the BOD decomposition (figure 3.28 and 3.30) where it is clear that the shear rate is null in the MRF gap.

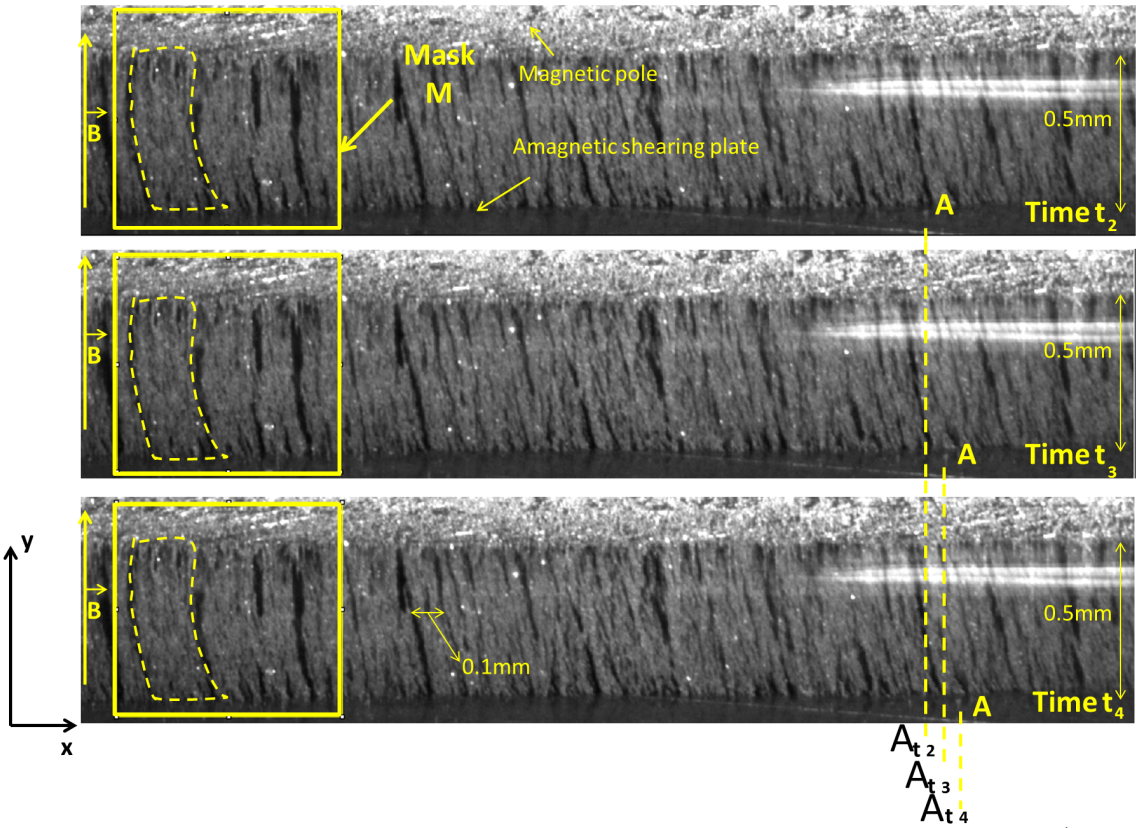

Figure 3.27 – MRF internal structure during loss of adhesion with the amagnetic shearing plate. (Top to bottom corresponds to the succession of the shearing moments with a time interval equal to Δt=10s).

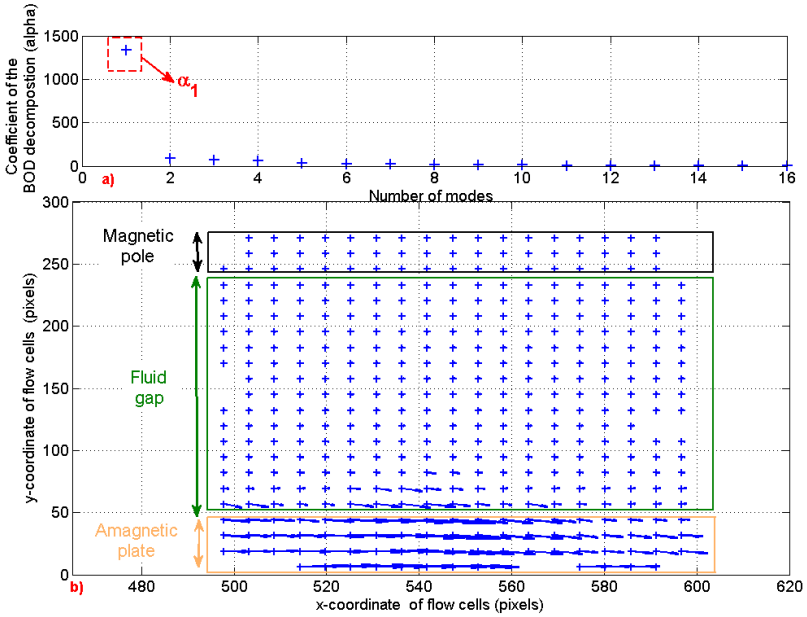

Figure 3.28 – BOD of the MRF shearing with an amagnetic plate in the no adhesion phase; top figure: eigen values α of the BOD decomposition; bottom figure: cartesian coordinates of the velocity in the α_1 mode.

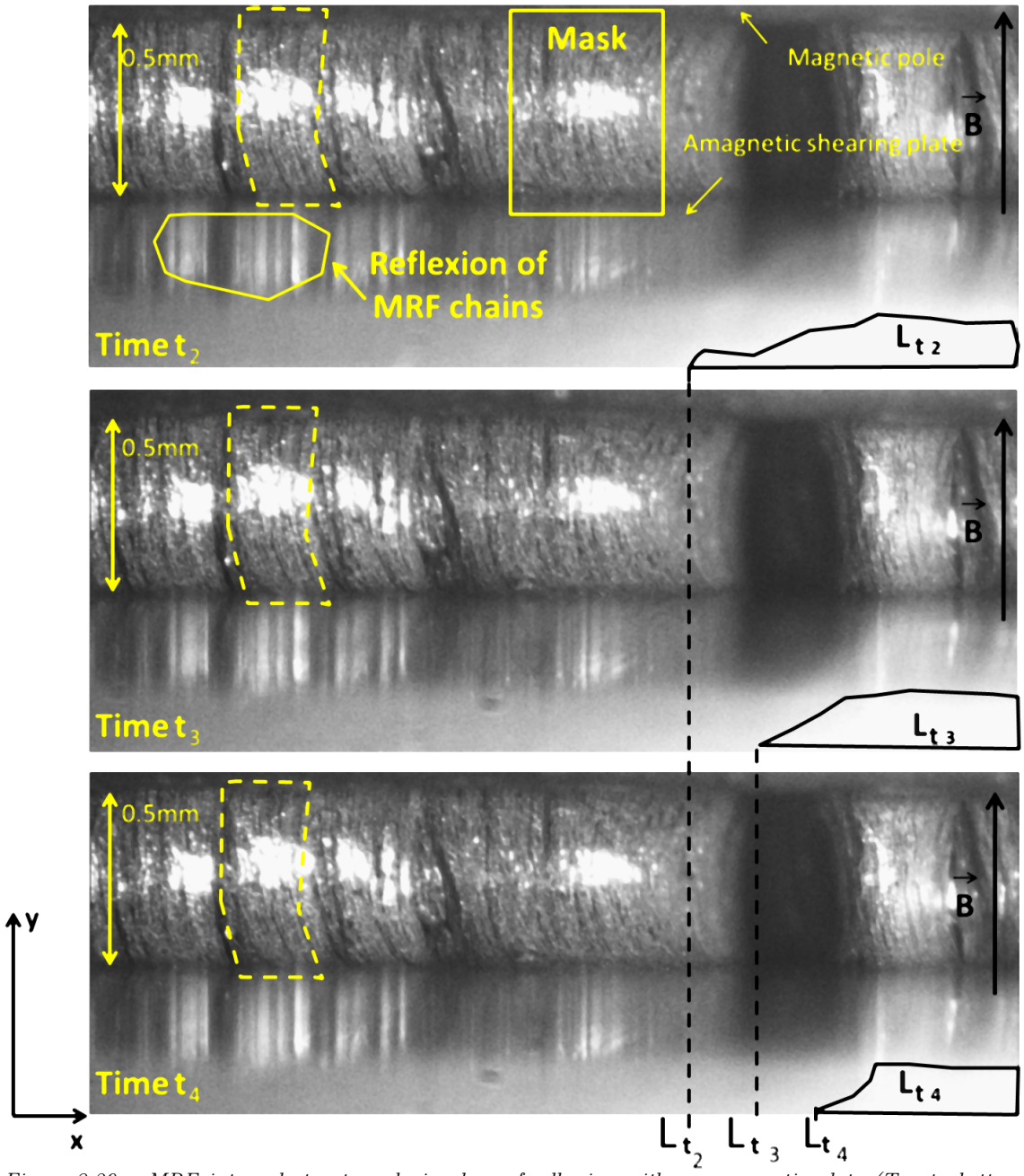

Figure 3.29 – MRF internal structure during loss of adhesion with an amagnetic plate (Top to bottom corresponds to the succession of the shearing moments with a time interval equal to Δt=55s).

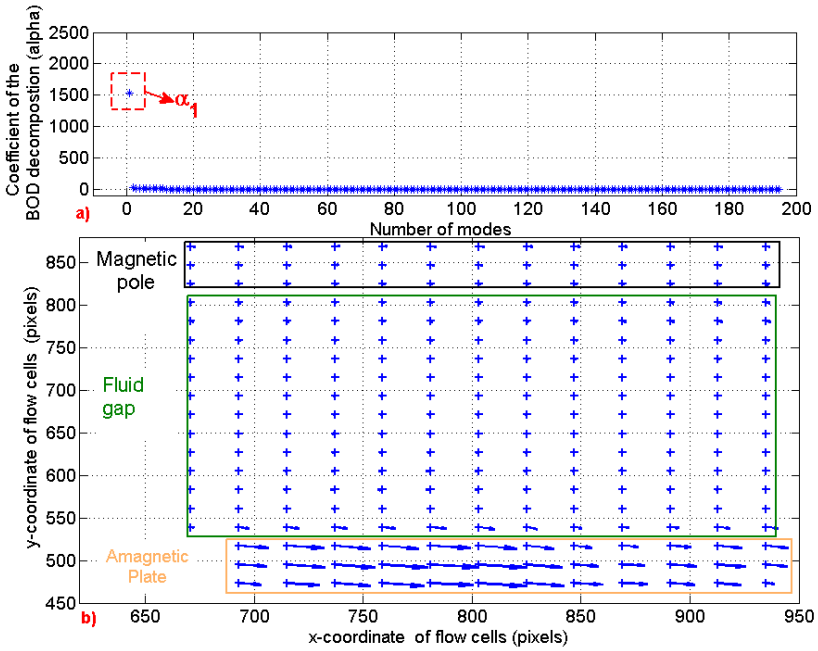

Figure 3.30 – BOD of the MRF shearing with an amagnetic plate in the no adhesion phase; top figure: eigen values α of the BOD decomposition; bottom figure: cartesian coordinates of the velocity in the α_1 mode.

At the macroscopic level the value of the maximum measured force F in the end of the shearing phenomenon, for the same value of magnetic field B, is stronger when the shearing plate used is magnetic (figure 3.20). In the microscopic level we notice that when the shearing plate used is magnetic, the loss of adhesion occurs between the system of shearing plate/MRF and the magnetic pole (figure 3.32).

As the force in the loss of adhesion regime, for both cases magnetic and amagnetic shearing plate, will be modeled as friction force, the increase of the force level is justified by the increase of roughness of the sheared surface.

I suppose that the diminution of the velocity field near the magnetic pole is due to the contact between the MRF chains and the MRF beards existing in the magnetic pole surface.

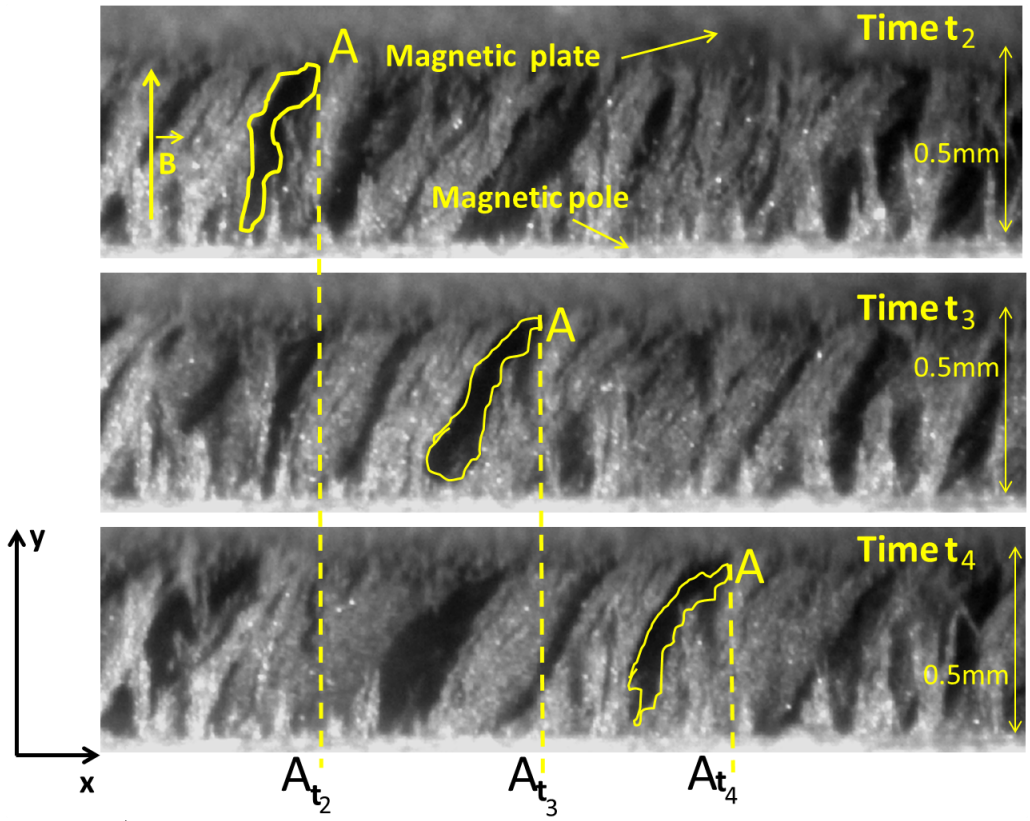

Figure 3.31 – a): MRF internal structure during loss of adhesion with the magnetic pole when shearing with a magnetic plate (Top to bottom corresponds to the succession of the shearing moments).

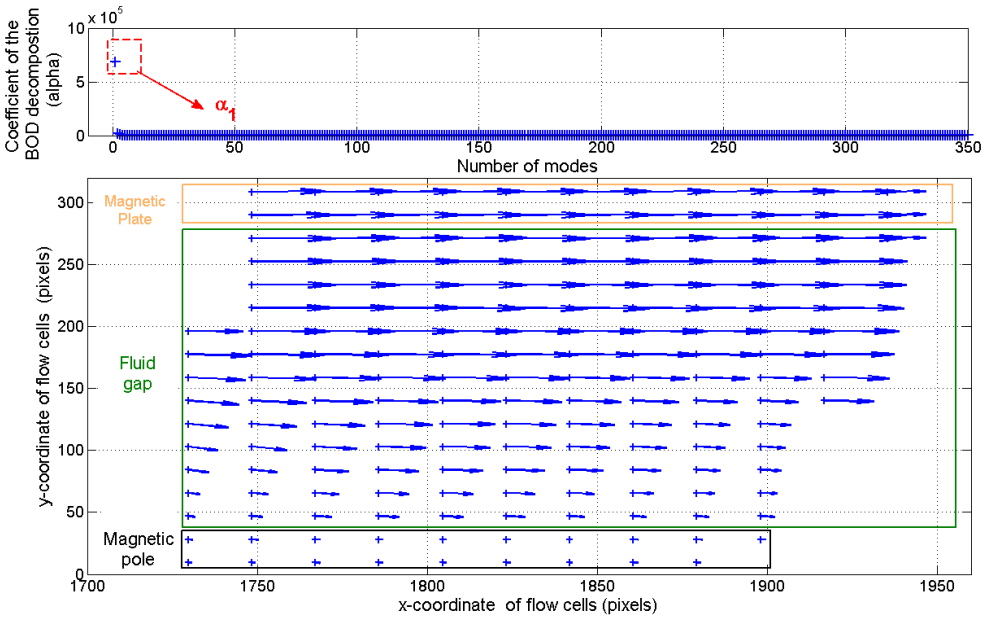

Figure 3.32 – BOD of the MRF shearing phase with a magnetic plate in the "No adhesion phase". Top figure: eigen values α; bottom figure: cartesian coordinates of the velocity in the α_1 mode.

5 Conclusion

With scanning electron microscopy we were able to reveal both chemical and structural compositions of the MRF particles. It was found that MRF magnetic particles are coated with a nanometric film of polymer responsible of their cohesion (Sec. 1.2).

An additional evidence on the independence of particle cohesion and magnetic field was revealed in optical observations where the increase and decrease of the magnetic field B and the degaussing process (a sinusoidal diminution of the magnetic field B) did not have any significant effect on the fluid internal structure (Sec. 3).

High microscopic resolution observations highlighted the basic magnetic effects in MRF presented in the literature but not depicted microscopically until nowadays (Sec 2).

The correspondence between macroscopic measurements , $F(u)$, and microscopic observations showed that during shearing two initial regimes are present:

- MRF shearing in which MRF chains are bent (Sec. 4.1);
- sliding of the shearing plate against the MRF in case of shearing with an amagnetic plate; and sliding of shearing plate/MRF against the magnetic pole in case of a magnetic shearing plate (Sec 4.2).

We assume that what is observed at the surface of the fluid is representative of the deeper MRF layers.

Chapter 4

1. Regime of initial shearing: Regime 1

Contents

1	**Reversibility**	**101**
2	**Internal fluid structure dependency**	**103**
3	**Shear modulus K_1**	**107**
4	**Limit of the initial shearing regime τ_{12}**	**112**
5	**Conclusion**	**117**

The measurement of the MRF shearing stress-strain relationship $\tau(\gamma)$ generated by shearing the MRF with a thin plate, is investigated. The effect of the applied magnetic field B, fluid concentration ϕ, shearing rate $\dot{\gamma}$ (shearing velocity v), shearing plate nature and thickness e and the fluid internal structure on the shearing response F (figure 4.1) are examined. Typical experimental measurements of the shearing stress τ as function of the shear strain γ (also their corresponding measured force F and shearing plate displacement u) are presented in figure 4.2.

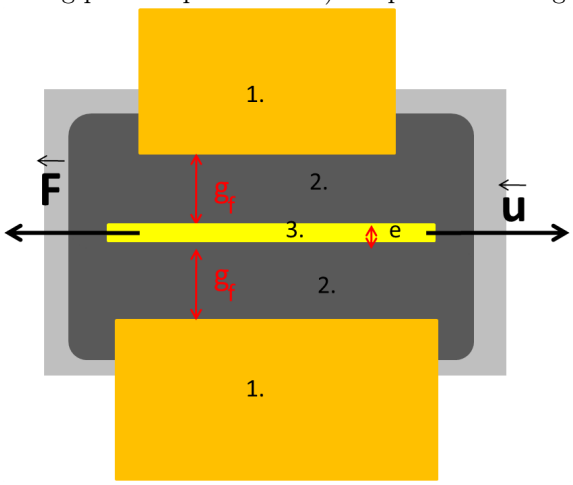

Figure 4.1 – Schematic illustration of the MRF measured resistance force; 1: coils; 2: MRF magnetized gap g_f; 3: shearing plate; e: shearing plate thickness.

The experimental measurements show a non-linear relationship in the MRF shearing response. It reveals three distinct regimes.

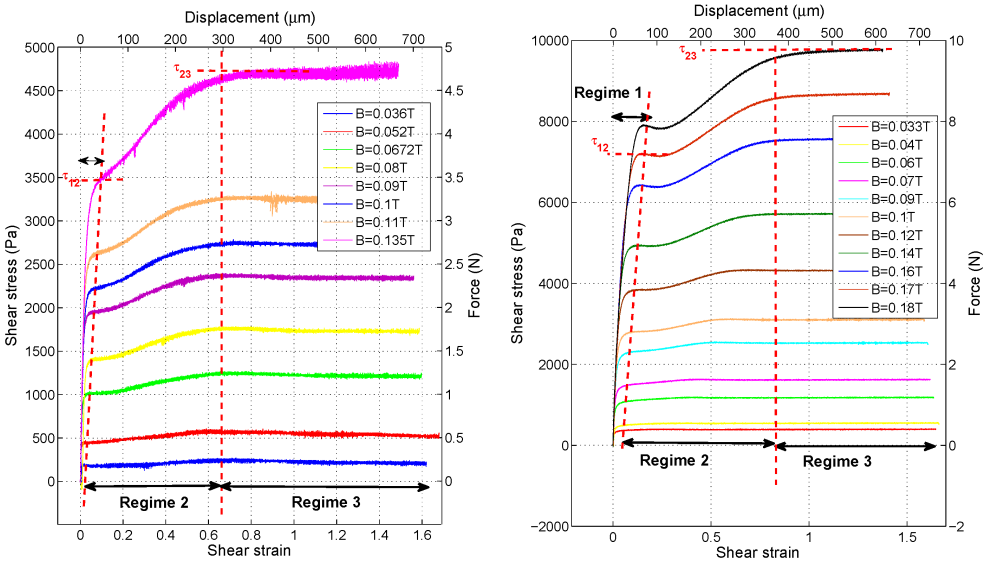

Figure 4.2 – Shear stress as function of the shear strain (also indicated: force and displacement), left :MRF-122; right: MRF-132.

In this chapter we restrict the discussion to the first regime which we call "Regime of initial shearing". Chapter 5 and 6 are dedicated to the study of the MRF response in the second and third shearing regimes. It is shown that in Regime1, the MRF behaves like a pseudo-elastic material, this regime of initial shearing is limited by a shearing-stress threshold τ_{12}. The effect of the following factors:

- internal fluid structure
- magnetic field B;
- shear rate dependency $\dot{\gamma}$;

- particle volume fraction ϕ ;
- shearing plate thickness e;
- nature and surface state of the shearing plate;

on the measured values of the stress threshold τ_{12} and the shear modulus K_1 are investigated.

1 Reversibility

To test the elasticity of the MRF in the initial shearing regime, the MR fluid is submitted to reversibility tests under relatively small deformations. The front view (figure 4.3a)) and side view (figure 4.3b)) of the experimental modified apparatus, used while experimenting, are presented below. In these tests, I proceed to loading and unloading tests of the MRF. A screw fixed to the motor holder pushes slowly and then let go almost instantaneously the shearing plate support. The laser displacement sensor is used to measure the plate support displacement while the LVDT measures the motor displacement (figure 4.4). The MRF-122 is the fluid used in these tests.

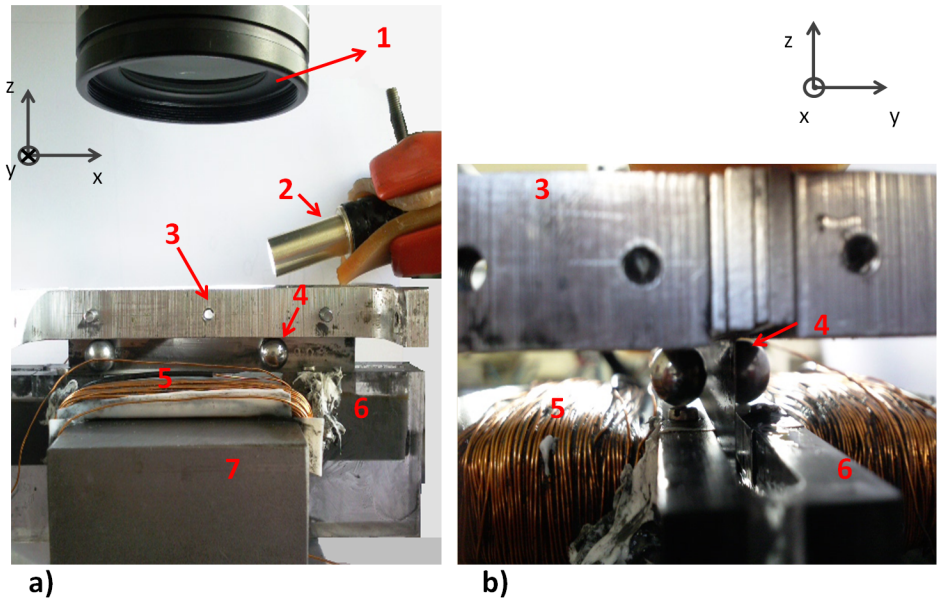

Figure 4.3 – Modified experimental test bench. 1: optical microscope; 2: light source; 3: shearing plate holder; 4: amagnetic ball; 5: coils; 6: MRF cavity; 7: magnetic pole.

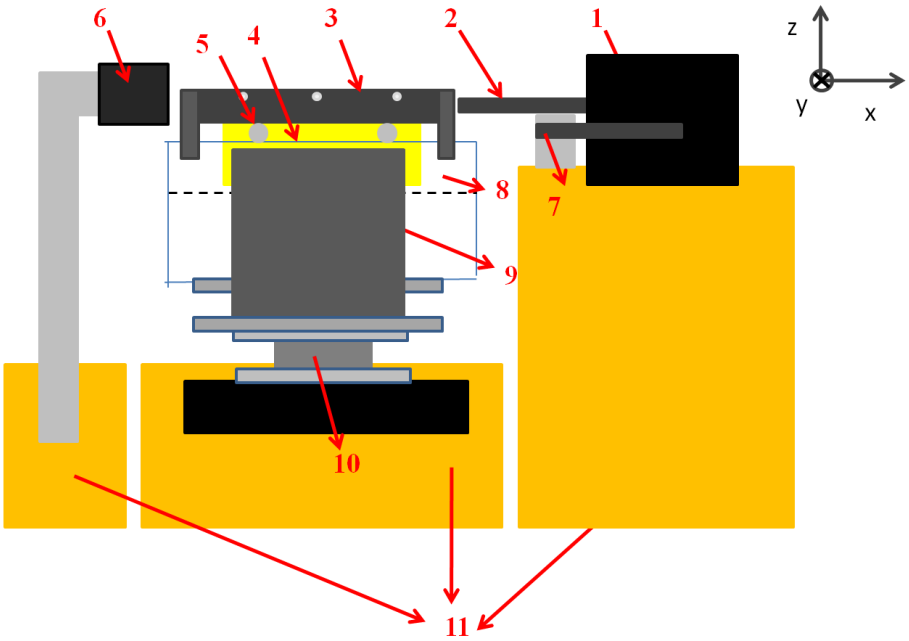

Figure 4.4 – Modified experimental test bench. 1: stepper motor; 2: pushing screw; 3: shearing plate holder; 4: shearing plate; 5: amagnetic ball; 6: laser sensor; 7: LVDT; 8: MRF cavity; 9: magnetic pole; 10: force sensor; 11: sand tanks.

Figure 4.5a) presents an example of the imposed displacement during the push-and-release shearing plate process. This displacement is measured by the LVDT in contact with the stepper motor. Figure 4.5b) is the plate displacement measured by the laser displacement sensor.

At the onset of the reversibility test presented in figure 4.5, the motor is distant from the non-magnetic brass plate. At t= 0.2s the motor comes into contact with the plate holder and drives it at a speed v=30μm/s. The plate holder is released at t=1.1s, the motor velocity being equal to v=1100μm/s. The magnetic field value is equal to B=0.2T.

From these observations, we conclude that once the shearing plate is released by the stepper motor, it returns to its original position.

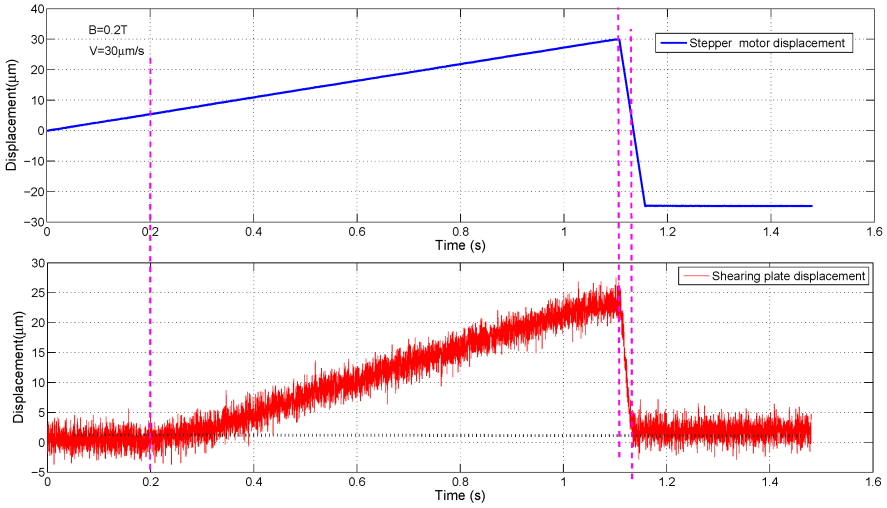

Figure 4.5 – Displacement of the motor and of the shearing plate during loading and unloading tests of the MRF in Regime1.

At the onset of the reversibility test presented in figure 4.6, the motor is distant from the non-magnetic brass plate. At t= 3.7s the motor comes into contact with the plate holder and

drives it. The velocity command of the motor is v=30μm/s. The plate holder is released at t=7s. The magnetic field in this test is B=0.4T. This value of the magnetic field B=0.4T supposes a large shearing resistance force and may explain the observed irregularities in the movement of the shearing plate held only by non-magnetic balls

From these observations (figure 4.6) one should conclude that when increasing the stepper motor displacement the shearing plate does not return to its initial position: the MRF has encountered a non-reversible regime and has gone in a pseudo-plastic zone (figure 4.6).

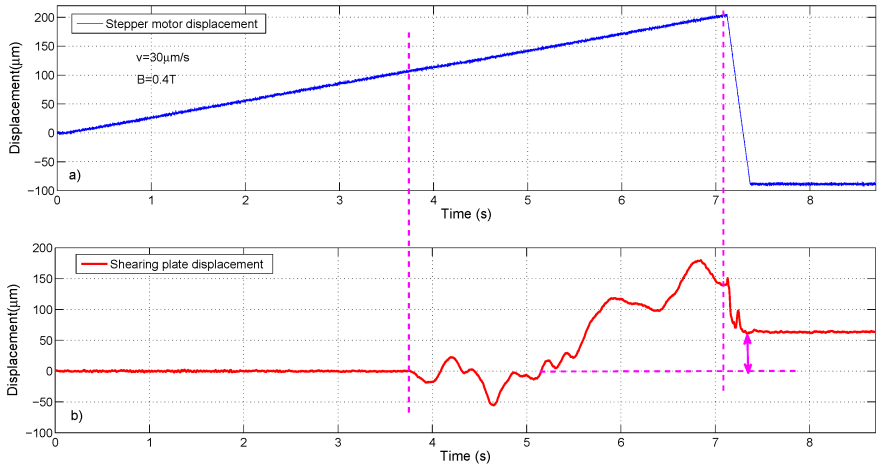

Figure 4.6 – Measured motor and shearing plate displacement during a large loading and unloading of the MRF.

2 Internal fluid structure dependency

A sequence of two shearing tests with different internal structures were done to identify the effect of MRF internal structure on its shearing response. The magnetic field B is the same for both tests B=0.16T.

Figure 4.7 summarizes the experimental shearing command.

In order to obtain an internal chain-like structure, several translation movements were imposed to the shearing plate before the series of two tests 4.7.

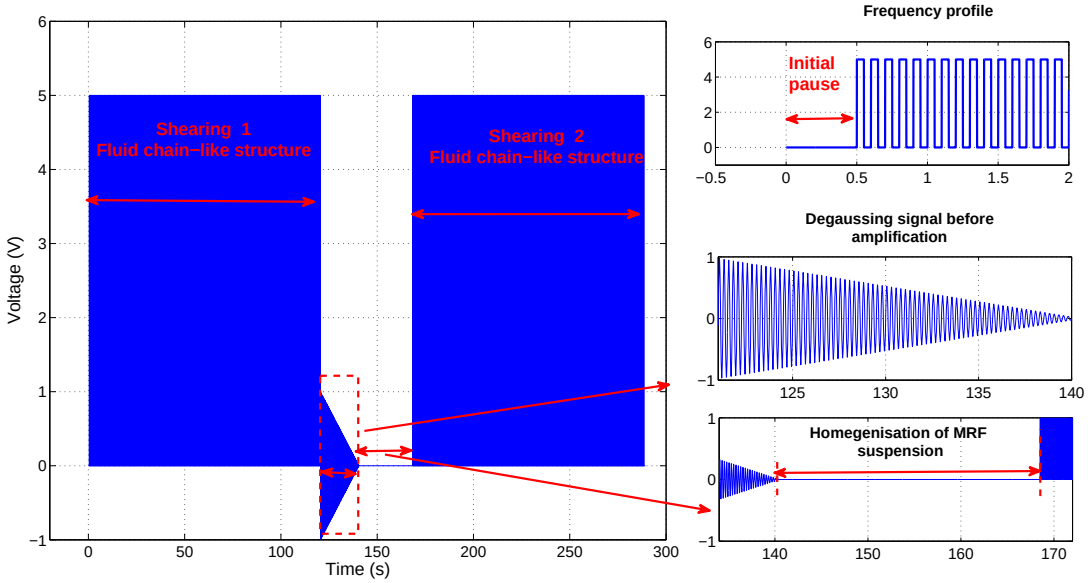

Figure 4.7 – Shearing command for the succession of experimental measurements.

A degaussing cycle takes place between the two shearing tests. The degaussing process is followed by an external mechanical agitation to ensure a quasi-destruction of the MRF chain structure (figure 4.8).

At the beginning of the first test the MRF is more or less in the state pictured in the top diagram of Fig. 4.8. The initial state of the second test (bottom diagram) although not fully isotropic, is quite different.

The shearing plate used in a non-magnetic brass plate, it has a thickness of e=0.1mm and the MRF-132 is the fluid tested. To be able to observe microscopically the MRF internal structure while experimenting the MRF cavity was filled so that the MRF level is lower than the magnetic pole top surface (figure 4.9). Since the experimental conditions in these measures are different than the previous ones, the $\tau(\gamma)$ dependency cannot be numerically compared with the measured obtained in a fully immersed plate.

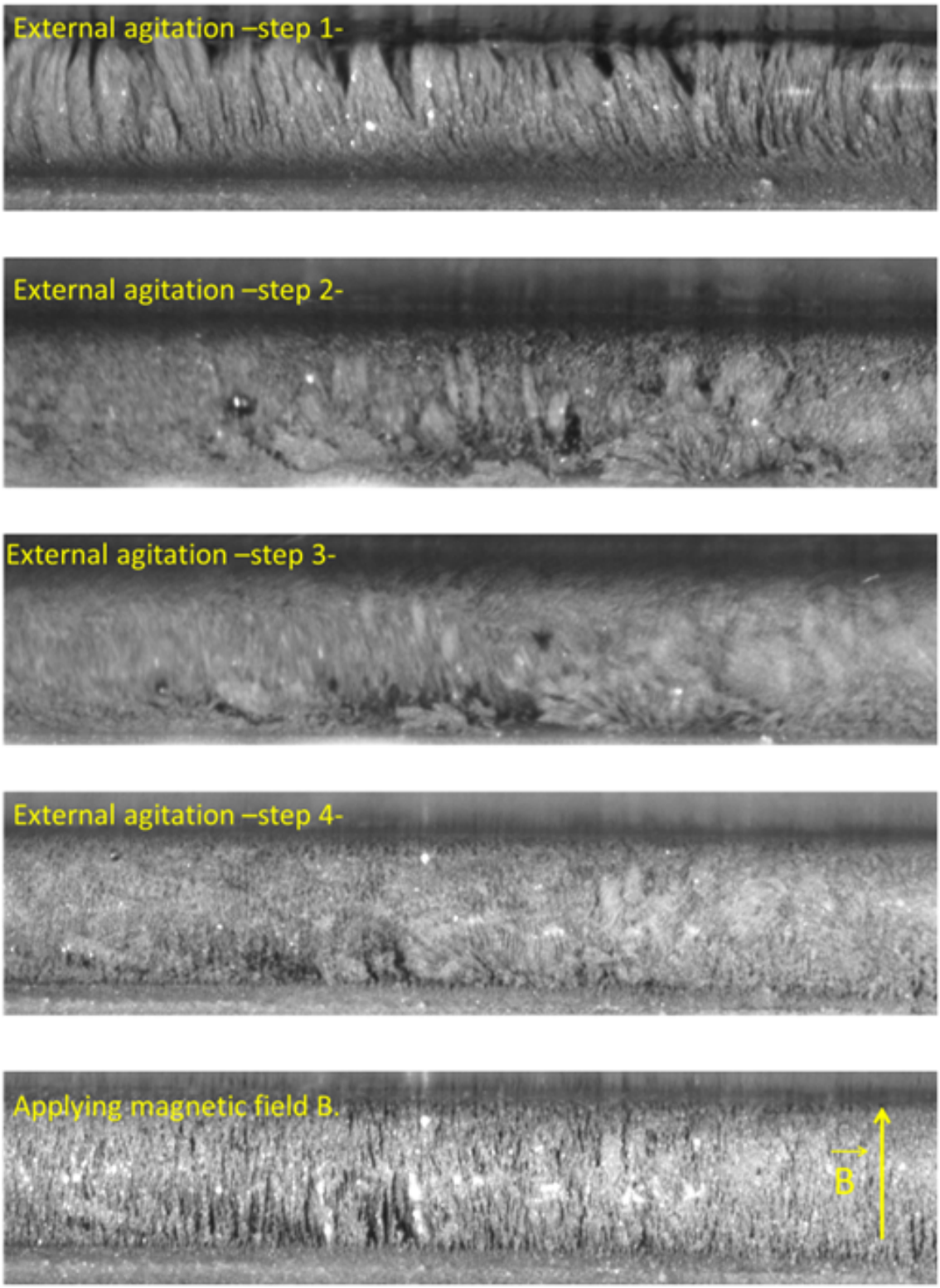

Figure 4.8 – Homogenisation of the MRF internal structure, in a 1mm gap thickness, between the two tests, after degaussing.

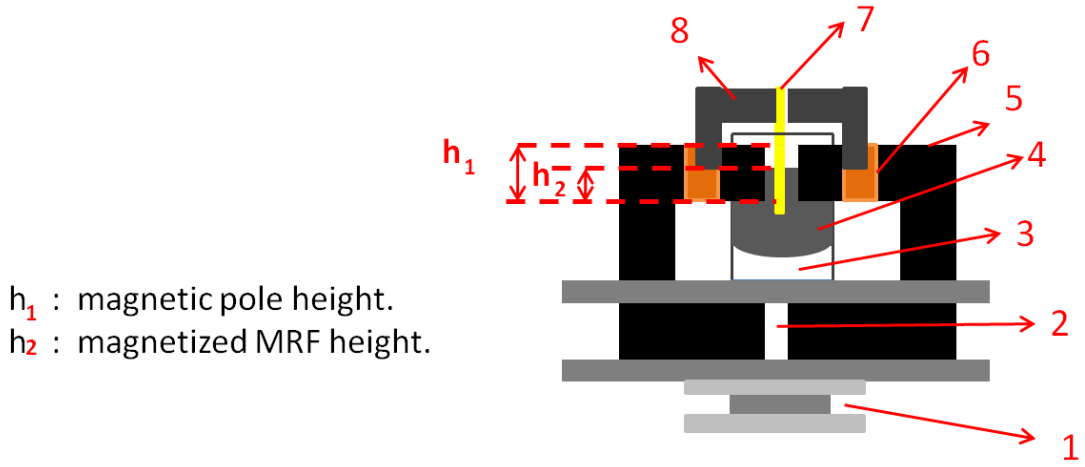

Figure 4.9 – Schematic presentation of the MRF cavity while microscopic observing. 1:force sensor; 2: air gap; 3: MRF cavity ; 4: MRF; 5: magnetic pole; 6: coils; 7:shearing plate; 8: plate holder.

Figures 4.10 and 4.11 show each shearing movement. The microscopic observations of the marked change in the MRF internal structure are also presented. The internal MRF structure during these observations are different: in the first test the chain-structure remains well organized while in the second test the structure remains more isotropic.

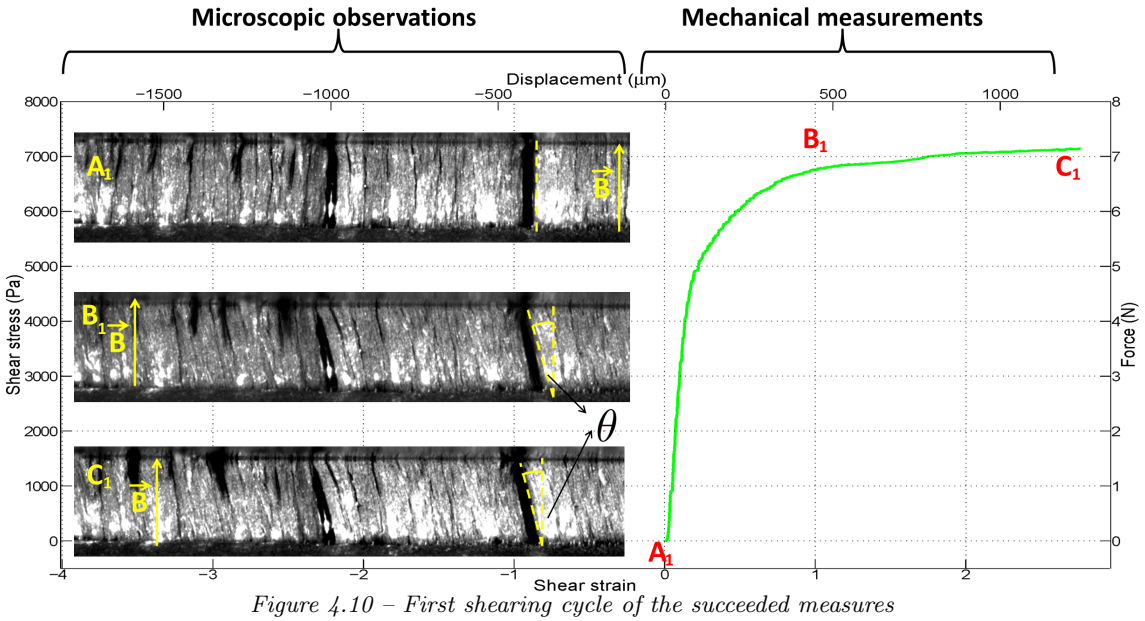

Figure 4.10 – First shearing cycle of the succeeded measures

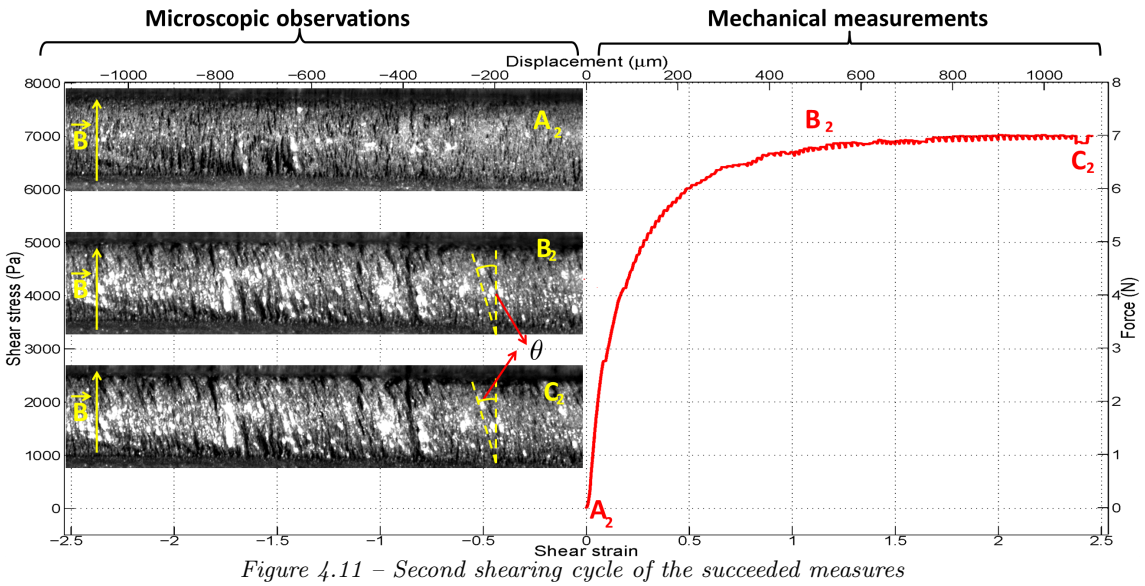

Figure 4.11 – Second shearing cycle of the succeeded measures

The comparison between the fluid response (figure 4.12 in both tests shows that the fluid internal structure does not have a significant effect on the fluid mechanical response in this regime.

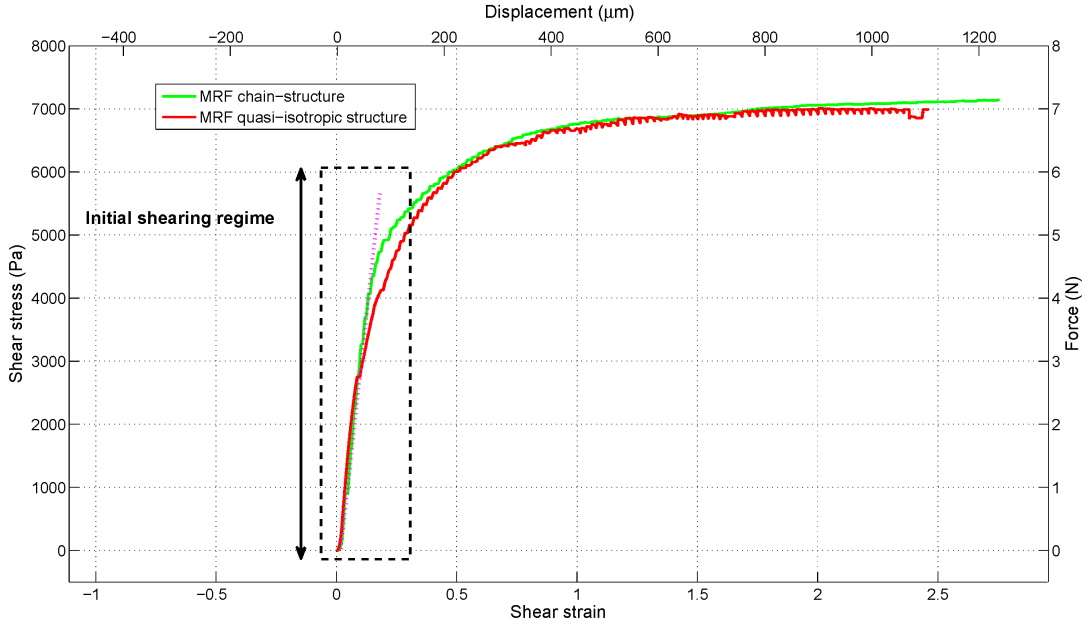

Figure 4.12 – Comparison of MRF response in the two succeeded shearing tests.

3 Shear modulus K_1

The pseudo-elastic initial shearing regime takes place in a very limited strain range (figure 4.2 and 4.19). To characterize this regime, more accurate tests with a small shearing plate displacement were done. It appears that the $\tau(\gamma)$ dependency is quasi-linear (figure 4.13). The shear modulus representing the ratio between the stress τ and strain γ is noted by K_1. The following sections will discuss the effect of the design parameters on the initial shear modulus K_1.

3.1 Magnetic field dependency B

Small shearing displacement tests are done with an applied magnetic field values of B= 0.1 T, 0.21 T, 0.3 T and 0.4 T (figure 4.13). These values of B are below the magnetic fluid and the iron saturation. The shearing plate used is amagnetic and its thickness e is equal to e=0.08mm. The MRF-122 (Lord) is used in these experiments. It appears that the fluid shear modulus K_1 is independent of the magnetic field B. The shear rate $\dot{\gamma}$ in these tests is $\dot{\gamma}$=0.02s^{-1}.

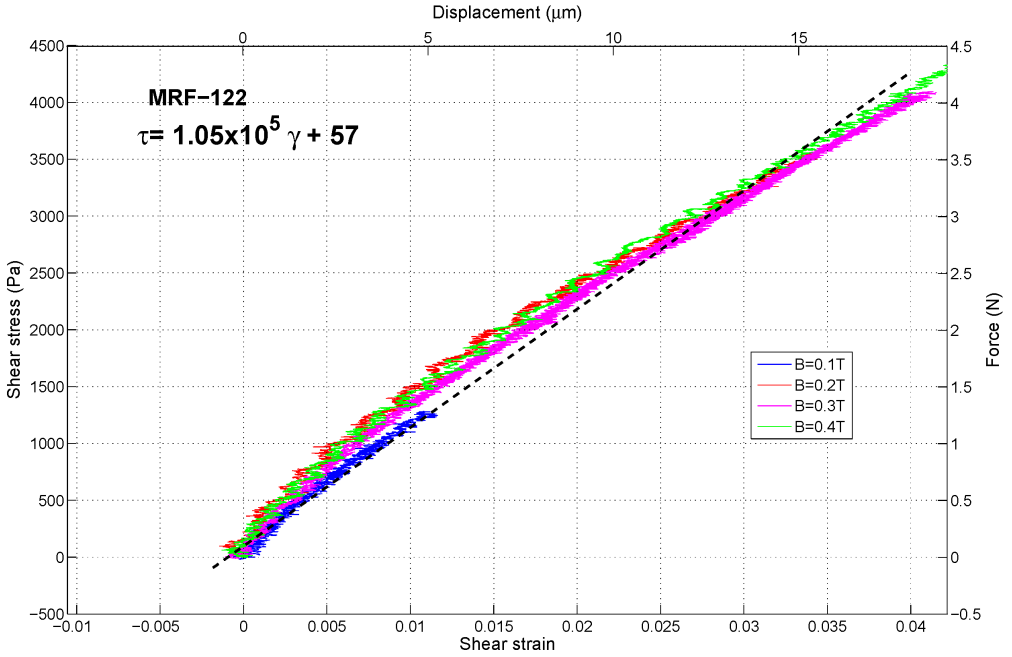

Figure 4.13 – Shear stress as function of shear strain (also indicated force and displacement) for magnetic field values between 0.1T and 0.4T at a shear rate $\dot{\gamma}$=0.02s^{-1}.

The calculated value of shear stress when the MRF is unmagnetized $\tau_{B=0}$=56Pa. This value is five times larger than the evaluted τ_{test} ($\tau_{B=0}$=56Pa= 5×τ_{test}) as presented at Sec. 6.2.3 in Chap. 2. This may due to additional friction forces generated by the transmission system.

3.2 Shearing rate dependency $\dot{\gamma}$

Figure 4.14 presents the $\tau(\gamma)$ behavior for shear rates ranging from $\dot{\gamma}$=1.4 10^{-2}s^{-1} to $\dot{\gamma}$=1.3s^{-1} (60μm/s< V< 600μm/s). The shear modulus K_1=1.1 10^5 Pa is obtained by a linear fit of the experimental measurements.

The shear modulus K_1 of the MRF response in the Initial regime of shearing does not seem to be dependent of the shearing rate (figure 4.14).

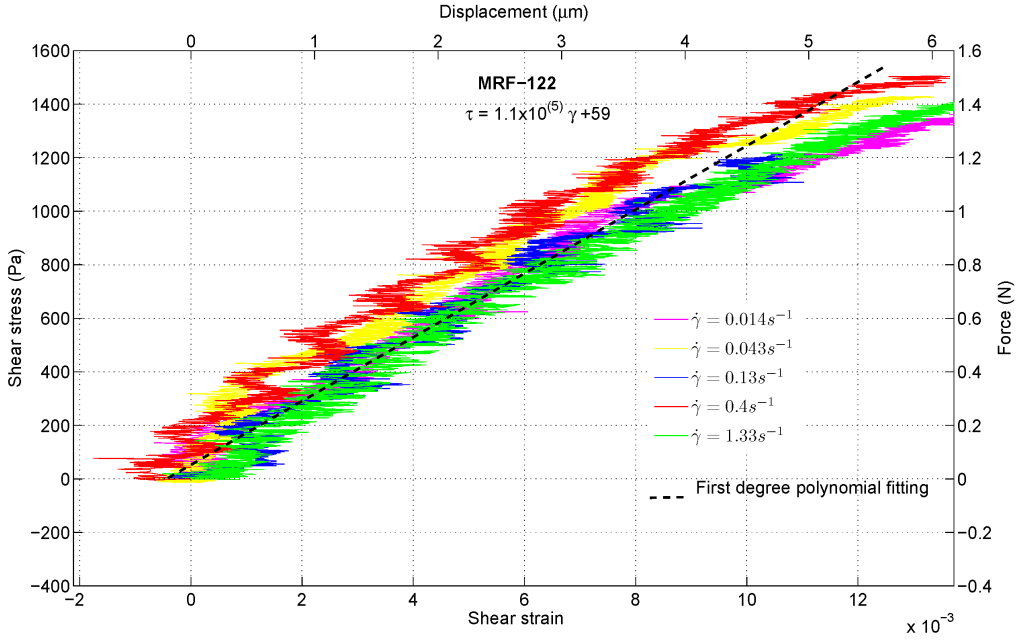

Figure 4.14 – Shear stress as function of shear strain (also indicated force and displacement) for shear rate values $\dot{\gamma}$ between $0.014s^{-1}$ and $1.33s^{-1}$.

3.3 Particle volume fraction dependency

The elastic slope of the initial shearing regime does not seem to depend significantly on the MRF particle volume fraction ϕ, (figure 4.15).

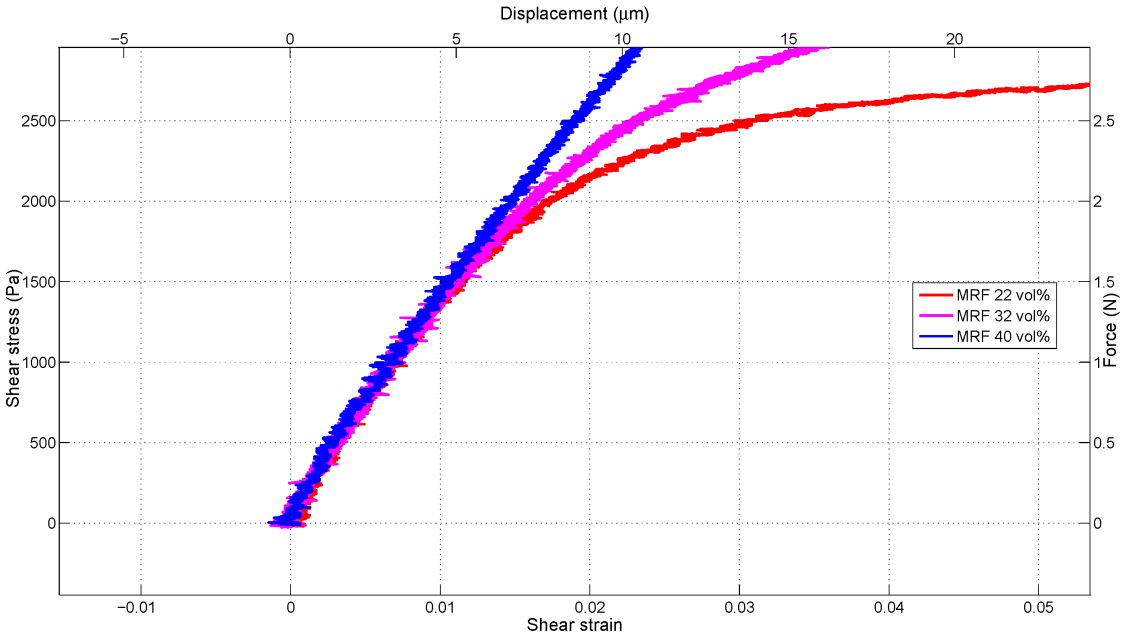

Figure 4.15 – Variation of shear stress as function of shear strain (also indicated force and displacement).

3.4 Shearing plate thickness dependency e

Figure 4.16 shows the measured stress-strain relationship $\tau(\gamma)$ obtained when shearing the MRF-132 (Lord) with four different non-magnetic shearing plates thickness e=0.08, 0.13, 0.25 and 0.45mm. The magnetic field value in these four tests is B=0.15T.

The comparison between the fluid response (figure 4.16) in the four tests shows that the shearing plate thicknesses e structure does not have a significant effect on the fluid mechanical response in the initial shearing regime. A different initial slope IS depicted in the green curve, when the non-magnetic brass shearing plate thickness is e=0.45mm. No physical explanation at this stage is proposed for this observation.

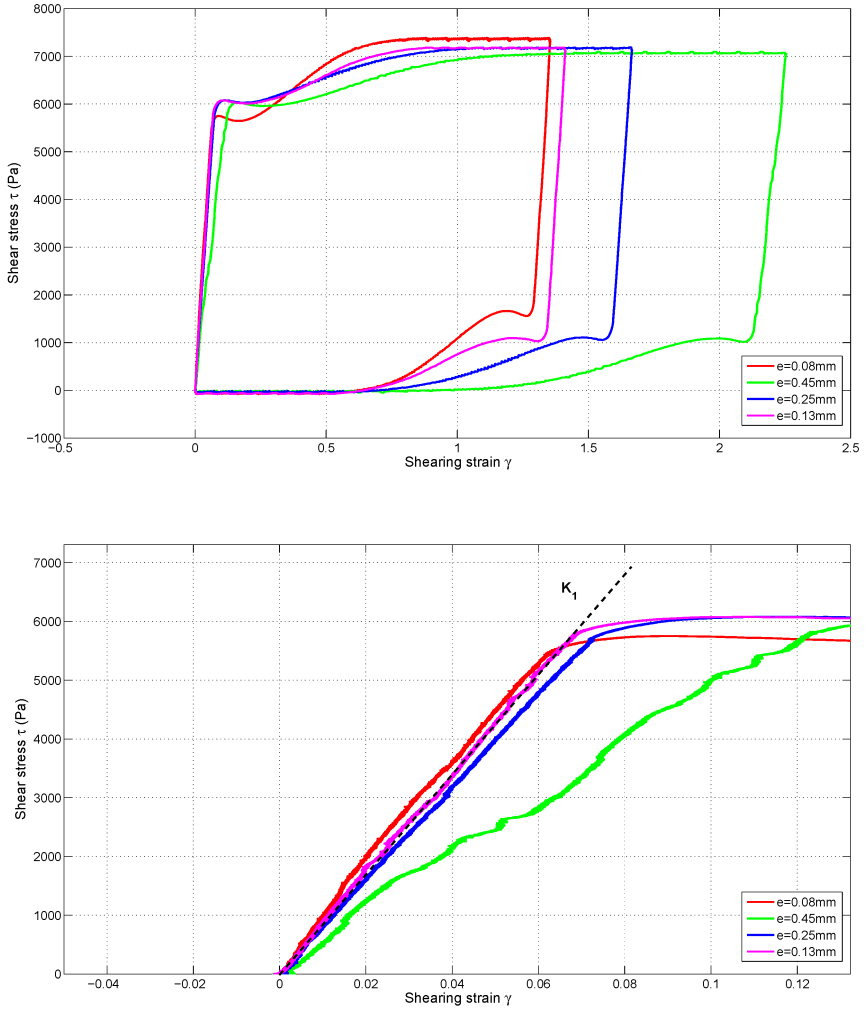

Figure 4.16 – Dependency of $\tau(\gamma)$ with shearing plate thickness. Top: total MRF shearing cycle; bottom: MRF response in the initial shearing regime.

3.5 Influence of the nature and surface state of the shearing plate on K_1

Figure 4.17top shows a comparison between the MRF response to linear shearing by a brass, glass, or aluminum plate while figure 4.17bottom shows the comparison between the responses to shearing with a magnetic or non-magnetic aluminum plate. The shearing rate in these experiments is $\dot{\gamma}$=0.2s^{-1}, the shearing plate thickness is e=0.1mm and the fluid particle volume fraction is ϕ=22% (MRF-122 (Lord)).

The experimental results presented in figures 4.17top) and 4.17bottom) show that the fluid

response in the regime of initial shearing is not affected by the magnetic properties of the shearing plate surface.

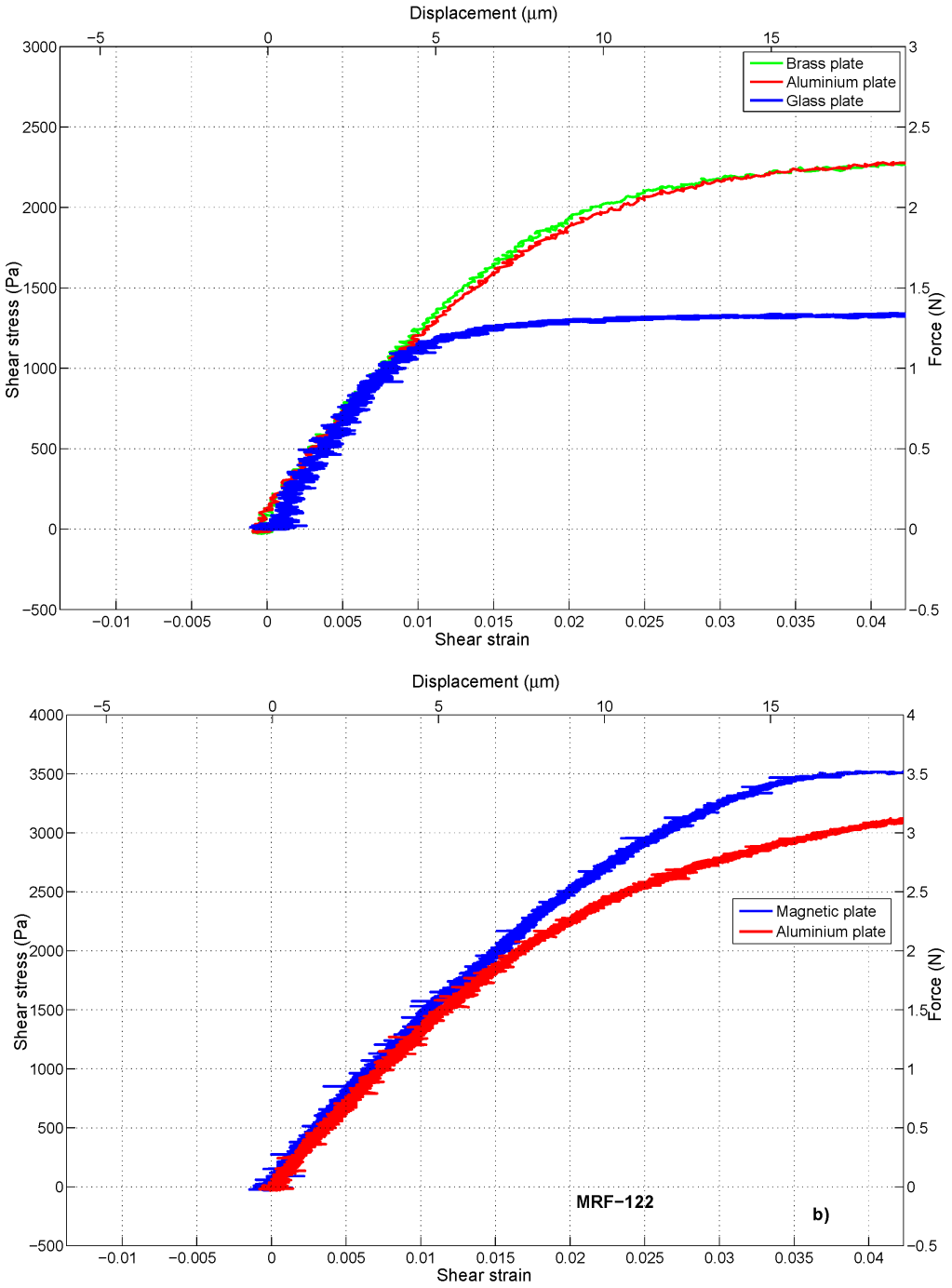

Figure 4.17 – Shear stress as function of shear strain in the initial shearing regime (also indicated force and displacement). Top: shearing with amagnetic plates; bottom: comparison of shearing with magnetic or non-magnetic plate.

4 Limit of the initial shearing regime τ_{12}

4.1 Magnetic field dependency B

When varying the MRF particle volume fraction ϕ (ϕ=22%, ϕ=32% and ϕ=40%) the stress threshold τ_{12} increases with the square of the magnetic field B^2. It appears that τ_{12} is related to B^2 by the following relation:

$$\tau_{12} = T.B^2 \tag{4.1}$$

The results shown in figure 4.18 are obtained with an amagnetic shearing plate of thickness e_{plate}=0.1mm.

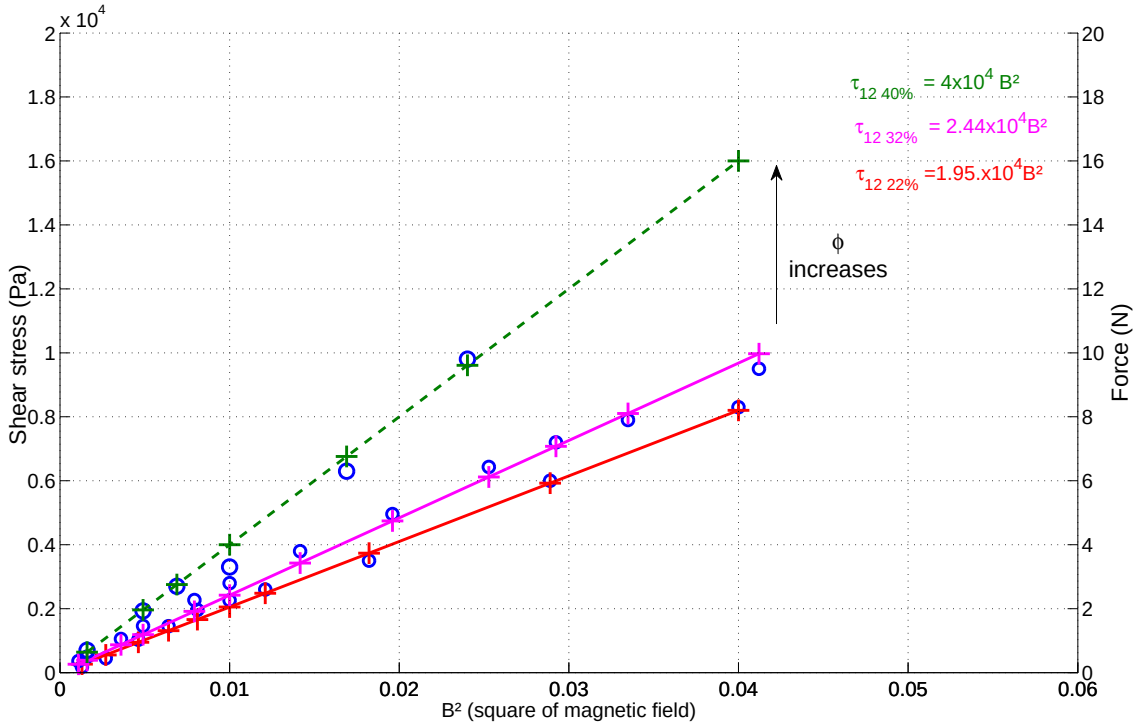

Figure 4.18 – Upper limit of Regime1 as function of B^2

Figure 4.19 shows a typical MRF stress response to shear when a magnetic plate is used while shearing. The shearing displacement is measured by the laser displacement sensor Keyence LB-12. Two threshold stresses $\tau_{12'}$ and $\tau_{12''}$ are noticed, their corresponding variation with the square of magnetic field B^2 are presented in figure 4.20.

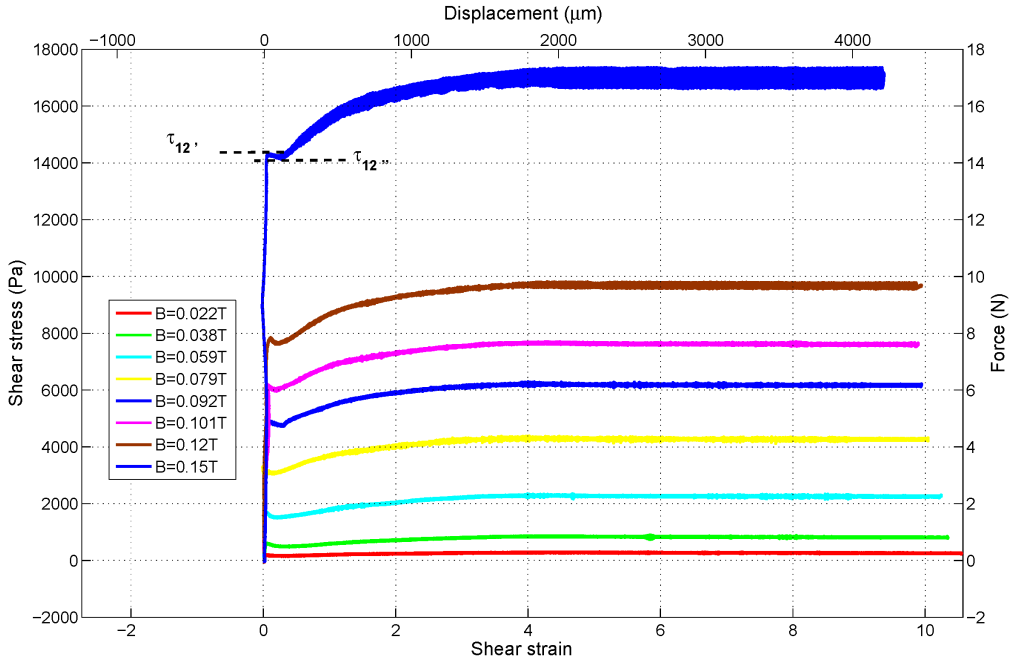

Figure 4.19 – Shear stress as function of the shear strain (also indicated: force and displacement) resulting from shearing with a magnetic plate.

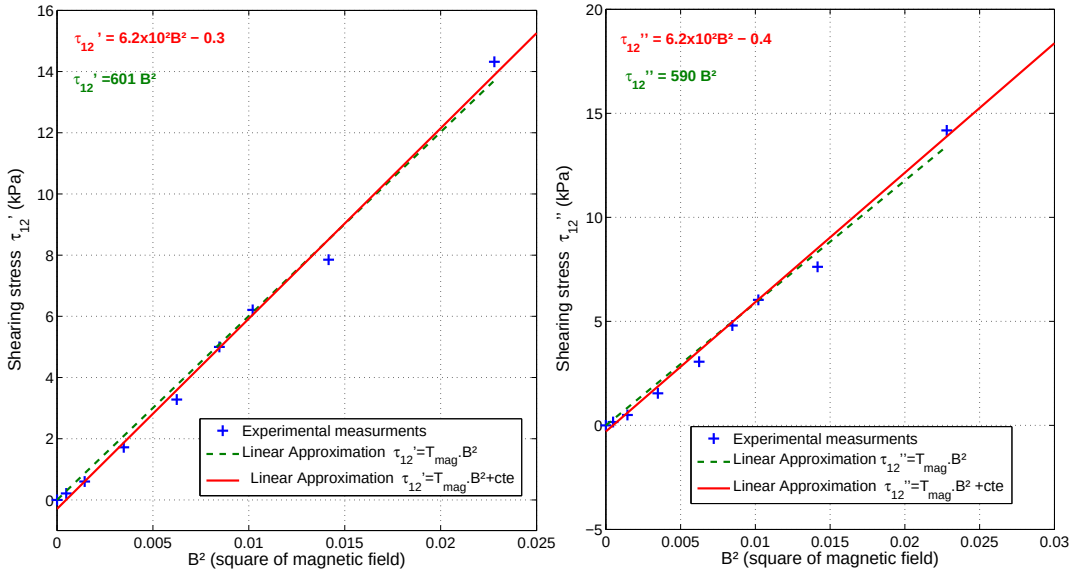

Figure 4.20 – Shear stress threshold $\tau_{12'}$ and $\tau_{12''}$ as function of the square of magnetic field B^2 in case of MRF-122 magnetic shearing.

The calculated ratio of the two threshold stresses $\tau_{12'}$ and $\tau_{12''}$ is equal to $\dfrac{\tau_{12'}}{\tau_{12''}} = \dfrac{600\,B^2}{590\,B^2} = 1.02$. Since the difference between the two threshold stresses values is small, only $\tau_{12'}$ will be considered as the threshold stresses in experimental comparisons.

4.2 Shearing rate dependency $\dot{\gamma}$

Figure 4.21 presents shearing tests at different shearing rates ranging from $\dot{\gamma}$=0.02s^{-1} to $\dot{\gamma}$=2.7s^{-1} (shearing velocities 10μm/s < V< 1000μm/s) with a magnetic or amagnetic shearing plate. In both shearing cases the value of τ_{12} is not affected by the variation of the shearing rate $\dot{\gamma}$. When increasing the shear rate 135 times $\dot{\gamma}_f$=135×$\dot{\gamma}_i$= 135×0.02=2.7 s^{-1}, the measured τ_{12} increases by 5%

$$e_{\tau_{12}} = \frac{3.2\,10^3 - 3.03\,10^3}{3.2\,10^3} = 5\%.$$

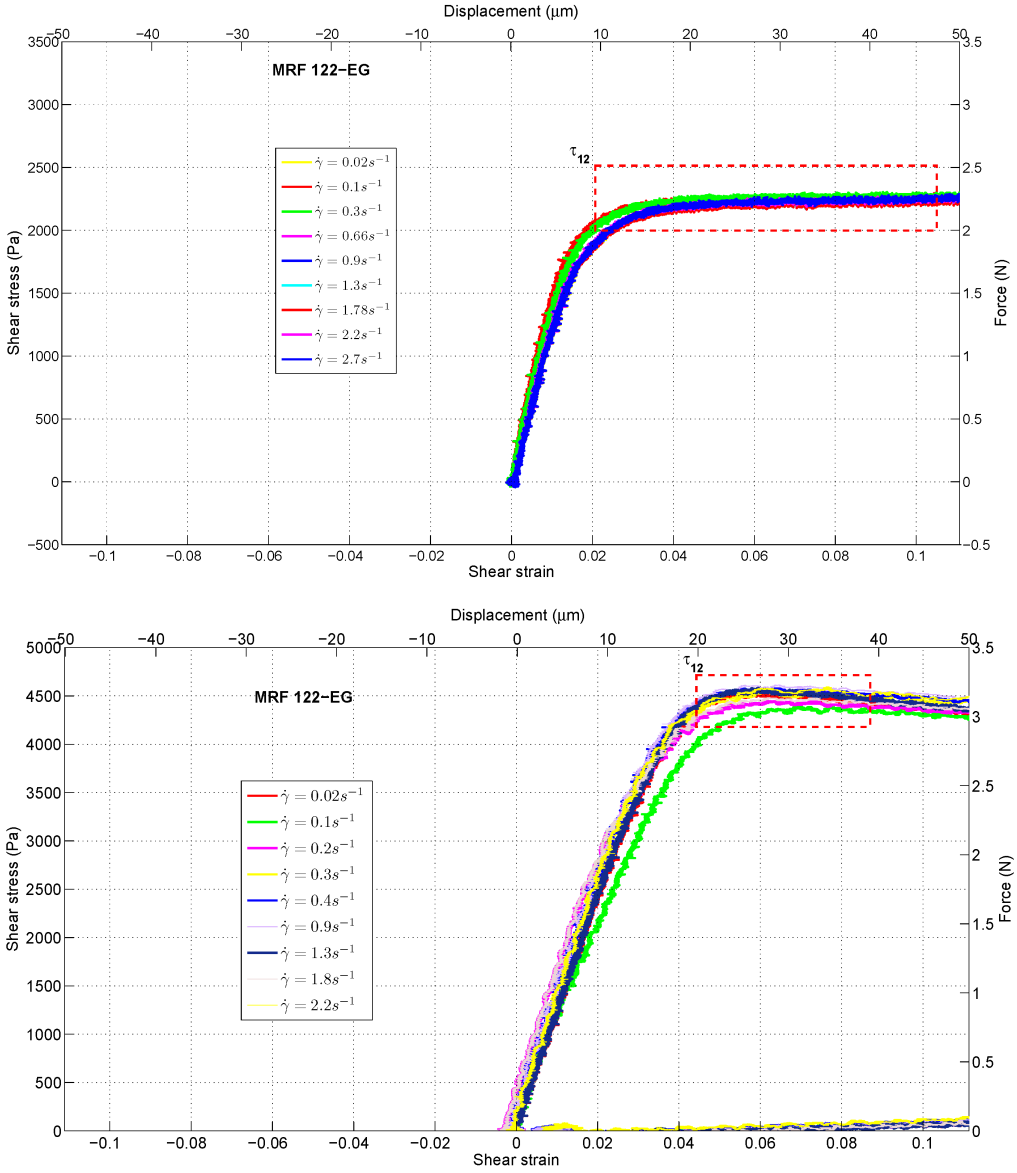

Figure 4.21 – Shear stress as function of the shear strain (also indicated: force and displacement) for different shearing rate values. Top: amagnetic shearing plate; bottom: magnetic shearing plate.

A highlight on the τ_{12} of a magnetic shearing plate cycles is presented in figure 4.21bottom.

Figure 4.22 presents a three axes plot of the MRF behavior in both (τ, $\dot{\gamma}$) and (τ,γ) plans. The x axis presents the shear rate $\dot{\gamma}$, the y axis the shearing γ and the shear stress values τ are plotted in the z axis.

With Bingham model the variation of the shear stress τ is supposed to vary linearly with the shear rate $\dot{\gamma}$. The value of shear stress for a zero shear rate $\dot{\gamma}$=0 is equal to τ=τ_y. In this

model, there is no dependency with the shear strain γ.

In our experimental results an independence between the shear stress τ and the shear rate $\dot{\gamma}$ was depicted. The MRF shear stress τ was found to be varying significantly with the shear strain γ (see fig. 4.21).

The yellow plane in the figure 4.22 presents a highlight on the MRF first regime response, Regime1, where the shear stress τ is found to be varying linearly with the shear strain γ. The green plan in figure 4.22 presents a 3D representation of the Bingham model.

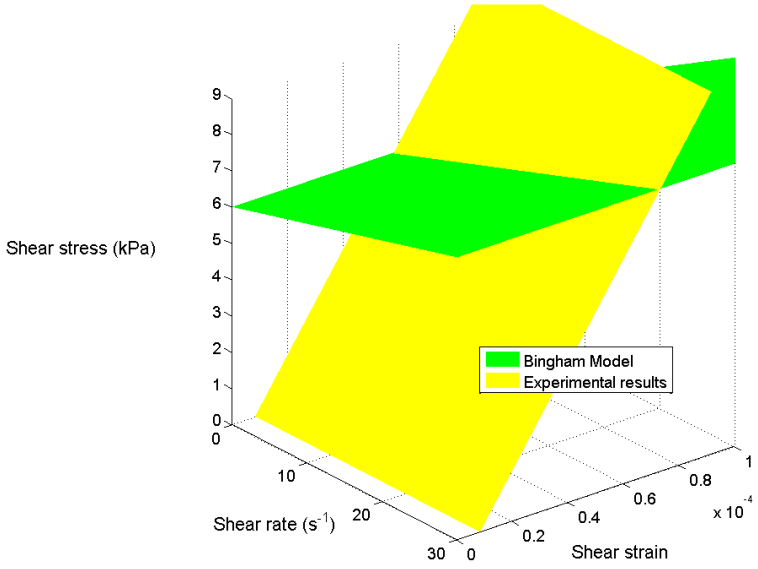

Figure 4.22 – 3D comparison between the MRF response obeying to Bingham model and our experimental results in the regime of initial shearing.

The maximum value of shear strain reached in our experiments, is γ=10, and considering that the MRF time response is T=1ms (Chap. 1 Sec. 1.2) the corresponding calculated shear rate will be $\dot{\gamma}=\frac{10}{10^{-3}}=10^4$ s^{-1}.

The maximum shear rate imposed in our experiments being less than $\dot{\gamma}_{\max}=2.7\text{s}^{-1} \ll 10^4\text{s}^{-1}$, we can confirm that our studies of the MRF are localized in the pre-yield regime.

4.3 Particle volume fraction dependency ϕ

The experimental measurements presents in figure 4.18 show that by increasing the MRF particle volume fraction, the levels of the shearing stress τ_{12} reached become larger. I note T the proportionality factor between τ_{12} and B^2 (Eq. 4.1). Figure 4.23 present the variation of the coefficient T with the particle volume fraction ϕ.

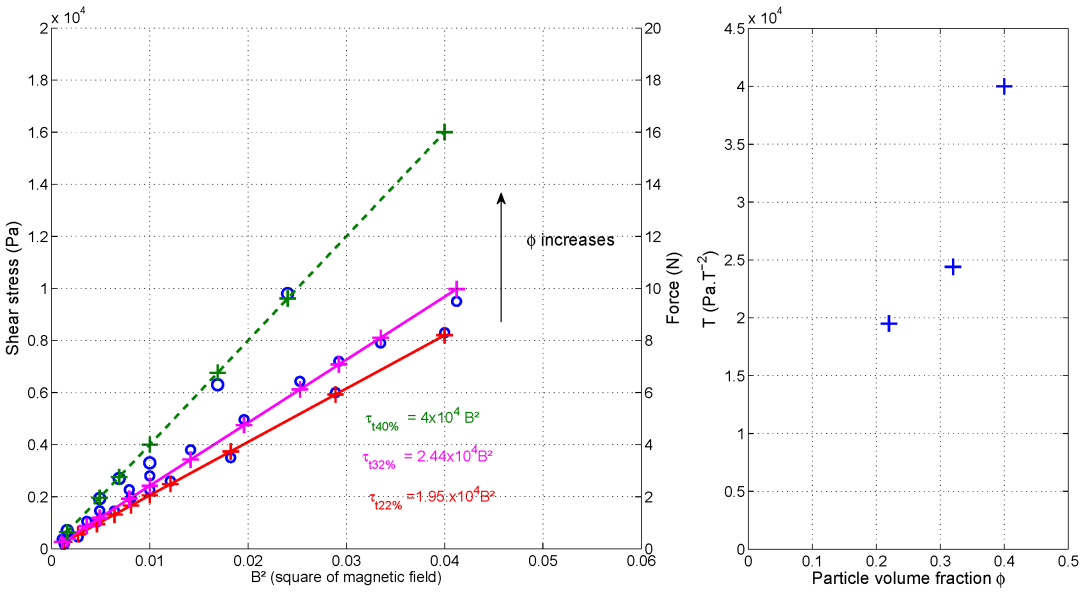

Figure 4.23 – Variation of T with ϕ.

4.4 Influence of the nature and surface state of the shearing plate on τ_{12}

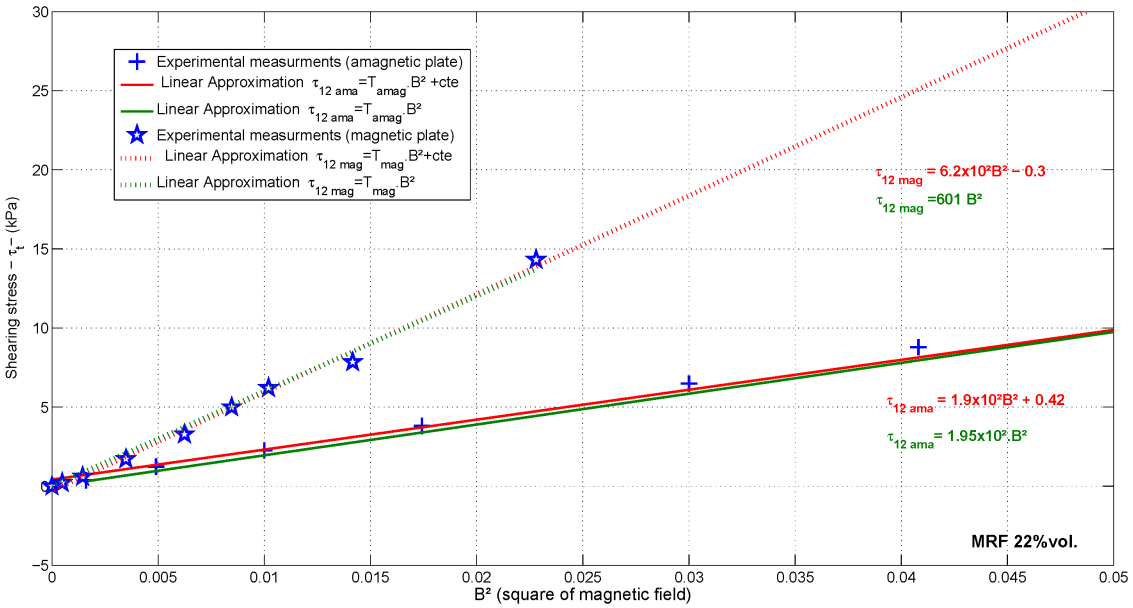

Figure 4.24 – Shear stress threshold as function on the applied magnetic field B. Left: a) magnetic shearing plate; b) amagnetic shearing plate.

The values of the threshold stress τ_{12} vary with the nature of the shearing plate (figure 4.24). For the same type of MRF (MRF122) the coefficient of proportionality T between the measured threshold stress τ_{12} and the square of the magnetic field B^2 in case of shearing with a magnetic plate is greater than the one calculated for an amagnetic plate $T_{\text{amag}} = 195\, Pa.T^{-2} < T_{\text{mag}} = 601\, Pa.T^{-2}$.

4.5 τ_{12} shearing plate thickness dependency e

Figure 4.25 shows the upper limit of the Regime1, τ_{12}, when varying the shearing plate thickness as described in Sec. 3.4.

Increasing the shearing plate thickness from e=0.08mm to e=0.45mm leads to same value of τ_{12}. The value of τ_{12}=5.6kPa depicted in the red curve of figure 4.25 being only lower by 6% of the measured values of the others τ_{12}=6kPa will not therefore affect our conculsions.

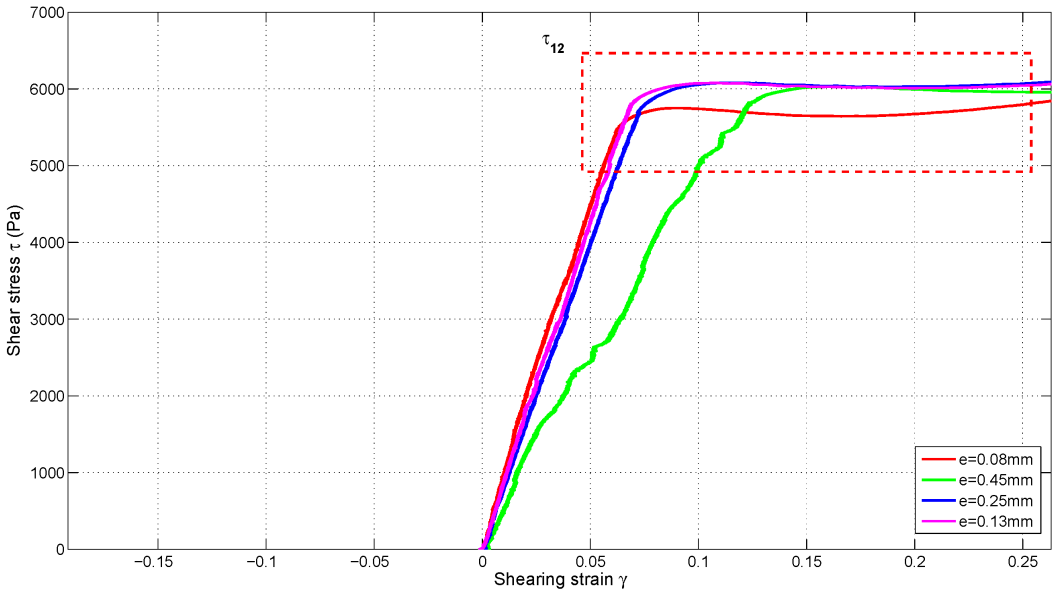

Figure 4.25 – Variation of τ_{12} with shearing plate thickness.

5 Conclusion

In the "initial shearing regime" the MRF deformation is reversible, the measured shear stress increases linearly with the shear strain until the MR fluid reaches a threshold stress τ_{12}. The elasticity of the MRF in this regime is quantified by the shear modulus K_1 and was found to be independent of the shearing rate $\dot{\gamma}$, plate shearing type and particle volume fraction ϕ (figure 4.15).

The shear modulus K_1 stays substantially constant as the value of the magnetic field B increases, whereas the value of the threshold stress τ_{12} increases with the square of the magnetic field B^2, the particle volume fraction ϕ.

The shear stress τ_{12} is found to be depended of the nature of the shearing plate $\tau_{12\,\mathrm{mag}} > \tau_{12\,\mathrm{amag}}$.

The variation of the initial MRF internal structure, from aggregates to isotropic suspension, did not have any notable effect on the MRF response to shear in Regime 1 shearing Sec. 2.

That K_1 does not depend on B nor on the initial configuration of the MRF particles, suggests that K_1 may correspond to a potential energy due to bounds between polymer chains attached to the surface of the particles.

Once the polymer bonds between MRF suspension planes are destroyed, the effect of the magnetic field B becomes dominant in the fluid internal structure and the MRF enters a new regime, Regime 2, where the magnetic field plays the main role. τ_{12} is the stress value separating these two different regimes.

Chapter 5

2. Intermediate shearing regime: Regime 2

Contents

1	**Microscopic observations**	**122**
2	**Shear modulus K_2**	**123**
3	**Interpretation**	**130**

A typical $\tau(\gamma)$ response is displayed in figure 5.1top. This chapter is devoted to the study of the windowed area presented in figure 5.1bottom. It looks like a pseudo plastic regime between the pseudo-elastic regime of initial shearing studied in Chap. 4and the sliding regime studied in Chap. 6. It was shown in Chap. 4 Sec 1 that this intermediate shearing regime is not reversible (figure 4.6 p. 103). However when the direction of shearing is reversed a succession of Initial-Intermediate and Sliding regimes is observed (figure 4.16 p. 110).

No mention of an intermediate shearing regime in the MRF response below the Bingham threshold is present in the literature studies. At the microscopic level, a chain bending was observed in this regime (§ 4 Chap. 3) as opposed to the chain titling in the initial shearing regime. This phenomenon is studied in § 1.

At the macroscopic level the MRF shearing stress τ (shearing force F) was found to vary with the shear strain γ (plate displacement u) as the following relation $\Delta(\tau) = K_2\gamma$. The slope K_2 is found to be depending on the square of the magnetic field B^2.

In our studies, the understanding of the MRF behavior in the second zone will be based on the internal structure modification the MRF passes through during shearing.

The mechanical behavior itself is discussed in later sections with an analysis of the dependency on the internal fluid structure, the magnetic field B, the shear rate dependency $\dot{\gamma}$, the particle volume fraction ϕ, the shearing plate thickness e, the nature and surface state of the shearing plate.

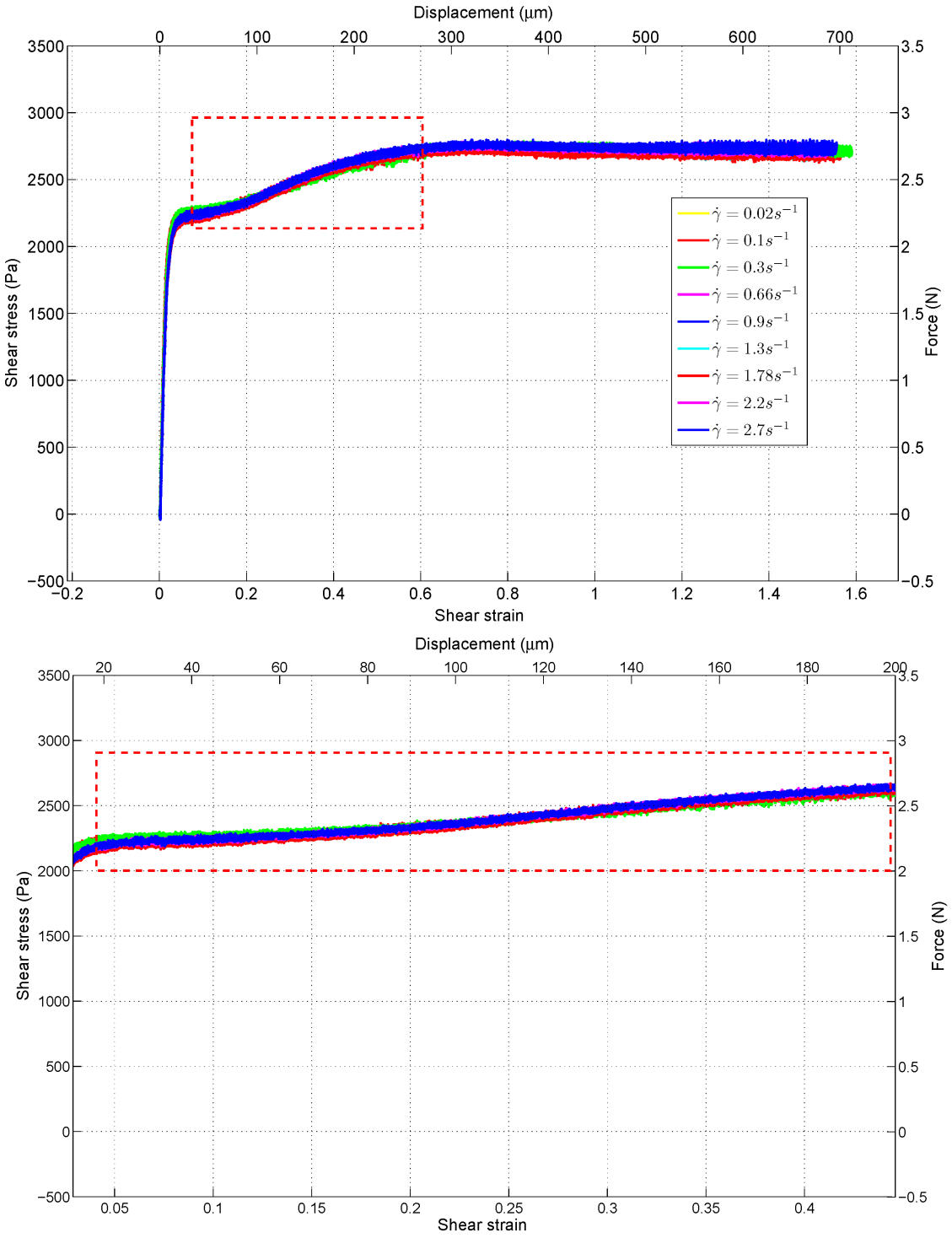

Figure 5.1 – Mean shear stress as a function of the mean shear strain (averaged over the fluid shearing gap g_f. Shearing with an amagnetic plate at different shearing velocity values (also indicated force and displacement). Top: total fluid response; bottom: highlight of MR fluid response in regime 2.

1 Microscopic observations

Figures 5.2 and 5.3 have been obtained by shearing the MRF with an amagnetic brass plate of thickness e=0.1mm moving at a velocity v=10μm/s as described in Sec. 2 in Chap. 4. The fluid used in these tests is the MRF-132 (Lord) with a particle volume fraction ϕ=32%. The magnetic field B is the same for both tests B=0.16T.

At the microscopic level the intermediate shearing regime is characterized by a chain-bending. This behavior is observed whether the shearing plate is magnetic or amagnetic. This chain-bending is also observed whether the fluid internal structure is well formed thick chains(figure 5.2) or thinner and denser chains (figure 5.3).

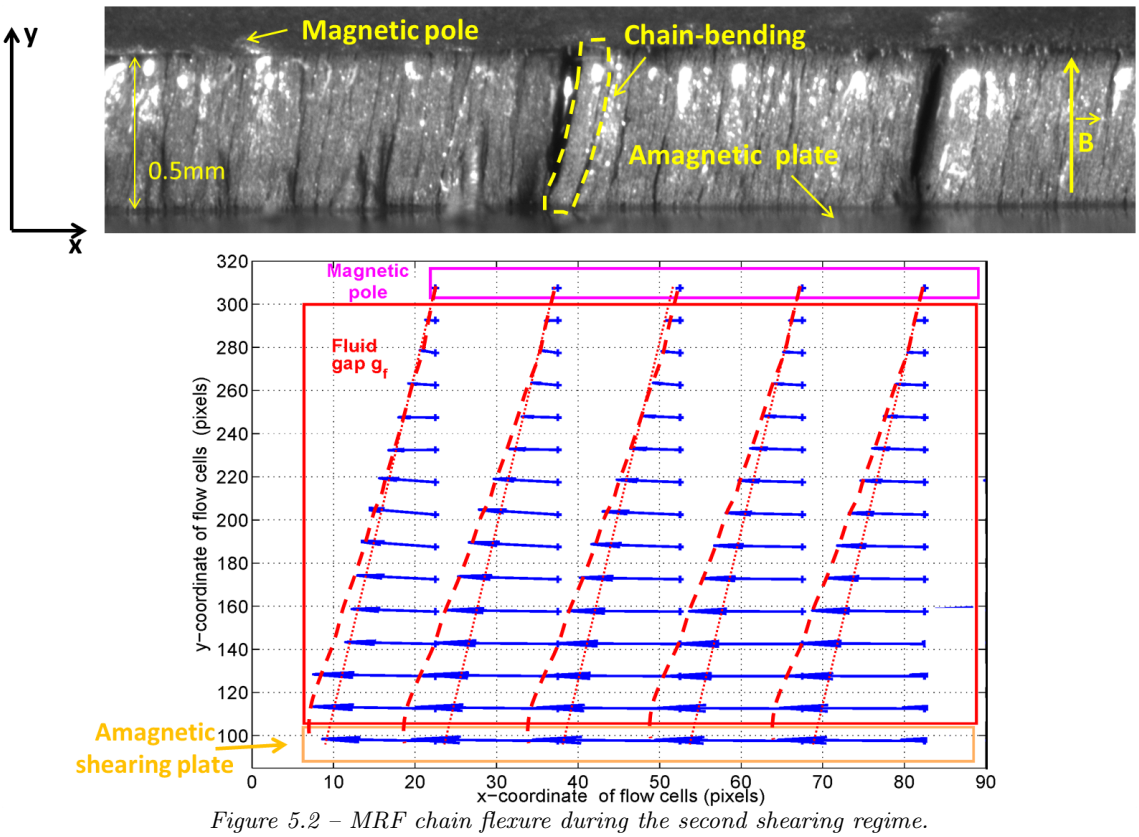

Figure 5.2 – MRF chain flexure during the second shearing regime.

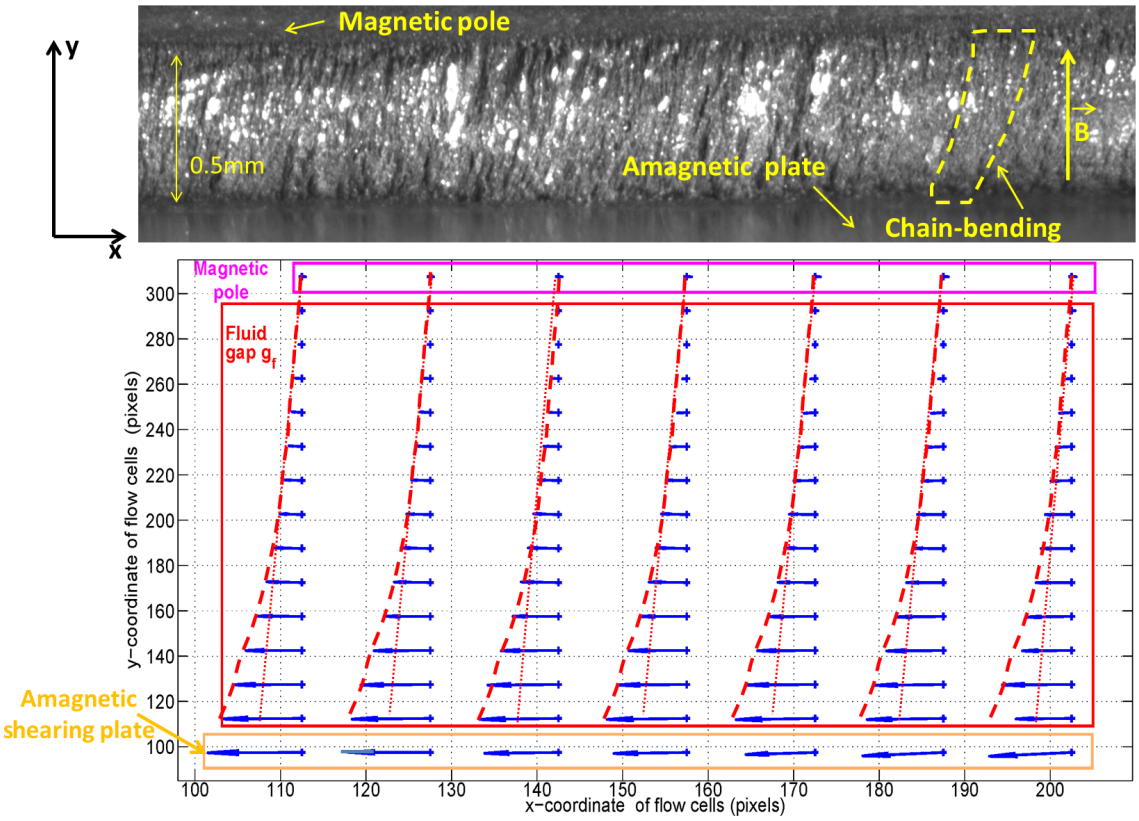

Figure 5.3 – MRF chain flexure during the second shearing regime.

Considering the chain as a material, it is shearing strain γ varies along the y direction, therefore we cannot attribute a shear-strain value to the whole fluid in this regime (idem for the shear stress). Thus, the mechanical observations that follow are presented in terms of the *average* shear strain and stress and alternatively in terms of force and displacement.

2 Shear modulus K_2

2.1 Internal fluid structure dependency

Figure 5.4 shows the comparison between the MRF response in the intermediate shearing regime, generated by the sequence of the two shearing tests with different internal structures as described in Sec 2 in Chap. 4. These results show that in both tests the fluid internal structure does not have a significant effect on the fluid mechanical response in this regime.

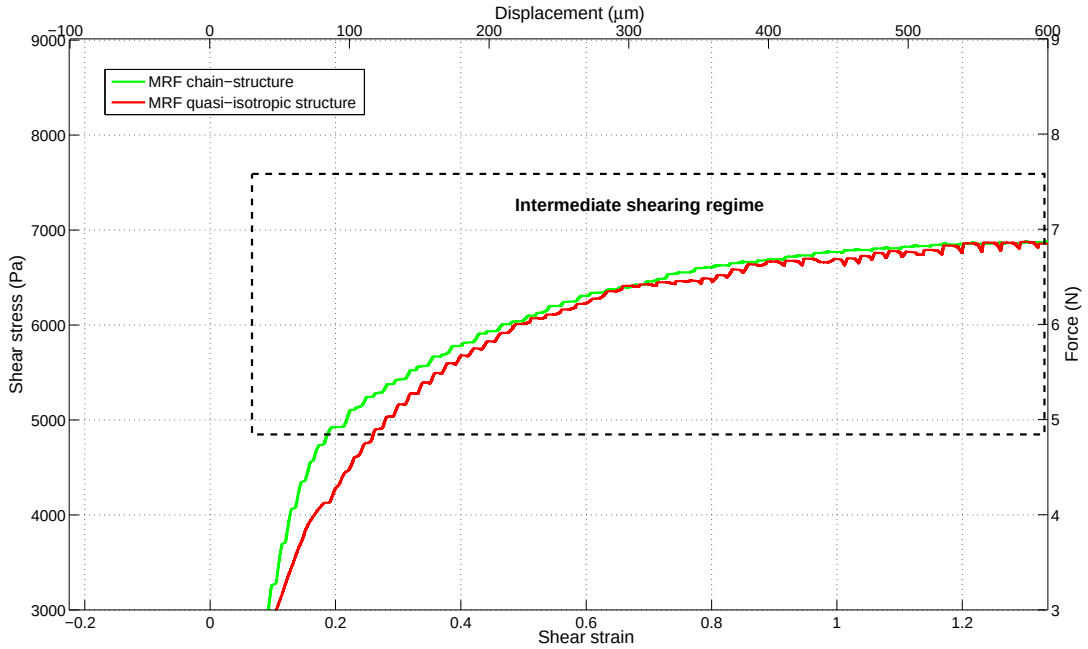

Figure 5.4 – Variation of the shear stress-strain $\tau(\gamma)$ (also presented force and displacement $F(u)$) with the MRF internal structure in the intermediate shearing regime.

2.2 Magnetic field dependency B

In the second regime, the variation of the MRF shearing force F is a linear function of the variation of the shearing plate displacement u. Figure 5.5 presents the values of K_2 obtained when the MRF-122 (Lord) is sheared with a brass amagnetic shearing plate of thickness e=0.1mm.

The shear coefficient K_2 is found to be proportional to B^2 for the three MRF volume fraction. The coefficient of proportionality is noted by S.

$$K_2 = S\,B^2 \tag{5.1}$$

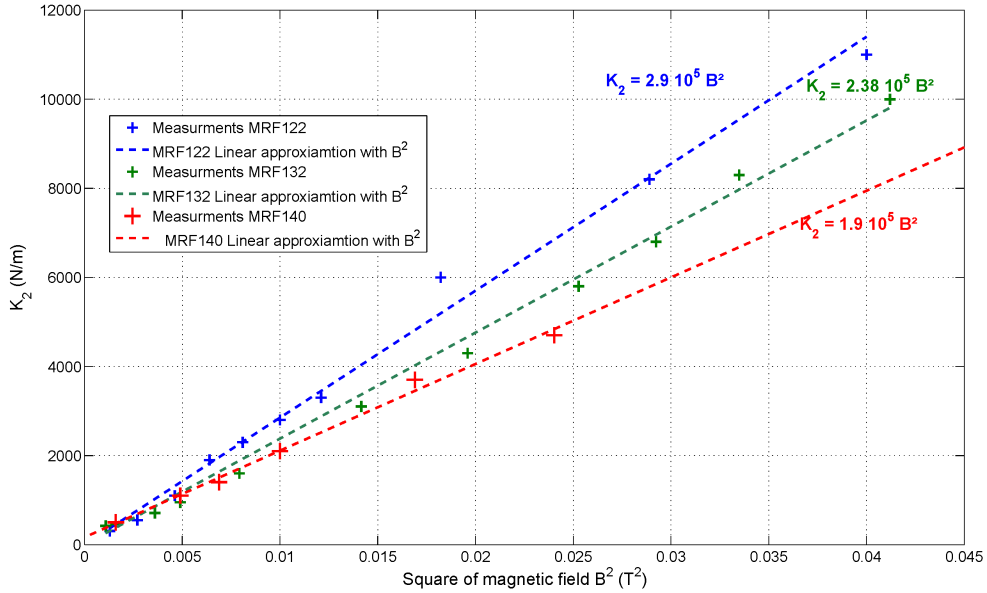

Figure 5.5 – Dependence of B^2 on the shearing stiffness K_2: MRF122EG (blue curves), MRF132DG (green curves) and MRF140CG (red curves).

2.3 Shearing rate dependency $\dot{\gamma}$

Figures 5.1 and 5.6 presents the stress-strain $\tau(\gamma)$(force-displacement F(u)) behavior in Regime2 for shear rates $\dot{\gamma}$ varying between $0.02\text{s}^{-1} < \dot{\gamma} < 2.7\text{s}^{-1}$ ($10\mu\text{m/s} < \text{V} < 1000\mu\text{m/s}$). Figure 5.1 shows the MRF behavior when sheared with an amagnetic shearing plate while in figure 5.6 the plate used is magnetic. The MRF particle volume fraction used in these tests is ϕ=22% and the value of the magnetic field is B=0.1T.

These results show that the MRF behavior in the intermediate shearing regime does not seem to depend on the imposed values of the shearing velocities.

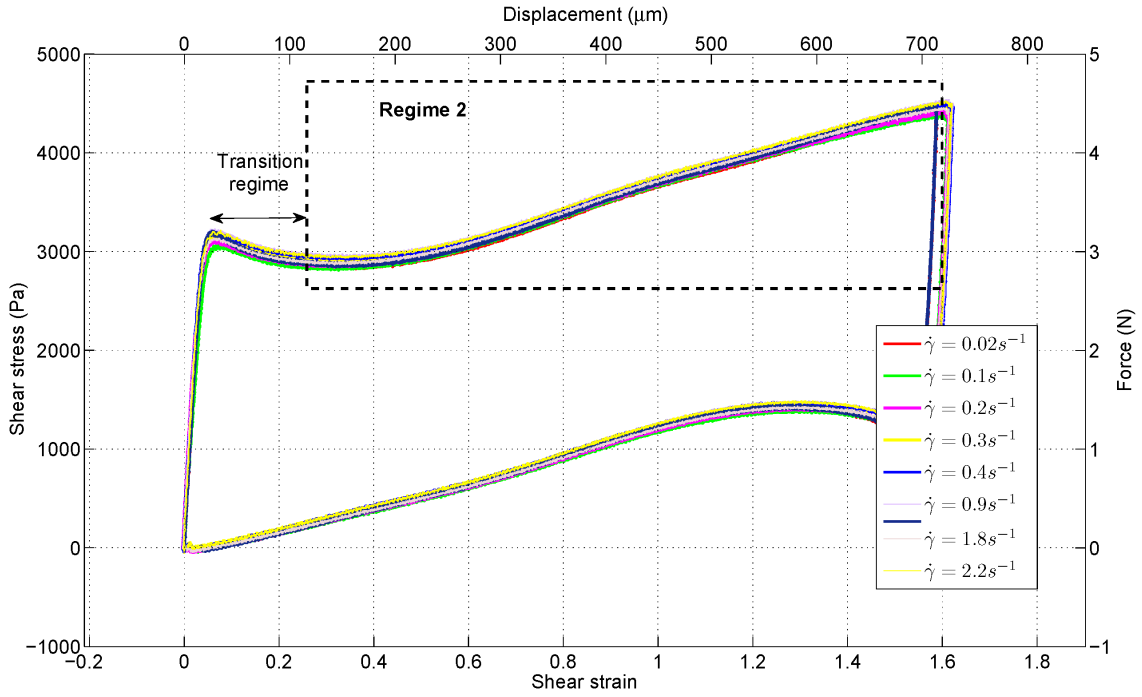

Figure 5.6 – Shear stress as function of the shear strain in case of shearing with a magnetic plate for different shearing velocities values.

2.4 Particle volume fraction dependency ϕ

The calculated shearing coefficients K_2, for the three tested MRF particle volume fraction ϕ=22%, 32%, and 40% are summarized in figure 5.5. The shear coefficient K_2 is given as the equation:

$$K_2 = S(\phi).B^2 \tag{5.2}$$

The shear modulus K_2 decreases with the increase of the MRF particle volume fraction ϕ. Figure 5.7 presents the variation of $S(\phi)$ with ϕ.

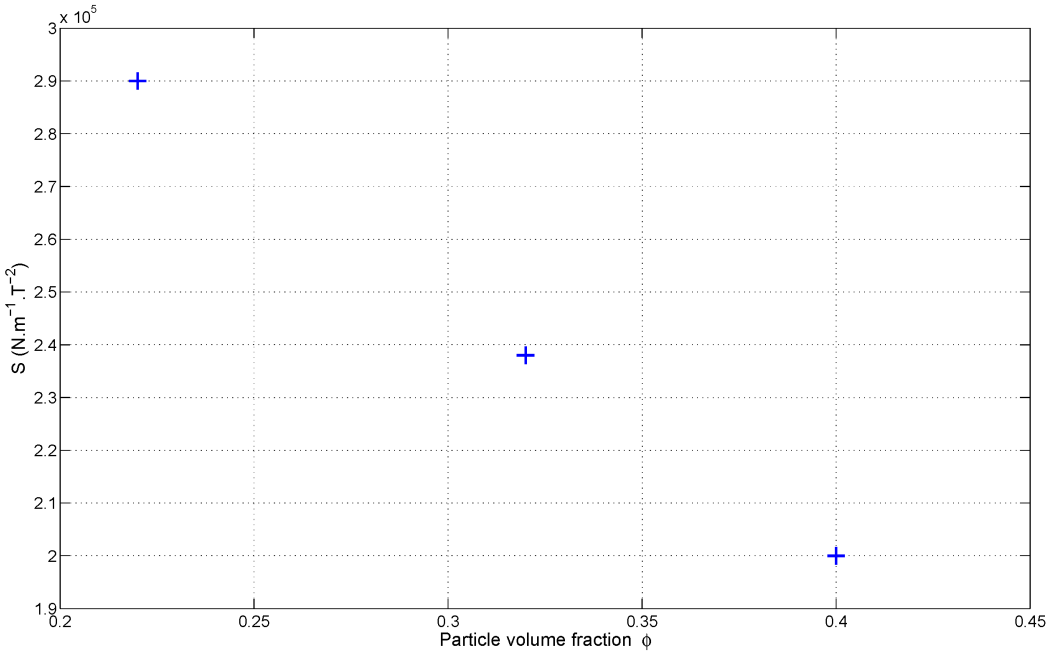

Figure 5.7 – Dependence of the particle volume fraction ϕ on the shearing stiffness K_2: MRF-122EG (blue curves), MRF-132DG (green curves) and MRF-140CG (red curves).

2.5 Shearing plate thickness dependency e

Figure 5.8 emphasizes the MRF response in the intermediate shearing regime, generated when shearing the MRF with four amagnetic shearing plate thicknesses as described in Sec. 3.4 in Chap. 4.

Figure 4.16 on page. 110 shows the total shearing cycles.

For the three plate thicknesses e=0.13, 0.25 and 0.45mm the fluid response to linear shearing $\tau(\gamma)$ $(F(u))$ is the same in this Regime. A variation on the shearing stiffness K_2 in the second zone is noticed when a brass plate of thickness e=0.08mm is used.

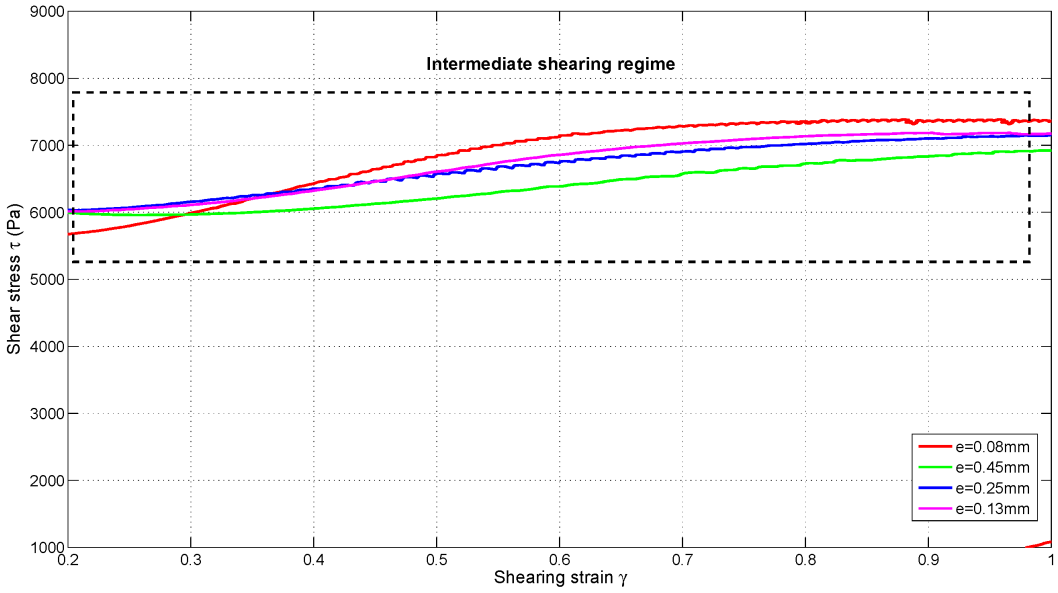

Figure 5.8 – Dependency of $\tau(\gamma)$ with shearing plate thickness in the intermediate shearing.

2.6 Influence of the nature and surface state of the shearing plate on K_2

Figure 5.9 shows the MRF shearing response in the intermediate shearing regime when a magnetic plate is used. One should notice that when the shearing plate used is magnetic, the intermediate shearing regime occurs for greater shearing displacement (figure 5.9) than when the shearing is done with an amagnetic plate (figure 5.1). The shearing plate thickness used in these tests is e=0.1mm and the fluid used is MRF-122 (Lord).

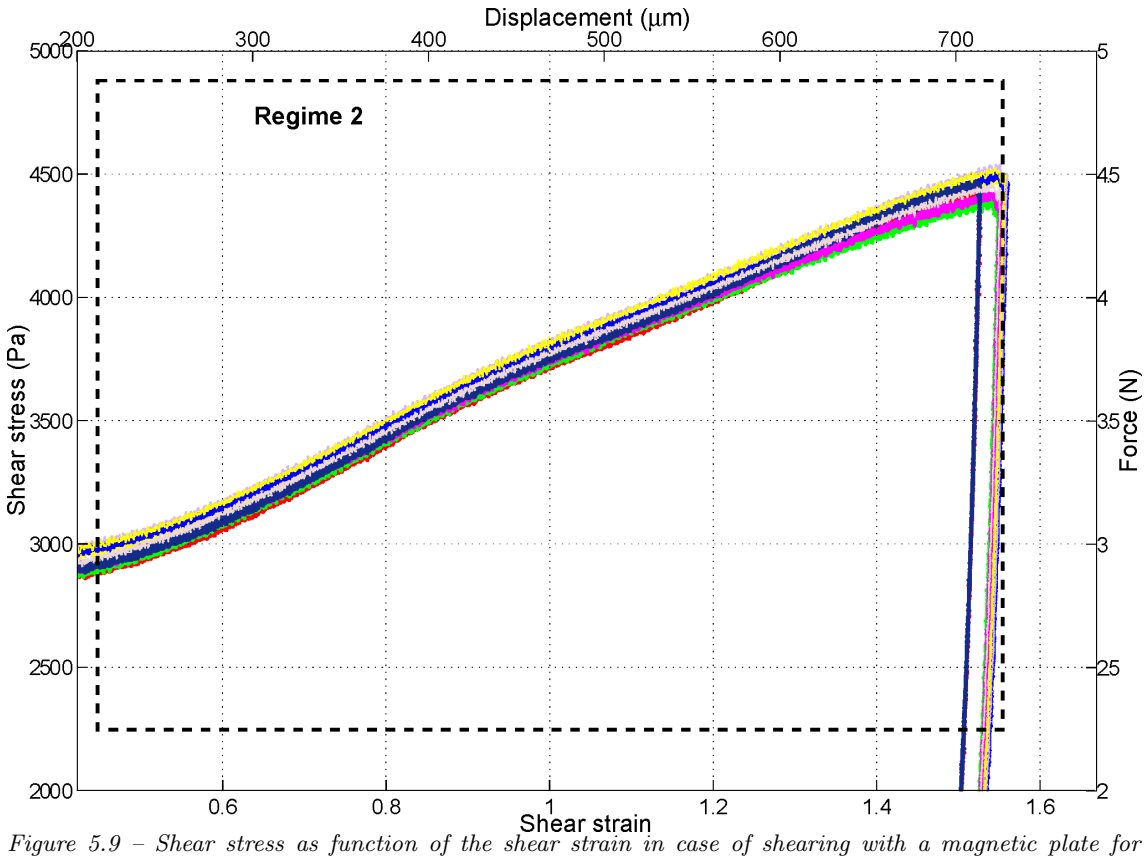

Figure 5.9 – Shear stress as function of the shear strain in case of shearing with a magnetic plate for different shearing velocities values.

However the experimental results presented in figure 5.10 show that the shearing coefficient K_2 does not undergo a significant variation when varying the magnetic properties of the shearing plate since the nature of the observed phenomenon (chain-bending), in both cases, is the same.

The evaluated relative error between the calculated values of K_2 for both shearing plate magnetic and non-magnetic (figure 5.10) is: $e_{K2}=\dfrac{2.9\,10^5 - 2.16\,10^5}{2.9\,10^5} = 0.25.$

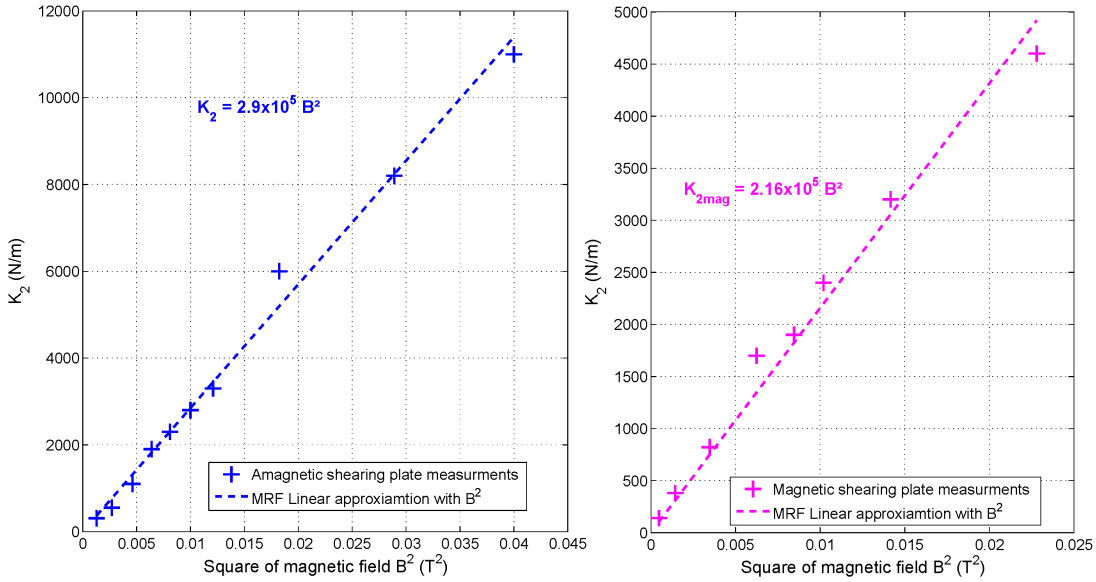

Figure 5.10 – Variation of the shearing stiffness K_2 with shearing plate nature.

3 Interpretation

Figure 5.11 presents a schematic representation of a MRF aggregate structure. l is the width of the aggregate, and g=R θ its length.

As an approximation for the shape of the aggregates, more or less consistent with the observations presented in Fig. 5.2 and 5.3, we consider a portion of circle.

For small shearing angles, θ is equal to:

$$\theta = \frac{u^2}{2\,g\,l} \tag{5.3}$$

The initial volume of the MRF aggregate is $\Sigma_{\text{cluster 0}} = g\,l\,H_{\text{cavity}}$. Due to the extension of the magnetic particles aggregates, the volume after chain flexure becomes $\Sigma_{\text{cluster f}} = \frac{\theta\,H_{\text{cavity}}}{2}(2\,R\,l + l^2)$ with $\Sigma_{\text{cluster f}} > \Sigma_{\text{cluster 0}}$. Hence the variation of the volume aggregates will be $\Delta\Sigma_{\text{cluster}} = \Sigma_{\text{cluster f}} - \Sigma_{\text{cluster 0}} = \frac{\theta\,l^2\,H_{\text{cavit}}}{2}$

Where H_{cavity} is the height of the magnetized MRF.

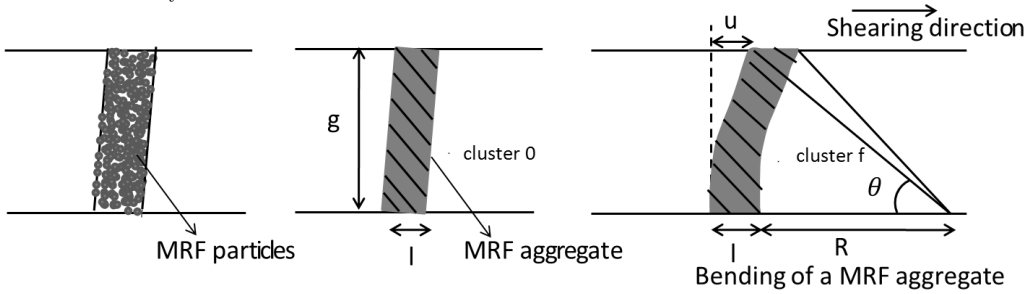

Figure 5.11 – MRF aggregates structure.

The resulting magnetic energy ΔE_{mag} will be therefore given by Eq 5.4:

$$\Delta E_{\text{mag}} = \frac{{B_{\text{cluster}}}^2}{2\,\mu_0}\Delta\Sigma\,N_{\text{cluster}} = \frac{K\,u^2}{2} \tag{5.4}$$

and therefore the final expression of $\Delta\Sigma_{\text{cluster}}$ will be:

$$\Delta\Sigma = \frac{u^2\, l}{4\, g} \tag{5.5}$$

Combining Eq: 5.4 and Eq: 5.5, the final theoretical expression of the shearing stiffness K_2 will be:

$$K_2 = \frac{B^2}{\mu_0 \phi} \frac{H_{\text{cavity}}\, L_{\text{cavity}}}{4\, g} \tag{5.6}$$

L_{cavity} is the width of the magnetic surface.

The theoretical shearing coefficients ratios for the different tested fluid concentration are $\frac{K_{22\text{vol}\%}}{K_{32\text{vol}\%}} = \frac{\phi_{32\text{vol}\%}}{\phi_{22\text{vol}\%}} = 1.45$ and $\frac{K_{32\text{vol}\%}}{K_{40\text{vol}\%}} = \frac{\phi_{32\text{vol}\%}}{\phi_{40\text{vol}\%}} = 1.25$.

The experimental calculated ratios are: $\frac{K_{2\,22\text{vol}\%}}{K_{2\,32\text{vol}\%}} = 1.22$; $\frac{K_{2\,32\text{vol}\%}}{K_{2\,40\text{vol}\%}} = 1.25$; the calcuted deviation between experimental and theoretical ratios values are $e_{32\%\,22\%} = \frac{1.22 - 1.45}{1.22} = 0.15$ and $e_{32\%\,40\%} = \frac{1.25 - 1.25}{1.25} = 0$.

Figure 5.12 presents a xy plot of $K_{2\ \text{measured}}$ as function of $K_{2\ \text{calculated}}$ from equation 5.6.

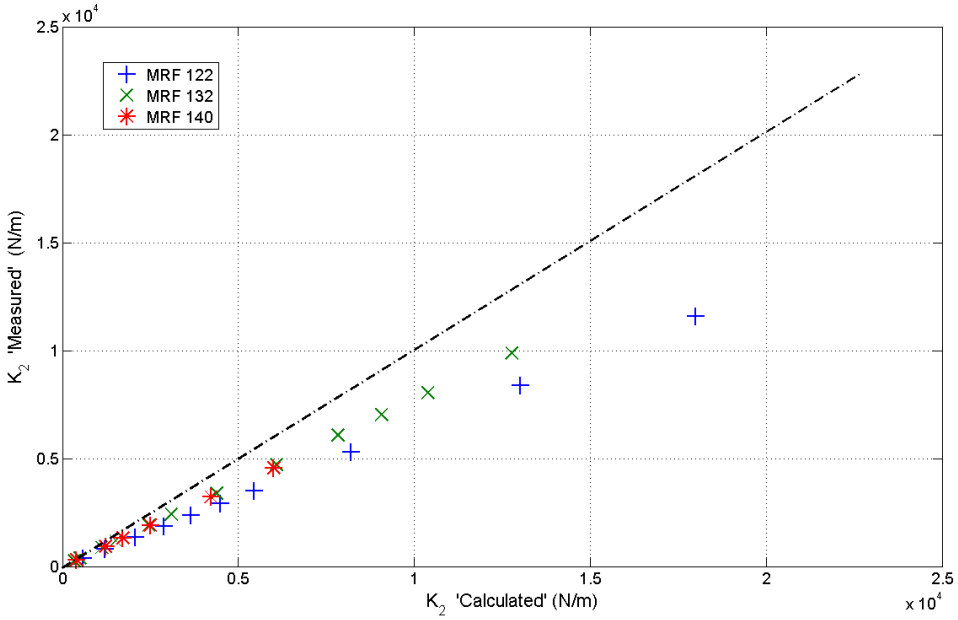

Figure 5.12 – $K_{2\ measured}$ as function of $K_{2\ calculated}$

Table 5.1 compares between the measured and the estimated values of the coefficient S(ϕ).

ϕ: particle volume fraction	S(ϕ)$_{\text{calculated}}$	S(ϕ)$_{\text{measured}}$
0.22	$4.5\,10^5$	$2.9\,10^5$
0.32	$3.1\,10^5$	$2.4\,10^5$
0.4	$2.5\,10^5$	$1.9\,10^5$

Table 5.1 – Comparison between the measured and the estimated values of S(ϕ).

It should be noted that what precedes is not a model for Regime 2 since the shape of the aggregates is chosen according to the observation. This simply shows that K_2 has a clear magnetic origin.

We also notice that, within this frame, γ is not constant along the aggregate only *average* shear stress τ and shear strain γ have been evaluated in this section.

Chapter 6

3. Sliding regime: Regime 3

Contents

1	**Maximum measured force F_{23}**	**134**
2	**Discussion**	**142**
3	**Comparison between Lord datas and my experiments**	**142**
4	**Interpretation and modelisation**	**144**
5	**Conclusion**	**147**

A typical $\tau(\gamma)$ or $F(u)$ response is displayed in figure 4.2 in Chap. 4. This chapter is devoted to the study of the MRF response zone noted by Regime3 or sliding shearing regime.

The sliding shearing regime is characterized by a constant shear force $F(u)$=F_{23}=cte. The apparent shear stress in this regime will be noted by τ_{23} whether this quantity represents a shear stress in the MRF or at the fluid-slider interface as discussed later in this chapter. When the direction of shearing is reversed a succession of Initial-Intermediate and sliding regimes is observed (figure 4.16).

The microscopic observations presented in Sec. 4.2 in Chap. 3 show that, during shearing, the internal fluid structure is not modified by the motion of the plate (magnetic or non-magnetic).

It was also found that the shearing velocity has no effect on the value of τ_{23} (figure 6.7) and that τ_{23} increases with the particle volume fraction ϕ (figure 6.8). τ_{23} is also found to be proportional to B^2.

This regime is identified as a sliding regime: phenomena are localized at particular locations essentially at the surface of the magnetic pole (when the shearing is done by a magnetic plate) or of the plate (when the shearing is done by a non-magnetic plate). Since it does not seem that the fluid state is homogeneous, therefore when explaining and modeling my experimental results I will be talking about shearing forces F_{23} and displacement u rather than shearing stress τ_{23} and strain γ.

The dependency of the sliding regime on the internal fluid structure, on the magnetic field B, on the shear rate dependency $\dot{\gamma}$, on the particle volume fraction ϕ, on the shearing plate thickness e, and on the nature and surface state of the shearing plate will be discussed in the following sections.

1 Maximum measured force F_{23}

1.1 Internal fluid structure dependency

Figure 6.1 shows the comparison between the MRF response in Regime3 as generated by the two shearing tests with different internal initial structures of the MRF, as described at Sec 2 in Chap. 4: quasi isotropic or organized in aggregates. These results show that the fluid internal structure does not have a significant effect on the fluid mechanical response in this regime;the measured value of F_{23} is the same ($F_{23}\cong$7 N) whether the fluid internal structure is chain-like or quasi-isotropic.

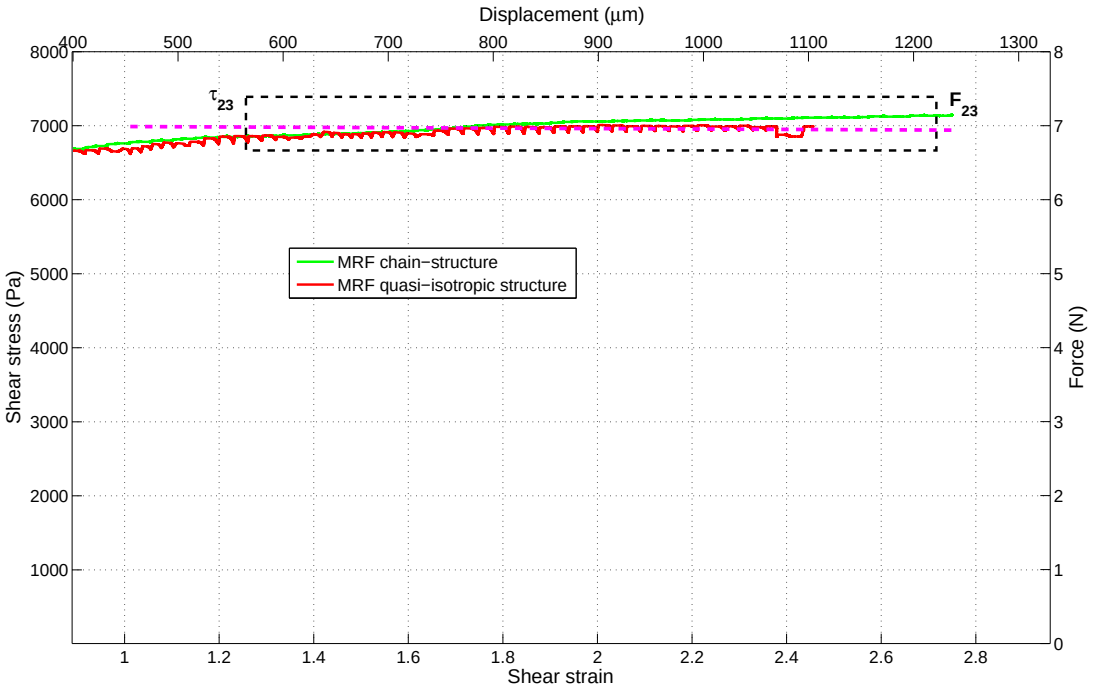

Figure 6.1 – Variation of the shear stress-strain $\tau(\gamma)$ (also presented force and displacement $F(u)$) with the MRF internal structure in the sliding shearing regime.

Figure 6.2 shows that the internal MRF structure did not have any effect on the nature of the observed fluid-plate interfacial shearing. A loss of adhesion between the MRF structure and the shearing plate takes place in Regime3; the tracking of points U_{to} and U_{t1}, for both MRF internal structure (MRF aggregates and quasi-isotropic), proves that while the MRF is being stationary the shearing plate continues its horizontal translation.

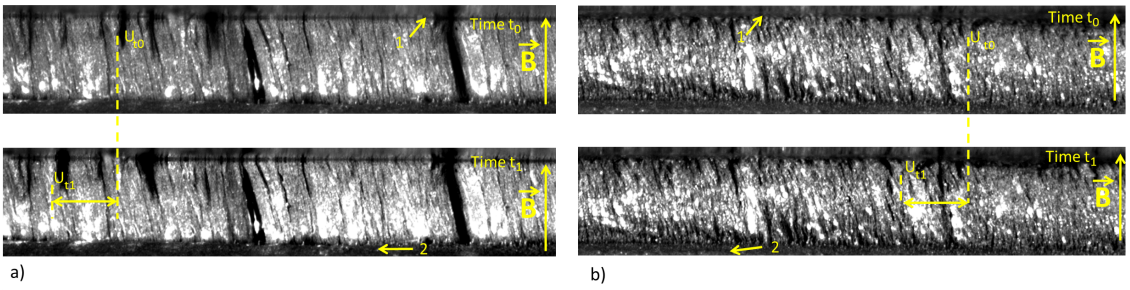

Figure 6.2 – Sliding of the non-magnetic shearing plate over the MRF. a) Organized MRF structure in aggregates; b) quasi-isotropic MRF structure.

The shearing velocity in these tests is v=10μm/s and the shearing plate used is non-magnetic. No similar tests with a magnetic plate were done whereas the similar MRF response to shearing carried out by a magnetic plate, for the same value of magnetic field B but on different days, suggests also an independence between the internal structure of the MRF and its shearing response. Figure 6.3 illustrates this result. the shearing velocity in these tests is v=10μm/s and the value of the magnetic field is B=0.1T.

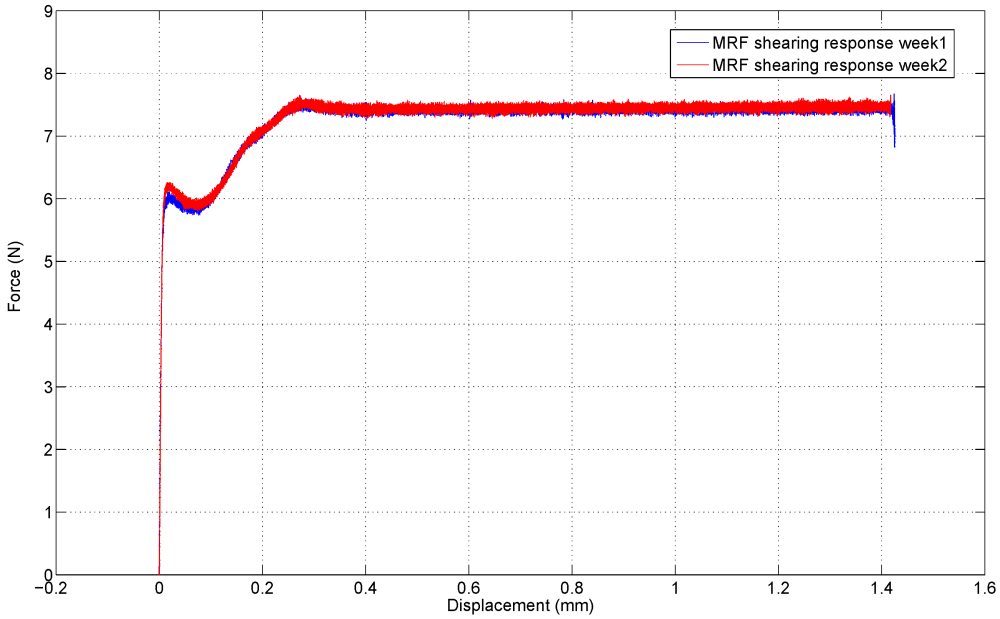

Figure 6.3 – MRF shearing response with a magnetic plate at two different experimenting dates.

1.2 Magnetic field dependency B

Figure 6.4 shows how the maximum shear stress τ_{23} (force F_{23}), in the loss of adhesion regime, varies with the square magnetic field for three different fluid concentrations (MRF-122 132 and 140). The shearing plate is non-magnetic and the shearing velocity is v=10μm/s.

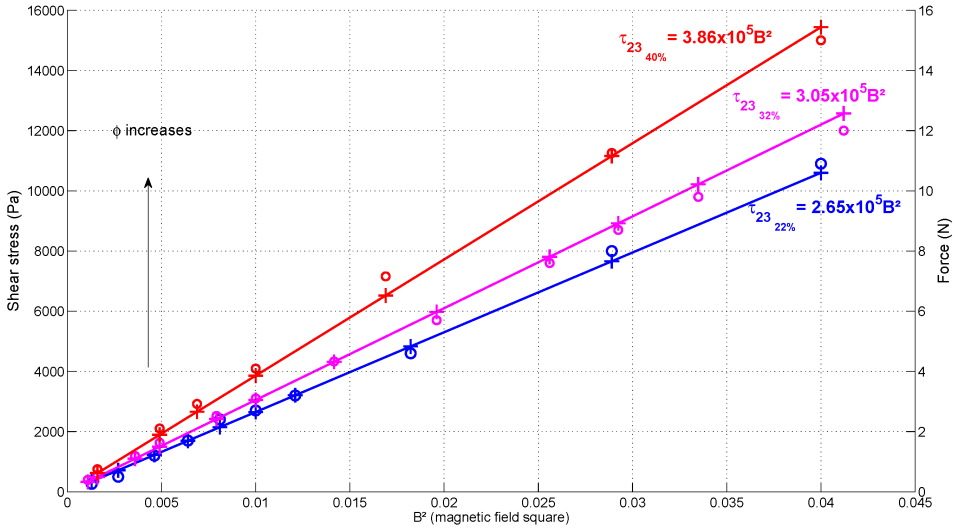

Figure 6.4 – Variation of the τ_{23} as a function of B^2 for different MRF particle volume fractions. Blue: ϕ=0.22. Magenta: ϕ=0.32. Red: ϕ=0.4. Shearing with an non-magnetic shearing plate (the corresponding forces also indicated).

When a magnetic plate is used for shearing, the measured values of τ_{23} are also found to increase with the square of magnetic field B^2. MRF-122 from Lord was used in these tests and the shearing velocity was v=10μm/s.

We call ζ the coefficient of proportionality between the measured force and the square of magnetic field in the third regime. The dependency of ζ on ϕ is analyzed in the §1.4.

$$F(u) = \zeta\, B^2 \tag{6.1}$$

The dependency of ζ with the nature and surface aspect of the plate is analyzed in §1.6.

Figure 6.5 presents the variation of τ_{23} with the square of the magnetic field H^2. It is clear that the τ_{23} increases with the square of the magnetic field H as presented in the physical models of the literature Sec 4.2 in Chap. 1.

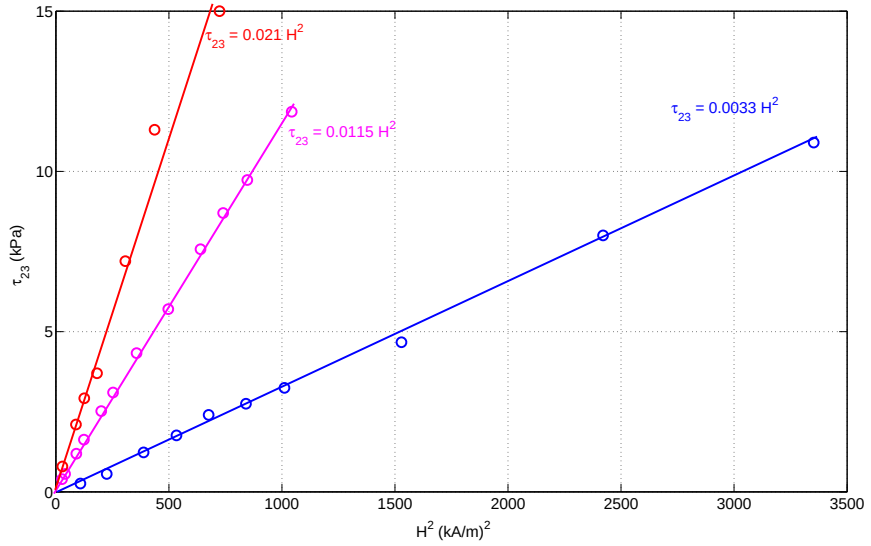

Figure 6.5 – Variation of the maximum shear stress as function of the square of the applied magnetic field H^2 with MRF particle volume fraction : blue curves: ϕ=0.22; magenta curves: ϕ=0.32; red curves: ϕ=0.4 when shearing with an amagnetic shearing plate.

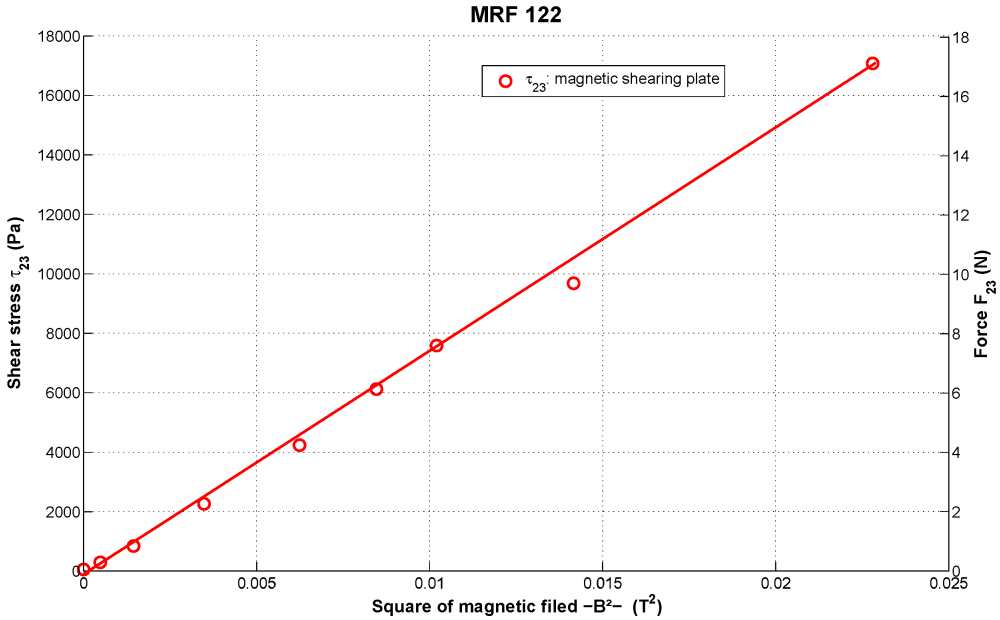

Figure 6.6 – Variation of τ_{23} as function of the square of the applied magnetic induction B^2 when shearing MRF-122 with a magnetic shearing plate.

1.3 Shearing rate dependency $\dot{\gamma}$

Shearing stresses (forces) of the MRF have been investigated at different shearing rate values ranging between $0.02s^{-1} < \dot{\gamma} < 2.7s^{-1}$(velocity 10μm/s< V< 1000μm/s). A brass shearing plate with a thickness e=0.1mm is used in the series of tests presented in figure 6.7 and MRF-122 is the fluid tested. These measurements show clearly that the shearing rate (shearing velocity) does not have any notable effect on the reached values of the maximum measured stress τ_{23} (F_{23}).

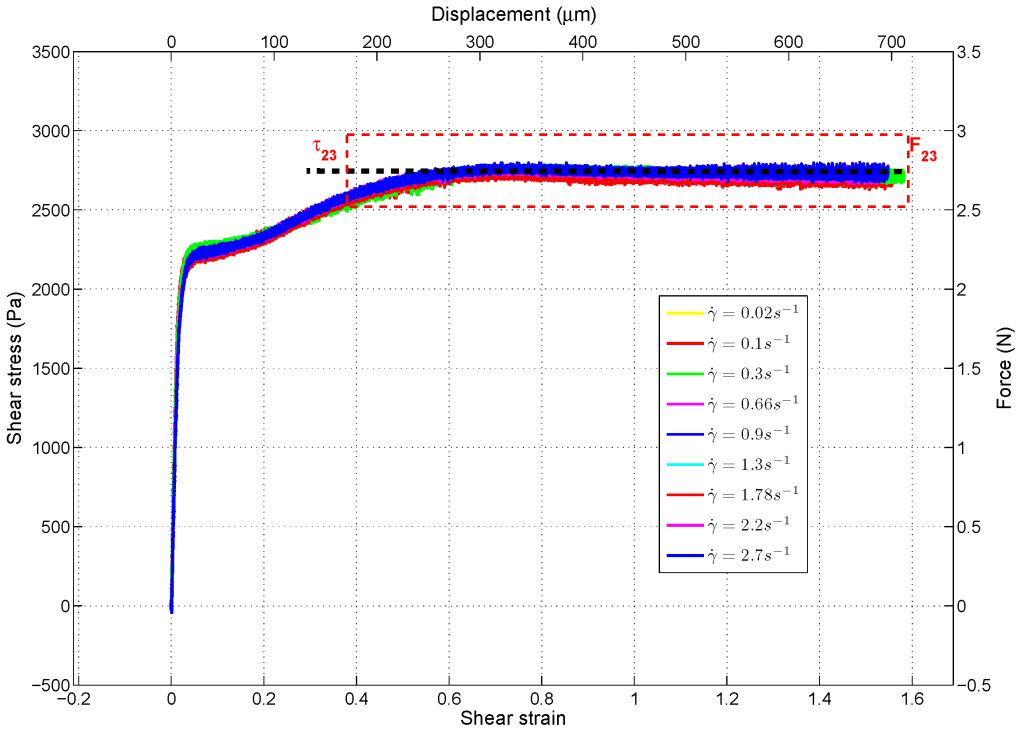

Figure 6.7 – Shear stress τ_{23} as function of the shear strain γ at different shearing rates $\dot{\gamma}$ (also indicated force F_{23} and shearing plate displacement).

1.4 Particle volume fraction dependency ϕ

The dependency of the coefficient ζ (Sec 1.2) with the particle volume fractions ϕ is presented in figure 6.8(ϕ=22%, 32% and 40 %). An increase in particle volume fraction induces an increase in the shearing force (figure 6.8). These tests are done with an amagnetic brass plate with thickness e=0.1mm. These results are consistent with the literature conclusions presented in Sec 4.2 in Chap. 1 depicting an increase in the measured stress with the MRF particle volume fraction.

A linear dependency between ζ and ϕ can only be conjectured at this point due to scarcity of experimental points.

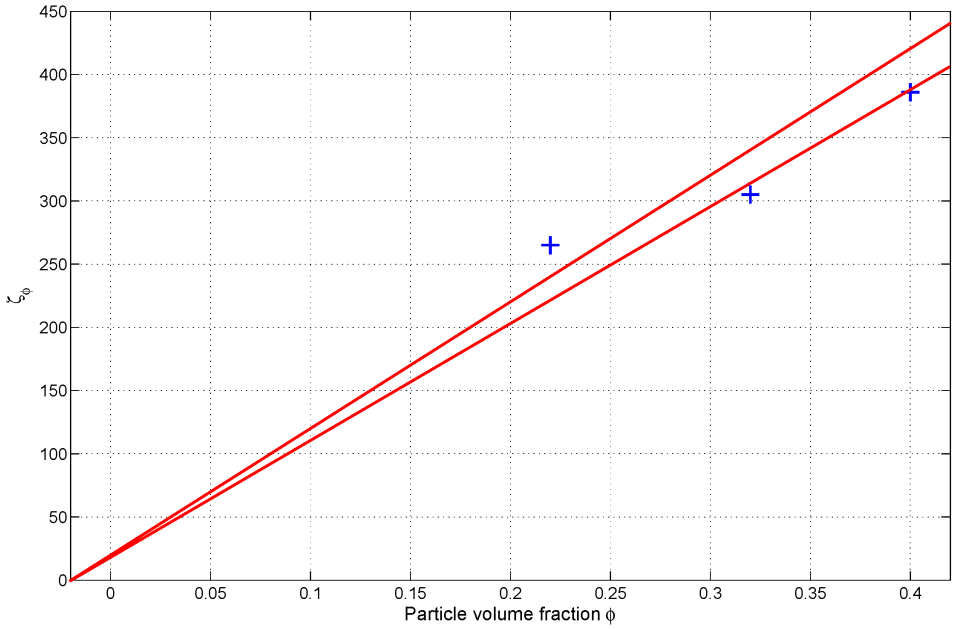

Figure 6.8 – Dependence of the maximum force measured F_{23} on the particle volume fraction ϕ.

1.5 Shearing plate thickness dependency e

Figure 6.9 emphasizes the MRF response in the sliding shearing regime, generated when shearing the MRF with four amagnetic shearing plate thicknesses as described in Sec. 3.4 of Chap. 4. Figure 4.16 in Chap. 4 shows the total MRF response including the three shearing regimes. The deviation between the measured values of F_{23} when varying the plate thickness e from e=0.08mm to e=0.45mm is 2%. The variation of the shearing plate thickness seems not to affect the MRF response F_{23}.

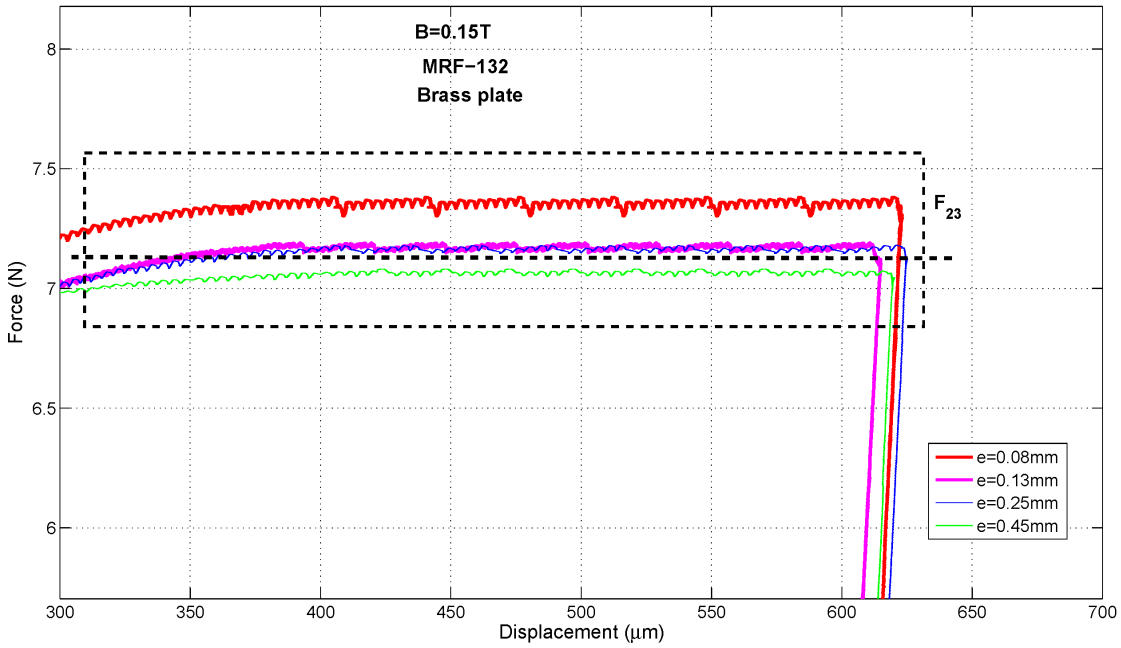

Figure 6.9 – Dependency of F_{23} with shearing plate thickness in the sliding shearing regime.

1.6 Influence of the nature and surface state of the shearing plate on F_{23}

Figure 6.10 shows that the measured stress τ_{23} is larger when the shearing plate used is magnetic. Figure 3.20 shows that for the magnetic plate the third regime, regime 3 occurs at a larger shear strain (shearing displacement) than with the non-magnetic plate. For this experiment, the LVDT (having a measuring range less than the acquired displacement) was replaced by the laser displacement sensor (Keyence LB-12).

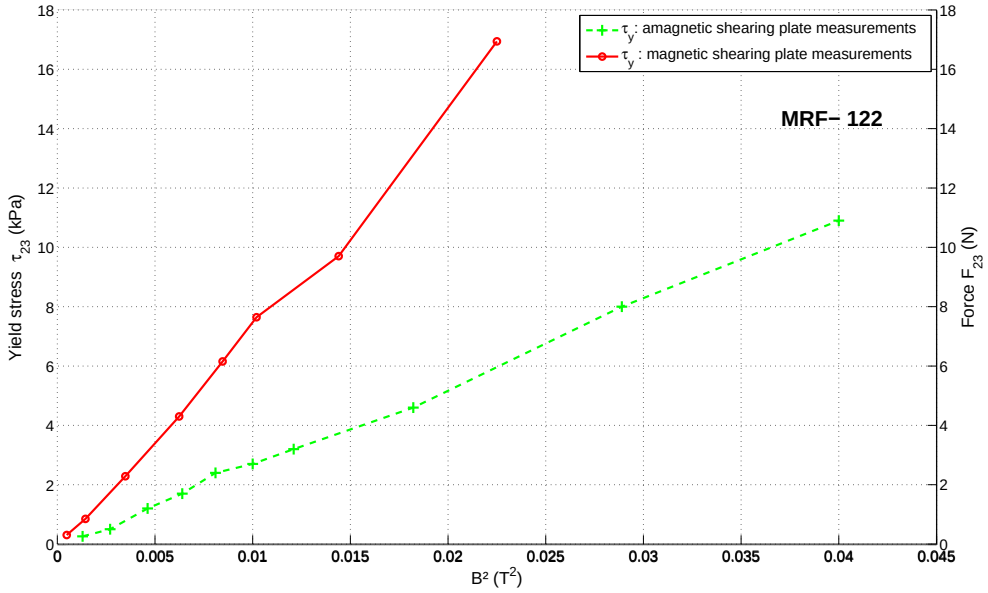

Figure 6.10 – Comparison between the maximum shear stress τ_{23} in case of shearing with a magnetic and a non-magnetic brass plate (also indicated: force F_{23}).

The $F{=}\zeta\, B^2$ law is kept, in case of shearing with both magnetic and non-magnetic plate, but the ζ value is not the same.

Measurements done with three types of amagnetic plate: aluminum, brass and glass plates are presented in figure 6.11. We notice that the value of F_{23} is the same whether the non-magnetic plate used is brass or aluminum, but is greater than the force reached with a glass plate. The reproducibility of these tests is insured by alternating the types of amagnetic shearing plates while experimenting.

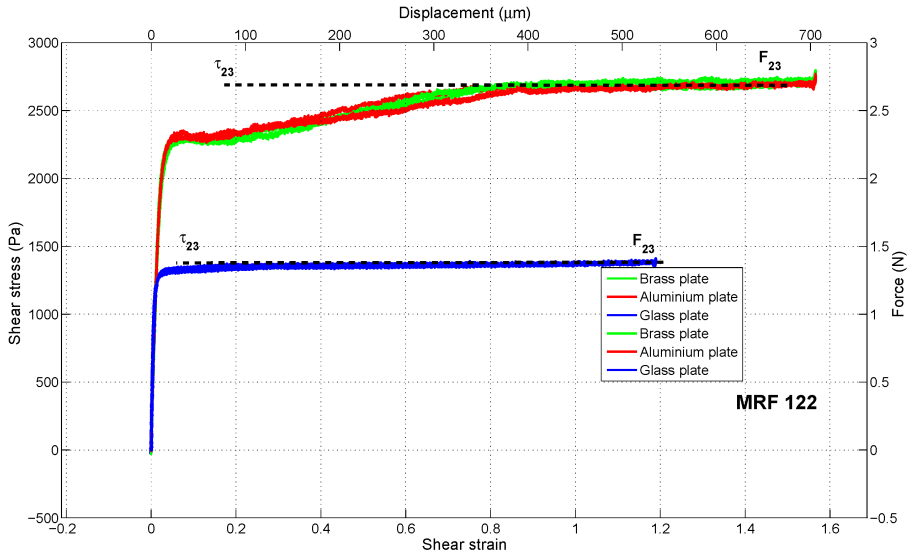

Figure 6.11 – Maximum shear stress as function of shear strain in case of shearing with three different types of amagnetic plates: blue curves: glass plate; green curves: brass plate; red curves: aluminum plate (also indicated: force and shearing plate displacement).

2 Discussion

One may wonder whether τ_{23} corresponds or not to τ_y, the yield stress on which much published researches has been devoted.

The yield stress is defined as the threshold value τ_y of that stress the MRF reaches at a null shear rate $\dot{\gamma}$=0 (figure 1). τ_y is presented as an intrinsic property of the MRF, it is widely used for modeling the MRF behavior and is regarded as an indicator of the MRF efficiency. Numerous experiments show that the measured τ_y is highly depended on the surface topography(Sec. 4.2 in Chap. 1).

2.1 MRF yield stress literature review

In this section, I present a summary of the experimental results of τ_y presented in the literature. Figure 6.12 shows a log-log representation of τ_y versus magnetic field B obtained when shearing the MRF with a particle volume fraction of ϕ=32%. Each curve color in figure 6.12, correponds to a different research experiment.

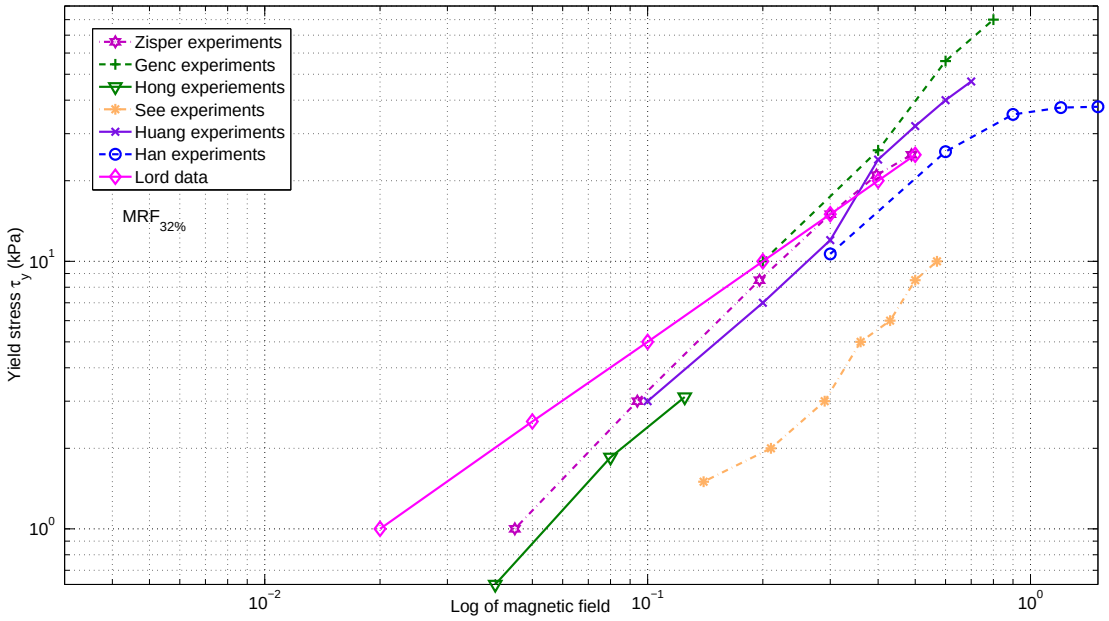

Figure 6.12 – Log-log presentation of yield stress as function of the square of magnetic field B^2 for MRF132DG: comparison between different experimental measurements.

Figure 1.26 presents the values of the measured MRF-132 yield stress τ_y resulting when varying the roughness of the shearing surface for the same value of magnetic field.

From above one should notice that the measured values of the yield stress vary between the different authors. As it was presented at Sec. 4.2 in Chap. 1, the values of the yield stress is also depended on the shearing wall surface [24, 46, 54, 33]. Also it was found that the increase of particle volume fraction ϕ and the particle diameter a leads to a greater yield stress.

The problematic arising from above experiments, is that what is presented in the literature is the yielding behavior of the MRF or the sliding regime of the MRF and the shearing plate?

3 Comparison between Lord datas and my experiments

Figure 6.13 shows that the measured values of τ_{23} for MRF-122 132 and 140 are less than their corresponding estimated values of τ_y proposed by the Lord data sheet when a non-magnetic shearing plate was used in my experiments. The values of τ_y from Lord are computed as following: once the magnetic field B is measured, the values of the magnetic field H are generated form Lord

data sheet figure 1.30 and therefore the corresponding values of τ_y are generated from figure 1.29 on page . 31.

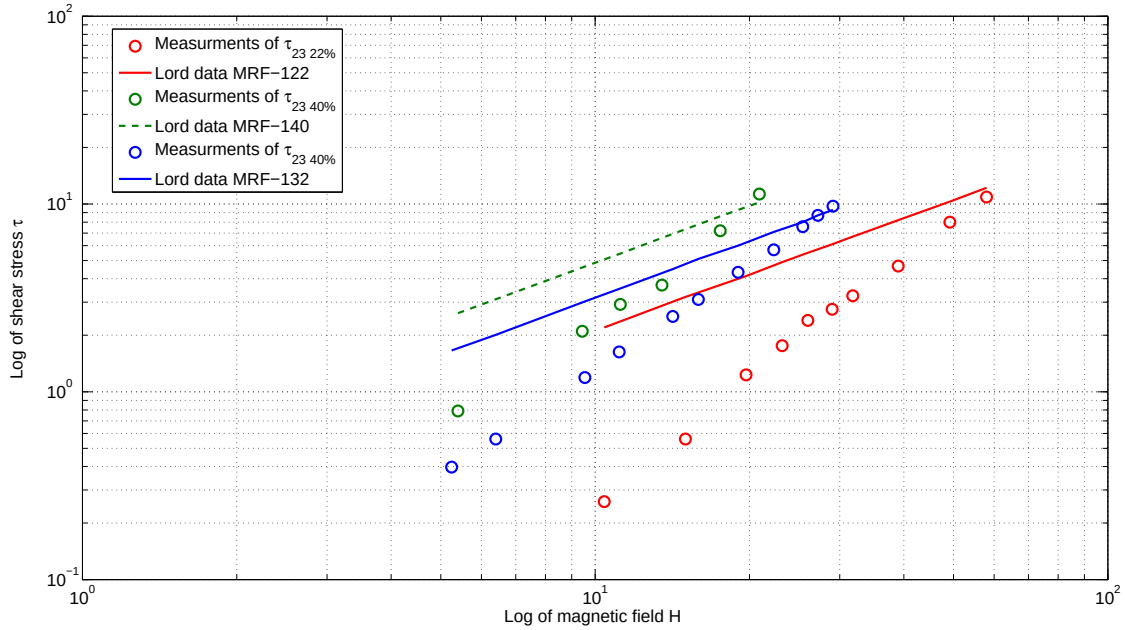

Figure 6.13 – Comparison between measured τ_{23} and τ_y computed from Lord data sheets when shearing with a non magnetic brass plate for the MRF-122 132 and 140.

The measured values of τ_{23} in case of shearing with a magnetic plate are larger than the values computed by the Lord data sheet (figure 6.14). The fluid used in these experiments is the MRF-122. This result is puzzling since τ_y should correspond to the maximum admissible stress.

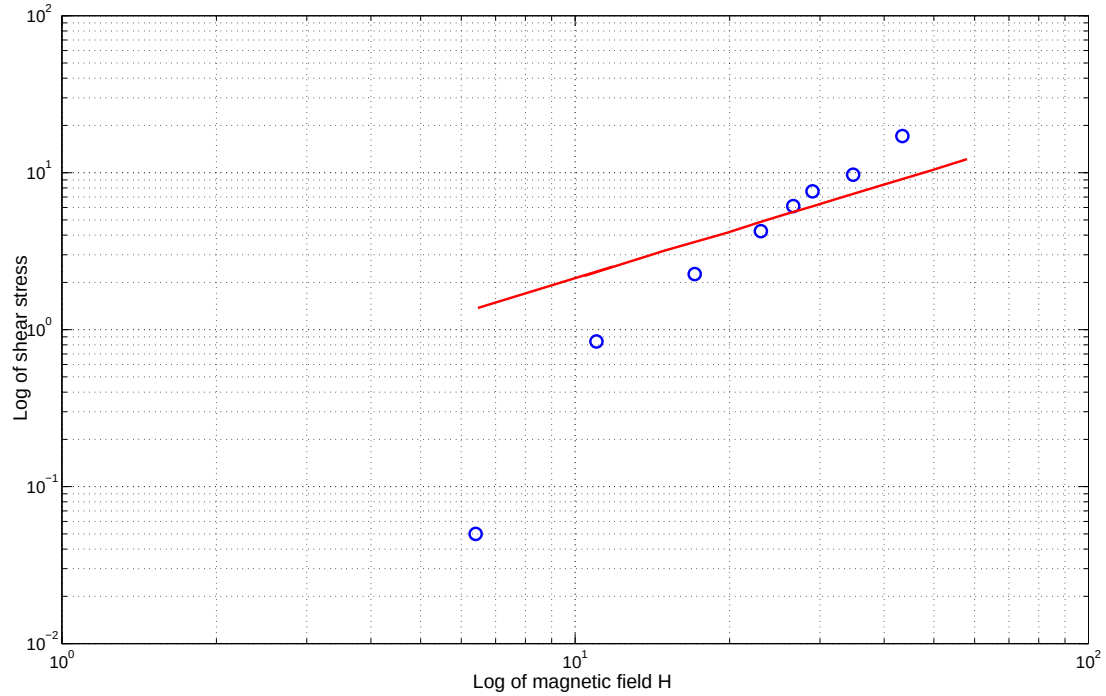

Figure 6.14 – Comparison between measured τ_{23} and τ_y computed from lord data sheets when shearing with a magnetic plate for the MRF-122.

The microscopic observation of the MRF shearing with a magnetic plate exhibits a variation

on the shearing plate positions at the starting of the shearing phenomenon Time t_0 (figure 6.15 left), the position of the magnetic shearing plate in the rest of the shearing process is depicted in figure 6.15 right. If the magnetic shearing plate is not originally centered, the magnetic forces tend to bring the shearing plate back to the middle plane. In such case, the MRF may be subject to a squeeze phenomenon.

Therefore, I suggest that the apparently too large values of τ_{23}, in case of shearing with a magnetic plate, may originate from the squeeze-strengthen effect described in the literature: under compression, the particle chains are bent and the attraction between chains becomes stronger. [54, 20, 41, 47, 50].

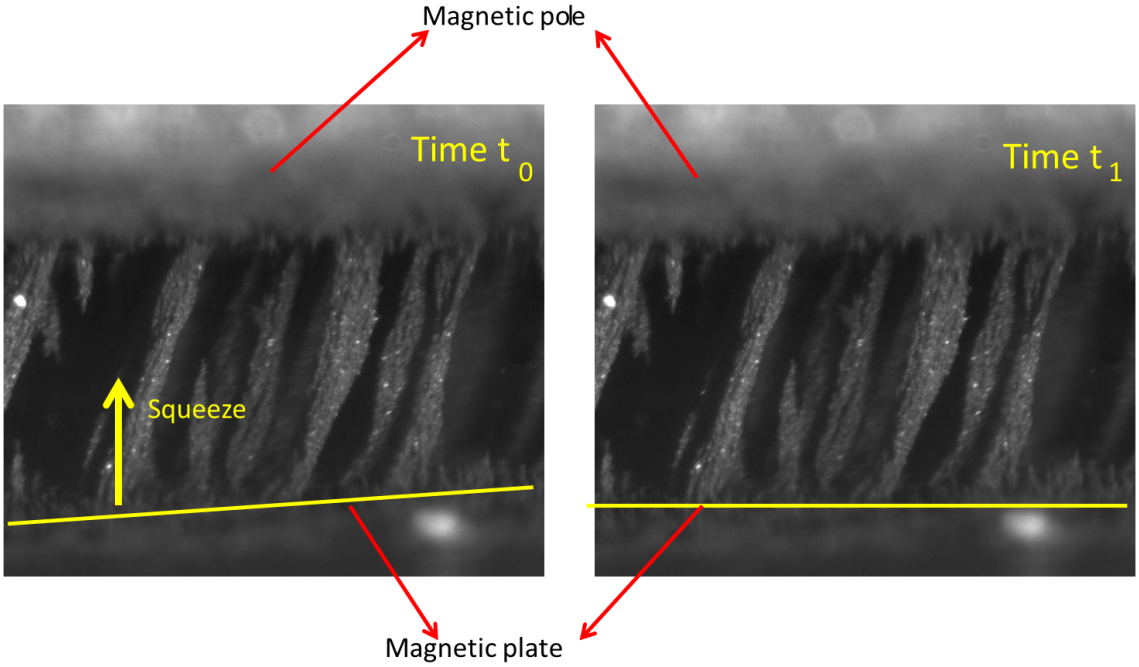

Figure 6.15 – Magnetic shearing plate position at the begening of MRF shearing.

4 Interpretation and modelisation

The optical microscopic observations show that the shearing plate is sliding across the MRF surface (Sec. 4.2 in Chap. 3). The value of the force resulting from sliding was found to be depending on the shearing plate material (Sec 1.6): the forces generated when a magnetic plate is used for shearing are larger than those resulting with an amagnetic shearing plate(figure 6.10), while the change in the amagnetic plate nature from aluminum and brass to glass generates lower shearing resistance force (figure 6.11).

It was also found that the shearing velocity has no effects on the values of F_{23} (figure 6.7) while the increase in particle volume fraction leads to its augmentation (figure 6.8). The measured resistance force F_{23} in this regime increases with the square of the magnetic field B^2 (figure6.4).

The total magnetic energy W_{mag} in terms of magnetic field B is:

$$W_{\text{mag}} = \int N\,I\,d\varphi = \int N\,I\,S\,dB = \int H\,V\,dB = \frac{B^2}{2\mu_0}V \tag{6.2}$$

and the normal magnetic force $F_\perp$, to the shearing plate surface, pushing the magnetic fluid and plate surface together will be given by:

$$F_\perp = \frac{dW_{\text{mag}}}{dx} = \frac{B^2}{2\,\mu_0}S \tag{6.3}$$

Where V and S represent the magnetic volume and surface.

The measured shear force F_{m} being dependent on the type of surface in contact, on the square of magnetic field B^2 (therefore the normal force $F_{\perp}$), and independent from the shearing strain $\dot{\gamma}$, we choose to model it by a friction model with C its sliding friction coefficient (Eq: 6.4).

$$\frac{F_m}{2} = C\,F_{\perp} \tag{6.4}$$

When studying the MRF internal structure with an applied magnetic field B to the fluid suspension, the literature reports two possible organisations of the magnetic particle within the fluid along the direction of the applied magnetic field B:

1. isolated chain structure [23, 4, 48];

2. bundle-like structures with a body centered tetragonal packing [38, 51, 35].

For the same particle volume fraction we suppose that the contact surface between the fluid internal structure and the shearing plate S_{shear} is not highly affected by the MRF internal structure, whereas the chaining of magnetized particles depends on the particle volumetric concentration ϕ; the increase in the MRF particle volume fraction ϕ leads to a larger number of magnetic chains or aggregates and hence a larger surface of contact (Eq: 6.5). We assume the existence of an effective shearing surface S_{eff} equal to the contact surface between the fluid magnetic structures and the shearing plate S_{eff} is less than the magnetized surface $S_{\mathrm{eff}} < S_{\mathrm{m}}$.

$$S_{\mathrm{eff}} = n_{\mathrm{cluster}}.S_{\mathrm{cluster}} \tag{6.5}$$

The experimental shearing surface ratios are:

$$r_{\text{exp-32\%/22\%}} = \frac{S_{\text{eff-32vol\%}}}{S_{\text{eff-22vol\%}}} = \frac{\zeta(\phi)_{32\text{vol\%}}}{\zeta(\phi)_{22\text{vol\%}}} = \frac{3.05 \times 10^2}{2.65 \times 10^2} = 1.15. \tag{6.6}$$

$$r_{\text{exp-40\%/32\%}} = \frac{S_{\text{eff-40vol\%}}}{S_{\text{eff-32vol\%}}} = \frac{\zeta(\phi)_{40\text{vol\%}}}{\zeta(\phi)_{32\text{vol\%}}} = \frac{3.86 \times 10^2}{3.05 \times 10^2} = 1.26. \tag{6.7}$$

The precision of our experimental measurements and the validity of our hypotheses are evaluated by calculating the accuracy e between theoretical and experimental ratios (r_{theo} and r_{exp}) of the sheared surfaces when varying the particle volume fraction.

The theoretical ratios r_{theo} and accuracy e are:

$r_{\mathrm{theo}} = \dfrac{S_{\text{shear-32vol\%}}}{S_{\text{shear-22vol\%}}} = \dfrac{\phi_{32\text{vol\%}}}{\phi_{22\text{vol\%}}} = 1.45$ and the accuracy will be e$= \frac{1.45-1.15}{1.45} = 0.2$;

$r_{\mathrm{theo}} = \dfrac{S_{\text{shear-40vol\%}}}{S_{\text{shear-32vol\%}}} = \dfrac{\phi_{40\text{vol\%}}}{\phi_{32\text{vol\%}}} = 1.25$ and e$=\frac{1.26-1.25}{1.26}=0.008$

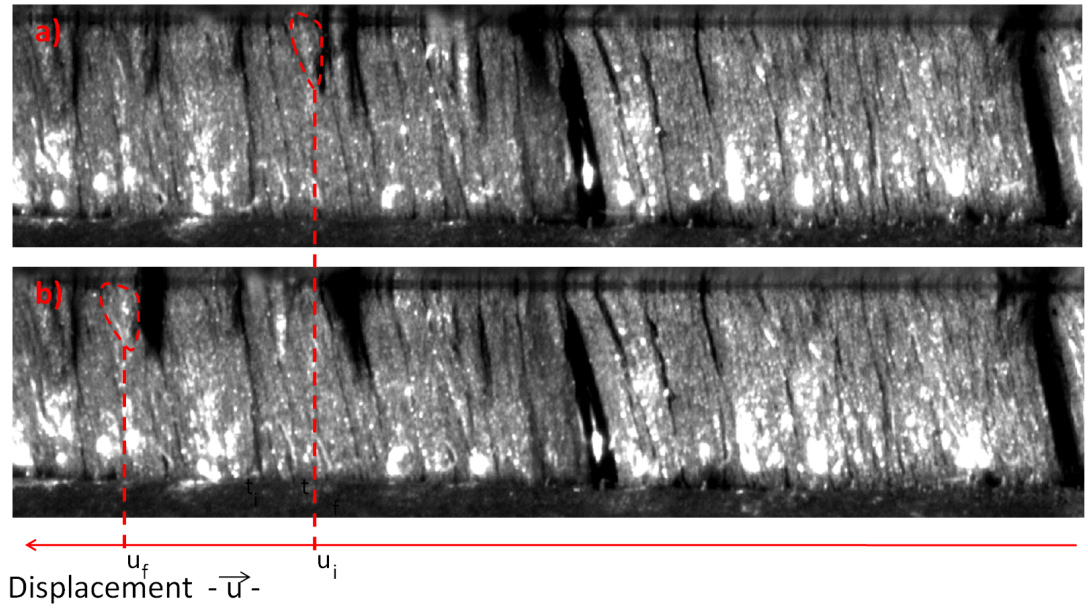

Figure 6.16 – Example of the MRF-132 internal structure in the sliding regime.

From figure 6.16 we can conclude that with a MRF-32vol% the ratio of $\frac{S_{\text{eff-32vol\%}}}{S_{\text{m}}}$=0.8 and hence $S_{\text{eff-32vol\%}} = 396\,10^{-6}m^2$. $S_{\text{eff-22vol\%}}$ and $S_{\text{eff-40vol\%}}$ are deduced as following:

$$S_{\text{eff-22vol\%}} = \frac{\phi_{32\%} S_{eff-22vol\%}}{\phi_{32\%}} = 495\,10^{-6}\text{m}^2;\; S_{\text{eff-40vol\%}} = \frac{\phi_{40\%} S_{eff-32vol\%}}{\phi_{32\%}} = 495\,10^{-6}\text{m}^2.$$

Figure 6.17a) presents the calculated values of the friction coefficient C (according to Eq: 6.4) for the three fluid concentration ϕ when varying magnetic field B. Figure 6.17b) represents the mean variation of the friction coefficient C and their standard variation.

We observe that the differences between the three mean values of the friction coefficient corresponding to the tested fluid concentrations are smaller than the standard deviations. This suggests that the observed differences are negligible when compared to the experimental variability. We can thus extract a common interval for the calculated friction coefficient C within the range of uncertainty of the three measurements. The values of the friction sliding coefficient C, calculated for a non-magnetic brass shearing plate, are $0.8 < C < 1.37$. These values seem to be logic for a friction coefficient.

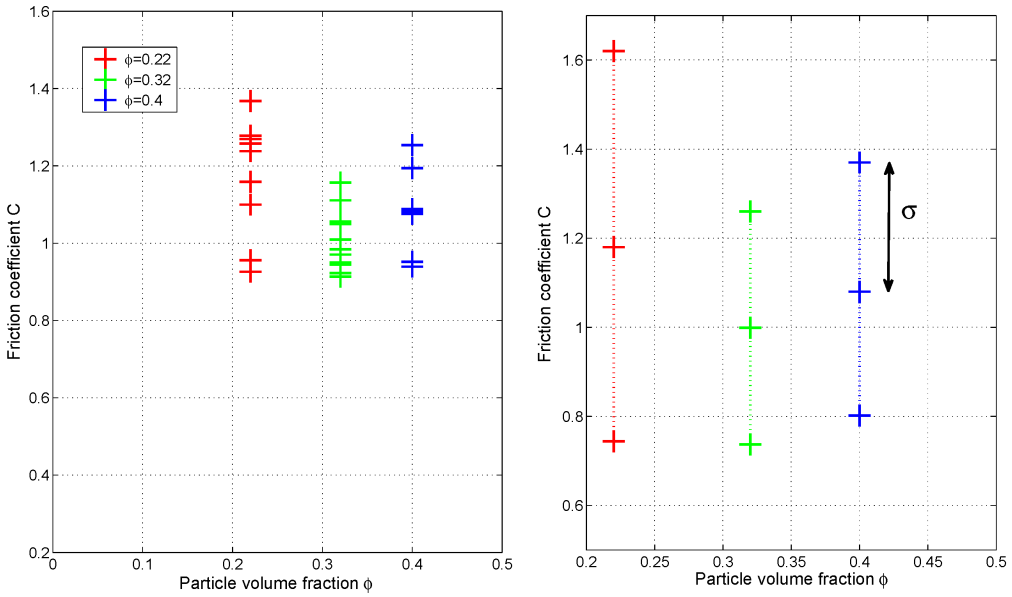

Figure 6.17 – Variation of the friction coefficient with ϕ.

5 Conclusion

From the above observations, one should conclude that no yield stress is reached in our case; the MRF aggregates do not break. The maximum measured stress corresponds to a friction force resulting from the sliding of the shearing plate over the MRF structure.

The magnetic field B, the particle volume fraction ϕ and the magnetic property of the shearing plate are the critical parameters that governs the strength of the measured F_{23}.

In conclusion I can say that the MRF response in the sliding shearing regime originates from a surface effect phenomenon.

Conclusion

As the literature suggests MR fluid has made significant advances. In this PhD report a review of the state of art in the MRF technology and in particular a focusing in the review of the MRF behavior modeling is presented. As the literature indicates, the basic model used to describe MRF behavior is the Bingham fluid model which predicts a Newtonian behavior once a yield-stress is reached. MRFs behavior in the pre-yield zone has received less attention.

Since the goal of my studies is to reproduce the traditional piano key haptic feedback, based on a controlled damping by a magneto-rheological fluid, it was essential to understand the MRF behavior below yield.

A designed measuring system was proposed to study the MRF in the pre-yield zone. The measuring device allows also the microscopic observations of the MRF internal structure, in the scale of its chain like structure, while shearing. With the present experimental setup it was not possible to carry out microscopic observations tests at the particle scale while shearing. However the present results suggested hypothethis on the MRF magnetic particles behavior in the different fluid regime response.

A series of rheological tests were carried out on the proposed experimental apparatus under a quasi-static constant velocity linear shearing. Effects of the magnetic field B, the shearing plate thickness e and nature, the shearing rate $\dot{\gamma}$, the particle volume fraction ϕ and the fluid internal structure were presented.

Based on the micro-structure of the MRF observed through SEM and high microscopy resolution, with and without magnetic field, the analysis of the interaction between particles and the macroscopic measured response to shearing, a microscopic model is proposed for the description of the MRF behavior below yield.

The investigation in the MRF response provided a reasonable explanation of the MRF response based on the MRF internal structure.

It was found that at little shear strain conditions, resulting stress are due to polymer shearing played an important role in the overall resulting stress. At larger shear strain conditions the resulting stresses are due to chain flexure and therefore magnetic field B will have the basic effect in the fluid response. Once the fluid chain gets to a stable state, bended chains, the sliding friction between the shearing plate and the sheared fluid will govern the MRF response.

The proposed model of the MRF behavior in the pre-yield regime combined to the Bingham model in the post-yield will allow the control of MRF and hence the command of several types of sensory interfaces.

Future work can address the physical nature of the MRF response on the scale of its magnetic particles. A real-time control scheme, of the proposed modified piano key, based on the proposed model of MRF behavior will also be achieved.

Bibliography

[1] M.K. Sain B.F. Spencer Jr., S.J. Dyke and J.D. Carlson. Phenomenological model of a magnetorheological damper. *ASCE Journal of Engineering Mechanics*, 1997.

[2] A. J. F. Bombard, M. R. Alcantara, M. Knobel, and P. L. O. Volpe. Experimental study of mr suspensions of carbonyl iron powders with different particle sizes, April 2005.

[3] Hyoung Jin Choi Bong Jung, Fei Fei Fang. Magnetorheology: materials and application. *Soft Matter*, 2010.

[4] G. Bossis, S. Lacis, A. Meunier, and O. Volkova. Magnetorheological fluids, November 2002.

[5] O BUTZ, T.; von Stryk. Modelling and simulation of electro- and magnetorheological fluid dampers. *MSC (2000): 65C20, 76A05*, 2000.

[6] P. Carletto and G. Bossis. Field-induced structures and rheology of a magnetorheological suspension confined between two walls. *Journal Of Physics-Condensed Matter*, 15(15):S1437–S1449, April 2003.

[7] J. D. Carlson. Critical factors for mr fluids in vehicle systems. *International Journal Of Vehicle Design*, 33(1-3):207–217, 2003.

[8] J. D. Carlson. Mr fluids and devices in the real world, April 2005.

[9] J. D. Carlson, D. M. Catanzarite, and K. A. StClair. Commercial magneto-rheological fluid devices, October 1996.

[10] Lord Corporation Thomas Lord Research Center. Engineering note designing with mr fluids. Technical report.

[11] K. C. Chen. On the macroscopic-mesoscopic mixture of a magnetorheological fluid. *Proceedings Of The Royal Society A-Mathematical Physical And Engineering Sciences*, 462(2068):1123–1144, April 2006.

[12] K. C. Chen and C. S. Yeh. Extended irreversible thermodynamics approach to magnetorheological fluids. *Journal Of Non-Equilibrium Thermodynamics*, 26(4):355–372, 2001.

[13] Wang XY Ni YQ. Chen, Z.Q. and LM. Ko. Field measurement on wind-rain-induced vibration of bridge cables with and without mr dampers", proe of the 3rd int. *Proc. of the 3rd Int. Conf. Structural Control, Como, Italy.*, 2002.

[14] 3 Le Sheng Chen2 QingWu1 Nan Liu1 Chen Fang1, Bin Yuan Zhao1 and Ke Ao Hu1. The effect of the green additive guar gum on the properties of magnetorheological fluid. *Smart Mater. Struct.*, 2004.

[15] H. J. Choi, B. J. Park, M. S. Cho, and J. L. You. Core-shell structured poly(methyl methacrylate) coated carbonyl iron particles and their magnetorheological characteristics. *Journal Of Magnetism And Magnetic Materials*, 310(2):2835–2837, March 2007.

[16] J. Claracq, J. Sarrazin, and J. P. Montfort. Viscoelastic properties of magnetorheological fluids. *Rheologica Acta*, 43(1):38–49, February 2004.

[17] A. Dominguez, R. Sedaghati, and I. Stiharu. A new dynamic hysteresis model for magnetorheological dampers. *Smart Materials & Structures*, 15(5):1179–1189, October 2006.

[18] Stiharu I Dominguez A, Sedaghati R. Modeling the hysteresis phenomenon of magnetorheological dampers. *Smart Mater Struct 13:1351Ũ1361*, 2004.

[19] P. Dominguez-Garcia, S. Melle, J. M. Pastor, and M. A. Rubio. Scaling in the aggregation dynamics of a magnetorheological fluid. *Physical Review E*, 76(5):051403, November 2007.

[20] Jeong-Hoi Koo Fernando D. Goncalves and Mehdi Ahmadian. A review of the state of the art in magnetorheological fluid technologies Ũ part i: Mr fluid and mr fluid models. *The Shock and Vibration Digest*.

[21] F. Gandhi and W. A. Bullough. On the phenomenological modeling of electrorheological and magnetorheological fluid preyield behavior. *Journal Of Intelligent Material Systems And Structures*, 16(3):237–248, March 2005.

[22] S. Genc and P. P. Phule. Rheological properties of magnetorheological fluids. *Smart Materials & Structures*, 11(1):140–146, February 2002.

[23] J. M. Ginder and L. C. Davis. Shear stresses in magnetorheological fluids - role of magnetic saturation. *Applied Physics Letters*, 65(26):3410–3412, December 1994.

[24] F. Gordaninejad, B. M. Kavlicoglu, and X. Wang. Friction factor of magneto-rheological fluid flow in grooved channels, April 2005.

[25] Y. M. Han, C. J. Kim, and S. B. Choi. A magnetorheological fluid-based multifunctional haptic device for vehicular instrument controls. *Smart Materials & Structures*, 18(1):015002, January 2009.

[26] J. M. He and J. Huang. Magnetorheological fluids and their properties, January 2005.

[27] H. Hirani and C. S. Manjunatha. Performance evaluation of a magnetorheological fluid variable valve. *Proceedings Of The Institution Of Mechanical Engineers Part D-Journal Of Automobile Engineering*, 221(D1):83–93, January 2007.

[28] S. R. Hong, S. John, N. M. Wereley, Y. T. Choi, and S. B. Choi. A unifying perspective on the quasi-steady analysis of magnetorheological dampers. *Journal Of Intelligent Material Systems And Structures*, 19(8):959–976, August 2008.

[29] S. R. Hong, N. M. Wereley, Y. T. Choi, and S. B. Choi. Analytical and experimental validation of a nondimensional bingham model for mixed-mode magneto rheological dampers. *Journal Of Sound And Vibration*, 312(3):399–417, May 2008.

[30] Hartmut janocha. Application potential of magnetic field driven new actuators. *Sensors and Actuators*, 2001.

[31] W. Matthis J.L. Sproston and J.R. Toscano. Industrial and commercial applications of smart structures technologies. In *SPIE Smart Structures and Materials 2001, pages 308Ũ316*, 2001.

[32] Moustafa Hafez José Lozada, Xavier Boutillon. A novel haptic interface for musical keyboards. *IEEE*, 2007.

[33] C. G. Joung and H. See. The influence of wall interaction on dynamic particle modelling of magneto-rheological suspensions between shearing plates. *Rheologica Acta*, 47(8):917–927, November 2008.

[34] H. J. Jung, B. F. Spencer, Y. Q. Ni, and I. W. Lee. State-of-the-art of semiactive control systems using mr fluid dampers in civil engineering applications, March 2004.

[35] J. O. Fossum K. D. Knudsen K. P.S Parmar, Y. Meheust and D. M. Fonesca. Packing and voids in electro-rheological structures of polarized clay particles.

[36] N. C. Kavlicoglu, B. M. Kavlicoglu, Y. M. Liu, C. A. Evrensel, A. Fuchs, G. Korol, and F. Gordaninejad. Response time and performance of a high-torque magneto-rheological fluid limited slip differential clutch. *Smart Materials & Structures*, 16(1):149–159, February 2007.

[37] H. M. Laun and C. Gabriel. Measurement modes of the response time of a magneto-rheological fluid (mrf) for changing magnetic flux density, May 2007.

[38] Ping Sheng Lei Zhou, Weijia Wen. Ground states of magnetorheologicall fluids. *Physical Review letters*, 1998.

[39] W. H. Li, H. Du, G. Chen, S. H. Yeo, and N. Q. Guo. Nonlinear rheological behavior of magnetorheological fluids: step-strain experiments. *Smart Materials & Structures*, 11(2):209–217, April 2002.

[40] W. H. Li, B. Liu, P. B. Kosasih, and X. Z. Zhang. A 2-dof mr actuator joystick for virtual reality applications. *Sensors And Actuators A-Physical*, 137(2):308–320, July 2007.

[41] W. H. Li and X. Z. Zhang. The effect of friction on magnetorheological fluids. *Korea-Australia Rheology Journal*, 20(2):45–50, June 2008.

[42] B. Liu, W. H. Li, P. B. Kosasih, and X. Z. Zhang. Development of an mr-brake-based haptic device. *Smart Materials & Structures*, 15(6):1960–1966, December 2006.

[43] R. Lima N.Aubry, R.Guyonnet. Spatio temporal analysis of complex signals: Theory and applications. *Journal of Statistical Physics 64 (1991) 683-739*, 1991.

[44] G. T. Ngatu, N. M. Wereley, J. O. Karli, and R. C. Bell. Dimorphic magnetorheological fluids: exploiting partial substitution of microspheres by nanowires. *Smart Materials & Structures*, 17(4):045022, August 2008.

[45] C. Olmi, G. Song, and Y. L. Mo. An innovative and multi-functional smart vibration platform. *Smart Materials & Structures*, 16(4):1302–1309, August 2007.

[46] X. Q. Peng, F. Shi, and Y. F. Dai. Magnetorheological fluids modelling: without the no-slip boundary condition. *International Journal Of Materials & Product Technology*, 31(1):27–35, 2008.

[47] H. See. Field dependence of the response of a magnetorheological suspension under steady shear flow and squeezing flow. *Rheologica Acta*, 42(1-2):86–92, January 2003.

[48] H. Si, X. Peng, and X. Li. A micromechanical model for magnetorheological fluids. *Journal Of Intelligent Material Systems And Structures*, 19(1):19–23, January 2008.

[49] In Bae Jang Hyoung Jin Choi* Sung Taek Lim, Min Seong Cho. Magnetorheological characterization of carbonyl iron based suspension stabilized by fumed silica. *Journal of magnetism and magnetic materials*, 2004.

[50] R. Tao. Super-strong magnetorheological fluids. *Journal Of Physics-Condensed Matter*, 13(50):R979–R999, December 2001.

[51] Hongru Ma Zhifang Lin Wing Yim Tam C.T Chan Weijia Wen, Ning Wang and Ping Sheng. Field induced structural transition in mesocrystallites. *Physical Review Letters, Volume 82, Number 21*, 1998.

[52] www.Lord.com. Mr products - lord corporation- magneto-rheological - military suspensions. Technical report.

[53] G. Z. Yao, F. F. Yap, G. Chen, W. H. Li, and S. H. Yeo. Mr damper and its application for semi-active control of vehicle suspension system. *Mechatronics*, 12(7):963–973, September 2002.

[54] X. Z. Zhang, X. L. Gong, P. Q. Zhang, and Q. M. Wang. Study on the mechanism of the squeeze-strengthen effect in magnetorheological fluids. *Journal Of Applied Physics*, 96(4):2359–2364, August 2004.

[55] ZIPSER. Magnetorheological fluides for actuators. 2000.